Title

Photophysical and Structural Properties of CdTe and HgTe Semiconductor Nanoplatelets Arising from their Two-Dimensional Morphology

Permalink

Author

Tenney, Stephanie Marie

Publication Date

2023

Peer reviewed|Thesis/dissertation

UNIVERSTY OF CALIFORNIA

Los Angeles

Photophysical and Structural Properties of CdTe and HgTe Semiconductor

Nanoplatelets Arising from their Two-Dimensional Morphology

A dissertation submitted in partial satisfaction

of the requirements for the degree Doctor of Philosophy

in Chemistry

by

Stephanie Marie Tenney

2023

ABSTRACT OF THE DISSERTATION

Photophysical and Structural Properties of CdTe and HgTe Semiconductor

Nanoplatelets Arising from their Two-Dimensional Morphology

by

Stephanie Marie Tenney

Doctor of Philosophy in Chemistry

University of California, Los Angeles, 2023

Professor Justin Ryan Caram, chair

Semiconductor nanoplatelets (NPLs) are nanocrystals with quantum confinement only in the thickness dimension and precise monolayer thicknesses. They have excellent monodispersity giving them narrow linewidths, high absorption cross-sections, and high photoluminescence quantum yields. In addition to their exceptional photophysical properties, they can have lateral extents that exceed 1000 nm, making them analogous to two-dimensional semiconductors such as transition metal dichalcogenides with the advantage of colloidal preparation. In this dissertation I explore how interesting photophysical properties can arise within these materials as a result of their anisotropic structure. Chapter 1 provides the foundation for understanding the electronic and physical structures of NPLs, briefly summarizes the current understandings in the field, and presents open questions that this dissertation aims to address.

In Chapter 2, we develop a new type of heterostructure through cation exchange from CdTe to HgTe NPLs. HgTe NPLs are promising candidates for optoelectronic applications in the short-

wave infrared (SWIR), but their absorption and photoluminescence has limited tunability. By taking advantage of their large, exposed surfaces following cation exchange, we grow HgTe quantum dots (QDs) on the lateral faces and establish a heterostructure capable of energy transfer from 2D NPL to 0D QD. We extend the tunability of photoluminescence through the energy transfer by controlling the confinement within the quantum dot, and observe high quantum yields across the SWIR.

Chapter 3 builds on our understanding of the HgTe NPL/QD heterostructure by exploring the mechanism and efficiency of energy transfer in greater depth. We compare the in-situ grown QD on NPL system to a system of mixed QDs and NPLs and demonstrate that the near unity energy transfer is only achieved using the in-situ method. We quantify this efficiency and find that the mixed case follows a Förster Resonance Energy Transfer while the in-situ case is likely a near field energy transfer. Using our estimates, we also model the exciton diffusion within HgTe NPLs and find that the magnitude of the diffusion constant is comparable to other extended 2D semiconductors.

In Chapter 4 we turn our focus to synthetic procedures for CdTe NPLs to control lateral area. We develop a seeded growth mechanism that can be used to reproducibly extend NPLs from their small size after initial synthesis (100-500 nm) to mesoscale length scales (1-2 μm). We show that these methods can be applied to CdTe and CdSe, and cation exchange from these extended NPLs produces mesoscale HgTe and HgSe NPLs. Using in-situ monitoring, we examine how the seeded growth proceeds and show that the extension follows the understood mechanism of lateral ripening. Finally, we image the photoluminescence of the mesoscale NPLs using correlative microscopy and demonstrate that their large extents allow for spatial resolution of their photophysical properties.

Chapter 5 develops another synthetic procedure for controlling lateral extent, but without the need for seeded growth. By closely examining the parameters used during a slow injection procedure, we are able to understand how the precursor, temperature, and ligands play a role in NPL area and directly synthesize mesoscale NPLs in one step. We systematically show how each parameter affects the lateral size and monolayer thickness of the final NPL product. Using the largest mesoscale NPLs, we use transmission electron and atomic force microscopy to examine their propensity for stacking, as well as Raman spectroscopy to observe strain with spatial resolution.

Chapter 6 describes a handful of remaining experiments and projects that were not fully developed for publication. This also includes some techniques and lessons learned in sample handling which may be useful for future students.

Finally, Chapter 7 describes our efforts in chemical education research within the general chemistry laboratory course for life science majors at UCLA. In this chapter we examine how the style of pre-lab affects student performance when tasked with learning a new technique. A cohort of students critically evaluate a series of videos demonstrating exemplary technique and poor technique before attending their lab sections, and these students are compared to a cohort who simply watched the exemplary technique before starting the experiment. Our goal is to reduce cognitive load during the experiment by establishing the proper steps before attempting to practice the technique. We show that although the majority of the class is unaffected by the intervention, we are able to reduce the percentage of students performing as outliers. We also demonstrate that the intervention reduces the dependence of students on instructor feedback during the lab sessions which is advantageous for large classrooms.

The thesis of Stephanie Marie Tenney is approved.

Richard Kaner

Chong Liu

Benjamin Schwartz

Justin Ryan Caram, Committee Chair

University of California, Los Angeles

2023

To my mom and dad, for aways being proud of me.

TABLE OF CONTENTS

LIST OF FIGURES

LIST OF TABLES

ACKNOWLEDGEMENTS

My journey in completing my PhD at UCLA would not have been possible without the following people. Their consistent support and community gave me the strength to find persistence and accomplish my goals.

First, I would like to thank my PhD advisor Justin Caram. It was clear from the start that his mentorship and research would be a great fit for me, and I have had an excellent experience in his group. Justin has always been encouraging of scientific and professional growth, pushing me to learn new skills and seek out opportunities for career development. He has also always been kind, supportive during challenging times, and kept my best interests in mind without question. Justin, I am beyond grateful to have had the opportunity of being your student and member of the group.

I would also like to thank my advisors within my teaching positions, Jennifer Casey and Arlene Russell. They are exemplary role models for teaching chemistry, and their enthusiasm for education sparked my interest in teaching and mentorship. Within my role as a graduate teaching assistant, they involved me in discussions about the course logistics and taught me how to incorporate evidence-based methods into practice. Teaching 14BL and 14AE were some of my most meaningful experiences at UCLA. They also gave me a new insight into science education through research. I am incredibly grateful for the opportunity to work with them and for their continued guidance and support.

I would like to thank my committee, Richard Kaner, Chong Liu, and Benjamin Schwartz who have offered invaluable advice and expertise throughout my time at UCLA. Ben was supportive as a teacher and mentor during my first years of coursework. Chong provided feedback on manuscripts and gave scientific advice that strengthened the impact of our work. Ric gave

excellent feedback during my candidacy exams that lead to further experiments with interesting results. All committee members gave me insight and advice on career development, suggesting opportunities and connections that helped me determine my path forward.

Within the chemistry department, I am grateful for the collaboration and support from so many other students and colleagues. Ellen Sletten was always very generous in allowing me to use her instrumentation and her students Maly Cosco, Anthony Spearman, and Ceasar Garcia helped me countless times with my experiments. Xiangfeng Duan's students Kijoon Bang and Boxuan Zhou provided help with sample preparation and Raman measurements that will lead to new collaborations. The department also has amazing staff including Ricky, Jose, and Nati who were always willing to help me troubleshoot my maintenance and supply needs. Maria and Zaneta in lab support were always dependable when teaching lab courses.

I feel incredibly lucky to have been able to work with and get to know all the members of the Caram Lab—I can't thank you all enough for the support and friendship that helped me over the past several years. Tim Atallah, you were an amazing mentor, giving me both scientific and general advice that helped me through the most challenging years of my PhD. You pushed me to explore questions that led to entire projects and were always willing to listen to any questions I had. Your mentorship largely shaped the way I approach science and I am lucky to also have you as a friend. Anu Deshmukh, Hannah Friedman, Danielle Cadena, and Danielle Koppel, my first years helping establish the lab and learning from you all were so much fun. I learned so much within such a short period of time, and you continued to give me mentorship that I was grateful for in later years. Victoria Vilchez and Sandrine Ithurria were incredible collaborators during my first project, teaching me the basics of nanoplatelets and providing research advice that led to many more interesting projects. Ashley Shin, Jill Williams, Anthony Sica, Austin Bailey, Belle Coffey,

xix

Tasnim Ahmed, and Richard Liu, your friendship made this experience so valuable, and I can't express how much I enjoyed our time spent together. TD Tan, Barry Li, Yongjia He, and Ash Hua, I really enjoyed having you all around in the office and lab—your presence always brightened my days. Elijah Cook, Arthur Odenheimer, Caleb Pike, and Lexi Wright, we didn't get much time to spend together but I am confident that you will lead the group in many interesting directions going forward. Finally, to the amazing undergraduate students Mika Sonnlietner, Chengye Huang, Laurie Tan, and Ricky Ronquillo, I truly would not have been successful in my research without your enthusiasm, trust, and many hours of dedication. Each of you exceeded my expectations and I am proud to have been a part of your scientific careers as your mentor and friend. I can't wait to see where your endeavors take you.

Lastly, I would like to thank my close friends and family for your unwavering support and love throughout this experience. Sidney and Hani, our virtual happy hours kept me sane over the past few years and I'm glad we were able to stay connected despite such great distances. Matt, some of my best memories in Los Angeles are of our outdoors and food explorations, and I was very lucky to have you there as a friend from the beginning. Alex, I am so grateful to have met you in our courses together at UCLA. You continued to become an amazing best friend, providing me with strength and many wonderful memories. Monica, you were truly a pillar for me during this experience, giving me confidence and encouragement, and more importantly for believing in me no matter what. I can't thank you enough for your constant support and for being an amazing partner. Granny, Shell, Ryan, and Peyton, you were always interested and encouraging about my studies, and I always looked forward to our beach weekends or holiday visits. Finally, Dad, Mom, Rebekah, and Aaron, you were always supportive of me in exploring my many interests which led

to me pursuing a career in science. Thank you for always standing by me throughout my decisions and for being there when I needed your help and guidance. I love you all very much.

Chapter 1 contains unpublished work by Stephanie Tenney

Chapter 2 contains work from the published paper "Tenney, S. M.; Vilchez, V.; Sonnleitner, M. L.; Huang, C.; Friedman, H. C.; Shin, A. J.; Atallah, T. L.; Deshmukh, A. P.; Ithurria, S.; Caram, J. R. Mercury Chalcogenide Nanoplatelet–Quantum Dot Heterostructures as a New Class of Continuously Tunable Bright Shortwave Infrared Emitters. *J. Phys. Chem. Lett.* **2020**, 3473–3480." SMT conducted experiments with VV, MS, and CH. AJS took spectroscopy measurements, TLA and HF provided discussion, TLA did reabsorption correction analysis. All authors provided editing, and SI and JRC were advisors.

Chapter 3 contains work from the unpublished paper in preparation "Tenney, S.M.; Tan, L.A.; Tan, X.; Sonnlietner, M.L.; Coffey, B.; Williams, J.; Ronquillo, R.; Atallah, T.L; Ahmed, T.; Caram,J.R. Efficient 2D to 0D Energy Transfer in HgTe Nanoplatelet-Quantum Dot Heterostructures through High-Speed Exciton Diffusion. *In preparation.*" SMT and LAT conducted experiments. XT completed FRET modeling. BC, RR, and TA collected spectra. JW collected TEM images. TLA and JRC provided advising.

Chapter 4 contains work from the published paper "Tenney, S.M.; Tan, L.A.; Sonnleitner, M.S.; Sica, A.V.; Shin, A.J.; Ronquillo, R.; Ahmed, T.; Atallah, T.L.; Caram, J.R. Mesoscale

Quantum-Confined Semiconductor Nanoplatelets through Seeded Growth. *Chem. Mater.* **2022**, 34, 13, 6048–6056." SMT conducted experiments with LAT, MS, and RR. TLA and AVS acquired photoluminescence images and AJS assisted with image processing and alignment. TA collected quantum yields and lifetimes. All authors edited the paper. JRC was the main advisor.

Chapter 5 contains work from the unpublished paper in preparation "Tenney S.M.; Ronquillo R; Williams. J; Ahmed, T.; Caram, J.R. Slow-Injection Gives Access to Lateral Size Control in CdTe Nanoplatelets. *In preparation."* SMT and RR conducted experiments. JW collected AFM measurements; TA collected quantum yields. JRC was the main advisor.

Chapter 6 contains preliminary and unpublished work by Stephanie Tenney

Chapter 7 contains work from the unpublished paper in preparation "Tenney, S.M.; Casey, J.R.; Rusell, A. Critiquing Lab Technique Videos Prior to Class. Can it Improve Demonstrated Technique? *In preparation.*" SMT completed data analysis. JRC conducted literature review and wrote the introduction sections. All authors edited the paper. JRC and AR provided advising.

BIOGRAPHICAL SKETCH

Education

2020 M.S. in Materials Chemistry

University of California, Los Angeles (UCLA)

2018 B.A. in Chemistry

Johns Hopkins University (JHU)

Publications

5. **Tenney, S.M**.; Tan, L.A.; Sonnleitner, M.S.; Sica, A.V.; Shin, A.J.; Ronquillo, R.; Ahmed, T.; Atallah, T.L.; Caram, J.R. Mesoscale Quantum-Confined Semiconductor Nanoplatelets through Seeded Growth. *Chem. Mater.* **2022**, 34, 13, 6048–6056.

4. Shin, A.J.; Hossain, A.; **Tenney, S. M.**; Tan, X.; Tan, L.A.; Foley, J.J.; Atallah, T.L.; Caram, J.R. Dielectric Screening Modulates Excitons in Nanoplatelets. *J. Chem. Phys.* **2021**, *12* (20), 4958-4964.

3. **Tenney, S. M**.; Vilchez, V.; Sonnleitner, M. L.; Huang, C.; Friedman, H. C.; Shin, A. J.; Atallah, T. L.; Deshmukh, A. P.; Ithurria, S.; Caram, J. R. Mercury Chalcogenide Nanoplatelet–Quantum Dot Heterostructures as a New Class of Continuously Tunable Bright Shortwave Infrared Emitters. *J. Phys. Chem. Lett.* **2020**, 3473–3480.

2. Li, M. M.; Claire, F. J.; Solomos, M. A.; **Tenney, S. M**.; Ivanov, S. A.; Siegler, M. A.; Kempa, T. J. Molecular Chains of Coordinated Dimolybdenum Isonicotinate Paddlewheel Clusters. *RSC Adv.* **2019**, *9* (29), 16492–16495.

1. Claire, F. J.; **Tenney, S. M**.; Li, M. M.; Siegler, M. A.; Wagner, J. S.; Hall, A. S.; Kempa, T. J. Hierarchically Ordered Two-Dimensional Coordination Polymers Assembled from Redox-Active Dimolybdenum Clusters. *J. Am. Chem. Soc.* **2018**, *140* (34), 10673–10676.

Presentations

2022 Center for Education, Innovation and Learning in the Sciences (UCLA) *(poster)*

2022 Biennial Conference on Chemical Education (Purdue University, IN) *(oral)*

2022 Materials Research Society Spring Conference (Honolulu HI) *(poster)*

2021 UC Chemical Symposium (Virtual) *(oral)*

2020 Organization for Cultural Diversity in Sciences, Research Presentation (UCLA) *(oral)*

2019 Glenn T. Seaborg Symposium (UCLA) *(poster)*

2019 American Chemical Society National Conference (San Diego CA) *(poster)*

Professional Employment

2021 Summer Research Intern

     Thin Films and Surfaces

     Corning Inc, Corning NY

Awards and Honors

2022 Graduate Division Dissertation Year Fellowship

2022 Materials Research Society Conference Best Poster Nominee

2021 Michael E. Jung Excellence in Teaching Award

2021 Jim and Barbara Tsay Excellence in Second Year Research and Academics Award

2019 Seaborg Symposium Poster Presentation Winner

2019 ACS San Diego Research Showcase Fellowship

2019 Stones Fellow

2018 Graduate Dean's Scholar Award

2014 JHU Bloomberg Scholar Award

Chapter 1

Introduction to Semiconductor Nanoplatelets

1.1 Historical Overview of Quantum Confined Semiconductor Nanocrystals

Semiconductor nanocrystals (NCs) are nanoscale crystallites (typically with few-nanometer diameters) that have been studied since the early 1980s for their exceptional light-matter interactions. Their crystal structures and solid-state properties are determined from their parent semiconductor composition, but many photophysical properties can be altered and realized by their small sizes. Alexei Ekimov, Alexander Efros, and Louis Brus led the first efforts towards synthesis of these materials by creating CuCl in a glassy matrix and aqueous colloidal suspensions of CdS.[1–3] These studies were later expanded to include Zn, Cd, and Pb sulfides and selenides.[4] Coined "quantum dots" (QDs), these materials exhibited a quantum mechanical phenomenon by the confinement of excitons due to the size of the particles (Figure 1.1a). This confinement can be modeled using a simple particle in a box model, where an exciton is confined within a zero potential box (NC) with infinite potential energy barriers outside of the box. The exciton is free to move within the length of the box, and its energy can be described by solving the Schrodinger Equation given that the wavefunction is limited to the size (L) of the box (equation 1.1).

$$E_n = \frac{n^2\pi^2\hbar^2}{2mL^2} \tag{1.1}$$

To describe the bandgap of a quantum confined semiconductor, one must consider how the bulk bandgap is affected by confinement. Two major effects are observed when the Bohr radius is confined. First, because the Bohr radius of the exciton in the bulk is larger than the physical size of the NC particle (box), it is considered quantum confined and its lowest energy transition increases relative to the bulk bandgap energy. (Figure 1.1b). The second effect is a change in the density of states near the band edges which results in fewer, discretized states that are dependent

on the morphology of the particle. This leads to different observed spectra for spheres, rods, or sheets. The general Hamiltonian for the lowest excited state is shown below in equation 1.2 where m_e and m_h are the effective masses of the electron and hole respectively.[4]

a)

Confined Exciton

diameter < bulk exciton
Bohr radius

b)

Energy

Bulk Semi-conductor

Semi-conductor Nanocrystal

Atomic Limit

unocccupied

E_{fermi}

occupied

Density of States

c)

decreasing size
increasing energy

Optical Density

21 Å diameter
23 Å
27 Å
30 Å
40 Å

CdSe

1.8 2.0 2.2 2.4 2.6 2.8 3.0 3.2 3.4 3.6
Energy (eV)
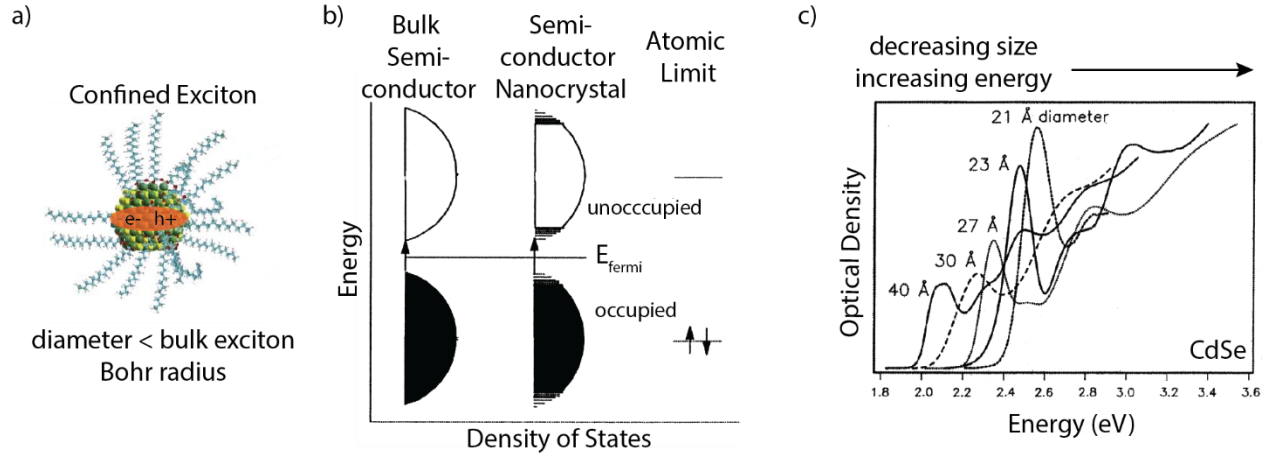
Figure 1.1 *a) an exciton confined by the size of the quantum dot diameter, b), and c). Figure a is adapted with permission from Ref 5, copyright 2011 Springer Nature. Figures b and c are adapted with permission from Ref 6, copyright 1996 American Chemical Society.[5,6]*

$$\hat{H} = \frac{-\hbar^2}{2m_e}\nabla_e^2 \frac{-\hbar^2}{2m_h}\nabla_h^2 - \frac{e^2}{\epsilon|r_e-r_h|} \tag{1.2}$$

The analytical solution for this Hamiltonian (equation 1.3) shows that the confined band gap (ΔE) is a sum of the bulk band gap, the confinement energy, and the bound exciton energy (coulombic interaction between electron and hole), where E_g is the bulk band gap, r^2 is the radius of the NC, and ϵ is the dielectric constant. The relationship between the semiconductor's quantum confined bandgap (ΔE) and the radius of the particle (r) shows that as the particle size decreases, the bandgap will increase. Another subtle consequence of this $1/r^2$ dependence is that changes in size have a much larger effect on the bandgap for small particles than they do for larger particles.

$$\Delta E\ (r) = E_g + \frac{\hbar^2\pi^2}{2r^2}\left(\frac{1}{m_e} + \frac{1}{m_h}\right) - \frac{1.8e^2}{\epsilon r} \tag{1.3}$$

Synthetic control over size therefore allows for tunability over wavelength of absorption and emission of the semiconductor (Figure 1.1c). Their photophysical tunability became revolutionary as one could change the optical properties of a semiconductor without changing the composition and do so using low-temperature colloidal syntheses. These materials quickly gained interest for their promising optoelectronic applications, and research efforts began focusing on both synthesis and photophysical understandings of these materials.

Continued advances through the 1990s involved a greater understanding of synthetic control and growth kinetics to improve the quality of colloidally grown QDs. Core-shell NCs were developed where an outer shell of a semiconductor with a different composition than an inner core provided a passivating layer for surface defects—significantly improving the core photoluminescence and providing greater tunability.[7–9] If the shell is a wider bandgap material, the exciton stays localized in the core. If it is smaller or aligned lower in energy than the core bandgap, then the electron and/or hole can be localized into the shell resulting in a shift in the emission. The monodispersity and crystallinity of cadmium chalcogenide QDs (CdS, CdSe, CdTe) was also improved through using a coordinating phosphine solvent such as trioctlyphosphine oxide (TOPO).[10] This ligand helped to stabilize the colloidal nanocrystals and improve their surfaces by passivating defects and dangling bonds, resulting in the removal of sub-band trap emission. Further significant advances in QD synthesis involved the development of safer procedures using CdO (compared to the highly toxic $Cd(CH_3)_2$), and a robust exploration of surface chemistry of different passivating ligands.[11]

To date, QDs have been realized of nearly every known semiconductor including group IV (Si), III-V (InGaAs, GaN), II-VI (ZnSe, CdSe, HgSe), III-VI (PbSe, PbS) and perovskites.[10,12–17] The possible morphologies of NCs have also expanded, from the 0D quantum dots, to 1D

nanorods, wires, and rings, and 2D nanosheets.[18–20] The remainder of the text will focus on the 2D nanosheet, called "nanoplatelet" (NPL), its synthesis and photophysical properties.

1.2 Structural Properties of II-VI NPLs
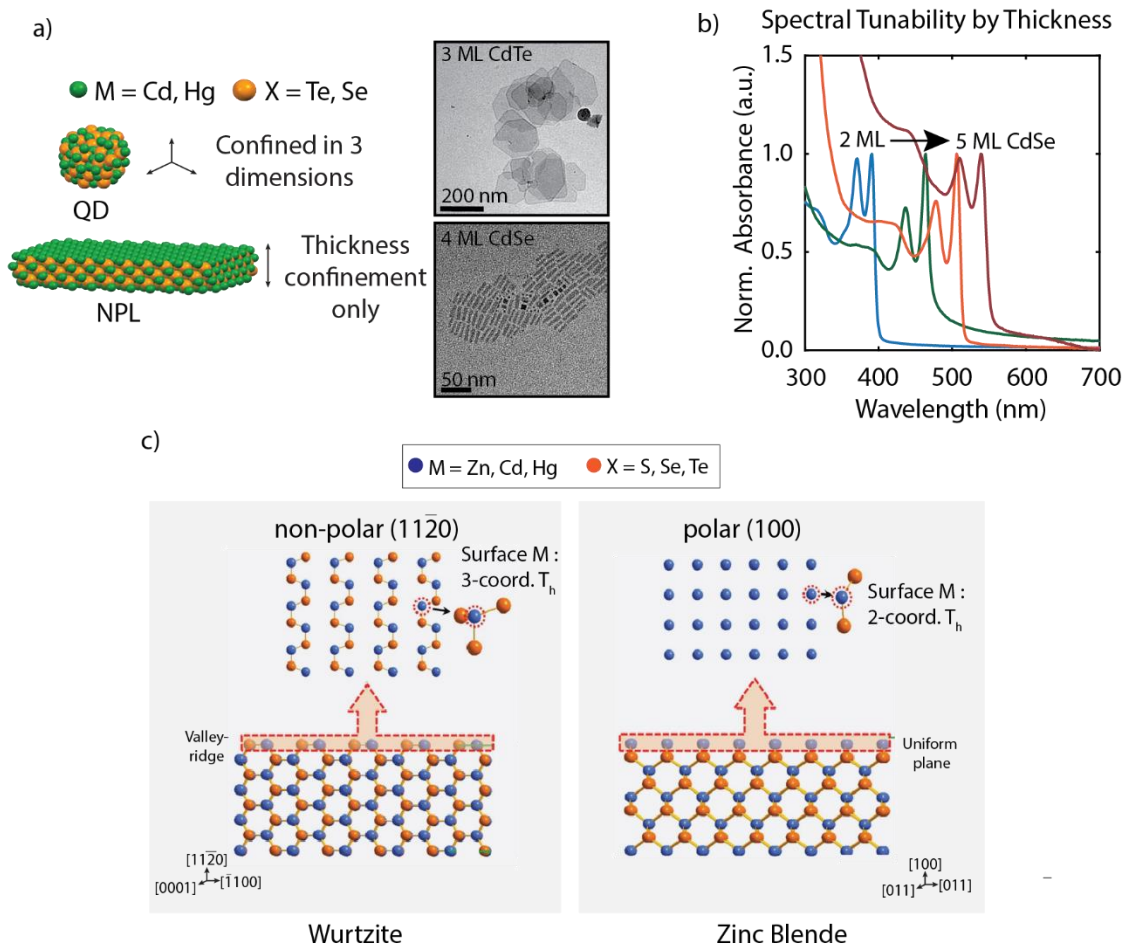
Figure 1.2 a) Scheme showing the quantum confinement occurs only in the thickness dimension in NPL and representative TEM images, b) the thickness can be used to tune absorption and emission properties, and c) the structural differences between wurtzite and zinc blende NPLs. The scheme depicts a cross-sectional view highlighting the surface facets and binding geometry of exposed atoms. Adapted with permission from Ref 21.[21] Copyright 2018 American Chemical Society.

Semiconductor nanoplatelets (NPLs) were first discovered in the mid-2000s by Sandrine Ithurria and Benoit Dubreret.[20,22] The earliest accounts focused on CdX (X= S, Se, Te), but have

since also been synthesized from HgX, PbX, and perovskites.[23–25] They display quantum confinement in only the thickness dimension (typically 1-2 nm) and can be laterally much larger, affording them a two-dimensional morphology (Figure 1.2a). Their absorption and emission properties are therefore tunable by changing their thickness although strain, ligand coverage, and dielectric interactions can also affect the wavelength of lowest transitions (Figure 1.2b).[26,27] Their unique morphology gives NPLs exceptional photophysical properties which have gained much attention and will be discussed further in section 1.4.

The quantum confinement of NPLs arises from their thickness dimension, where the thickness must be smaller than the exciton Bohr radius. For example, the bulk Bohr radius for CdSe is 5.4 nm while the total thickness of CdSe NPLs is typically 1-2 nm or 7-9 atoms thick. This extreme level of confinement is difficult to reach in other morphologies (QDs for example) but can be well controlled with a high degree of precision in NPLs. Their lateral size can range from few nm (where lateral confinement is also possible) up to many microns, but typical reported NPL synthesis produces lateral dimensions of 100-500 nm along its longest edge.[28]

II-VI NPLs can adopt either a wurtzite or zinc blende structure (Figure 1.2c). The wurtzite structure is hexagonal and is synthesized using an amine lamellar template.[29–31] The facets are primarily non-polar (with the exception of their small end facets) and have an equal number of metal and chalcogen atoms exposed on the surfaces in a ridge-valley configuration.[32] Zinc blende NPLs, on the other hand, are synthesized with carboxylate ligands and are primarily polar on the top and bottom facets, and nonpolar on the sides. They demonstrate a monolayer-type structure with alternating layers of metal and chalcogen, but always have one extra metal layer such that the outer surfaces are metal terminated. They are frequently referred to by their number of monolayers (ML)—for example a 3 ML NPL contains 4 metal layers (3 + one extra surface layer) and 3

chalcogen layers. The difference in surfaces for wurtzite and zinc blende NPLs imparts different growth dynamics, ligation properties, and lateral size/shape. Their surfaces are typically passivated with organic ligands as will be discussed further in section 1.5.

1.3 Synthesis of II-VI Semiconductor Nanoplatelets (NPLs)
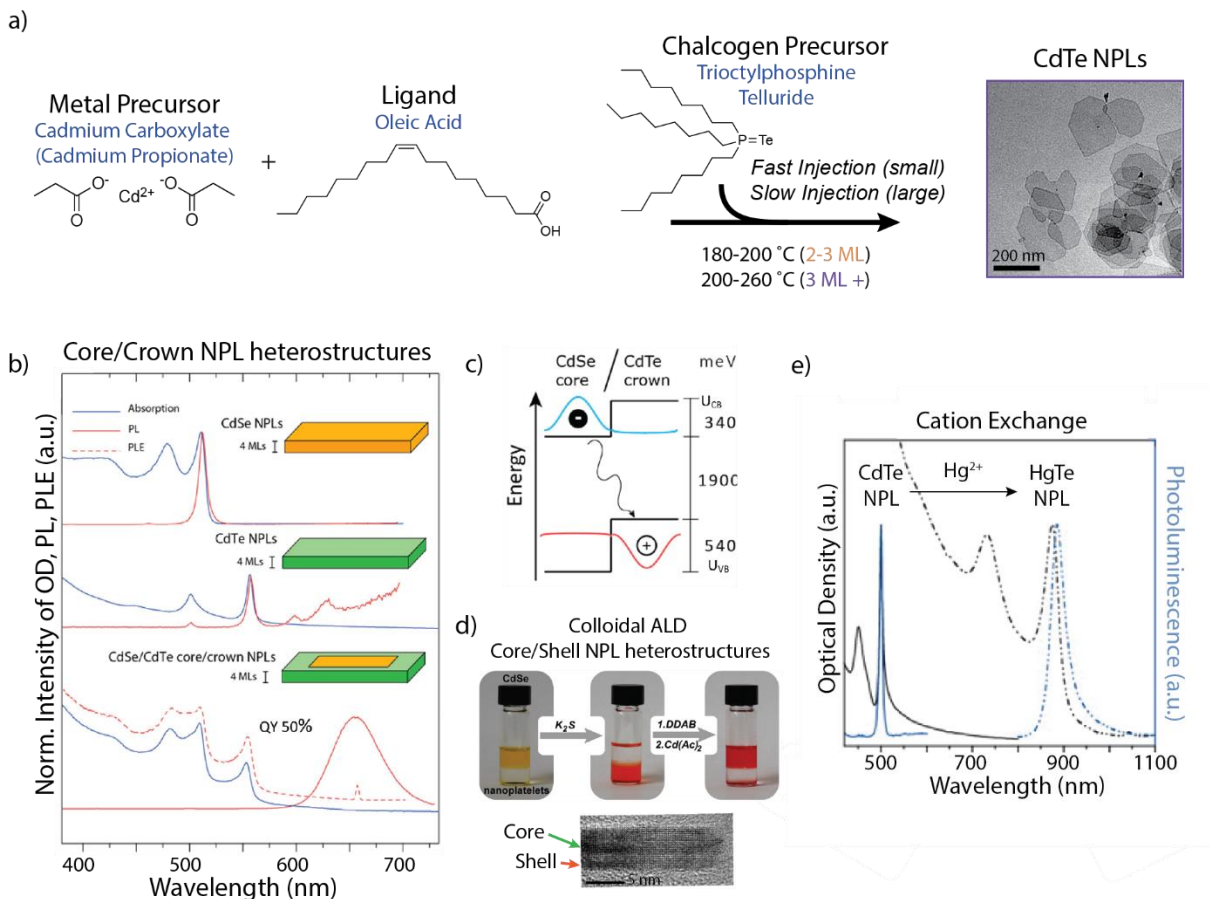
Figure 1.3. *a) A general synthetic scheme for CdTe NPLs which requires a metal precursor, ligand, and chalcogen precursor, b) core/crown CdSe/CdTe NPLs showing bright PL, c) band diagrams of CdSe and CdTe showing exciton recombination across the interface in type-II NPL heterostructure, d) colloidal ALD using phase transfer to add top and bottom layers for core/shell NPLs, and e) cation exchange demonstrating shift in absorption and PL from visible to near-infrared. Figure 1.3b-e are adapted with permission from Refs 33, 34, and 35. Copyright 2014 and 2016 American Chemical Society.*[33–35]

The synthesis of NPLs is quite similar to QDs, but with a few notable differences. NPL growth requires a cadmium carboxylate precursor (QDs typically only require CdO), a phosphine-chalcogenide (TOP-Te or TOP-Se), and a carboxylate ligand (Figure 1.3a). The cadmium precursor is typically in excess so that the reaction can be controlled using the injection and concentration of the chalcogen precursor. The reaction is typically done at temperatures between 180-250 ºC (this is lower than the typical QD temperature of 250-300 ºC), and the chalcogen injection can be conducted either rapidly or slowly. The combination of lower temperatures, higher local precursor concentration, and control over reaction kinetics is hypothesized to lead to 2D formation rather than spherical QD growth, though the precise mechanism remains an open question.[36]

Various modulation of structures including heterostructures of NPLs have been demonstrated including core/crown and core/shell NPLs. Core/crown NPLs involve a two-step synthesis where a core is first made following typical procedures, and then used to seed a second synthesis where the chalcogen precursor is of a different composition (Figure 1.3b). The resulting structure has the core composition in the center and the crown composition around the edges. This can result in a type-II heterostructure such as CdSe/CdTe where the exciton is delocalized into the crown or type-I such as in CdSe/CdS where it stays localized to the core (Figure 1.3c).[33,37] For core/shell syntheses, layers must be added on one by one to the top and bottom facets, alternating between metal and chalcogen using colloidal ALD (Figure 1.3d). This method takes advantage of phase transfer by solubilizing the metal and chalcogen into separate polar and non-polar phases, and cycling the nanoplatelet between the phases to sequentially build up layers.[34] This works for CdS, CdSe, and ZnS, but has limitations for tellurides, likely because there are fewer available Te precursors and CdTe NPLs are very sensitive to harsh reactants.[38,39]

Additional compositions of semiconductor NPLs are accessible through cation exchange (Figure 1.3e). In these procedures, a pre-synthesized core is introduced to a solution containing cations of another metal, and the host cations are replaced with guest cations without interrupting the existing network of anions. Cation exchange readily proceeds from ZnSe to CdSe, and from CdSe to HgSe in NCs because of the similar crystal structures.[40,41] In NPLs, cation exchange has been demonstrated from CdSe to ZnSe, CdX (X= Se, Te) to HgX, and from CdSe to PbSe.[23,35,42–44] In addition to providing tunable transitions by altering the bandgap, cation exchange gives access to NPL morphology for compositions where direct synthesis is not yet available. For example, a direct synthesis of HgX NPLs has not been demonstrated, but high quality HgX NPLs can be achieved through exchange from their parent CdX NPLs.

1.4 Current Understanding of Growth Mechanisms
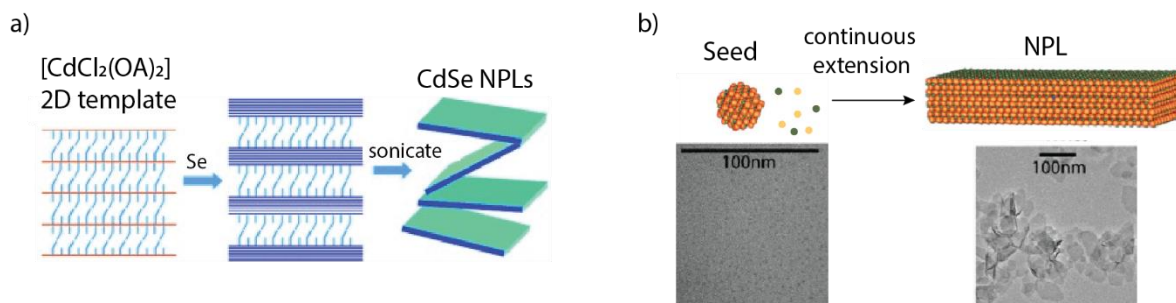
Figure 1.4. Early proposed mechanisms for NPL growth. a) Templated growth of lamellar CdSe NPLs, and b) continuous extension of seeds by free monomer into 2D NPLs. Adapted with permission from Refs 29 and 45.[29,45] Copyright 2009 John Wiley and Sons and 2011 American Chemical Society.

The origin of NPL's 2D morphology has been explored in recent years and a few mechanisms of their growth have been proposed. Early studies utilizing amine ligands showed that a soft colloidal template could be used to grow CdSe lamellar NPLs.[29] The cadmium halide/amine self-organizes and template either stabilizes assemblies of CdSe or directs nucleation in 2D (Figure

8

1.4a). This mechanism has only been shown to produce wurtzite II-VI NPLs, however, and did not explain the growth of the more common zinc blende II-VI NPLs. In 2011, zinc blende CdSe was synthesized using a heat-up method and by monitoring TEM of aliquots, the authors proposed that small seeds form followed by lateral extension without any change in thickness.[45] This mechanism was explained as a continuous extension of seeds to NPLs (Figure 1.4b), where free monomer from solution adds onto a seed rather than oriented attachment of multiple seeds and recrystallization which was shown for PbS NPLs.[46] Later in 2019, in-situ small-angle x-ray scattering during NPL growth proved the absence of a lamellar template and confirmed continuous growth through monomers instead of seed attachment.[47]
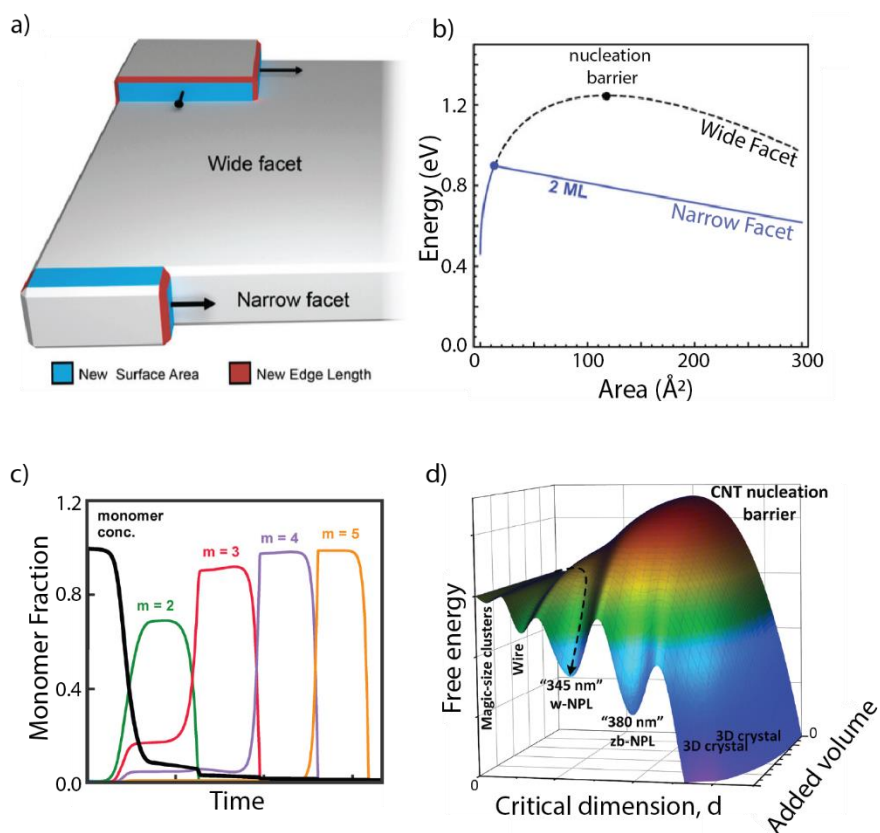
Figure 1.5. Recent mechanisms of NPL growth. a) Growth proceeds by islands reaching the critical size before nucleation across facet is favorable and b) the nucleation barrier on narrow facets are lower than the wide facet. c) Thickness evolution proceeds through lateral ripening

where thinner NPLs deposit monomer onto thicker NPLs. d) In ZnSe, a unified reaction pathway can be used to predict morphology at a given temperature. Adapted with permission from Refs 36, 48, and 49.[36,48,49] Copyright 2017 Springer Nature, 2017 and 2020 American Chemical Society.

None of these studies, however, could explain the puzzling nature of how 2D growth is possible from a cubic zinc blende crystal structure. Typically, anisotropic nanocrystals take advantage of an axis or plane of asymmetry to direct growth along certain dimensions. In 2017, the kinetic instability model was proposed to describe that by kinetically controlling the reaction, a difference in energetic barrier for nucleation arises for the wide and narrow facets of a NPL (Figure 1.5a,b) driving growth in 2D.[36] The model suggests that because a high precursor concentration is required for NPL growth, diffusion to the NPL is so fast that the reaction is limited by nucleation of islands on their surfaces. The island must nucleate and reach a critical size for it to be able to expand and create a new layer, which is more energetically favorable to occur along the sides of the NPL rather than the top because of a smaller critical size. The model also predicted thermodynamic stability of NPLs with thickness; thinner NPLs grow fastest but are least stable and will eventually evolve into thicker NPLs. A more thorough explanation of the NPL thickness evolution was proposed shortly thereafter, by lateral ripening.[48,50] In this model, the early nucleation event in the NPL reaction produces seeds of many sizes, and the concentration of monomer is important for controlling which population is present. After monomer gets incorporated into the thinner, faster growing NPLs, the free monomer concentration drops and the NPLs become soluble. They then dissolve and deposit monomer onto thicker seeds and continuation of this cycle results in successively thicker NPL growth (Figure 1.5c).

These ideas were expanded to ZnSe NPLs, where a general reaction pathway was proposed to unify magic-sized 0D clusters, 1D nanowires, 2D NPLs, and 3D nanocrystals.[49] This mechanism

proposes that the reaction trajectory depends on the energy provided to overcome nucleation barriers, and can be related back to classical nucleation theory where the favorable volume formation and unfavorable surface area formation strongly depends on morphology (Figure 1.5d). Therefore, the choice of temperature provided to overcome activation barriers can predict the morphology of the final product. While similar to CdX NPLs, this mechanism does not explain how ripening in CdX NPLs is observed by holding the NPL solution at a constant temperature for prolonged periods of time.

1.5 Photophysical Properties of II-VI NPLs
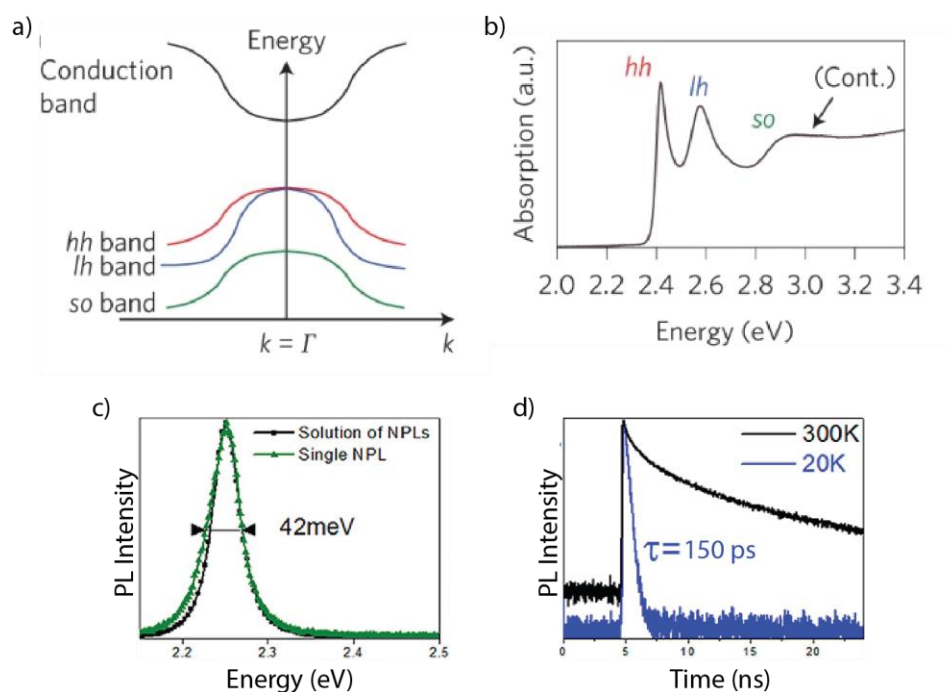
Figure 1.6. *The a) band diagram illustrating the band-edge transitions, and b) a representative absorption spectrum highlighting these transitions. Their PL b) has narrow linewidths, similar for both single and ensemble NPLs, and d) shows fast radiative lifetimes. Adapted with permission from Refs 51 and 52.*[51,52]*Copyright 2017 Springer Nature and 2012 American Chemical Society.*

The general absorption and emission properties of NPLs are summarized in Figure 1.6. They typically have a band-edge in the visible for CdX NPLs and in the Near-IR to IR for HgX NPLs. The excitonic features appear as sharp transitions in the absorption spectrum and arise from the

splitting of the valence band by spin-orbit coupling into a heavy-hole and light-hole (hh and lh) along with a higher energy split-off (so) band (Figure 1.6a and 1.6b). The transitions are slightly offset from the bandgap by their exciton binding energies (few hundred meV) and can also be affected by strain.[26] Their photoluminescence comes from the lowest energy hh transition which is a direct transition, typically has a very small Stokes-shift, and can have a high QY (> 80%) — making NPLs very good emitters.[53] They also have large radiative decay rates with lifetimes in in the picosecond to nanosecond range (Figure 1.6d).[52] The controllable thickness of NPLs gives them spectral tunability from the visible to near-IR, similar to other II-VI colloidal nanocrystals. Their 2D extent, however, results in photophysical properties that have drawn much interest to NPLs for optoelectronic applications. From their synthesis, only integer monolayer thicknesses are reported, and often only one population at a time. This gives NPL ensemble solutions extremely narrow linewidths from their monodispersity with a full-width half-maximum of <50 meV for CdSe, unlike QD solutions where monodispersity is often challenging (Figure 1.6c).[52]
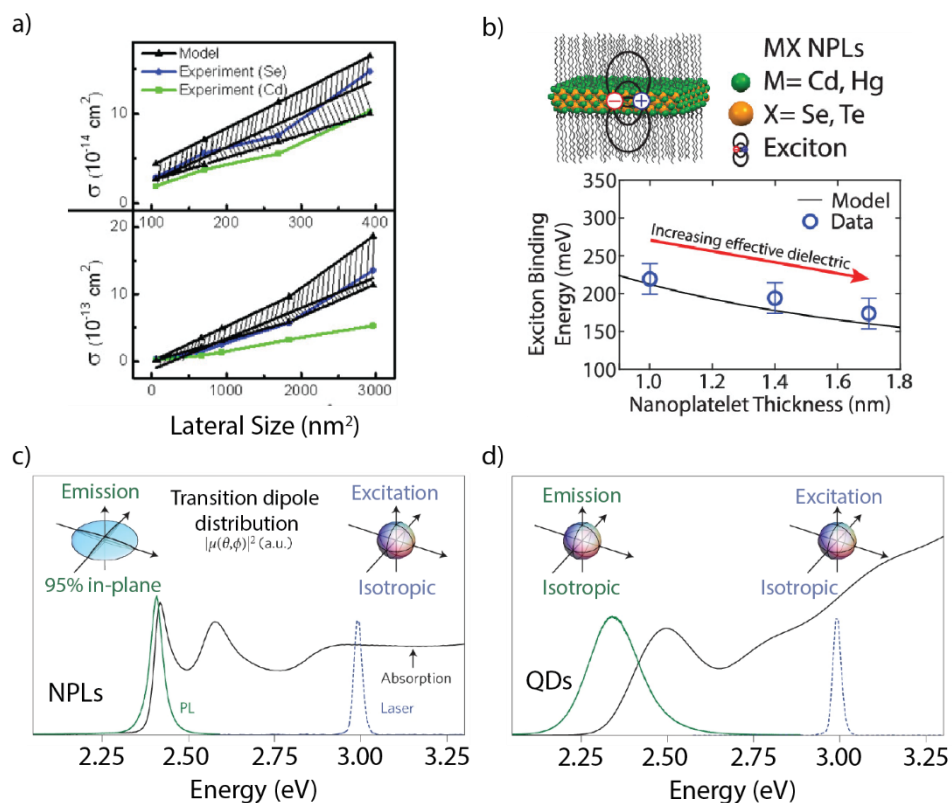
Figure 1.7. *a) The absorption coefficient of NPLs scales with lateral size, b) their exciton binding energy is large due to the external dielectric, c) NPLs display directed emission along the plane of the lateral area unlike d) QDs which emit isotropically. Adapted with permission from Refs 27, 51, and 54.*[27,51,54] *Copyright 2015 and 2021 American Chemical Society and 2017 Springer Nature.*

Their 2D extent affords NPLs giant oscillator strength transitions and high absorption cross-sections which scales with their lateral area (Figure 1.7a), giving them promise in efficient light absorbing devices.[20,54] They also have large exciton binding energies (~150-650 meV) due to their finite thickness and influence of the external dielectric.[27] The electric field lines from the electron-hole coulombic interaction in the exciton extend into the surrounding ligands which have a much lower dielectric than the semiconductor NPL (Figure 1.7b). This reduces the ability to screen charge and the resulting binding energy of the 2D exciton is stronger than a bulk 3D exciton.[55] The binding energy is also able to be modulated by changing the dielectric of the surrounding environment, which can be used to fine-tune the lowest energy transition.

Their anisotropic shape also gives rise to directed emission; the heavy hole exciton in NPLs has an anisotropic transition dipole which aligns with the lateral plane. Scott et al. (Achstein) showed that 95% of the emission in NPLs occurs in-plane when excited with an isotropic source, compared to quantum dots which show isotropic emission (Figure 1.7c and d).[51] The heavy-hole Bloch state has mixed p_x and p_y symmetry (unlike the light hole and split off band which contain p_x, p_y and p_z) which creates an electronic dipole along the xy (lateral) plane of the NPL. Since the heavy hole is the lowest energy transition, most of the emission is then directed along this anisotropic orientation which gives promise for energy collection and funneling applications such as solar cells or luminescent solar concentrators.

1.6 Surface and Ligand Environment of II-VI NPLs
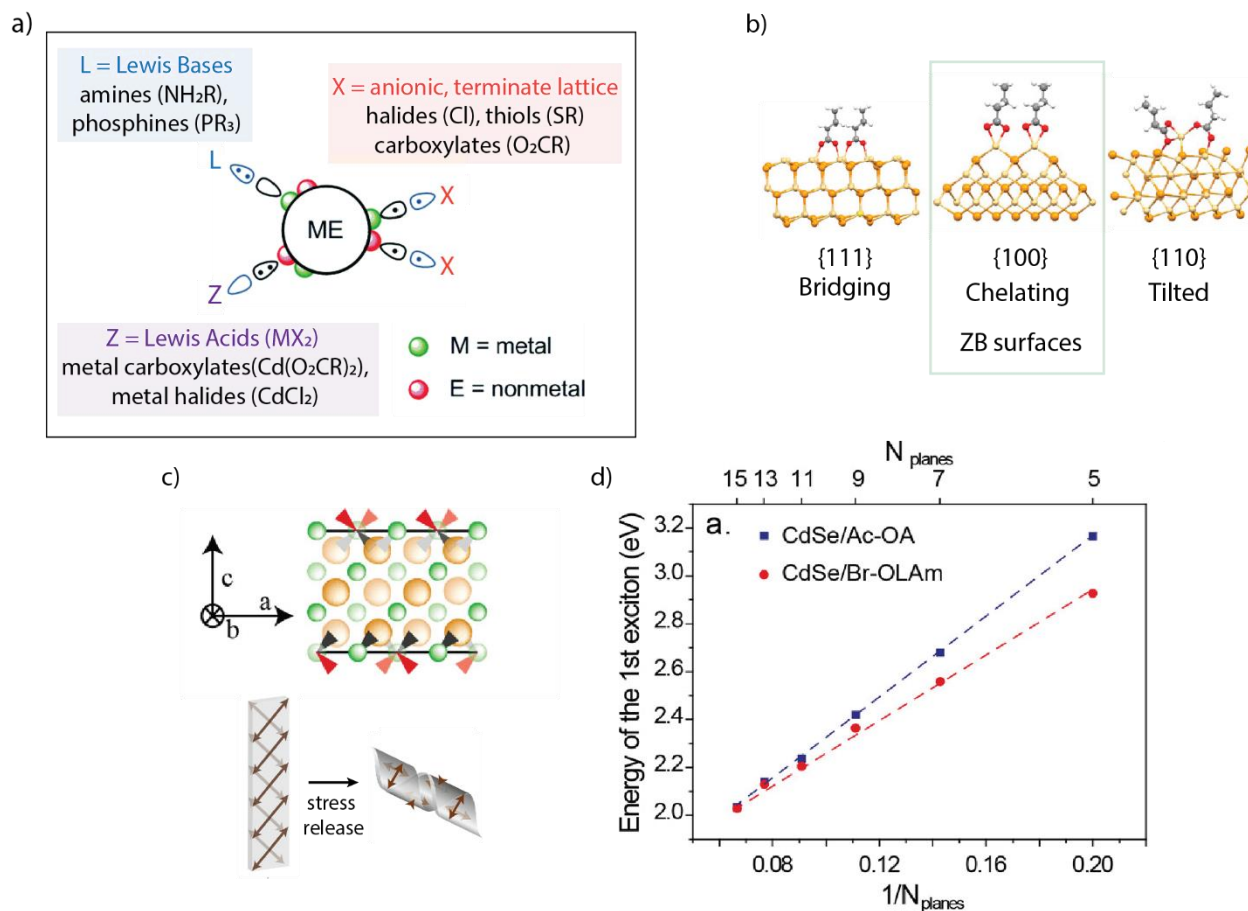
Figure 1.8. *a) The classification of ligand types by the number of electrons donated to a NC-ligand bond, b) the binding motifs of ligands based on the exposed facet, c) strain induced by orientation of the top and bottom facet bonds, and d) strain induced and released by ligand type. Adapted with permission from Refs 26, 56, and 57.*[26,56,57]*Copyright 2016 Royal Society of Chemistry, 2019 American Chemical Society.*

Due to their flat, anisotropic morphologies, NPLs have a higher surface-to-volume ratio than other nanocrystals such as QDs. Their surface chemistry therefore becomes important and can strongly influence their structural and photophysical properties. NPLs are terminated with metal (or non-metal) atoms that are bound to ligands—typically long chain organic compounds such as carboxylic acids or amines. The ligand's primary role is to passivate charge and defects

with its polar headgroup while allowing the nanocrystal to remain colloidally suspended in solution via the nonpolar tail.

Classification of ligands follows the covalent bond classification method (Green nomenclature), where ligands are described by the number of electrons that the ligand donates to the ligand-NC bond (Figure 1.8a).[56,58,59] L-type ligands are Lewis bases which donate 2 electrons, and bind to surface metal atoms. Z-type ligands are Lewis acids which donate 0 electrons, and bind to surface non-metal atoms. Finally, X-type ligands are typically anionic, contribute 1 electron, and might bind with either the metal or non-metal atoms.

In NPLs, the type of ligand necessary for effective passivation depends largely on the outer surfaces, which are polar (metal terminated) in zinc blende, and non-polar (with equal parts metal and non-metal) in wurtzite crystal structures—as shown previously in Figure 1.2c. The difference in facets results in a different preference for type of ligand.[32] Zinc blende NPLs have polar charged Cd atom surfaces and can be passivated by X type ligands (commonly carboxylates such as long-chain oleates and short chain acetates). Ligand exchanges from X to Z or L are typically not very successful and may lower the photoluminescence quantum yield. For example, CdSe NPLs passivated with carboxylates will readily undergo a ligand exchange from carboxylate to halide or thiol (X to X') and remain stable, but exchange from carboxylate to amine (X to L) is unsuccessful unless it undergoes an intermediate halide exchange step to form a cadmium halide-amine complex.[26,32] It is worth noting that the surface metal atom such as cadmium typically has a strong binding affinity for X type ligands such as carboxylates and once passivated, the cadmium-carboxylate will participate in further ligand exchanges as a Z type unit and can remove surface Cd atoms.[59] On the other hand, wurtzite NPLs have non-charged surfaces and can be passivated

by Z or L ligands (commonly amines or MX_2 ligands). They will readily and reversibly undergo a ligand exchange between the two types of ligand without removal of surface atoms.[32]

Zinc blende NPLs are commonly passivated with carboxylates which could bind monodentate or bidentate. A computational and experimental study of bidentate carboxylates on different facets revealed that the chelating motif is the dominant binding mode for II-VI ZB NPLs, as their surfaces are entirely {100} facets (Figure 1.8b).[57] Their side facets are largely {110} and have very weakly coordination through the tilting mode, but recent evidence also predicts that the edges may be comprised of {111} or {101} facets as well depending on the ratio of precursors used.[60] The ligand desorption energy of Cd terminated {111} or {101} facets are much lower than the {100} or Se terminated {111} facets, which may contribute to the current understanding of growth along a certain direction or facet leading to different aspect ratios in NPLs.

The coverage of ligands on nanocrystal surfaces can typically be quantified using titration studies which utilize a displacement of ligands through exchange. Early work by Anderson et al. (Owen) found that CdSe QDs contain about 3.3–3.7 carboxylates per nm^2.[59] They also note that the photoluminescence quantum yield is very sensitive to coverage, and is near 0 once the coverage drops to or below 2 carboxylates per nm^2. The coverage is slightly higher in NPLs due to their large flat faces which can accommodate more ligands – 5.4 carboxylates per nm^2, of which 3.4 were classified as strongly bound by a computational study.[61] This was confirmed in a similar study which demonstrated a coverage of 5.4 (compared to the theoretical 5.5) ligands per nm^2 on the surfaces, and barely, if any, passivation on the sides.[57]

Finally, ligands can have a strong effect on the morphology of the NPL, mainly through strain effects. ZB NPLs have an intrinsic strain that results from the additional layer of surface metal, which always imposes a difference of 90 degrees in the orientation of the top vs bottom

surface bonds (Figure 1.8c). In addition, the ligands may impart additional strain if the lattice spacing does not match the preferred spacing of ligands—as is the case for CdX terminated with carboxylates. This results in a slight tetragonal distortion where the thickness axis compresses slightly, and has the strongest effect in thinner NPLs (Figure 1.8d).[26] In CdSe, NPLs will commonly twist or bend to relieve this strain, but CdTe will remain flat as it consists of more polarizable atoms and has a slightly larger lattice parameter. Ligand exchange to halides or amines can also relieve this strain, unroll the highly twisted NPLs, and improve the photoluminescence quantum yield (Figure 1.8d).[26]

1.7 Comparisons to Other Materials and Applications

As will be explored in more detail in later chapters, NPLs are highly analogous to 2D semiconductors such as transition metal dichalcogenides (TMDs). These materials are typically comprised of a metal such as molybdenum or tungsten and a chalcogen such as sulfur, selenium, or tellurium. Similar to NPLs, TMDCs can be isolated with different layer thicknesses, and their electronic bandgap will increase with decrease thickness.[62] Both NPLs and TMDCs show dielectric confinement effects due to their finite thicknesses and favorable photophysical properties for optoelectronic applications.[27,55,63] Unlike NPLs, TMDCs are typically generated through mechanical or chemical exfoliation, whereas NPLs are grown through colloidal solution based synthesis and are passivated with organic ligands. NPLs also have much higher photoluminescence quantum yields than TMDs, making them more favorable for light-emitting applications.[64,65] Despite their differences, the lateral extent and morphology of NPLs allows one to draw strong comparisons to these 2D semiconductors and will be discussed further in Chapters 4 and 5. Perovskite NPL synthesis has been developed very recently in the literature and shows promise

for photovoltaic application, however further studies to enhance their stability and seperation from stacks to single NPLS to make them competitive with II-VI NPLs are still needed.[66,67]

Applications of NPLs are largely focused on light absorbing and emitting devices due to their photophysical properties. NPLs have been explored for lasing, as their lateral size and giant oscillator strength of NPLs was shown to have strong effects on their lasing thresholds, which were up to 10 times lower than QDs.[68] Heterostructure compositions further enhance the potential for NPLs as an optical gain media due to the ability to extend the lifetime of multiexcitons through spatial seperation between a core and crown for example, and increased absorption cross sections.[69,70] Copper doping of CdSe NPLs for Stokes-shift engineering has also been shown to give excellent light concentration properties for luminescent solar concentrators with near-unity quantum efficiency.[71] The sharp absorption features in NPLs is highly beneficial for minimizing reabsorption losses, and the dopant can be tuned to push the emission far red enough that reabsorption becomes negligible which is crucial for an efficient LSC. Finally, the most explored application for NPLs is in light emitting diodes (LEDs). NPLs have very narrow linewidths compared to other semiconductor nanocrystals, and as such are valued for their color purity. NPLs display electroluminescence and devices from NPLs of different colors (primarily green and red) have reached high external quantum efficiencies.[72,73] Composition tuning through alloying and heterostructures have also allowed for a continuous range of accessible colors and NPLs with bicolor emission.[74,75]

1.7 Remaining Questions and Challenges
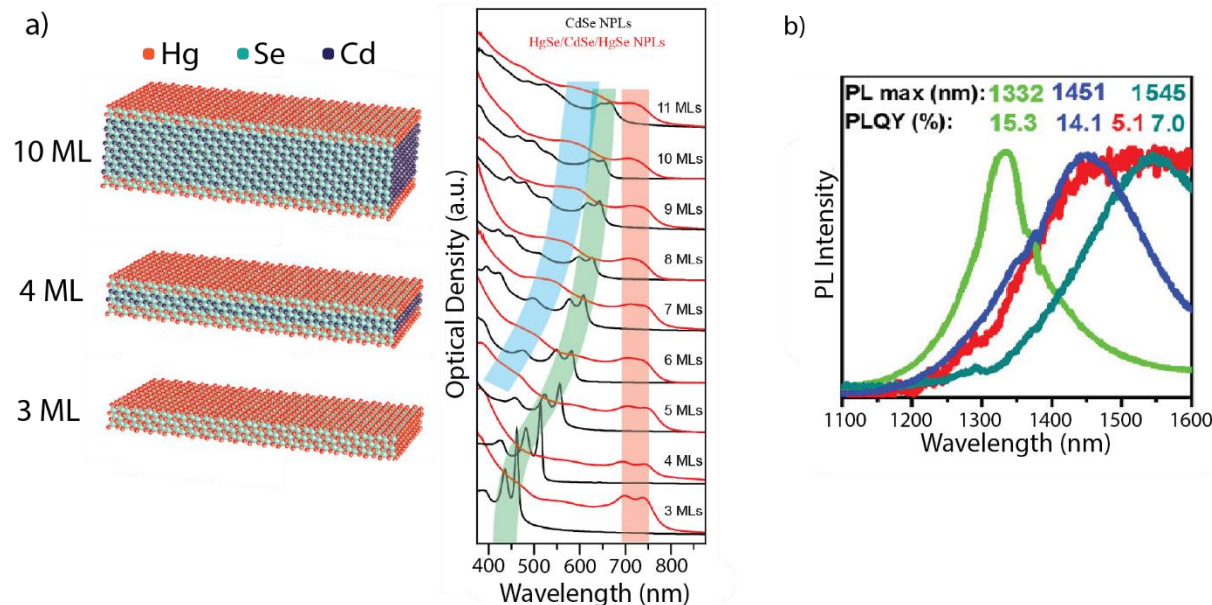
Figure 1.9. *Infrared emissive NPLs. a) Cation exchange from CdSe to HgSe demonstrates that exchange only works up to 3ML. b) PbSe NPLs show emission up to 1600 nm. Adapted with permission from Refs 23 and 76.*[23,76] *Copyright 2018 and 2019 American Chemical Society.*

Expansion of Infrared emissive NPLs

The shortwave infrared (SWIR, 1000-2000 nm) is a promising spectral region for imaging and telecom. Along with lower Rayleigh scattering, photons within this window are often lower in energy than electronic transitions and higher in energy than vibrational modes which reduces background absorption and emission. While some organic chromophores and nanocrystals have been developed within the SWIR, the range of materials with promising optical properties is not yet fully explored.[77,78] NPLs with infrared emission have been limited to 3 ML HgTe (near-IR) and PbSe.[35,76,79] HgX NPLs have not yet been grown through direct synthesis, and require a cation exchange from CdX NPLs. While the cation exchange is a straightforward procedure, it requires the HgX NPL to maintain the structure of the original NPL and is also limited in thickness. Hg^{2+} cations will only exchange with the outer 3ML of the CdX NPL. If the parent CdX NPL is thicker,

cation exchange will produce a core/shell heterostructure (Figure 1.9a).[23] This 3ML limit only allows for absorption and emission up to the near-infrared (~900 nm). Cation exchange from CdSe to PbSe does work beyond 3 ML (up to 6 ML) with emission up to 1600 nm, but the photoluminescence quantum yields remain below 20%, and lifetimes are long—between 0.7 and 2.7 microseconds.[76] HgTe NPLs show much shorter lifetime of 50 ns.[35]

To overcome this synthetic barrier, either i) a direct synthesis towards HgX NPLs should be developed, or ii) cation exchange should be improved to work beyond 3 ML. For direct growth, the major challenge is that HgTe QDs are the favorable product when using common conditions and precursors for NPL synthesis. They will nucleate at low temperatures (even below room temperature).[80] To overcome this, careful consideration of precursors is likely to be necessary to inhibit 3D QD growth. For cation exchange, an understanding of why it only works for 3 ML should be explored. Most likely, the diffusion of the larger Hg^{2+} cation might not be favorable beyond a certain thickness, however this has only been explored in HgSe. Cation exchange with a slightly smaller Pb^{2+} works up to 6 ML.[76] CdTe may demonstrate greater diffusion of guest cation into the NPL due to its slightly larger lattice constant than CdSe, but synthesis of CdTe beyond 3 ML is also lacking.

Expanded Understanding of Growth Mechanisms

A more fundamental question remaining is how to control the lateral size of NPLs. Because NPLs have many similar properties to 2D materials such as TMDs, they offer a middle ground between nanocrystals and 2D semiconductors. The major limitation for implementing NPLs in 2D material applications is that their lateral size is still orders of magnitude smaller than can be physically manipulated. The growth mechanisms have only recently been explored in the literature, but many aspects of their formation are still unclear. Every variable in the NPL synthesis

from precursors to temperature to time can have a significant influence on the final product (whether it be NPL size, thickness, quality, etc.). There does not yet exist a single theory that unifies how these variables all come together, but it is necessary for the rational design of large area NPLs. There are not any spectral signatures of lateral size, unlike thickness, so producing NPLs with a specific lateral size can be inefficient and labor intensive. With a clear understanding of how monomer adds onto NPLs under different conditions, areal control can be added to the toolbox of NPL tunability and these materials can then be utilized as extendable 2D semiconductors rather than just as colloidal nanocrystals.

The remainder of the thesis will focus on work done in the Caram Lab to overcome or provide insight into some of these limitations. This includes creating a new NPL heterostructure for tunable SWIR emission and developing synthetic procedures to controllably extend the lateral size of NPLs both in seeded and direct growth.

REFERENCES

(1)   Ekimov, A. I.; Efros, A. L.; Onushchenko, A. A. Quantum Size Effect in Semiconductor

        Microcrystals. *Solid State Commun.* **1985**, *56* (11), 921–924.

(2)   Rossetti, R.; Nakahara, S.; Brus, L. E. Quantum Size Effects in the Redox Potentials,

        Resonance Raman Spectra, and Electronic Spectra of CdS Crystallites in Aqueous

        Solution. *J. Chem. Phys.* **1983**, *79* (2), 1086–1088.

(3)   Brus, L. E. Electron-Electron and Electron-Hole Interactions in Small Semiconductor

        Crystallites: The Size Dependence of the Lowest Excited Electronic State. *J. Chem. Phys.*

        1984, *80* (9), 4403–4409.

(4)   Brus, L. Electronic Wave Functions in Semiconductor Clusters: Experiment and Theory.

        J. Phys. Chem. **1986**, *90* (12), 2555–2560.

(5)   Tang, J.; Kemp, K. W.; Hoogland, S.; Jeong, K. S.; Liu, H.; Levina, L.; Furukawa, M.;

        Wang, X.; Debnath, R.; Cha, D.; Chou, K. W.; Fischer, A.; Amassian, A.; Asbury, J. B.;

        Sargent, E. H. Colloidal-Quantum-Dot Photovoltaics Using Atomic-Ligand Passivation.

        Nat. Mater. **2011**, *10* (10), 765–771.

(6)   P. Alivisatos, A. Perspectives on the Physical Chemistry of Semiconductor Nanocrystals.

        J. Phys. Chem. **1996**, *100* (31), 13226–13239.

(7)   Weller, H.; Koch, U.; Gutiérrez, M.; Henglein, A. Photochemistry of Colloidal Metal

        Sulfides. 7. Absorption and Fluorescence of Extremely Small ZnS Particles (The World of

        the Neglected Dimensions). *Berichte der Bunsengesellschaft für Phys. Chemie* **1984**, *88*

        (7), 649–656.

(8)   Kortan, A. R.; Hull, R.; Opila, R. L.; Bawendi, M. G.; Steigerwald, M. L.; Carroll, P. J.;

        Brus, L. E. Nucleation and Growth of CdSe on ZnS Quantum Crystallite Seeds, and Vice

Versa, in Inverse Micelle Media. *J. Am. Chem. Soc.* **1990**, *112* (4), 1327–1332.

(9)   Mews, A.; Eychmueller, A.; Giersig, M.; Schooss, D.; Weller, H. Preparation,

        Characterization, and Photophysics of the Quantum Dot Quantum Well System

        CdS/HgS/CdS. *J. Phys. Chem.* **1994**, *98* (3), 934–941.

(10)   Murray, C. B.; Norris, D. J.; Bawendi, M. G. Synthesis and Characterization of Nearly

        Monodisperse CdE (E = S, Se, Te) Semiconductor Nanocrystallites. *J. Am. Chem. Soc.*

        1993, *115* (19), 8706–8715.

(11)   Peng, Z. A.; Peng, X. Formation of High-Quality CdTe, CdSe, and CdS Nanocrystals

        Using CdO as Precursor. *J. Am. Chem. Soc.* **2001**, *123* (1), 183–184.

(12)   A. Littau, K.; J. Szajowski, P.; J. Muller, A.; R. Kortan, A.; E. Brus, L. A Luminescent

        Silicon Nanocrystal Colloid via a High-Temperature Aerosol Reaction. *J. Phys. Chem.*

        2002, *97* (6), 1224–1230.

(13)   Gazis, T. A.; Cartlidge, A. J.; Matthews, P. D. Colloidal III–V Quantum Dots: A Synthetic

        Perspective. *J. Mater. Chem. C* **2023**, *11* (12), 3926–3935.

(14)   Shen, H.; Wang, H.; Li, X.; Niu, J. Z.; Wang, H.; Chen, X.; Li, L. S. Phosphine-Free

        Synthesis of High Quality ZnSe, ZnSe/ZnS, and Cu-, Mn-Doped ZnSe Nanocrystals. *Dalt.*

        Trans. **2009**, No. 47, 10534–10540.

(15)   Deng, Z.; Seob Jeong, K.; Guyot-Sionnest, P. Colloidal Quantum Dots Intraband

        Photodetectors. *ACS Nano* **2014**, *8* (11), 11707–11714.

(16)   Hines, M. A.; Scholes, G. D. Colloidal PbS Nanocrystals with Size-Tunable Near-Infrared

        Emission: Observation of Post-Synthesis Self-Narrowing of the Particle Size Distribution.

        Adv. Mater. **2003**, *15* (21), 1844–1849.

(17)   Murphy, J. E.; Beard, M. C.; Norman, A. G.; Ahrenkiel, S. P.; Johnson, J. C.; Yu, P.;

Mićić, O. I.; Ellingson, R. J.; Nozik, A. J. PbTe Colloidal Nanocrystals: Synthesis, Characterization, and Multiple Exciton Generation. *J. Am. Chem. Soc.* **2006**, *128* (10), 3241–3247.

(18)   Li, Y.-D.; Liao, H.-W.; Ding, Y.; Qian, Y.-T.; Yang, L.; Zhou, G.-E. Nonaqueous Synthesis of CdS Nanorod Semiconductor. *Chem. Mater.* **1998**, *10* (9), 2301–2303.

(19)   Huang, M. H.; Mao, S.; Feick, H.; Yan, H.; Wu, Y.; Kind, H.; Weber, E.; Russo, R.; Yang, P. Room-Temperature Ultraviolet Nanowire Nanolasers. *Science.* **2001**, *292* (5523), 1897–1899.

(20)   Ithurria, S.; Tessier, M. D.; Mahler, B.; Lobo, R. P. S. M.; Dubertret, B.; Efros, A. L. Colloidal Nanoplatelets with Two-Dimensional Electronic Structure. *Nat. Mater.* **2011**, *10* (12), 936–941.

(21)   Gao, X.; Zhang, X.; Zhao, L.; Huang, P.; Han, B.; Lv, J.; Qiu, X.; Wei, S.-H.; Tang, Z. Distinct Excitonic Circular Dichroism between Wurtzite and Zincblende CdSe Nanoplatelets. *Nano Lett.* **2018**, *18* (11), 6665–6671.

(22)   Ithurria, S.; Dubertret, B. Quasi 2D Colloidal CdSe Platelets with Thicknesses Controlled at the Atomic Level. *J. Am. Chem. Soc.* **2008**, *130* (49), 16504–16505.

(23)   Izquierdo, E.; Dufour, M.; Chu, A.; Livache, C.; Martinez, B.; Amelot, D.; Patriarche, G.; Lequeux, N.; Lhuillier, E.; Ithurria, S. Coupled HgSe Colloidal Quantum Wells through a Tunable Barrier: A Strategy to Uncouple Optical and Transport Band Gap. *Chem. Mater.* **2018**, *30* (12), 4065–4072.

(24)   Khan, A. H.; Brescia, R.; Polovitsyn, A.; Angeloni, I.; Martín-García, B.; Moreels, I. Near-Infrared Emitting Colloidal PbS Nanoplatelets: Lateral Size Control and Optical Spectroscopy. *Chem. Mater.* **2017**, *29* (7), 2883–2889.

(25)   Shamsi, J.; Dang, Z.; Bianchini, P.; Canale, C.; Stasio, F. Di; Brescia, R.; Prato, M.;
         Manna, L. Colloidal Synthesis of Quantum Confined Single Crystal CsPbBr3 Nanosheets
         with Lateral Size Control up to the Micrometer Range. *J. Am. Chem. Soc.* **2016**, *138* (23),
         7240–7243.

(26)   Dufour, M.; Qu, J.; Greboval, C.; Méthivier, C.; Lhuillier, E.; Ithurria, S. Halide Ligands
         to Release Strain in Cadmium Chalcogenide Nanoplatelets and Achieve High Brightness.
         ACS Nano **2019**, *13* (5), 5326–5334.

(27)   Shin, A. J.; Hossain, A. A.; Tenney, S. M.; Tan, X.; Tan, L. A.; Foley, J. J.; Atallah, T. L.;
         Caram, J. R. Dielectric Screening Modulates Semiconductor Nanoplatelet Excitons. *J.
         Phys. Chem. Lett.* **2021**, *12*, 4958–4964.

(28)   Tenney, S. M.; Tan, L. A.; Sonnleitner, M. L.; Sica, A. V; Shin, A. J.; Ronquillo, R.;
         Ahmed, T.; Atallah, T. L.; Caram, J. R. Mesoscale Quantum-Confined Semiconductor
         Nanoplatelets through Seeded Growth. *Chem. Mater.* **2022**, *34* (13), 6048–6056.

(29)   Son, J. S.; Wen, X. D.; Joo, J.; Chae, J.; Baek, S.; Park, K.; Kim, J. H.; An, K.; Yu, J. H.;
         Kwon, S. G.; Choi, S. H.; Wang, Z.; Kim, Y. W.; Kuk, Y.; Hoffmann, R.; Hyeon, T.
         Large-Scale Soft Colloidal Template Synthesis of 1.4 Nm Thick Cdse Nanosheets. *Angew.
         Chemie - Int. Ed.* **2009**, *48* (37), 6861–6864.

(30)   Sun, H.; Wang, F.; Buhro, W. E. Tellurium Precursor for Nanocrystal Synthesis:
         Tris(Dimethylamino)Phosphine Telluride. *ACS Nano* **2018**, *12* (12), 12393–12400.

(31)   Wang, Y.; Zhou, Y.; Zhang, Y.; E. Buhro, W. Magic-Size II–VI Nanoclusters as Synthons
         for Flat Colloidal Nanocrystals. *Inorg. Chem.* **2015**, *54* (3), 1165–1177.

(32)   Sun, H.; Buhro, W. E. Contrasting Ligand-Exchange Behavior of Wurtzite and Zinc-
         Blende Cadmium Telluride Nanoplatelets. *Chem. Mater.* **2021**, *33* (5), 1683–1697.

(33)   Pedetti, S.; Ithurria, S.; Heuclin, H.; Patriarche, G.; Dubertret, B. Type-II CdSe/CdTe Core/Crown Semiconductor Nanoplatelets. *J. Am. Chem. Soc.* **2014**, *136* (46), 16430–16438.

(34)   Ithurria, S.; Talapin, D. V. Colloidal Atomic Layer Deposition (c-ALD) Using Self-Limiting Reactions at Nanocrystal Surface Coupled to Phase Transfer between Polar and Nonpolar Media. *J. Am. Chem. Soc.* **2012**, *134* (45), 18585–18590.

(35)   Izquierdo, E.; Robin, A.; Keuleyan, S.; Lequeux, N.; Lhuillier, E.; Ithurria, S. Strongly Confined HgTe 2D Nanoplatelets as Narrow Near-Infrared Emitters. *J. Am. Chem. Soc.* **2016**, *138* (33), 10496–10501.

(36)   Riedinger, A.; Ott, F. D.; Mule, A.; Mazzotti, S.; Knüsel, P. N.; Kress, S. J. P.; Prins, F.; Erwin, S. C.; Norris, D. J. An Intrinsic Growth Instability in Isotropic Materials Leads to Quasi-Two-Dimensional Nanoplatelets. *Nat. Mater.* **2017**, *16* (7), 743–748.

(37)   Schlosser, A.; Graf, R. T.; Bigall, N. C. CdS Crown Growth on CdSe Nanoplatelets: Core Shape Matters. *Nanoscale Adv.* **2020**, *2* (10), 4604–4614.

(38)   Meerbach, C.; Tietze, R.; Voigt, S.; Sayevich, V.; Dzhagan, V. M.; Erwin, S. C.; Dang, Z.; Selyshchev, O.; Schneider, K.; Zahn, D. R. T.; Lesnyak, V.; Eychmüller, A. Brightly Luminescent Core/Shell Nanoplatelets with Continuously Tunable Optical Properties. *Adv. Opt. Mater.* **2019**, *7* (7), 1801478.

(39)   Hazarika, A.; Fedin, I.; Hong, L.; Guo, J.; Srivastava, V.; Cho, W.; Coropceanu, I.; Portner, J.; T. Diroll, B.; P. Philbin, J.; Rabani, E.; Klie, R.; V. Talapin, D. Colloidal Atomic Layer Deposition with Stationary Reactant Phases Enables Precise Synthesis of "Digital" II–VI Nano-Heterostructures with Exquisite Control of Confinement and Strain. *J. Am. Chem. Soc.* **2019**, *141* (34), 13487–13496.

(40)   Groeneveld, E.; Witteman, L.; Lefferts, M.; Ke, X.; Bals, S.; Van Tendeloo, G.; de Mello

Donega, C. Tailoring ZnSe–CdSe Colloidal Quantum Dots via Cation Exchange: From

Core/Shell to Alloy Nanocrystals. *ACS Nano* **2013**, *7* (9), 7913–7930.

(41)   M. Smith, A.; Nie, S. Bright and Compact Alloyed Quantum Dots with Broadly Tunable

Near-Infrared Absorption and Fluorescence Spectra through Mercury Cation Exchange. *J.

Am. Chem. Soc.* **2010**, *133* (1), 24–26.

(42)   Lee, S.; Yoon, D. E.; Kim, D.; Shin, D. J.; Jeong, B. G.; Lee, D.; Lim, J.; Bae, W. K.;

Lim, H. K.; Lee, D. C. Direct Cation Exchange of CdSe Nanocrystals into ZnSe Enabled

by Controlled Binding between Guest Cations and Organic Ligands. *Nanoscale* **2019**, *11*

(32), 15072–15082.

(43)   B.V. Salzmann, B.; de Wit, J.; Li, C.; Arenas-Esteban, D.; Bals, S.; Meijerink, A.;

Vanmaekelbergh, D. Two-Dimensional CdSe-PbSe Heterostructures and PbSe

Nanoplatelets: Formation, Atomic Structure, and Optical Properties. *J. Phys. Chem. C*

2022, *126* (3), 1513–1522.

(44)   Galle, T.; Spittel, D.; Weiß, N.; Shamraienko, V.; Decker, H.; Georgi, M.; Hübner, R.;

Metzkow, N.; Steinbach, C.; Schwarz, D.; Lesnyak, V.; Eychmüller, A. Simultaneous

Ligand and Cation Exchange of Colloidal CdSe Nanoplatelets toward PbSe Nanoplatelets

for Application in Photodetectors. *J. Phys. Chem. Lett.* **2021**, *12* (21), 5214–5220.

(45)   Ithurria, S.; Bousquet, G.; Dubertret, B. Continuous Transition from 3D to 1D

Confinement Observed during the Formation of CdSe Nanoplatelets. *J. Am. Chem. Soc.*

2011, *133* (9), 3070–3077.

(46)   Schliehe, C.; Juarez, B. H.; Pelletier, M.; Jander, S.; Greshnykh, D.; Nagel, M.; Meyer,

A.; Foerster, S.; Kornowski, A.; Klinke, C.; Weller, H. Ultrathin PbS Sheets by Two-

Dimensional Oriented Attachment. *Science.* **2010**, *329* (5991), 550–553.

(47) Castro, N.; Bouet, C.; Ithurria, S.; Lequeux, N.; Constantin, D.; Levitz, P.; Pontoni, D.;

Abécassis, B. Insights into the Formation Mechanism of CdSe Nanoplatelets Using in Situ

X-Ray Scattering. *Nano Lett.* **2019**, *19* (9), 6466–6474.

(48) Ott, F. D.; Riedinger, A.; Ochsenbein, D. R.; Knüsel, P. N.; Erwin, S. C.; Mazzotti, M.;

Norris, D. J. Ripening of Semiconductor Nanoplatelets. *Nano Lett.* **2017**, *17* (11), 6870–

6877.

(49) Cunningham, P. D.; Coropceanu, I.; Mulloy, K.; Cho, W.; Talapin, D. V. Quantized

Reaction Pathways for Solution Synthesis of Colloidal ZnSe Nanostructures: A

Connection between Clusters, Nanowires, and Two-Dimensional Nanoplatelets. *ACS*

Nano **2020**, *14*, 12.

(50) Knüsel, P. N.; Riedinger, A.; Rossinelli, A. A.; Ott, F. D.; Mule, A. S.; Norris, D. J.

Experimental Evidence for Two-Dimensional Ostwald Ripening in Semiconductor

Nanoplatelets. *Chem. Mater.* **2020**, *32* (7), 3312–3319.

(51) Scott, R.; Heckmann, J.; Prudnikau, A. V.; Antanovich, A.; Mikhailov, A.; Owschimikow,

N.; Artemyev, M.; Climente, J. I.; Woggon, U.; Grosse, N. B.; Achtstein, A. W. Directed

Emission of CdSe Nanoplatelets Originating from Strongly Anisotropic 2D Electronic

Structure. *Nat. Nanotechnol.* **2017**, *12* (12), 1155–1160.

(52) Tessier, M. D.; Javaux, C.; Maksimovic, I.; Loriette, V.; Dubertret, B. Spectroscopy of

Single CdSe Nanoplatelets. *ACS Nano* **2012**, *6* (8), 6751–6758.

(53) Tessier, M. D.; Mahler, B.; Nadal, B.; Heuclin, H.; Pedetti, S.; Dubertret, B. Spectroscopy

of Colloidal Semiconductor Core/Shell Nanoplatelets with High Quantum Yield. *Nano*

Lett. **2013**, *13* (7), 3321–3328.

(54)   Yeltik, A.; Delikanli, S.; Olutas, M.; Kelestemur, Y.; Guzelturk, B.; Demir, H. V. Experimental Determination of the Absorption Cross-Section and Molar Extinction Coefficient of Colloidal CdSe Nanoplatelets. *J. Phys. Chem. C* **2015**, *119* (47), 26768–26775.

(55)   Chernikov, A.; Berkelbach, T. C.; Hill, H. M.; Rigosi, A.; Li, Y.; Aslan, O. B.; Reichman, D. R.; Hybertsen, M. S.; Heinz, T. F. Exciton Binding Energy and Nonhydrogenic Rydberg Series in Monolayer WS 2. *Phys. Rev. Lett.* **2014**, *113*, 076802.

(56)   Roo, J. De; Keukeleere, K. De; Hens, Z.; Driessche, I. Van. From Ligands to Binding Motifs and beyond; the Enhanced Versatility of Nanocrystal Surfaces. *Dalt. Trans.* **2016**, *45* (34), 13277–13283.

(57)   Zhang, J.; Zhang, H.; Cao, W.; Pang, Z.; Li, J.; Shu, Y.; Zhu, C.; Kong, X.; Wang, L.; Peng, X. Identification of Facet-Dependent Coordination Structures of Carboxylate Ligands on CdSe Nanocrystals. *J. Am. Chem. Soc.* **2019**, *141* (39), 15675–15683.

(58)   Green, M. L. H. L. H. *A New Approach to the Formal Classification of Covalent Compounds of the Elements*; Elsevier, 1995; Vol. 500, pp 127–148.

(59)   Anderson, N. C.; Hendricks, M. P.; Choi, J. J.; Owen, J. S. Ligand Exchange and the Stoichiometry of Metal Chalcogenide Nanocrystals: Spectroscopic Observation of Facile Metal-Carboxylate Displacement and Binding Scheme 1. Nanocrystal Ligand Binding Motifs According to the Covalent Bond Classification Method. *J. Am. Chem. Soc* **2013**, *135*.

(60)   Yoon, D. E.; Lee, J.; Yeo, H.; Ryou, J.; Lee, Y. K.; Kim, Y. H.; Lee, D. C. Atomistics of Asymmetric Lateral Growth of Colloidal Zincblende CdSe Nanoplatelets. *Chem. Mater.* **2021**, *33* (12), 4813–4820.

(61) Singh, S.; Tomar, R.; Ten Brinck, S.; De Roo, J.; Geiregat, P.; Martins, J. C.; Infante, I.; Hens, Z. Colloidal CdSe Nanoplatelets, A Model for Surface Chemistry/Optoelectronic Property Relations in Semiconductor Nanocrystals. *J. Am. Chem. Soc.* **2018**, *140* (41), 13292–13300.

(62) Manzeli, S.; Ovchinnikov, D.; Pasquier, D.; Yazyev, O. V; Kis, A. 2D Transition Metal Dichalcogenides. *Nature Reviews Materials*. **2017**, *2* (17033).

(63) Lin, Y.; Ling, X.; Yu, L.; Huang, S.; Hsu, A. L.; Lee, Y. H.; Kong, J.; Dresselhaus, M. S.; Palacios, T. Dielectric Screening of Excitons and Trions in Single-Layer MoS2. *Nano Lett.* **2014**, *14* (10), 5569–5576.

(64) Yuan, L.; Huang, L. Exciton Dynamics and Annihilation in WS2 2D Semiconductors. *Nanoscale* **2015**, *7* (16), 7402–7408.

(65) Amani, M.; Lien, D. H.; Kiriya, D.; Xiao, J.; Azcatl, A.; Noh, J.; Madhvapathy, S. R.; Addou, R.; Santosh, K. C.; Dubey, M.; Cho, K.; Wallace, R. M.; Lee, S. C.; He, J. H.; Ager, J. W.; Zhang, X.; Yablonovitch, E.; Javey, A. Near-Unity Photoluminescence Quantum Yield in MoS2. *Science.* **2015**, *350* (6264), 1065–1068.

(66) Otero-Martínez, C.; Ye, J.; Sung, J.; Pastoriza-Santos, I.; Pérez-Juste, J.; Xia, Z.; Rao, A.; Hoye, R. L. Z.; Polavarapu, L. Colloidal Metal-Halide Perovskite Nanoplatelets: Thickness-Controlled Synthesis, Properties, and Application in Light-Emitting Diodes. *Adv. Mater.* **2022**, *34* (10), 2107105.

(67) C. Weidman, M.; J. Goodman, A.; A. Tisdale, W. Colloidal Halide Perovskite Nanoplatelets: An Exciting New Class of Semiconductor Nanomaterials. *Chem. Mater.* **2017**, *29* (12), 5019–5030.

(68) Li, M.; Zhi, M.; Zhu, H.; Wu, W. Y.; Xu, Q. H.; Jhon, M. H.; Chan, Y. Ultralow-Threshold Multiphoton-Pumped Lasing from Colloidal Nanoplatelets in Solution. *Nat. Commun.* **2015**, *6* (1), 1–8.

(69) Guzelturk, B.; Kelestemur, Y.; Olutas, M.; Delikanli, S.; Volkan Demir, H. Amplified Spontaneous Emission and Lasing in Colloidal Nanoplatelets. *ACS Nano* **2014**, *8* (7), 6599–6605.

(70) Li, Q.; Xu, Z.; R. McBride, J.; Lian, T. Low Threshold Multiexciton Optical Gain in Colloidal CdSe/CdTe Core/Crown Type-II Nanoplatelet Heterostructures. *ACS Nano* **2017**, *11* (3), 2545–2553.

(71) Sharma, M.; Gungor, K.; Yeltik, A.; Olutas, M.; Guzelturk, B.; Kelestemur, Y.; Erdem, T.; Delikanli, S.; McBride, J. R.; Demir, H. V. Near-Unity Emitting Copper-Doped Colloidal Semiconductor Quantum Wells for Luminescent Solar Concentrators. *Adv. Mater.* **2017**, *29* (30), 1700821.

(72) Giovanella, U.; Pasini, M.; Lorenzon, M.; Galeotti, F.; Lucchi, C.; Meinardi, F.; Luzzati, S.; Dubertret, B.; Brovelli, S. Efficient Solution-Processed Nanoplatelet-Based Light-Emitting Diodes with High Operational Stability in Air. *Nano Lett.* **2018**, *18* (6), 3441–3448.

(73) Bai, P.; Hu, A.; Deng, Y.; Tang, Z.; Yu, W.; Hao, Y.; Yang, S.; Zhu, Y.; Xiao, L.; Jin, Y.; Gao, Y. CdSe/CdSeS Nanoplatelet Light-Emitting Diodes with Ultrapure Green Color and High External Quantum Efficiency. *J. Phys. Chem. Lett.* **2022**, *13* (39), 9051–9057.

(74) Fan, F.; Kanjanaboos, P.; Saravanapavanantham, M.; Beauregard, E.; Ingram, G.; Yassitepe, E.; M. Adachi, M.; Voznyy, O.; K. Johnston, A.; Walters, G.; Kim, G.-H.; Lu, Z.-H.; H. Sargent, E. Colloidal CdSe1–XSx Nanoplatelets with Narrow and Continuously-

Tunable Electroluminescence. *Nano Lett.* **2015**, *15* (7), 4611–4615.

(75) Dabard, C.; Guilloux, V.; Gréboval, C.; Po, H.; Makke, L.; Fu, N.; Xu, X. Z.; Silly, M. G.; Patriarche, G.; Lhuillier, E.; Barisien, T.; Climente, J. I.; Diroll, B. T.; Ithurria, S. Double-Crowned 2D Semiconductor Nanoplatelets with Bicolor Power-Tunable Emission. *Nat. Commun.* **2022**, *13* (1), 1–10.

(76) Galle, T.; Samadi Khoshkhoo, M.; Martin-Garcia, B.; Meerbach, C.; Sayevich, V.; Koitzsch, A.; Lesnyak, V.; Eychmüller, A. Colloidal PbSe Nanoplatelets of Varied Thickness with Tunable Optical Properties. *Chem. Mater.* **2019**, *31* (10), 3803–3811.

(77) Cosco, E. D.; Caram, J. R.; Bruns, O. T.; Franke, D.; Day, R. A.; Farr, E. P.; Bawendi, M. G.; Sletten, E. M. Flavylium Polymethine Fluorophores for Near- and Shortwave Infrared Imaging. *Angew. Chemie - Int. Ed.* **2017**, *56* (42), 13126–13129.

(78) Lu, H.; M. Carroll, G.; R. Neale, N.; C. Beard, M. Infrared Quantum Dots: Progress, Challenges, and Opportunities. *ACS Nano* **2019**, *13* (2), 939–953.

(79) Klepzig, L. F.; Biesterfeld, L.; Romain, M.; Niebur, A.; Schlosser, A.; Hübner, J.; Lauth, J. Colloidal 2D PbSe Nanoplatelets with Efficient Emission Reaching the Telecom O-, E- and S-Band. *Nanoscale Adv.* **2022**, *4* (2), 590–599.

(80) Piepenbrock, M. O. M.; Stirner, T.; Kelly, S. M.; O'Neill, M. A Low-Temperature Synthesis for Organically Soluble HgTe Nanocrystals Exhibiting near-Infrared Photoluminescence and Quantum Confinement. *J. Am. Chem. Soc.* **2006**, *128* (21), 7087–7090.

Chapter 2

Mercury Chalcogenide Nanoplatelet-Quantum Dot Heterostructures as a New Class of Continuously Tunable Bright Shortwave Infrared Emitters

Despite broad applications in imaging, energy conversion and telecommunications, there are few nanoscale moieties that emit light efficiently in the shortwave infrared (SWIR, 1000-2000 nm or 1.24-0.62 eV). In this chapter we discuss quantum confined mercury chalcogenide (HgX, X=Se, Te) nanoplatelets (NPLs) with bright (QY >30%) and tunable (900-1500+ nm) infrared emission from attached quantum dot (QD) "defect" states. This QD defect emission is kinetically tunable, enabling controlled mid-gap emission from NPLs and providing a potential platform for novel optoelectronics in the SWIR.

2.1 Relevance of HgTe nanocrystals as infrared emitters

Photons in the shortwave infrared (SWIR) spectral window are lower in energy than most molecular HOMO-LUMO gaps, yet higher in energy than vibrational states. Without natural sources of background radiation or absorption, imaging in this spectral window shows superlative contrast and feature resolution.[1,2] Decreased Rayleigh scatter for longer wavelength light also

results in improved penetrative imaging—through fog, foliage, skin and bone.[1,3] Fluorescent microscopy in the SWIR has already shown extraordinary background-free deep tissue imaging in living animals.[4,5] Increasing the scope of SWIR absorbing and fluorescing materials may enable applications in sensing biological, chemical or physical changes in complex and opaque environments.

Mercury chalcogenides are a class of binary semiconductors with narrow or negative bandgaps used primarily in infrared photodetection.[6–8] Like their more commonly studied cadmium chalcogenide analogs, quantum confined HgX (X = S, Se, Te) nanocrystals (NCs) can be synthesized with size-tuned bandgaps that vary from near zero to 1 eV.[9,10] Despite a few reports of high infrared quantum yields (QY),[11] HgX nanocrystals have not been extensively explored as compact fluorophores for the short or midwave infrared, unlike their PbX analogs.[12,13] In this manuscript, we demonstrate that ligand-exchanged two and three monolayer HgX nanoplatelets show previously unreported highly tunable emission in the SWIR *while* maintaining size-confined nanoplatelet absorption features. These materials represent a new platform for SWIR optoelectronics.

Recently, highly confined 3ML HgX nanoplatelets (NPLs) have been synthesized through a cation exchange from 3ML CdX NPLs using a mercury salt precursor.[14] NPLs are 2D structures with quantum confinement along their integer atomic thicknesses, where the number of monolayers is defined by the number of anionic layers *e.g.* a 3 ML HgX NPL will consist of 3 layers of X and 4 layers of Hg. The spatial extent, material constituents, and self-assembly of NPLs can be tuned to achieve an extremely versatile set of photophysical properties and applications, including near unity exciton and biexciton quantum yield, efficient lasing, electroluminescence, and usage as substrates for photodetectors.[14–23]

Building upon previous work, we find that ligand exchange of two and three monolayer HgSe and HgTe NPLs produces growth of emissive QD-like defects on the NPL surface, similar to dot-on-platelet heterostructures. This gives a continuously tunable set of mid-gap states with a high degree of synthetic control over the wavelength of emission arising from the colloidal growth of the QD while maintaining high QY. In the exemplar case, 3ML HgTe exhibits tuned narrowband emission from 1000-1500 nm with a FWHM of ~100-200 meV and QY >30% across this range. Although the emission linewidths are slightly broader than highly monodisperse PbS QDs, these properties match the most emissive PbX/InAs quantum dots[24–26] without any synthetic optimization, and the emission is stable over several months. We correlate the exchange of ligand type to the formation and tunability of the SWIR emission, and demonstrate how kinetic conditions influence its rate of evolution. Finally, using superconducting nanowire single photon detectors (SNSPDs), we obtain time-resolved band-edge and sub-band emission showing that the radiative lifetime is significantly faster than PbX analogs. Our results suggest that HgX NPLs are potential substrates for tunable fluorescent applications including lighting, imaging, and as materials for luminescent solar concentrators.[27]
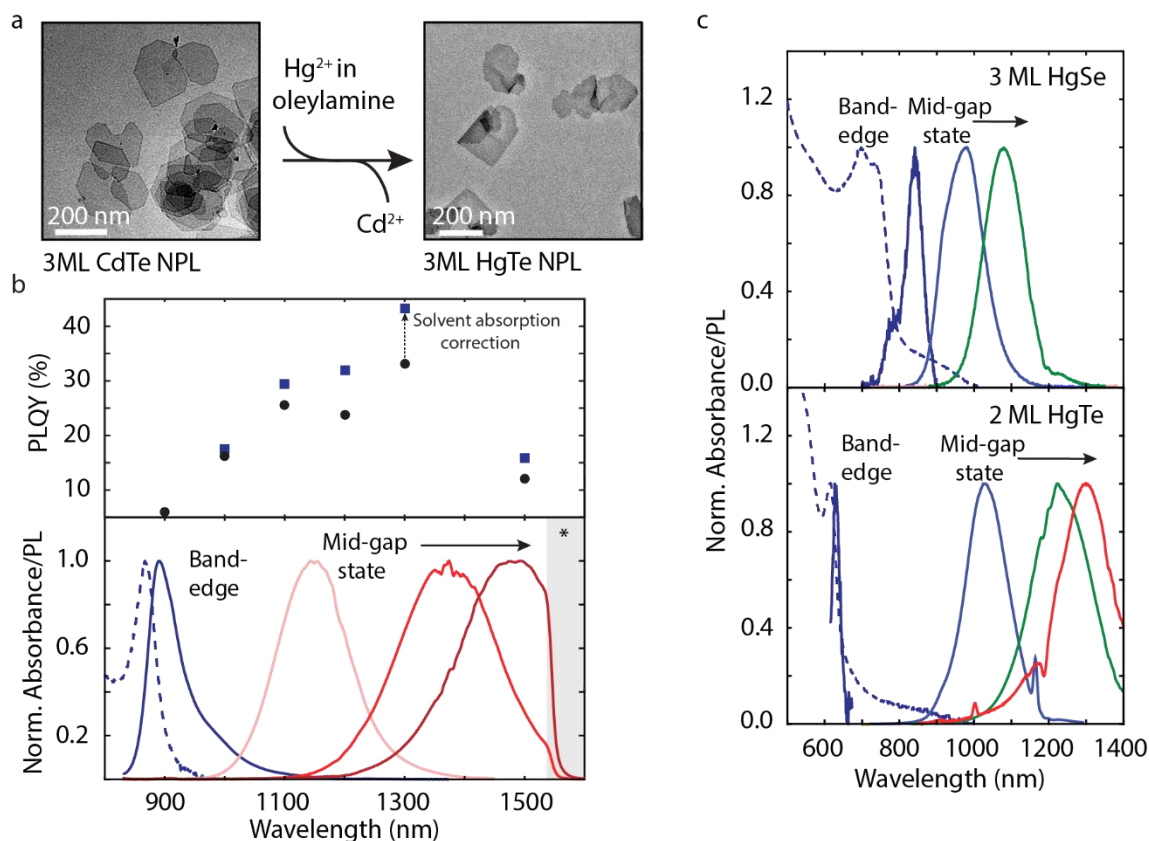
Figure 2.1. *TEM shows the morphology of the NPLs is maintained after exchange. (b) The absorption (dashed line) and PL (solid lines) of 3ML HgTe NPL shows band-edge emission after synthesis, and mid-gap emission which appears and red-shifts over the following days. Typical QY for these states are 25-35%. The PL spectra are corrected for solvent absorption to better visualize position and width. Uncorrected data and details are provided in the supporting information. (c) Cation exchange in 3ML HgSe and 2ML HgTe shows similar behavior.*

2.2 Cation exchange to Synthesize HgX (X= Se,Te) NPLs

We synthesize HgX NPLs based on the cation exchange procedures developed by Izquierdo *et al.*[14,28] (details provided in the supporting information). For example for 3ML HgTe NPLs, 3ML CdTe NPLs are first synthesized using slow injection of trioctylphosphine telluride to a degassed solution of cadmium propionate precursor and oleic acid in octadecene at 215 °C.[29] Once the reaction is complete, the NPLs are purified by precipitation and resuspended in hexanes.

FTIR spectroscopy of the CdTe NPLs shows that they are passivated with acetate and/or oleate ligands after synthesis (Figure 2.12). To exchange to HgTe, mercury (II) acetate is dissolved in oleylamine and introduced at room temperature to a solution of CdTe NPLs in hexanes (ranging from 2.4 to 16% v/v). Ligand exchange accompanies cation exchange where acetate/oleate are exchanged for oleylamine (Figure 2.13), and transmission electron microscopy confirms that the morphology of the NPL is maintained (Figure 2.1a). A similar procedure is used for the synthesis and exchange of CdSe to HgSe as described in the supporting information.

We monitor the progress of the cation exchange using absorbance and photoluminescence (PL) (Figure 2.14). Unlike previously reported NPL cation exchanges, when PL is monitored several hours after exchange a bright Stokes-shifted emission (~1000-1100 nm) appears along with band-edge emission (Figure 2.1b). This new emissive state shifts further into the infrared as a function of time while the band edge emission quenches. Despite large continual changes in observed emission, features in the absorption spectrum do not proportionally shift. The PL line-width of the red-shifted emission is approximately 200-300 nm and the quantum yield (QY) remains high; centered around 30% (Figure 2.1b) but reaching up to 56% (Figure 2.11).

The high QY is consistent across a number of different samples and appears to be stable over an extended period of time. The absolute QY measured across different wavelengths gives values between 10-56% (Figure 2.11), and systematic error is explored using relative QY determination with a SWIR emitting dye standard giving a consistent value of 18% (Figure 2.12). These reported values do not account for losses due to solvent reabsorption, however we apply a correction to our QY for the reabsorption of hexanes in Figure 1b (details in the supporting information). After aging for 8 months, we see the NPLs retain QY up to 32% (Figure 2.11) which indicates long-term stability of the emissive species. Furthermore, this behavior consistently

occurs given the appropriate set of synthetic conditions and extends to other systems of HgX NPLs such as HgSe and 2ML HgTe, suggesting the mechanism of bright mid-gap state evolution may be general and applicable to other materials (Figure 2.1c).

We explored several mechanisms that could give rise to a large Stokes-shifted emission. We discount the possibility of retaining any Cd in the 3 ML structure by energy dispersive x-ray (EDX) measurements that show complete exchange (Figure 2.15) as well as a loss of CdTe features in the absorption spectrum indicating no formation of type II CdTe/HgTe heterostructures[28] or $Cd_xHg_{1-x}Te$ NPL alloys.[30] A lack of change in the NPL absorption spectrum suggests that neither aggregation nor relaxation of quantum confinement through growth of thicker NPLs plays a role in the emission. We also do not observe any intraband transitions in the absorption spectrum which could be indicative of electronic doping due to the surface chemistry.[31] Therefore, we hypothesize that a mid-gap state is induced by conditions used during exchange,[32] especially as we do not observe mid-gap emission from the CdTe NPLs prior to the addition of Hg in OLA. Immediately after synthesis, we see no absorption features beyond the band-edge of the NPL, however in aged samples (5 months) we see features that resemble HgTe QDs. This suggests that the SWIR emission arises from room temperature colloidal growth of HgX nanoparticles following the cation exchange.[11,33,34] We assign the mid-gap emission to these QDs as the spectral changes follow the expected mechanisms of colloidal growth and energy transfer, however we cannot definitively conclude the mechanism of nucleation of QD or direct attachment onto the NPL. Our structural understanding arises from changes in the NPL and further studies are needed to elucidate the nature of the QDs. Nonetheless we find the formation of sub-band emission to be general in HgX NPLs with varying composition and thickness and focus our efforts on the 3ML HgTe NPLs to explore the parameters which give rise to the observed emission.
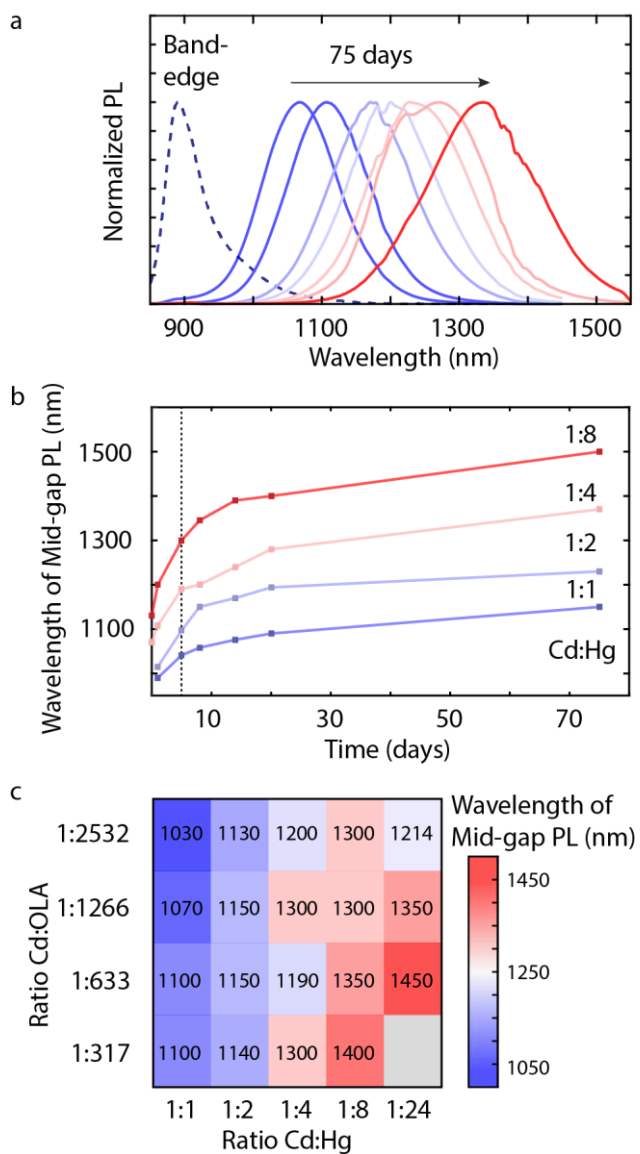
Figure 2.2. *(a) The evolution of mid-gap emission over time for 1:4:1266 (Cd:Hg:OLA) used during exchange. The spectra have been corrected for solvent absorption as described in the supporting information. (b) The depth of the mid-gap state can be varied by changing the ratio of Cd:Hg used during exchange. (c) Synthetic conditions explored to induce mid-gap emission by changing the concentration of Hg^{2+} in oleylamine (OLA), relative to cadmium. The wavelengths are reported for day 5 after synthesis (indicated by the dotted line in b)*

2.3 The Effect of Exchange Parameters on Photophysical Properties Over Time

To explore the role of the exchange parameters on the evolution of the mid-gap state, we vary (i) the amount of Hg added in excess to the amount of Cd in the CdTe NPL (ratio Cd:Hg), (ii) the amount of oleylamine added in conjunction with Hg^{2+} during exchange, and (iii) the length of time the colloidal system is left in a solution of hexanes after exchange. In Figure 2 we show how the PL changes for a matrix of these synthetic variables. In Figure 2.2a, we plot the band-edge emission obtained directly after cation exchange and the evolution of the mid-gap emission, monitored over 75 days (although temperature can control the rate, Figure 2.24). The mid-gap emission red-shifts rapidly in the days immediately after exchange and slows over longer time scales towards a maximum which appears to be intrinsic to the amount of excess Hg added (Figure 2.2b). In general, we obtain further red-shifted emission with greater excesses of Hg, but having excess is not strictly necessary to induce formation—we see evolution occur when using a 1:1 ratio (Cd:Hg). We also explore the influence of oleylamine (Figure 2.2c) by changing the concentration of dissolved Hg and monitoring the PL after exchange (shown after five days). We find that greater excess of Hg will produce a larger red shift while greater excess of oleylamine suppresses the rate of this shift. Therefore, the final position of the mid-gap emission wavelength is tunable through control of precursors.

Our results suggest that the formation of an emissive sub-band state requires both cation and ligand exchange. During the cation exchange reaction, the NPLs also experience a change in coating from oleic acid/oleate ligand to oleylamine (confirmed using FTIR in Figure 2.13). The formation of mid-gap emission is thus accompanied by an exchange from X-type ligands $(Hg(O_2R)_2)$ to L-type ligands such as oleylamine (by the Green nomenclature).[35] X-type ligands are one electron donors which form a covalent bond with the metal while L-type ligands are two electron donors (often a lone pair) which form a dative bond with the metal. This type of ligand

exchange from X to L has been explored in CdSe NCs capped with oleic acid, where a displacement is observed when an L-type ligand is introduced to a carboxylate bound to a metal site.[32,36] Because the metal-carboxylate ($M(O_2R)_2$) can act as a ligand itself, exchange with the L-type ligand removes a surface metal atom with two carboxylates as one unit. Similarly, in HgTe QDs this type of ligand displacement can introduce intragap emission which has been attributed to surface localized states.[37] We hypothesize that following this mechanism, HgTe NPLs capped with oleic acid/oleate may undergo this type of exchange with oleylamine, removing some of the surface Hg atoms from the newly formed NPLs. This could then introduce surface sites or defects from under-coordinated Te or dangling bonds which are reactive towards growth of QDs.

The absorption spectrum of the NPLs is also sensitive to ligand type and we see a red-shift characteristic of an OA to OLA exchange.[14,36,38] In the case of exchange with a sterically-hindered amine, such as triisobutylamine, we find that the NPLs do not experience this same behavior. They retain the oleic acid/oleate and acetate ligands by FTIR (Figure 2.13) and while we do observe mid-gap emission, the evolution is arrested (Figure 2.20). In addition, the absorption and emission spectra do not show the slight red-shift as seen in the OA to OLA exchange. Ligand exchange does not appear to be occurring in the same manner, and mid-gap state evolution is hindered. This suggests that the interaction of oleylamine with the surface is critical for the evolution of QDs on the surface.
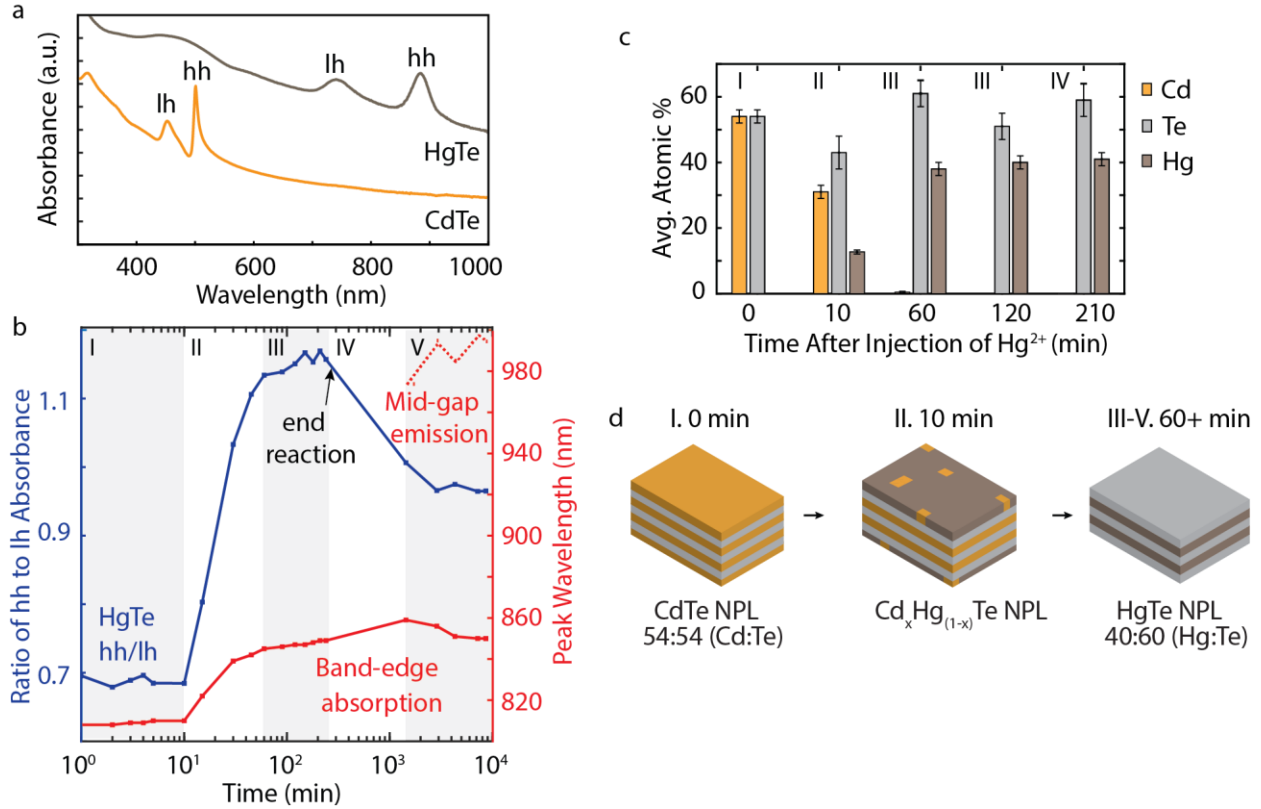
Figure 2.3. *(a) The absorption spectra for CdTe and HgTe NPL and their light hole (lh) and heavy hole (hh) features. (b) The ratio of HgTe hh/lh (blue line) and wavelength of hh (red line) monitored by changes in the absorption spectrum during different timepoints of exchange. The dashed line indicates formation of mid-gap emission. (c) EDX monitoring stoichiometry changes during exchange. (d) A possible mechanism for observed stoichiometry changes where Hg atoms are removed from the NPL surfaces.*

2.4 Structural Transformation during Cation Exchange

In Figure 2.3, we explore the emergence and evolution of the mid-gap emissive state through absorption, emission, and EDX spectroscopies. We find that the overall exchange is a multi-step process which we qualitatively divide by significant changes in the absorption and photoluminescence spectra, beginning with cation exchange from CdTe to HgTe. The behavior is similar for different samples and conditions (Figure 2.21).

The rapid initial stage (**I**) occurs with the exchange of Cd with Hg. Removal of the Cd atoms happens within the first 10-15 minutes, as we see the CdTe hh/lh disappear and give rise to the HgTe hh/lh in the absorption spectrum (Figure 2.3a). These HgTe features then begin to red-shift and grow in intensity during the second stage (**II**). During this first hour, the formation of HgTe NPLs is monitored by the intensity of the hh/lh where the ratio is expected to exceed one, indicating a complete exchange.[14] We find that by hour one, this ratio reaches 1.1 and EDX confirms the completed exchange of Cd to Hg (Figure 2.3c, 60 min). Moreover, the stoichiometry of the NPLs is 40:60 (Hg:Te) which suggests that Te is now in excess and supports the notion of loss of Hg atoms occurring simultaneously to a changing ligand environment. The 40:60 (Hg:Te) ratio suggests that surface Hg atoms are being stripped as Hg-oleate ligands are displaced by oleylamine, leaving two Hg layers and three Te layers in the NPL and changing the charge at the surface. This is surprising given the lack of blue-shift in the absorption spectrum as would be expected by a stronger confinement in thinner NPLs. We cannot eliminate the possibility of severe depletion of Hg in the system (perhaps from internal Hg layers) while maintaining 3ML thickness, but further studies are needed to fully characterize the sites of Hg loss in the NPL.

From 1-4 hrs (**III**), the hh/lh ratio stabilizes around 1.1 while the wavelength of absorption gradually red-shifts toward 860-880 nm. During this stage, the ratio of Hg:Te does not significantly change and Te remains in excess. Despite significant changes in stoichiometry during the total reaction (**I-III**), the loss of surface Hg atoms *precedes mid-gap state emission* and NPLs show only band edge emission (~900 nm) by this timepoint.

In the hours following exchange (**IV**), there is a decrease in the ratio of hh/lh suggesting some change in the electronic structure—potentially arising from the physical changes on the surface of the NPLs, although we see no continual changes in the stoichiometry (Table 2.1). After

washing the NPLs at 3.5hr, the hh/lh ratio stabilizes again around 1. We mark the final stage (**V**) as the formation and evolution of mid-gap emission which occurs between 4-24 hrs after exchange, depending on the conditions explored in Figure 2.2. The band edge absorption and emission remain around 880 and 900 nm respectively as the mid-gap emission begins to red shift into the SWIR.
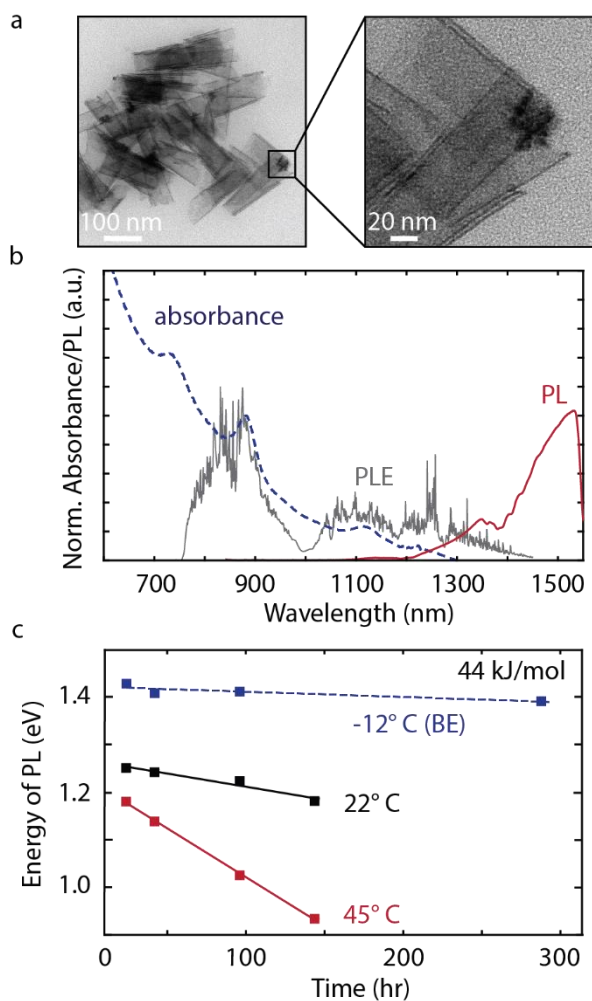
Figure 2.4. (a) TEM of 3ML HgTe NPLs showing quantum dot growths after aging. (b) Absorbance (blue dashed line), PL (red solid line), and PLE (grey solid line) for a sample aged 5 months.(c) The energy of mid-gap PL from solutions held at elevated temperatures (solid lines) after exchange. When kept cold (blue dashed line), no shift from band-edge emission is observed.

2.4 Growth of HgTe QDs and Energy Transfer Mechanism of Midgap Emissions

TEM of NPLs after exchange shows the presence of quantum dot-like moieties growing

on or attached to NPLs in aged samples that show mid-gap emission (Figure 2.4a). These QDs survive washing steps by centrifugation and syringe filtering suggesting that they are either growing from the NPLs (possibly epitaxially) or attach to the NPLs after nucleation (Figure 2.18). Given the influence of excess precursor in solution, this suggests that depletion of surface Hg atoms on the NPLs following ligand exchange with oleylamine may be giving rise to room temperature colloidal growth of HgX nanoparticles which act as quantum-confined defects.[11,33,34] The removal of surface atoms may be inducing a surface rearrangement or simply providing reactive sites for growth of these nanoparticles without affecting the confinement of the NPLs, as seen in the absorption spectrum of aged samples showing only SWIR emission. Additionally, we see temperature dependence on the rate of evolution which also suggests a growth mechanism. In Figure 2.4b, we monitor the evolution of the emission energy for the mid-gap state at three temperatures. We observe a significant rate of PL shift increase at elevated temperatures, which we fit to an activation barrier of 44 kJ/mole (Figure 2.25). These temperature kinetics are comparable to the bond energy in bulk HgTe ($\sim$78 kJ/mol)[39] and may be consistent with bond-forming or bond-breaking processes.

We hypothesize that the QDs are in direct contact with the NPLs due to the quenching of the NPL band-edge emission suggesting an energy transfer from platelet to dot which is much faster than radiative recombination in the NPL. We believe that the system is experiencing a near field energy transfer rather than a FRET process where we would expect the QY to be limited to 10% by the donor (NPL band-edge). Rather, we find that the QY is consistently higher than 10% suggesting that the QD is either very close to or growing from the NPL surface.

Similar large Stokes-shifted emission due to defects has been seen in other colloidal NCs such as metal dopants in $CuInSe_2$ or CdSe/ZnS[40] and non-coordinated surface selenium in

ultrasmall CdSe,[41] but tunability of these defect states is dependent on defect dopant concentration, and these systems do not display SWIR emission. Dot-on-nanoplatelet heterostructures have been observed for CdSe/ZnSe[42] and more recently PbSe/CdSe,[43] but these systems do not show the same continual room-temperature growth dynamics. Our mechanism produces a new type of heterostructure SWIR emitter with large Stokes-shifts that is tunable through the SWIR. Our data suggests that these emissive states may arise from energy transfer to defect-like SWIR emitting nanoparticles attached to the NPLs which evolve over time, possibly through structural rearrangement or colloidal growth.
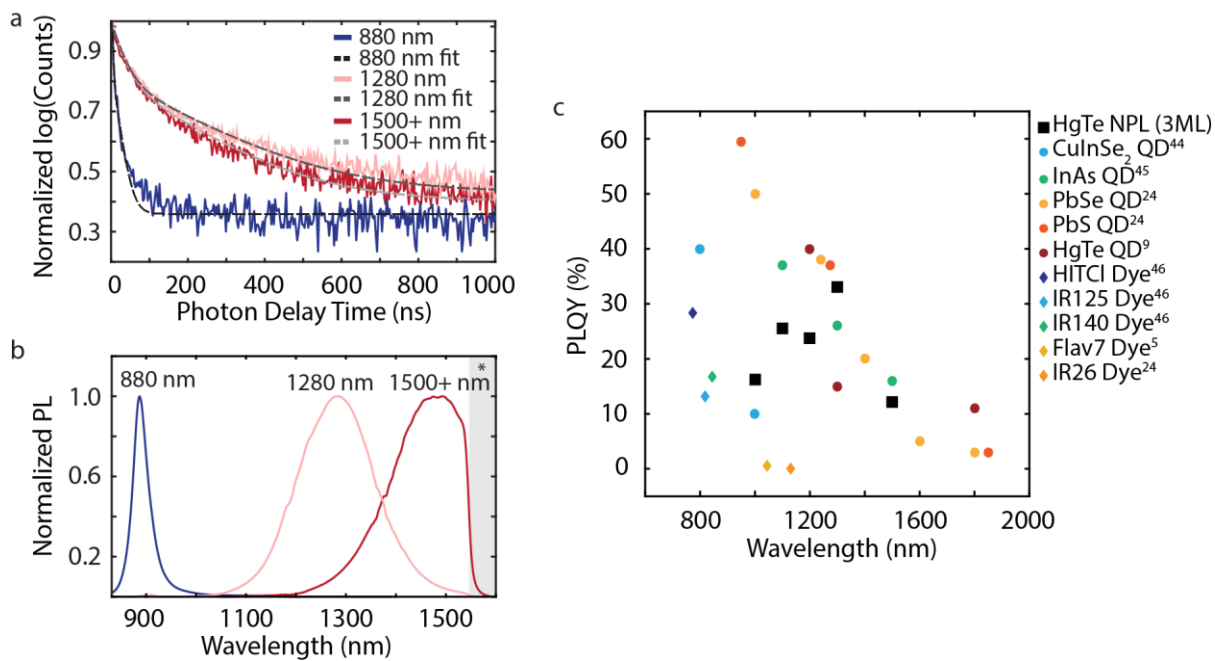
Figure 2.5.*(a) Photoluminescence lifetimes from HgTe NPLs showing only band-edge (880 nm) and two samples with varying mid-gap emission (1280 and 1500+ nm). (b) The corresponding PL spectra, which are corrected as described in the supporting information (Figure 2.26). The (*) indicates the limits of the detector. (c) The QY of organic dye and QD fluorophores across the NIR/SWIR.[5,9,24,44–46]*

2.6 PLQY and Lifetime Properties of NPL/QD Heterostructure

Using superconducting nanowire single photon detectors and a time-tagged photon counting module, we are able to obtain time-resolved photoluminescence of SWIR emitting NPLs at varying stages of mid-gap emission evolution (Figure 2.5a,b). Lifetimes collected from NPLs showing only band-edge have an average lifetime of 7.4 ns while those which show mid-gap emission from the QDs have an average lifetime of 130 ns (Table 2.2). Taking the QY of our SWIR emitting QD-on-NPLs to be (0.3) this lifetime suggests a radiative rate of approximately 430 ns. Various mid-gap emitting NPLs (regardless of their central wavelength) show similar dynamics (Figure 2.26), suggesting a common nature to the mid-gap emission, regardless of depth. The carrier lifetimes for these SWIR emitting HgTe NPLs are significantly faster than PbS QDs, which are known to have lifetimes on the order of microseconds.[47–49] and slightly faster than HgTe QDs which are reported to be 480 ns.[37] Recent work towards 2D PbS NPLs has shown great improvement towards decreasing these lifetimes, with similar values as this work (50-60 ns), however tuneability into the SWIR while maintaining high QY has yet to be shown.[50–52] While maintaining fast radiative rates, our HgTe NPLs/QD heterostructures demonstrate high QY that are competitive with other quantum dots which emit in this region of the spectrum (Figure 2.5c).

2.7 Conclusions

We show bright and continuously tuneable mid-gap state emission in HgX NPL heterostructures by post-synthetic growth of QD-like surface defects. Quantum yields for these emissive states are >30% making them comparable to the best infrared emitting PbX and HgTe QDs, while showing markedly faster radiative rates of 430 ns without any added optimizations. We find that the energy of this mid-gap state is a function of both cation and ligand exchange properties and is consistent with slow activated growth of HgX QD defects on the NPL structure. The mechanism of the SWIR evolution appears to be applicable to the family of HgX nanoplatelets

including 2 ML HgTe and 3 ML HgSe. Their highly tuneable emission and radiative lifetimes while maintaining the large area NPL morphology give them potential applications in higher flux light emission technologies, such as LEDs, sensors, and single photon emitters.

2.8 Experimental Details

Cadmium acetate dihydrate (Acros, 98%), selenium powder (Acros, 99.5%), tellurium powder (Acros, 99.8%) 1,2-dichlorobenzene (Acros, 99%), cadmium oxide (Alfa Aesar, 99.95%) , oleic acid (Alfa Aesar, 99%), tri-n-octylphosphine (TOP) (Alfa Aesar, 90%) and 1-octadecene (ODE) (Alfa Aesar, 90%) mercury (II) acetate (Chem-Impax International, 98.0%), ethanol (Fisher, 95.27%), hexanes (Fisher, 98.5%), toluene (Alpha Aesar, 99.8%), propionic acid (Fisher) oleylamine (Tokyo Chemical, 50.0%), and triisobutylamine (Sigma Aldrich, 98%) were used.

2.8.1 Synthesis of Precursors

Cadmium Propionate (Cd(prop)$_2$). 1.036g of CdO powder was mixed with 10 mL propionic acid under Ar flow for 1 hour. The flask was then opened to atmosphere and heated at 140 ℃ until the volume was reduced to half. The white solution was precipitated with acetone and centrifuged. The supernatant was discarded, and the solid was dried and stored in a vacuum desiccator.

1M TOP-X (X= Se, Te). In a small flask, 5mmol of X powder and 2 mL of tri-n-octylphosphine were degassed under vacuum at room temperature. Then, under Ar flow, the solution was stirred (at room temperature for TOP-Se, or at 275 ℃ for TOP-Te) until the dissolution was complete.

10 mM mercury acetate (Hg(OAc)₂). In a small vial, 9.2 mg of mercury (II) acetate and 3 mL of oleylamine were stirred at room temperature until dissolved. The same procedure was repeated with triisobutylamine solution. For concentrations less than 10mM, solutions were diluted from a 10mM stock solution with oleylamine and stirred at room temperature. For concentrations greater than 10mM, solutions were individually made and sonicated at 35 °C for 20 min to dissolve all of the salt.

2.8.2 Nanoplatelet Synthesis

Synthesis of 3ML CdSe NPL. In a three-neck flask, 240 mg of $Cd(OAc)_2•2H_2O$, 0.150 mL of oleic acid and 15 mL of octadecene (ODE) were degassed under vacuum at 80 ºC for 1 hour. Under Ar flow, the solution was then heated to 195 ºC and 0.4 mL of 1M TOP-Se mixed with 3.75 mL ODE was injected with a syringe pump at a rate of 5 mL/hr. The solution was then cooled and the NPLs were precipitated with ethanol, centrifuged, and re-suspended in 20 mL of hexanes. Assuming that 0.4 mmol of Se has reacted, we obtain an approximate final concentration of 26 mM Cd in the NPLs.

Synthesis of 3ML CdTe NPL. In a three-neck flask, 260 mg of $Cd(prop)_2$, 0.160 mL of oleic acid and 20 mL of octadecene were degassed under vacuum at 90 ºC for 1 hour. Under Ar flow, the solution was then heated to 210 ºC and 0.200 mL of 1M TOP-Te mixed with 3.75 mL of octadecene was injected with a syringe pump at a rate of 5 mL/hr. The solution was then cooled and 0.500 mL of oleic acid was injected. The NPLs were precipitated with ethanol and centrifuged at 14000 rpm for 5 min, followed by resuspension in 20 mL hexanes.

Assuming that the 0.2 mmol of Te has reacted, we obtain an approximate final concentration of 13 mM Cd in the NPLs.

Synthesis of 2ML CdTe NPL. In a 3 neck flask, 130 mg of Cd(prop)$_2$, 0.080 mL oleic acid, and 10 mL of octadecene were degassed at 90 ℃ for 1 hour. Under Ar flow, the solution was then heated to 180 ℃. When the temperature was reached, 0.100 mL of 1M TOP-Te mixed with 0.500 mL octadecene were swiftly injected. After 20 min, the reaction was cooled to room temperature and 1 mL of oleic acid was injected. The NPLs were precipitated with ethanol and centrifuged at 14000 rpm for 5 min, followed by resuspension in 10 mL hexanes.

Cation exchange from CdX to HgX NPL (X= Te, Se). In a round-bottom flask, 0.240 mL of 6mM CdX NPL and 6 mL of hexanes were mixed. Then, 0.300 mL of 10 mM Hg(OAc)$_2$ in oleylamine was added and stirred at room temperature. This results in a 1:2 (Cd:Hg) ratio where Hg^{2+} is added in excess. The reaction was considered complete when the absorption of the hh exceeds that of the lh (typically 3-4 hr). The NPLs were then centrifuged at 14000 rpm for 5 minutes and resuspended in 5 mL hexanes. Samples that do not undergo the washing procedure experience the same mid-gap formation and evolution, however at a different rate. All data reported corresponds to washed NPLs unless stated otherwise.

Cation exchange in triisobutlyamine. The procedure was repeated for exchange from CdTe to HgTe NPL using 10 mM Hg(OAc)$_2$ in triisobutylamine.

2.8.3 Material Characterization.

Absorption spectra were acquired with an Agilent Cary 60 UV-Vis spectrophotometer. Photoluminescence (PL) was obtained from a Horiba Scientific PTI QuantaMaster400 equipped with liquid nitrogen cooled InGaAs photodiode and Si photomultiplier tube detectors. Absolute quantum yield was obtained using an integrating sphere. Lifetime measurements were performed on a home-built optical imaging set up, using short wave sensitive superconducting nanowire single photon detectors (SNSPDs) and a time-lagged single photon counting module.[49] For all measurements, the approximate power used was 6.7×10^{-7} J/cm^2 for a 532 nm laser at a 1 MHz repetition rate.

Transmission electron microscopy (TEM) images were acquired with a FEI Tecnai G2 TF20 200 kV TEM. The NPLs were diluted in hexanes and drop casted on Ted Pella, Inc. Formvar 300 mesh copper grids. HAADF images were obtained at 200kV on a FEI Titan 80-300 kV S/TEM. The NPLs were diluted in hexanes and dropcast onto Ted Pella, Inc carbon only 200 mesh copper grids. Infrared (IR) spectroscopy was performed using a Perkin-Elmer Spectrum Two Fourier Transform IR spectrometer equipped with a universal Diamond/ZnSe ATR. Energy dispersive X-ray (EDX) measurements were obtained on a JEOL JSM-6700F FE scanning electron microscope equipped with an EDX detector. The NPLs were filtered using the above syringe filter method, and dropcast onto either aluminum or silicon substrate. EDX measurements were collected using an operating bias of 9 kV. Resonance Raman was obtained with a Horiba LabRAM HR Evolution spectrometer using a 488 nm laser excitation. NPLs were dropcast from a solution of hexanes onto a glass microscope slide.

2.9 Supporting Information

This section contains additional optical characterization, elemental and structural analysis including: absorption and PL, EDX, FTIR, and TEM.

Solvent Reabsorption Correction (Inner Filter Effect Correction)

When measuring our PL spectra, $I_{measured}(\lambda)$, in the SWIR we observe attenuation of the spectrum at specific wavelengths (λ) due to absorption of the solvent from vibrational overtone bands. Therefore, the substructure within the spectra data is an artifact of the PL spectra measurements in the presence of hexanes, not intrinsic to the NPLs themselves. Hence,

$$\frac{I_{measured}(\lambda)}{I_{emitted}(\lambda)} = T_{Hexanes}(\lambda) = \left(1 - A_{Sample,Hexanes}(\lambda)\right) \qquad (2.1)$$

where $I_{emitted}(\lambda)$ is the spectrum actually emitted by the NPLs, $T_{Hexanes}(\lambda)$ is the fraction of transmitted light through the solvent (hexanes this case) and $A_{Sample,Hexanes}(\lambda)$ is the fraction of absorbed light from the hexanes. The $A_{Sample,Hexanes}(\lambda)$ depends on hexanes' molar extinction, molar volume density, and the exact geometry of the Horiba Fluorometer PTI QM-400 setup involving focusing a cylindrical shaped excitation beam on a sample from which the (cylindrically-shaped) emission is collected and focused into a monochromator. As such, conventional solvent reabsorption correction formulas assuming a collimated beam through the same cannot be applied.

In order to approximate a reabsorption correction to determine peak location and width we estimate $A_{Sample,Hexanes}(\lambda) = D \times A_{Known,Hexanes}(\lambda)$, where $A_{Known,Hexanes}(\lambda)$ is measured absorption spectrum of hexanes using a UV-Vis-NIR spectrometer and D is a constant scaling factor to account for differences in geometry from the measured spectrum and that of NPL PL. We measured $A_{Known,Hexanes}(\lambda)$ using a cuvette 0.2 mm of pure hexanes and is plotted as the red curve in Figure 2.6a.

We can express our measured PL spectrum as:

$$I_{measured}(\lambda) = I_{emitted}(\lambda)\left(1 - D \times A_{Known,Hexanes}(\lambda)\right) \tag{2.2}$$

Rearranging equation 2.2 we have

$$I_{emitted}(\lambda) = I_{measured}(\lambda) + I_{emitted}(\lambda)D \times A_{Known,Hexanes}(\lambda) \tag{2.3}$$

For the $I_{emitted}(\lambda)c\, A_{Known,Hexanes}(\lambda)$ term, $I_{emitted}(\lambda)$ serves as a guess envelope function $I_{emitted}(\lambda) \sim I_{envelope}(\lambda)$, to scale the hexanes absorbance by the emitted intensity at λ. So, we have:

$$I_{emitted}(\lambda) = I_{measured}(\lambda) + I_{envelope}(\lambda)D \times A_{Known,Hexanes}(\lambda) \tag{2.4}$$

From other literature of nanocrystals with mid-gap emissions and from HgSe NPL PL with negligible hexanes absorption (Figure 2.6b), we can estimate this envelope function to be described by one or two Gaussian curves, $I_{emitted}(\lambda) \sim I_{envelope}(\lambda) = A_1 e^{\left(\frac{\lambda - B_1}{C_1}\right)} + A_2 e^{\left(\frac{\lambda - B_2}{C_2}\right)}$ which describes the general shape of the NP PL spectra hence serving as a good envelope for the hexanes absorption.[53] Substituting $I_{emitted}(\lambda)$ for $I_{envelope}(\lambda)$ in equation 2.2 obtain and adding for I_0 a constant baseline offset:

$$I_{measured}(\lambda) = \left(A_1 e^{\left(\frac{\lambda - B_1}{C_1}\right)} + A_2 e^{\left(\frac{\lambda - B_2}{C_2}\right)}\right)\left(1 - D \times A_{Known,Hexanes}(\lambda)\right) + I_0 \tag{2.5}$$

Equation 2.5 describes a fitting function for the measured PL spectrum, $I_{measured}(\lambda)$, with 8 free parameters, six pertaining to the two Gaussians for the envelope function, one for the scaling of the hexanes absorption, and one for a baseline offset, I_0. In order to determine the fit parameters, we obtain a function form of $A_{Known,Hexanes}(\lambda)$ from the measured spectrum. As Gaussian curves form a basis for any continuous function and are appropriate to describe inhomogeneously broadened spectra, we determine a functional form of $A_{Known,Hexanes}(\lambda)$ from a fit to a sum of 23 Gaussian curves with a cubic baseline correction, as shown in Figure 2.6. (We ascribe no significance to these Gaussians curves but rather use them as functions to describe the data.)
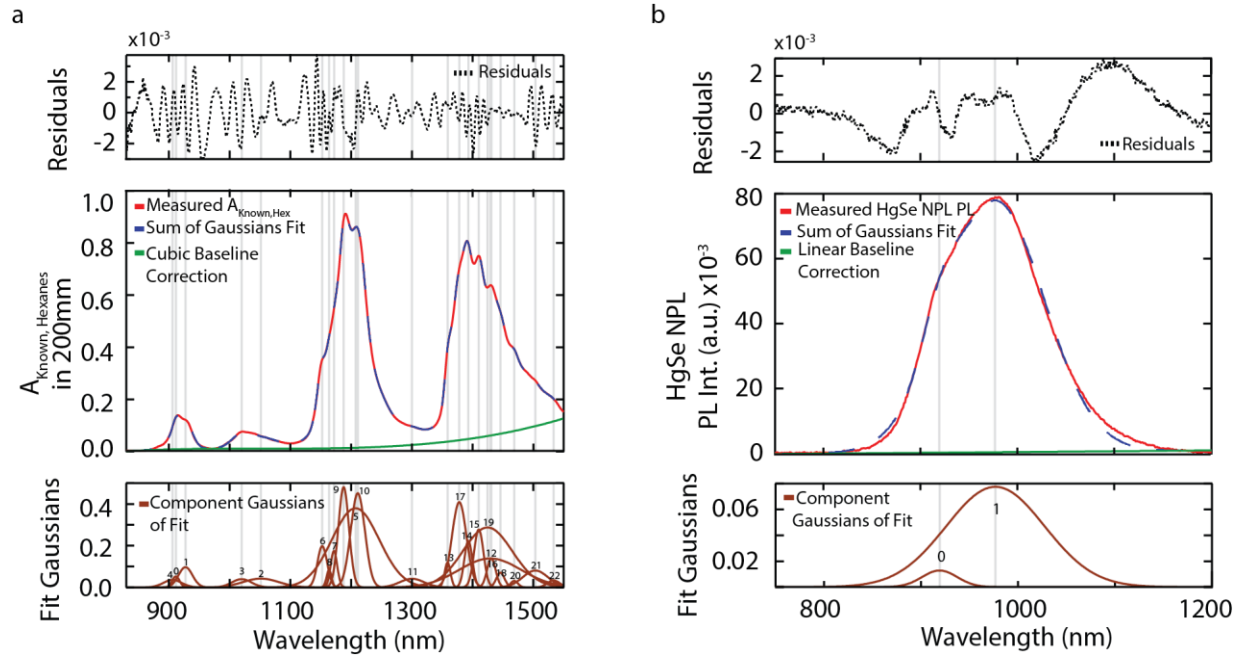
Figure 2.6*. (a) Measured percent absorbance spectrum (red) of hexanes fit to a function of sum of 23 Gaussian curves (dashed blue) with a cubic baseline correction (green). Above the fit shows the residuals (dotted black) and below shows the component Gaussian curves (brown). (b) Measured PL spectrum of mid-gap emission from HgSe NPL (red) fit to a function of two Gaussian curves (dashed blue). Above the fit shows the residuals (dotted black) and below shows the component Gaussian curves (brown).*

Using equation 2.5 we fit the 8 parameters to the measured NPL PL spectrum and then use the parameters to determine the $I_{emitted}(\lambda)$ from equation 2.4. This process was done for each mid-gap NPL PL spectrum. We determined the correction factor D, which predominately depends on the setup geometry, to be 0.7 ± 0.02 across different measurements/fits. An example is shown below in Figure 2.7.
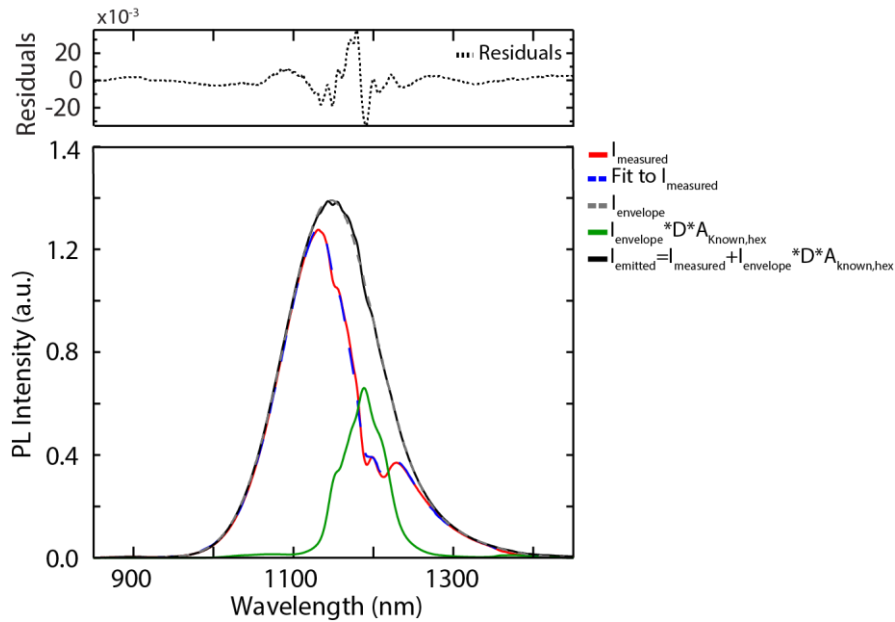
Figure 2.7. An example of parts of the reabsorption correction of a SWIR emission from HgTe NPL mid-gap states. The measured SWIR PL spectrum is given in red, and the fit is dashed blue with black dots above giving the residuals. The envelope function is given in dashed grey, with the calculated loss spectral intensity loss from hexanes is given in green. The final corrected spectrum is shown in black.

We emphasize that this correction was done to only determine approximate losses due hexanes, peak location and width. Any substructure observed may be artifacts from approximate nature of the correction should not be given interpreted as significant. Using two Gaussian curves as an envelope function also enforces a similar peak shape on the corrected $I_{emitted}(\lambda)$, hence we avoid any further analysis and interpretation. The peak

location and FWHM was determined by fitting a single Gaussian give on a corrected $I_{emitted}(\lambda)$ (Figure 2.8). The reabsorption corrected quantum yield was determined by:

$$QY_{corrected} = QY_{measured}\left(1 + \frac{\int I_{envelope}(\lambda)D \times A_{Known,Hexanes}(\lambda)d\lambda}{\int I_{measured}(\lambda)d\lambda}\right) \qquad (2.6)$$
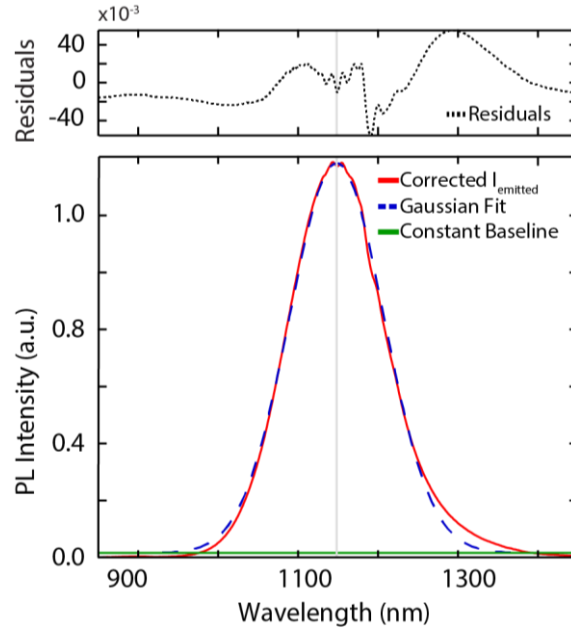
Figure 2.8. Reabsorption corrected HgTe NPL PL spectrum fit to a single Gaussian curve to extract peak location and FWHM
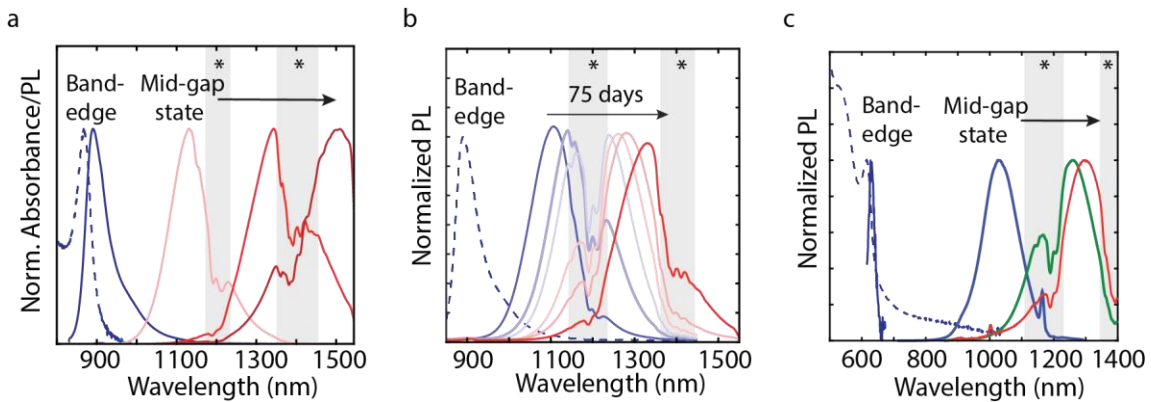
Figure 2.9.The uncorrected HgTe NPL PL corresponding to the corrected spectra shown in (a) Figure 2.1b, (b) Figure 2.2, (c) Figure 2.1c. The (*) denotes where solvent reabsorption due to hexanes occurs.

To determine how this correction for hexanes reabsorption compares to the PL taken in a SWIR transparent solvent, we compared NPL emission taken in hexanes and tetrachloroethylene in Figure 2.10. We find that this correction recovers the features seen in the TCE PL. For this sample, experimental absolute PLQY was determined to be 21% and the correction predicts a PLQY of 26%. Compared to experimental absolute PLQY in TCE which was found to be 42%, we are confident that the correction is not over-reporting the PLQY values.
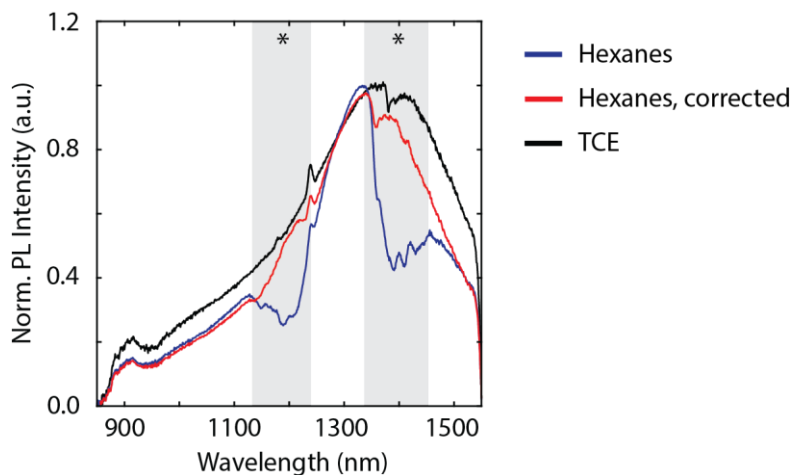
Figure 2.10. The comparison of a solvent reabsorption corrected spectra for 3ML HgTe NPLs suspended in hexanes (red) and tetrachloroethylene (TCE) (black). The (*) indicates features due to hexanes solvent reabsorption which are corrected for.

Photoluminescence Quantum Yield Measurements

Absolute quantum yields were obtained using an integrating sphere. All solutions were diluted to have an absorbance below 0.75. All samples were excited at 824 nm.
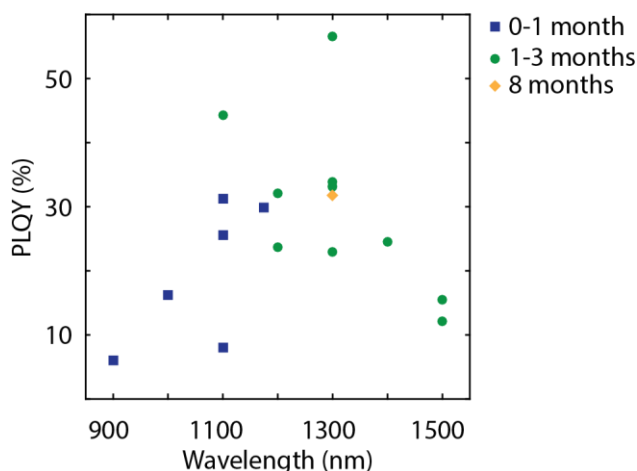
Figure 2.11. The measured absolute photoluminescence quantum yields (PLQY) of various samples of HgTe NPLs showing band edge (900 nm) emission and mid-gap (1000+ nm) emission. Typical yields are between 25-35%, but can reach up to 56%. QY remains high even in NPL aged up to 8 months. Note that none of the values above are corrected for solvent reabsorption, and yields are likely higher as depicted in Figure 1b.

As a standard of comparison, we measured the quantum yield of the SWIR dye Flav7 in dichloromethane (DCM), with reported literature values of 0.53% QY.[5] The Flav7 was diluted to match the absorbance of the nanoplatelets at the excitation wavelength of 824 nm. Using the relative method of QY determination where

$$\phi_{NPL} = \phi_{Flav7} \left(\frac{F_{NPL}}{F_{Flav7}}\right)\left(\frac{f_{Flav7}}{f_{NPL}}\right)\left(\frac{n_{Hex}^2}{n_{DCM}^2}\right) \qquad (2.7)$$

and,

$$f = 1 - 10^{-A(\lambda_{ex})} \qquad (2.8)$$

as described by Würth et al.[54] F is the integrated fluorescence intensity, f is the absorption factor calculated by equation 2.8, and n is the refractive index of the respective solvents.

Using this method, we fit the data using a linear regression (Figure 2.10) to obtain $\left(\frac{F_{sample}}{f_{sample}}\right)$ for both Flav7 and HgTe and find the quantum yield of the HgTe NPLs to be $18 \pm 5\%$. An absolute quantum yield of the same HgTe NPL sample using an integrating sphere was then determined and found to be 25.6%. While the relative quantum yield is not entirely optimized considering the difference in solvent between the two samples (DCM vs. hexanes) and non-linearity of the HgTe in Figure 2.12c, this value provides us with an estimate about the magnitude of QY for these NPLs and gives greater confidence in the reported absolute quantum yield where concentration is not as strict of a concern.
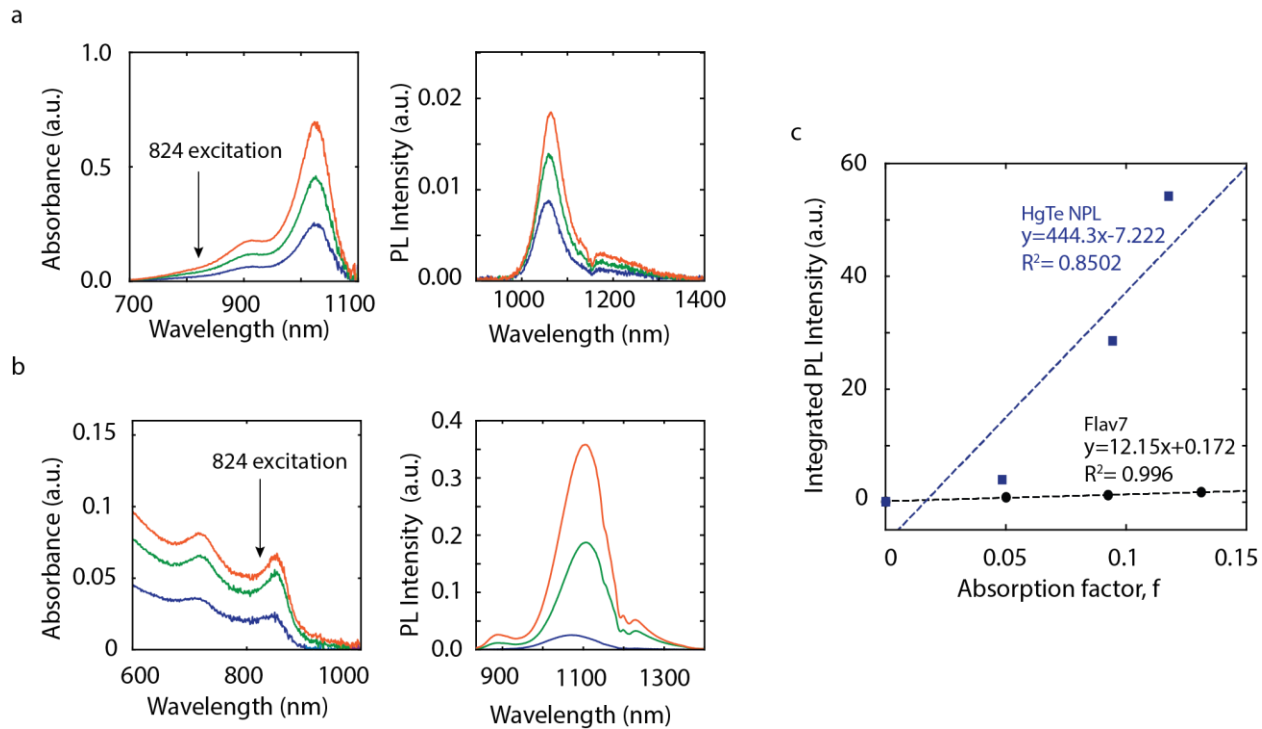
Figure 2.12. *The relative quantum yield determination of HgTe NPLs. a) the absorbance and PL of Flav7, b) the absorbance and PL of HgTe NPLs, and c) the integrated PL intensity of the diluted solutions and their fit lines (dashed lines) used to determine the relative quantum yield in equation 2.7.*
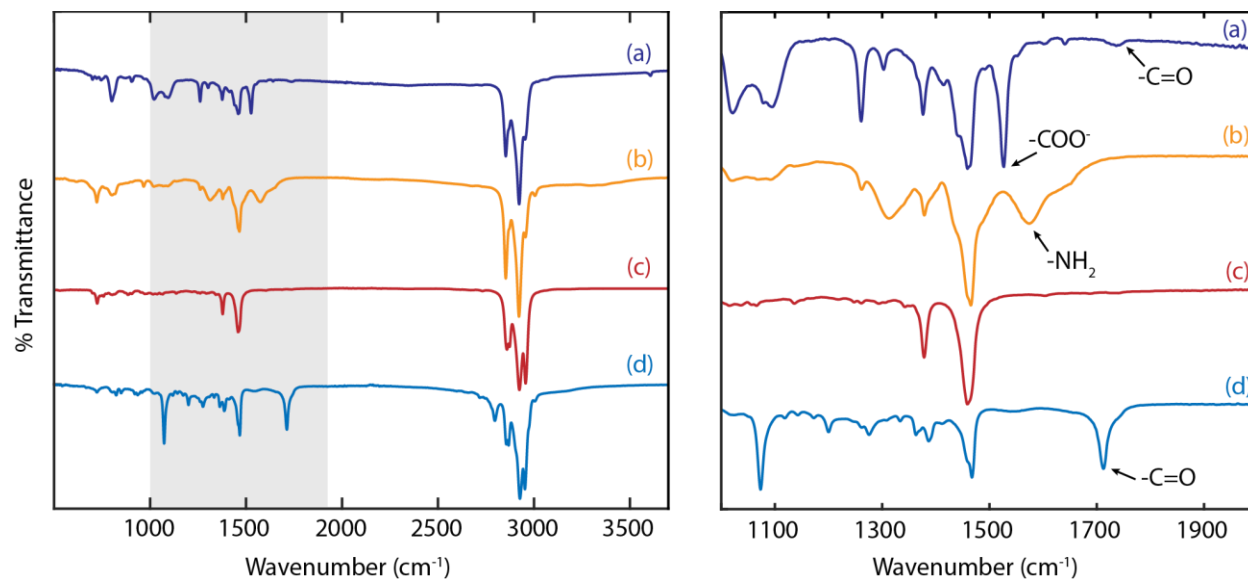
Figure 2.13. *FTIR spectroscopy of (a) 3ML CdTe NPL before exchange, (b) 3ML HgTe NPL immediately after exchange in oleylamine, (c) 3ML HgTe NPL after deep mid-gap formation, and (d) 3ML HgTe NPL obtained through exchange in triisobutylamine.*

The spectra reveal that the CdTe NPLs are primarily capped with bridging –COO⁻ type ligands—likely oleate or precursor acetates (namely propionate). In addition, there appears to be oleic acid either free or bound as non-bridging. Lack of a broad –OH peak from 3000-3500 cm⁻¹ suggests the latter. Once exchanged with Hg^{2+} in oleylamine, these features are lost and those indicative of an amine are visible. When NPLs that have been aged and show mid-gap state emission are compared, we see loss of any distinct features other than those associated with aliphatic –CH₂ and –CH₃ bends (1459 and 1378 cm⁻¹ respectively).[55,56,57] When the exchange is completed in triisobutylamine instead of oleylamine, the dominant features resemble dimeric oleic acid with peaks at 1715 and 2798 cm⁻¹ which suggests the oleic acid is free. There is a small feature which suggests bridging –COO⁻ ligands, but none which suggest bound amine.

Figure 2.14. *(a) In-situ absorbance and (b) photoluminescence measurements used to monitor the progress of the reaction. After the disappearance of the CdTe excitonic features in the absorption spectrum, the HgTe features appear and gradually redshift towards the band-edge (hh) of 880nm. Photoluminescence shows that during formation the emission shifts from 850nm to about 900 nm and narrows to a FWHM of about 40 nm.*

Figure 2.15. *Elemental Dispersive X-Ray Spectroscopy (EDX) of (a) CdTe NPLs and (b) HgTe NPLs. The (*) denotes substrate and impurities.*

Table 2.1. *The average atomic percent obtained by Scanning Electron Microscope-EDX following the exchange from CdTe NPLs to HgTe NPLs over time. Time 0 min indicates only CdTe NPL before any Hg^{2+} is added, and the remaining intermediates correspond to time after the Hg^{2+} is injected. Each value is a weighted average of 10 scans, and the error of each was propagated using the error of each individual scan to find the weighted average and its uncertainty.*

Relative Average Atomic Percent (%)								
Element	0 min	10 min	1hr	2hr	3.5hr	6hr	1 day	14 days
Cd	54 ± 2	31 ± 2	0.4 ± 0.3	0	0	0	0	0
Hg	0	12.7 ± 0.6	38 ± 2	40 ± 2	41 ± 2	39 ± 2	39 ± 5	43 ± 2
Te	54 ± 2	43 ± 5	61 ± 4	51 ± 4	59 ± 5	60 ± 5	61 ± 10	57 ± 4

Figure 2.16. *(a) Low Frequency Resonance Raman of a sample showing mostly band edge emission (blue) and a sample showing mostly mid-gap state emission (red), both excited at 488 nm. The peak around 120 cm^{-1} is attributed to an HgTe TO mode and the peak at 140 cm^{-1} to the LO mode.[58] Lack of a mode at 166 cm^{-1} indicates the absence of CdTe.[59]*

There is a visible shift in the Raman spectrum from a fresh sample showing only band-edge emission (BE) to one which has aged and shows predominately mid-gap (MG) state emission. This shift towards lower energies could be indicative of a number of changes in the NPL structure post-exchange.

It has been shown that in CdSe QDs, the presence of tensile stress and/or confinement of phonons will shift the optical modes in the resonant Raman spectrum towards lower energies, while compressive stress will shift towards higher energies.[60] In CdSe NPLs, a change in the thickness direction has been associated with the shift of the LO phonon where smaller thickness results in a decrease in frequency and broadening of these peaks.[61,62] Prior work suggests that a decrease in thickness of NPLs may result in a spatial confinement of LO phonons.

These results could explain the trend seen in our system, where the TO and LO modes decrease in energy and the LO mode increases in relative intensity as the mid-gap state has evolved. While it is still unclear whether the shift towards lower frequencies can be attributed to a decrease of compressive stress or change in the confinement of phonons by decreasing thickness, it points to a structural difference between NPLs that emit from the band-edge and those which emit from the mid-gap state.

Absorption of HgTe NPLs and QD in the SWIR

To test for the presence of HgTe QDs as the SWIR emitters, we measured absorbance, PL, and photoluminescence excitation (PLE) in aged samples. Typical samples show a long Urbach tail and no strong absorptive features despite the SWIR emission (Figure 2.17), and we attribute this to a low concentration of QDs with a distribution of sizes. In an aged sample with far red-shifted emission (Figure 2.4a) we observe absorption around 1100 nm. PLE of the emission at 1500 nm shows a population of states below the band-edge of the NPL which can be directly excited to produce the SWIR emission.
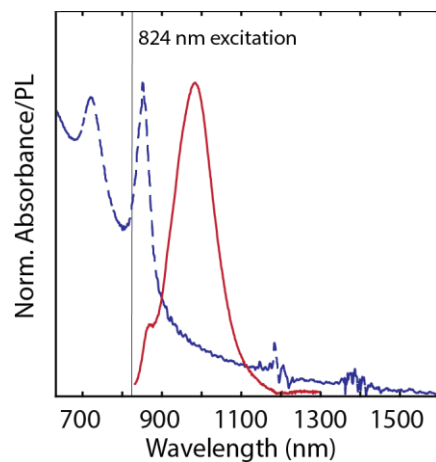
Figure 2.17. (a) Typical absorbance (blue dashed line) of HgTe NPLs in the SWIR and the corresponding photoluminescence (red solid line). The features at 1200 and 1400 nm are due to the solvent (hexanes).
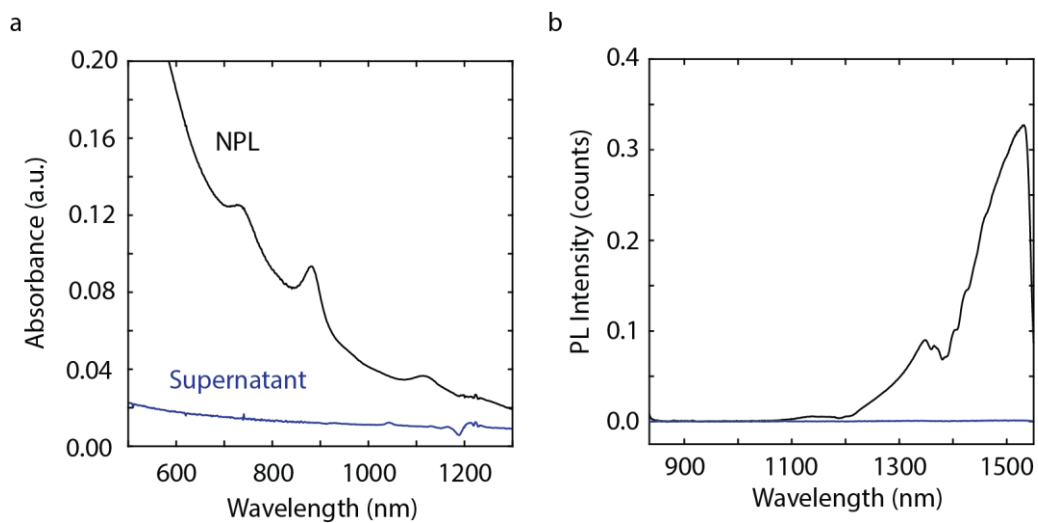
Figure 2.18. *The absorbance (a) and PL (b) of an aged sample of NPLs (black lines), separated from the supernatant (blue lines) by gentle centrifugation. The absence of any features in the supernatant suggest that any SWIR emitting QDs are attached to the NPLs.*

The NPLs were separated from the supernatant to determine if the QDs are attached or free in solution by gentle centrifugation (3000 rpm) and ultrafiltration with a 0.05 micrometer syringe filter. The resulting supernatant shows no absorptive or emissive features (Figure 2.18) suggesting that the QDs are directly attached to the NPLs.
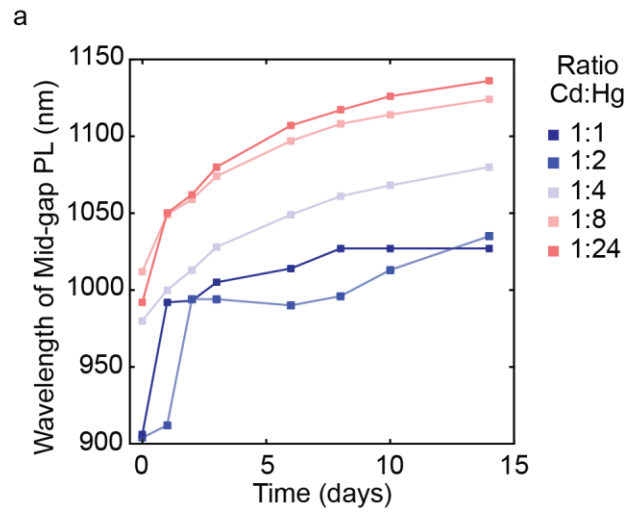
Figure 2.19. *The evolution of the mid-gap state for varying ratios of Cd:Hg. The formation of a mid-gap state begins between about 900-1000 nm and redshifts, but at a slower rate than the HgTe NPLs.*

Cation exchange using triisobutylamine

Exchange from CdTe to HgTe NPLs can be done using the hindered amine, triisobutylamine (TIBAM). Izquierdo *et al.* have studied various amines for cation exchange, but we use TIBAM as a sterically hindered amine that will interact with the surface far less than long chain amines.[14] The band edge emission occurs blue-shifted relative to the oleylamine exchanged NPLs (830 nm vs 900 nm). When varying the ratio of excess Hg, the ratio does not appear to have a significant effect, as mid-gap state evolution remains centered around about 1100 nm for each case shown in Figure 2.20b. Furthermore, while mid-gap state emission does form in samples which initially show only band edge emission, it appears to remain stationary at 1100 nm even over long timescales.
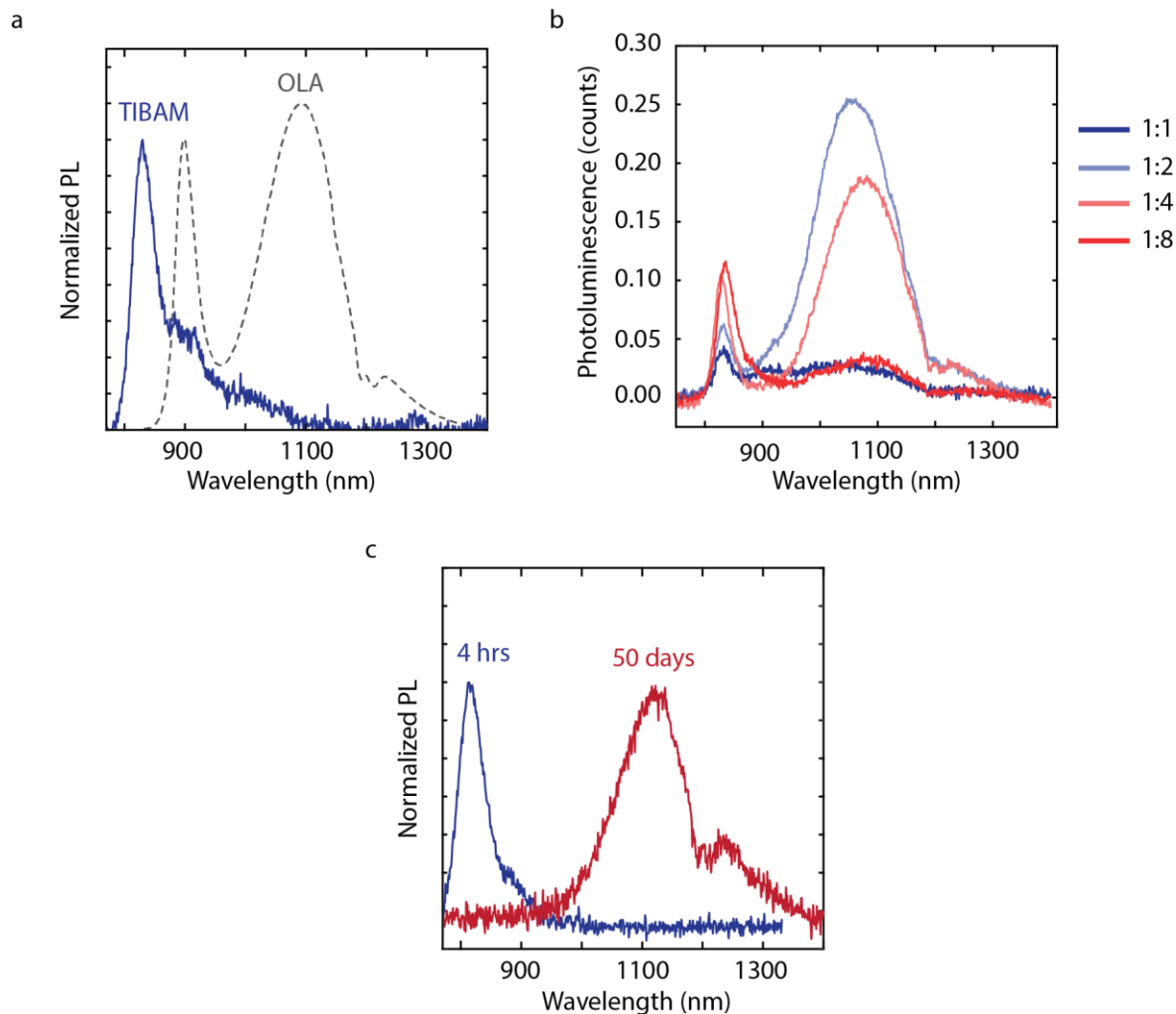
Figure 2.20. Photoluminescence of HgTe NPLs obtained through exchange in triisobutylamine. (a) PL of triisobutlyamine (TIBAM) exchanged NPLs compared to OLA exchanged NPLs. (b) PL of NPLs using varying ratios of Hg^{2+} dissolved in triisobutylamine. (c) PL of a freshly synthesized sample showing only band edge emission, and a sample aged for 50 days. Sample-to-sample variability due to the washing step
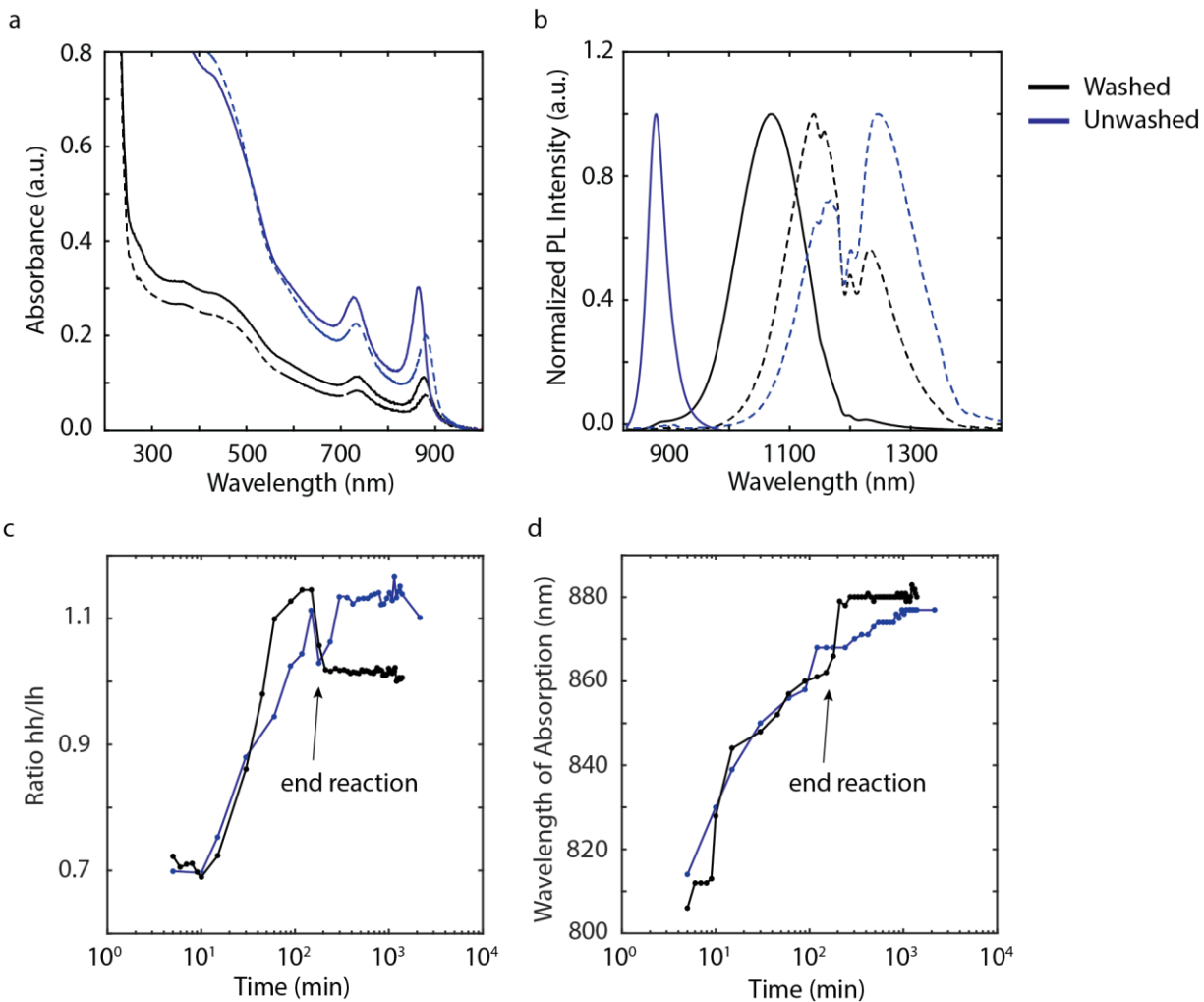
Figure 2.21. *The effect of washing on the absorption (a) and emission (b) spectra over time. Solid lines are samples measured immediately after synthesis and dotted lines are measured after 5 days. Time dynamics of changes in the absorption spectra are further explored by (c) changes in the hh/lh ratio and (d) changes in the shift of wavelength. Samples are washed (black) at 3.5hr, indicated by the end of the reaction.*

To examine the effect of washing on the changes in the absorption and emission spectra (Figure 2.21b) we compare samples that have been washed to those which have not, over the course of 5 days. We see that washing samples results in an immediate red-shift in the absorption spectra accompanied by formation of the mid-gap emission immediately after synthesis. Samples that have

not been washed show the expected band-edge absorption and emission immediately after synthesis but do show similar evolution over time. To more closely monitor changes in the absorption spectra as described in Figure 3b, we examine the hh/lh ratio (Figure 2.21c) and shift in absorption wavelength for washed vs unwashed samples during the exchange process. Typically, the sample are washed via centrifugation after 3.5hr, at the end of the reaction.

While we see some sample-to-sample variability when monitoring the hh/lh ratio (Figure S2.21c) and the shift in the band edge absorption (Figure 2.21d), we find that the overall trend remains the same. We see that this washing accelerates the change in ratio of hh/lh from 1.1 to 1. This process has less of an effect on the position of the band edge absorption, however we do see a slower red shift in the absorption spectrum when unwashed.
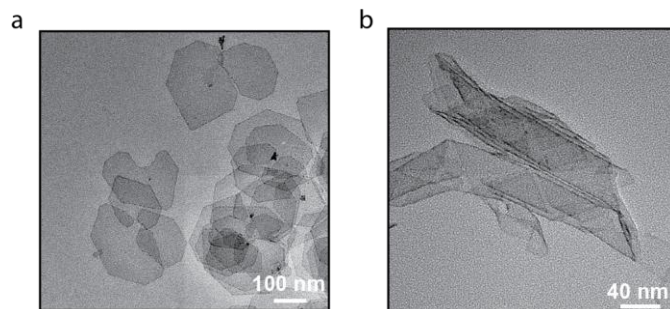
Figure 2.22. *TEM images of (a) 3ML CdTe NPLs and (b) 3ML CdSe NPLs*
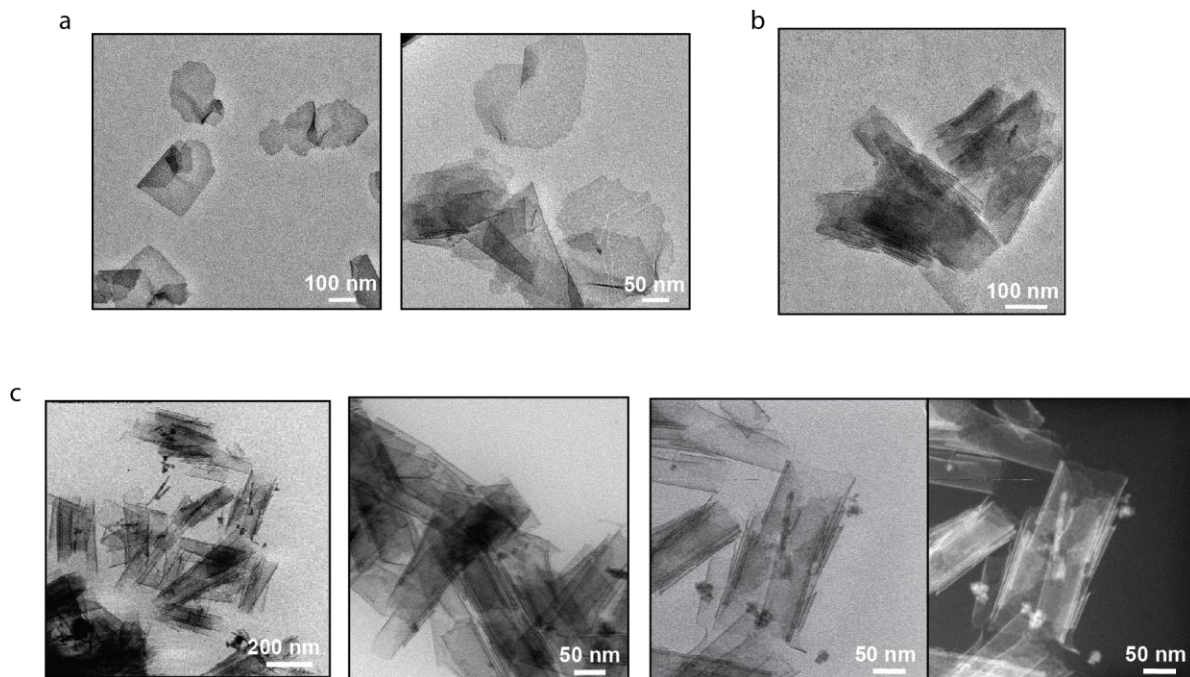
Figure 2.23. *TEM images of (a) freshly synthesized 3ML HgTe NPLs, (b) freshly synthesized 3ML HgSe, and (c) bright field and HAADF of aged 3ML HgTe NPLs showing QD growths.*

Influence of Temperature on Mid-gap State Evolution
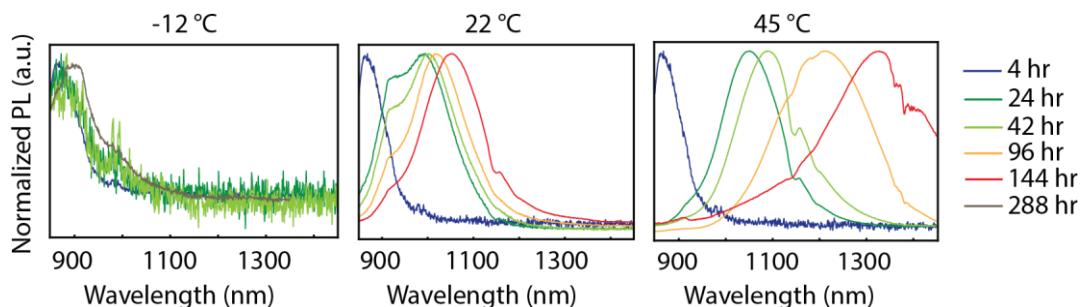
Figure 2.24. The temperature dependence on the rate of mid-gap state evolution. Solutions were held at constant temperature after exchange and monitored by PL over the course of a week (or 12 days in the case of the cold sample).

To understand the impact of temperature on the rate of mid-gap state evolution, we monitored the photoluminescence of solutions kept consistently at -12 °C, 22 °C, and 45 °C after the exchange. We find that when stored in the cold, the mid-gap state does not form, or forms very slowly. In contrast, when held at elevated temperatures, the mid-gap state emission evolves much faster than when cold or room temperature. To obtain a rough estimate for the activation energy of this process we evaluate the kinetics as following Arrhenius type behavior.

Although the rate of evolution of the mid-gap state slows on long timescales (Figure 2.2b), we see that in the first days after exchange the shifting appears linear with time (Figure 2.3e). Therefore, on short timescales we assume that the concentration of the species contributing to the mid-gap state are in such excess that we can model the process as zeroth order with respect to the concentration. By assuming that the energy of the mid-gap state is linearly related to the reaction progress, we obtain a rate in units of eV/hr (Figure 2.3e) where

$$rate(v) = k[reactants]^n \tag{2.9}$$

and because we take n=0 at early timepoints,

$$rate(v) = k \tag{2.10}$$

The rate constant is then related to the activation energy by the Arrhenius equation.

$$k = Ae^{\frac{-Ea}{k_BT}} \tag{2.11}$$

assuming that the factor A is temperature independent, we can obtain the ratio of $\frac{k_1}{k_2}$ at two temperatures T_1 and T_2.

$$\frac{k_1}{k_2} = \frac{v_1}{v_2} = \frac{Ae^{\frac{-Ea}{k_BT_1}}}{Ae^{\frac{-Ea}{k_BT_2}}} = e^{\frac{Ea}{k_BT_2} - \frac{Ea}{k_BT_1}} \tag{2.12}$$

$$\ln v_1 - \ln v_2 = \frac{Ea}{k_BT_2} - \frac{Ea}{k_BT_1} \tag{2.13}$$
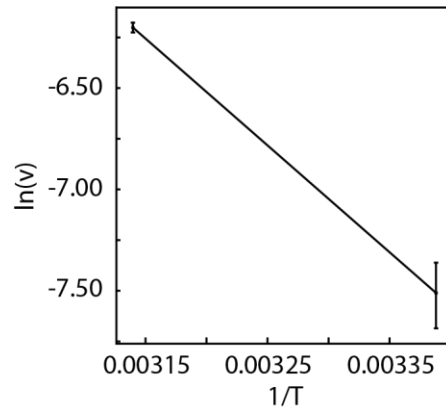
Figure 2.25. *The Arrhenius behavior of the NPLs during the immediate days post exchange, where the slope of the line gives an approximate activation energy for the early evolution of the mid-gap state.*

When we plot ln(v) vs. 1/T we obtain a slope of $-\frac{Ea}{k_B}$ and a value of $E_a \approx 43.8$ kJ/mol. While the assumptions we make may not hold at longer time scales, this gives us insight into what types of processes could be occurring. Given that the bond for bulk HgTe is on the order of 77 kJ/mol, this activation energy could indicate the process is related to the forming or breaking of Hg-Te bonds in the NPLs.[39]

a

b
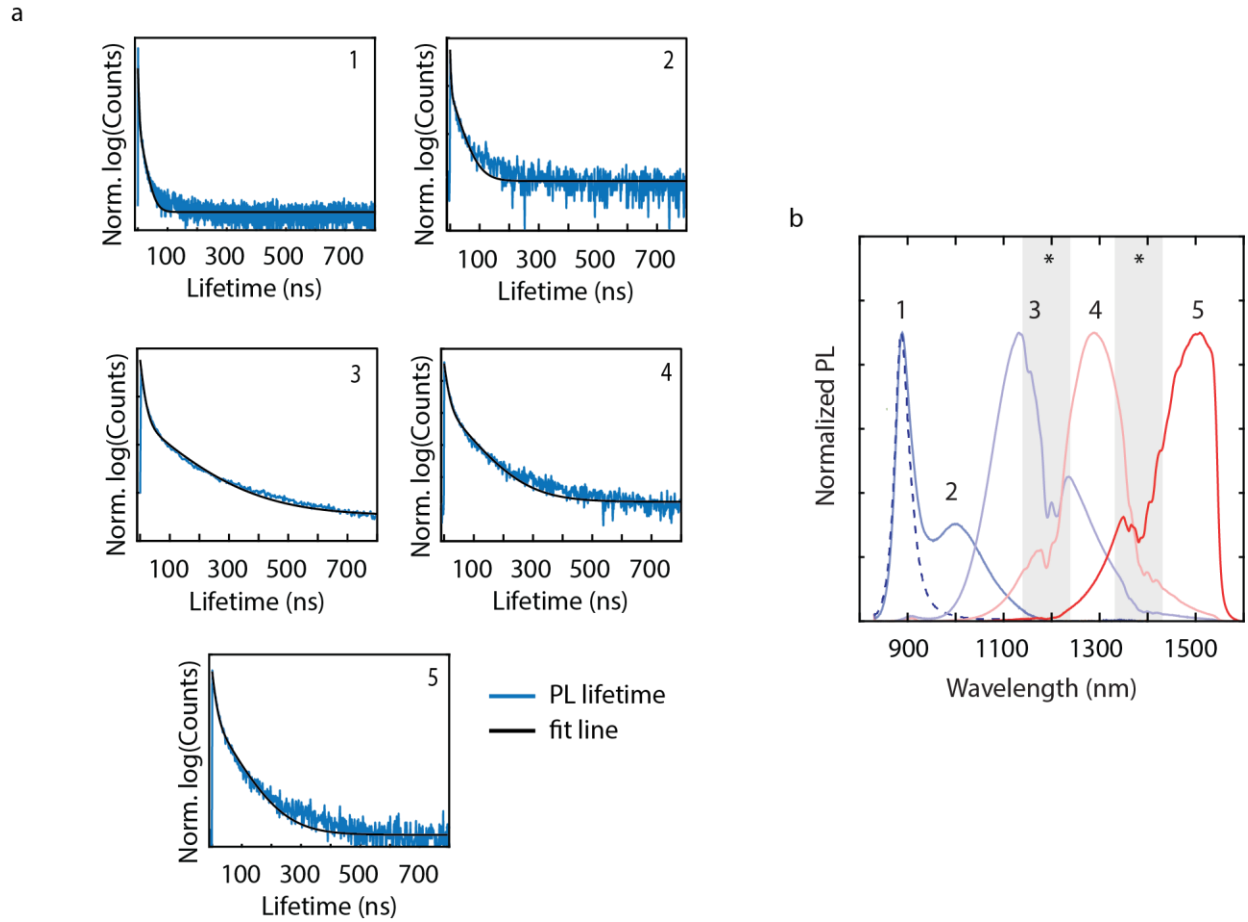
Figure 2.26. *(a) The PL lifetimes and their fits of HgTe NPLs showing only band edge emission (1), intermediate mid-gap emission (2-4), and deep mid-gap (5, 1500 nm+) emission. (b) The respective PL spectra. Note that the (*) indicates solvent reabsorption and the detector cutoff is 1550 nm.*

The photoluminescence lifetimes were fit using the biexponential function given in equation 2.14 while the amplitude weighted average lifetimes were determined by equation 2.15.[63]

$$f(t) = A_1 e^{\frac{-t}{\tau_1}} + A_2 e^{\frac{-t}{\tau_2}} + C \tag{2.14}$$

$$\tau_{avg} = \frac{A_1\tau_1^2 + A_2\tau_2^2}{A_1\tau_1 + A_2\tau_2} \tag{2.15}$$

Table 2.2. *The fit parameters and average lifetimes for HgTe NPLs showing only band edge (BE)*

emission, mixed band edge and mid-gap emission, and only mid-gap emission.

Photoluminescence	A	$1/\tau$ (ns^{-1})	τ (ns)	Amplitude (%)	Fit RMSE	Average Lifetime (ns)
880 nm (BE)	5585.5	0.4356	2.29	90	0.9956	7.4
	645.2	0.0689	14.5	10		
900 nm (BE) + 1100 nm (mid-gap)	385.5	0.2160	4.63	79	0.9035	32.6
	104.9	0.0230	43.5	21		
1200 nm (mid-gap)	12508	0.0750	13.33	75	0.9836	131.9
	4227	0.0062	161	35		
1300 nm (mid-gap)	1377.6	0.0384	26.1	76	0.9807	135.3
	425.5	0.0054	185.12	24		
1500 nm (mid-gap)	803.7	0.0369	27.09	74	0.9740	122.4
	278.7	0.0060	167.0	26		

REFERENCES

(1)   Hansen, M. P.; Malchow, D. S. Overview of SWIR Detectors, Cameras, and Applications.
        Proc. SPIE **2008**, *6939*, 69390I.

(2)   Miron, A.; Bensrhair, A.; Fedriga, R. I.; Broggi, A. SWIR Images Evaluation for
        Pedestrian Detection in Clear Visibility Conditions. In *IEEE Conference on Intelligent
        Transportation Systems, Proceedings, ITSC*; 2013; pp 354–359.

(3)   Hong, G.; Diao, S.; Chang, J.; Antaris, A. L.; Chen, C.; Zhang, B.; Zhao, S.; Atochin, D.
        N.; Huang, P. L.; Andreasson, K. I.; Kuo, C. J.; Dai, H. Through-Skull Fluorescence
        Imaging of the Brain in a New near-Infrared Window. *Nat. Photonics* **2014**, *8* (9), 723–
        730.

(4)   Wan, H.; Du, H.; Wang, F.; Dai, H. Molecular Imaging in the Second Near-Infrared
        Window. *Advanced Functional Materials*. Wiley-VCH Verlag June 21, 2019.

(5)   Cosco, E. D.; Caram, J. R.; Bruns, O. T.; Franke, D.; Day, R. A.; Farr, E. P.; Bawendi, M.
        G.; Sletten, E. M. Flavylium Polymethine Fluorophores for Near- and Shortwave Infrared
        Imaging. *Angew. Chemie - Int. Ed.* **2017**, *56* (42), 13126–13129.

(6)   Melchior, H.; Fisher, M. B.; Arams, F. R. Photodetectors for Optical Communication
        Systems. *Proc. IEEE* **1970**, *58* (10), 1466–1486.

(7)   Jagtap, A.; Goubet, N.; Livache, C.; Chu, A.; Martinez, B.; Gréboval, C.; Qu, J.; Dandeu,
        E.; Becerra, L.; Witkowski, N.; Ithurria, S.; Mathevet, F.; Silly, M. G.; Dubertret, B.;
        Lhuillier, E. Short Wave Infrared Devices Based on HgTe Nanocrystals with Air Stable
        Performances. *J. Phys. Chem. C* **2018**, *122* (26), 14979–14985.

(8)   Martinez, B.; Ramade, J.; Livache, C.; Goubet, N.; Chu, A.; Gréboval, C.; Qu, J.;
        Watkins, W. L.; Becerra, L.; Dandeu, E.; Fave, J. L.; Méthivier, C.; Lacaze, E.; Lhuillier,

E. HgTe Nanocrystal Inks for Extended Short-Wave Infrared Detection. *Adv. Opt. Mater.* **2019**, *7* (15), 1900348.

(9)   Kovalenko, M. V.; Kaufmann, E.; Pachinger, D.; Roither, J.; Huber, M.; Stangl, J.; Hesser, G.; Schäffler, F.; Heiss, W. Colloidal HgTe Nanocrystals with Widely Tunable Narrow Band Gap Energies: From Telecommunications to Molecular Vibrations. *J. Am. Chem. Soc.* **2006**, *128* (11), 3516–3517.

(10)   Goubet, N.; Jagtap, A.; Livache, C.; Martinez, B.; Portalès, H.; Zhen Xu, X.; P. S. M. Lobo, R.; Dubertret, B.; Lhuillier, E. Terahertz HgTe Nanocrystals: Beyond Confinement. *J. Am. Chem. Soc.* **2018**, *140* (15), 5033–5036.

(11)   Abdelazim, N. M.; Zhu, Q.; Xiong, Y.; Zhu, Y.; Chen, M.; Zhao, N.; Kershaw, S. V; Rogach, A. L.; Kong, H. Room Temperature Synthesis of HgTe Quantum Dots in an Aprotic Solvent Realizing High Photoluminescence Quantum Yields in the Infrared. *Chem. Mater* **2017**, *29*, 6.

(12)   Moreels, I.; Lambert, K.; Smeets, D.; De Muynck, D.; Nollet, T.; Martins, J. C.; Vanhaecke, F.; Vantomme, A.; Delerue, C.; Allan, G.; Hens, Z. Size-Dependent Optical Properties of Colloidal PbS Quantum Dots. *ACS Nano* **2009**, *3* (10), 3023–3030.

(13)   Pietryga, J. M.; Schaller, R. D.; Werder, D.; Stewart, M. H.; Klimov, V. I.; Hollingsworth, J. A. Pushing the Band Gap Envelope: Mid-Infrared Emitting Colloidal PbSe Quantum Dots. *J. Am. Chem. Soc.* **2004**, *126* (38), 11752–11753.

(14)   Izquierdo, E.; Robin, A.; Keuleyan, S.; Lequeux, N.; Lhuillier, E.; Ithurria, S. Strongly Confined HgTe 2D Nanoplatelets as Narrow Near-Infrared Emitters. *J. Am. Chem. Soc.* **2016**, *138* (33), 10496–10501.

(15)   Tessier, M. D.; Mahler, B.; Nadal, B.; Heuclin, H.; Pedetti, S.; Dubertret, B. Spectroscopy

of Colloidal Semiconductor Core/Shell Nanoplatelets with High Quantum Yield. *Nano Lett.* **2013**, *13* (7), 3321–3328.

(16) Dufour, M.; Qu, J.; Greboval, C.; Méthivier, C.; Lhuillier, E.; Ithurria, S. Halide Ligands to Release Strain in Cadmium Chalcogenide Nanoplatelets and Achieve High Brightness. *ACS Nano* **2019**, *13* (5), 5326–5334.

(17) Bertrand, G. H. V.; Polovitsyn, A.; Christodoulou, S.; Khan, A. H.; Moreels, I. Shape Control of Zincblende CdSe Nanoplatelets. *Chem. Commun.* **2016**, *52* (80), 11975–11978.

(18) Naeem, A.; Masia, F.; Christodoulou, S.; Moreels, I.; Borri, P.; Langbein, W. Giant Exciton Oscillator Strength and Radiatively Limited Dephasing in Two-Dimensional Platelets. *Phys. Rev. B - Condens. Matter Mater. Phys.* **2015**, *91* (12), 121302.

(19) Abécassis, B.; Tessier, M. D.; Davidson, P.; Dubertret, B. Self-Assembly of CdSe Nanoplatelets into Giant Micrometer-Scale Needles Emitting Polarized Light. *Nano Lett.* **2014**, *14* (2), 710–715.

(20) Diroll, B. T.; Cho, W.; Coropceanu, I.; Harvey, S. M.; Brumberg, A.; Holtgrewe, N.; Crooker, S. A.; Wasielewski, M. R.; Prakapenka, V. B.; Talapin, D. V.; Schaller, R. D. Semiconductor Nanoplatelet Excimers. *Nano Lett.* **2018**, *18* (11), 6948–6953.

(21) Nasilowski, M.; Mahler, B.; Lhuillier, E.; Ithurria, S.; Dubertret, B. Two-Dimensional Colloidal Nanocrystals. *Chem. Rev.* **2016**, *116* (18), 10934–10982.

(22) She, C.; Fedin, I.; Dolzhnikov, D. S.; Dahlberg, P. D.; Engel, G. S.; Schaller, R. D.; Talapin, D. V. Red, Yellow, Green, and Blue Amplified Spontaneous Emission and Lasing Using Colloidal CdSe Nanoplatelets. *ACS Nano* **2015**, *9* (10), 9475–9485.

(23) Chen, Z.; Nadal, B.; Mahler, B.; Aubin, H.; Dubertret, B. Quasi-2D Colloidal Semiconductor Nanoplatelets for Narrow Electroluminescence. *Adv. Funct. Mater.* **2014**,

24 (3), 295–302.

(24)   Semonin, O. E.; Johnson, J. C.; Luther, J. M.; Midgett, A. G.; Nozik, A. J.; Beard, M. C.
Absolute Photoluminescence Quantum Yields of IR-26 Dye, PbS, and PbSe Quantum
Dots. *J. Phys. Chem. Lett.* **2010**, *1* (16), 2445–2450.

(25)   Franke, D.; Harris, D. K.; Chen, O.; Bruns, O. T.; Carr, J. A.; Wilson, M. W. B.; Bawendi,
M. G. Continuous Injection Synthesis of Indium Arsenide Quantum Dots Emissive in the
Short-Wavelength Infrared. *Nat. Commun.* **2016**, *7*.

(26)   C. Weidman, M.; E. Beck, M.; S. Hoffman, R.; Prins, F.; A. Tisdale, W. Monodisperse,
Air-Stable PbS Nanocrystals via Precursor Stoichiometry Control. *ACS Nano* **2014**, *8* (6),
6363–6371.

(27)   Meinardi, F.; Colombo, A.; Velizhanin, K. A.; Simonutti, R.; Lorenzon, M.; Beverina, L.;
Viswanatha, R.; Klimov, V. I.; Brovelli, S. Large-Area Luminescent Solar Concentrators
Based on 'Stokes-Shift-Engineered' Nanocrystals in a Mass-Polymerized PMMA Matrix.
Nat. Photonics **2014**, *8* (5), 392–399.

(28)   Izquierdo, E.; Dufour, M.; Chu, A.; Livache, C.; Martinez, B.; Amelot, D.; Patriarche, G.;
Lequeux, N.; Lhuillier, E.; Ithurria, S. Coupled HgSe Colloidal Quantum Wells through a
Tunable Barrier: A Strategy to Uncouple Optical and Transport Band Gap. *Chem. Mater.*
2018, *30* (12), 4065–4072.

(29)   Pedetti, S.; Nadal, B.; Lhuillier, E.; Mahler, B.; Bouet, C. C.; Abécassis, B. A.; Xu, X.;
Dubertret, B. Optimized Synthesis of CdTe Nanoplatelets and Photoresponse of CdTe
Nanoplatelets Films. *Chem. Mater* **2013**, *25*.

(30)   Gupta, S.; Zhovtiuk, O.; Vaneski, A.; Lin, Y. C.; Chou, W. C.; Kershaw, S. V.; Rogach,
A. L. Cd x Hg (1-x) Te Alloy Colloidal Quantum Dots: Tuning Optical Properties from

the Visible to near-Infrared by Ion Exchange. *Part. Part. Syst. Charact.* **2013**, *30* (4), 346–354.

(31) Deng, Z.; Jeong, K. S.; Guyot-Sionnest, P. Colloidal Quantum Dots Intraband Photodetectors. *ACS Nano* **2014**, *8* (11), 11707–11714.

(32) Singh, S.; Tomar, R.; Ten Brinck, S.; De Roo, J.; Geiregat, P.; Martins, J. C.; Infante, I.; Hens, Z. Colloidal CdSe Nanoplatelets, A Model for Surface Chemistry/Optoelectronic Property Relations in Semiconductor Nanocrystals. *J. Am. Chem. Soc.* **2018**, *140* (41), 13292–13300.

(33) Mirzai, H.; Nordin, M. N.; Curry, R. J.; Bouillard, J. S.; Zayats, A. V.; Green, M. The Room Temperature Phosphine-Free Synthesis of near-Infrared Emitting HgSe Quantum Dots. *J. Mater. Chem. C* **2014**, *2* (12), 2107–2111.

(34) Piepenbrock, M. O. M.; Stirner, T.; Kelly, S. M.; O'Neill, M. A Low-Temperature Synthesis for Organically Soluble HgTe Nanocrystals Exhibiting near-Infrared Photoluminescence and Quantum Confinement. *J. Am. Chem. Soc.* **2006**, *128* (21), 7087–7090.

(35) Green, M. L. H. L. H. *A New Approach to the Formal Classification of Covalent Compounds of the Elements*; Elsevier, 1995; Vol. 500, pp 127–148.

(36) Anderson, N. C.; Hendricks, M. P.; Choi, J. J.; Owen, J. S. Ligand Exchange and the Stoichiometry of Metal Chalcogenide Nanocrystals: Spectroscopic Observation of Facile Metal-Carboxylate Displacement and Binding Scheme 1. Nanocrystal Ligand Binding Motifs According to the Covalent Bond Classification Method. *J. Am. Chem. Soc* **2013**, *135*.

(37) Geiregat, P.; Houtepen, A. J.; Sagar, L. K.; Infante, I.; Zapata, F.; Grigel, V.; Allan, G.;

Delerue, C.; Van Thourhout, D.; Hens, Z. Continuous-Wave Infrared Optical Gain and Amplified Spontaneous Emission at Ultralow Threshold by Colloidal HgTe Quantum Dots. *Nat. Mater.* **2018**, *17* (1), 35–41.

(38)   Chen, O.; Yang, Y.; Wang, T.; Wu, H.; Niu, C.; Yang, J.; Cao, Y. C. Surface-Functionalization-Dependent Optical Properties of II-VI Semiconductor Nanocrystals. *J. Am. Chem. Soc.* **2011**, *133* (43), 17504–17512.

(39)   Chen, A.-B.; Sher, A. *Semiconductor Alloys : Physics and Materials Engineering*; Springer US, 1996.

(40)   Wu, K.; Li, H.; Klimov, V. I. Tandem Luminescent Solar Concentrators Based on Engineered Quantum Dots. *Nat. Photonics* **2018**, *12* (2), 105–110.

(41)   Bowers, M. J.; McBride, J. R.; Rosenthal, S. J. White-Light Emission from Magic-Sized Cadmium Selenide Nanocrystals. *J. Am. Chem. Soc.* **2005**, *127* (44), 15378–15379.

(42)   Yadav, S.; Adhikary, B.; Tripathy, P.; Sapra, S. Efficient Charge Extraction from CdSe/ZnSe Dots-on-Plates Nanoheterostructures. *ACS Omega* **2017**, *2* (5), 2231–2237.

(43)   Williams, K. R.; Diroll, B. T.; Watkins, N. E.; Rui, X.; Brumberg, A.; Klie, R. F.; Schaller, R. D. Synthesis of Type i PbSe/CdSe Dot-on-Plate Heterostructures with Near-Infrared Emission. *J. Am. Chem. Soc.* **2019**, *141* (13), 5092–5096.

(44)   Cassette, E.; Pons, T.; Bouet, C.; Helle, M.; Bezdetnaya, L.; Marchal, F.; Dubertret, B. Synthesis and Characterization of Near-Infrared Cu-In-Se/ZnS Core/Shell Quantum Dots for in Vivo Imaging. *Chem. Mater.* **2010**, *22* (22), 6117–6124.

(45)   Franke, D.; Harris, D. K.; Chen, O.; Bruns, O. T.; Carr, J. A.; Wilson, M. W. B.; Bawendi, M. G. Continuous Injection Synthesis of Indium Arsenide Quantum Dots Emissive in the Short-Wavelength Infrared. *Nat. Commun.* **2016**, *7*.

(46) Rurack, K.; Spieles, M. Fluorescence Quantum Yields of a Series of Red and Near-Infrared Dyes Emitting at 600-1000 Nm. *Anal. Chem.* **2011**, *83* (4), 1232–1242.

(47) Clark, S. W.; Harbold, J. M.; Wise, F. W. Resonant Energy Transfer in PbS Quantum Dots. *J. Phys. Chem. C* **2007**, *111* (20), 7302–7305.

(48) Nienhaus, L.; Wu, M.; Geva, N.; Shepherd, J. J.; Wilson, M. W. B.; Bulović, V.; Van Voorhis, T.; Baldo, M. A.; Bawendi, M. G. Speed Limit for Triplet-Exciton Transfer in Solid-State PbS Nanocrystal-Sensitized Photon Upconversion. *ACS Nano* **2017**, *11* (8), 7848–7857.

(49) Atallah, T. L.; Sica, A. V.; Shin, A. J.; Friedman, H. C.; Kahrobai, Y. K.; Caram, J. R. Decay-Associated Fourier Spectroscopy: Visible to Shortwave Infrared Time-Resolved Photoluminescence Spectra. *J. Phys. Chem. A* **2019**, *123* (31), 6792–6798.

(50) Khan, A. H.; Brescia, R.; Polovitsyn, A.; Angeloni, I.; Martín-García, B.; Moreels, I. Near-Infrared Emitting Colloidal PbS Nanoplatelets: Lateral Size Control and Optical Spectroscopy. *Chem. Mater.* **2017**, *29* (7), 2883–2889.

(51) Khan, S.; Jiang, Z.; Premathilka, S. M.; Antu, A.; Hu, J.; Voevodin, A. A.; Roland, P. J.; Ellingson, R. J.; Sun, L. Few-Atom-Thick Colloidal PbS/CdS Core/Shell Nanosheets. *Chem. Mater.* **2016**, *28* (15), 5342–5346.

(52) Antu, A. D.; Jiang, Z.; Premathilka, S. M.; Tang, Y.; Hu, J.; Roy, A.; Sun, L. Bright Colloidal PbS Nanoribbons. *Chem. Mater.* **2018**, *30* (11), 3697–3703.

(53) Allen, P. M.; Bawendi, M. G. Ternary I-III-VI Quantum Dots Luminescent in the Red to near-Infrared. *J. Am. Chem. Soc.* **2008**, *130* (29), 9240–9241.

(54) Würth, C.; Grabolle, M.; Pauli, J.; Spieles, M.; Resch-Genger, U. Relative and Absolute Determination of Fluorescence Quantum Yields of Transparent Samples. *Nat. Protoc.*

2013, *8* (8), 1535–1550.

(55) Thistlethwaite, P. J.; Hook, M. S. Diffuse Reflectance Fourier Transform Infrared Study of the Adsorption of Oleate/Oleic Acid onto Titania. *Langmuir* **2000**, *16* (11), 4993–4998.

(56) Chen, P. E.; Anderson, N. C.; Norman, Z. M.; Owen, J. S. Tight Binding of Carboxylate, Phosphonate, and Carbamate Anions to Stoichiometric CdSe Nanocrystals. *J. Am. Chem. Soc.* **2017**, *139* (8), 3227–3236.

(57) Mourdikoudis, S.; Liz-Marzán, L. M. Oleylamine in Nanoparticle Synthesis. *Chemistry of Materials*. May 14, 2013, pp 1465–1476.

(58) Ingale, A.; Bansal, M. L.; Roy, A. P. Resonance Raman Scattering in HgTe: TO-Phonon and Forbidden-LO-Phonon Cross Section near the E1 Gap. *Phys. Rev. B* **1989**, *40* (18), 12353–12358.

(59) Amirtharaj, P. M.; Pollak, F. H. Raman Scattering Study of the Properties and Removal of Excess Te on CdTe Surfaces. *Appl. Phys. Lett.* **1984**, *45* (7), 789–791.

(60) Meulenberg, R. W.; Jennings, T.; Strouse, G. F. Compressive and Tensile Stress in Colloidal CdSe Semiconductor Quantum Dots. *Phys. Rev. B - Condens. Matter Mater. Phys.* **2004**, *70* (23), 1–5.

(61) Cherevkov, S. A.; Fedorov, A. V; Artemyev, M. V; Prudnikau, A. V; Baranov, A. V. Anisotropy of Electron-Phonon Interaction in Nanoscale CdSe Platelets as Seen via off-Resonant and Resonant Raman Spectroscopy. *RAPID Commun. Phys. Rev. B* **2013**, *88*, 41303.

(62) Lebedev, A. I. Lattice Dynamics of Quasi-Two-Dimensional CdSe Nanoplatelets and Their Raman and Infrared Spectra. *Phys. Rev. B* **2017**, *96*, 184306.

(63) Lakowicz, J. R. *Principles of Fluorescence Spectroscopy*, 3rd ed.; Springer, 2006.

Chapter 3

Efficient 2D to 0D Energy Transfer in HgTe Nanoplatelet-Quantum Dot Heterostructures through High-Speed Exciton Diffusion

This chapter contains unpublished work by Stephanie M. Tenney, Lauren A. Tan, Xuanheng Tan, Mikayla L. Sonnleitner, Belle Coffey, Jillian Williams, Ricky Ronquillo, Timothy L Atallah, Tasnim Ahmed, and Justin R Caram. The results are preliminary and based on available data.

In the previous chapter we establish a method for developing a new HgTe NPL/QD heterostructure. We further explore the energy transfer properties in this chapter, highlighting the efficiency and application towards energy concentration. Large area absorbers with localized defect emission are of interest for energy concentration via the antenna effect. Transfer between 2D and 0D quantum confined structures is of particular interest as it affords maximal lateral area antenna with continuously tunable emission. We report the quantum efficiency of energy transfer to be near unity (>85%) in in-situ grown HgTe nanoplatelet (NPL)/quantum dot (QD) heterostructures with photoluminescence in the shortwave infrared. By comparison, energy transfer from a solution of HgTe NPLs to separately synthesized QDs only reaches $47 \pm 11\%$ at considerably higher QD concentration. This energy transfer is most optimal in 3 ML HgTe NPLs. Using Kinetic Monte Carlo, we estimate the exciton diffusion constant in HgTe NPLs required to achieve >80% energy transfer. We find that a 2D random walk requires an exciton diffusion constant of 1-10 cm^2/s. This constant is of the same magnitude as other two-dimensional semiconductors and highlights the advantage of NPLs two-dimensional morphology, as well as the efficiency of the NPL/QD heterostructure for energy harvesting.

3.1 Introduction to 2D-0D Energy Concentration

Antennas collect diffuse energy and concentrate it at a receiver, often a localized instrument. Antenna-like exciton harvesting takes absorbed light and moves it a centralized location, where it can be transformed to different wavelengths or used for chemical transformations. Such behavior has been leveraged across material systems, including natural and artificial photosynthetic systems, organic photovoltaics, self-assembled light-harvesting nanotubes, quantum dot heterostructures, all systems where excitons are funneled from a large collection area to a bright emitter or reaction center.[1–6] Converting diffuse and low intensity light into localized emitters limits parasitic reabsorption and is crucial to a number of waveguiding luminescent solar concentration and photocatalytic applications.

Semiconductor nanoplatelets (NPLs) are a class of colloidal nanocrystals which have been primarily studied for their optoelectronic properties afforded by their unique two-dimensional morphology including large absorption cross-sections, high quantum yields, directed emission, and large exciton binding energies.[7–10] They are commonly classified by number of monolayers (ML) where one ML is one layer of MX where M=Cd, Hg and one of X=S, Se, Te and are commonly 2-5 ML thick.. Although their thickness is only few-nanometers their lateral extent can range tens to hundreds of nm and have recently been demonstrated to micron scale.[11] For this reason, NPLs are promising antennas for anisotropic exciton collection. In addition, they offer the advantage of bandgap tuneability and broad absorption across visible and near infrared spectral regions.[7,12,13] However they require the appropriate acceptor in order to concentrate energy to a single point.

We focus our attention to our previously reported HgTe NPL/quantum dot (QD) heterostructures where we observed efficient energy transfer from NPL to QD derived *from the same material*.[14] Other reports in the literature have shown energy transfer energy transfer to QDs in dot-on-nanoplatelet heterostructures such as CdSe/ZnS, PbSe/CdSe, CdSe/PbSe, and CdSe/Au clusters.[15–18] We believe that the high efficiency of our HgTe/QD systems arises from the fact that the NPL antenna and QD acceptor are of identical composition but differing confinement. This arrangement only works because the HgTe NPL is in a highly confined regime of only a few monolayers, while the small QDs have a continuous absorption that shifts relative to the NPL band-edge PL.

We complement our prior synthetic work by systematically characterizing the efficiency of exciton transport in our NPL/QD system. We conduct further systematic controls comparing in-situ grown QDs to QD/NPL mixtures. We simply hypothesized that based on the average lateral lengths of the NPL (~500 nm) and the apparent high quantum yield of the emissive heterostructures at the quantum dot emission energy, the energy transfer must be near unity. This implies that the excitons must be sampling a large area of the NPL before being quenched by transfer into the QD. By understanding the efficiency of this quenching, we can use this system to estimate the NPL exciton diffusion constant. In this paper we demonstrate 1) The efficiency of energy transfer is highest (near unity) when QDs are grown in-situ, in comparison to a mixed substrate, and 2) this efficiency is near unity despite having extremely low concentrations of QDs per unit area of NPL, suggesting long-range exciton transport. 3) Using Monte Carlo simulations, we then model the process of energy transfer to estimate the exciton diffusion constant and find that it is comparable to extended 2D semiconductors such as TMDs. 4) We finally place our results in the context of

other 2D to 0D energy transfer systems in the literature and highlight the advantages of our HgTe

NPL/QD heterostructure for energy concentration.
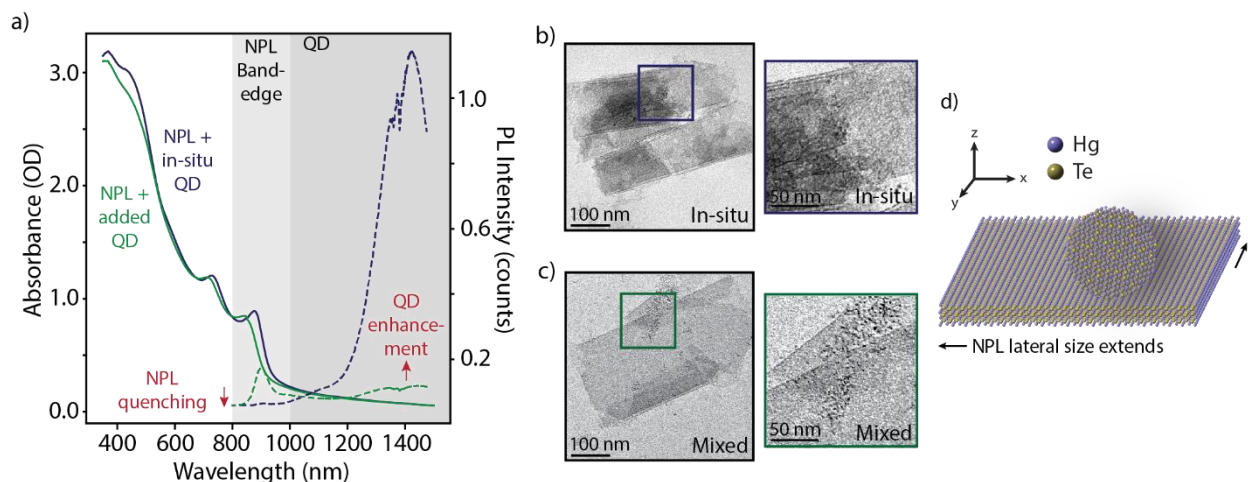
Figure 3.1. *a) Representative spectra demonstrating the enhancement in photoluminescence when HgTe QDs are grown via an in-situ QD/NPL heterostructure compared to simply mixed with NPLs. The in-situ heterostructure experiences complete band-edge quenching, suggesting energy transfer. b-c) TEM showing in-situ and mixed systems of HgTe NPLs and QDs. d) A schematic of QD on NPL where the QD is in close contact with the NPL. Note that the ligands have been removed for clarity.*

3.2 Comparison of In-Situ Grown HgTe QD/NPL Heterostructures and Mixed Systems

We previously found that HgTe QDs will grow in the solution of HgTe NPLs following a cation and ligand exchange from oleic acid passivated CdTe NPLs to oleylamine passivated HgTe.[14] The growth can be controlled by precursor concentrations and is temperature activated—holding the cation-exchanged NPLs at elevated temperatures will speed up growth, and storing in a freezer will inhibit growth. This growth is specific to HgTe because QDs will form at room temperature with the same precursors required for cation exchange.[19] These in-situ grown HgTe QDs appear to be attached to the surfaces of the NPLs, possibly growing epitaxially from reactive sites introduced by the labile surface Hg, and result in near complete NPL band-edge quenching

92

along with high PLQY from the resultant HgTe quantum dots (Figure 3.1a, blue trace). Overall, the HgTe energy transfer is occurring from NPL to QD and allows for a continuously tunable Stokes shift depending on the bandgap of the QD. We previously showed that the photoluminescence quantum yield (PLQY) of the QD grown through this method is very high, with values from ~30-50%.[14] These results are comparable to some of the highest PLQY reported for HgTe QDs, and indicates that the transfer must be near unity.[19]

To highlight the efficiency of the in-situ NPL/QD heterostructure, we perform a control experiment by first separately synthesizing oleylamine passivated HgTe QDs with sizes that match the in-situ grown QDs (Figure 3.5), and then mix a comparable concentration with 3 ML HgTe NPLs isolated immediately after cation exchange (further details in Figure 3.6 and Table 3.1). Hereafter we will refer to this sample as mixed NPLs and QDs. While we are able to reproduce energy transfer by mixing QDs and NPLs, there is less quenching of the band edge emission (Figure 3.1a, green trace) suggesting lower efficiencies of transfer. From TEM we observe in-situ grown QDs in contact with the surface of the NPLs that are not washed away during centrifugation, while the mixed QDs are easily removed using gentle centrifugation which recovers some of the NPL band edge PL (Figure 3.9). We predict that the in-situ grown quantum dots are epitaxially attached or in very close proximity to the NPLs in the heterostructure which affords it such high energy transfer efficiencies compared to separately synthesized QDs and NPLs which are likely not adsorbing to the NPL surfaces. The in-situ NPL/QD heterostructure not only allows for slow controlled growth of a low concentration of high PLQY QDs, but also overcomes distance limitations of energy transfer systems when the donor and acceptor are synthesized separately. While we predict the mechanism in the NPL/QD heterostructure is a near-field energy transfer, the

QDs simply mixed with NPLs are likely demonstrating FRET-like energy transfer. We will treat both cases as FRET transfer to compare their quantum efficiencies.
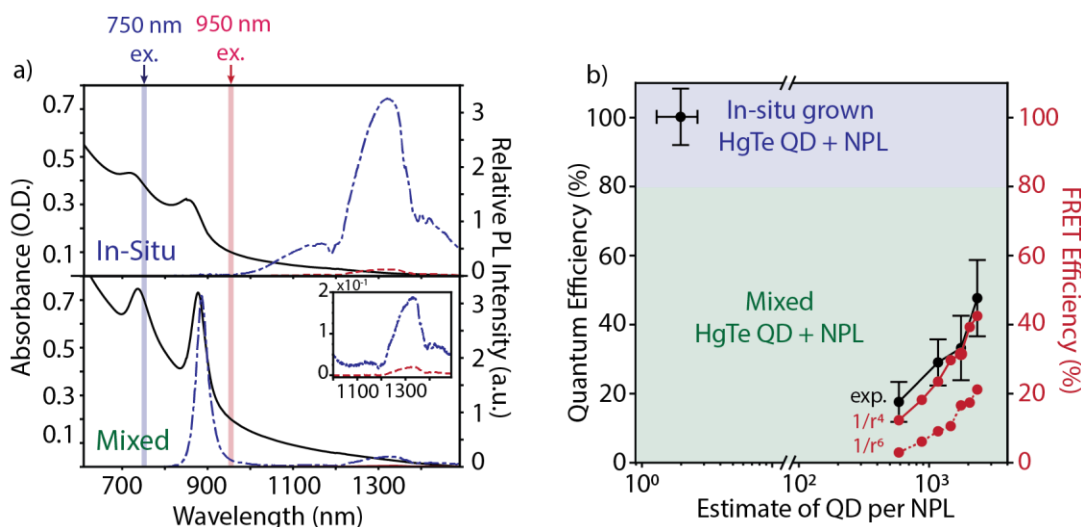
Figure 3.2. *a) The absorption (solid line) and emission (dashed line) spectra of in-situ grown HgTe QDs + NPLs and mixed QDs + NPLs. Both samples are excited above and below the NPL bandgap (750 nm and 950 nm, respectively) to excite the donor + acceptor and acceptor only. The inset highlights the difference in PL intensity between the in-situ and mixed heterostructures. b) The quantum efficiency (QE) of energy transfer is calculated for both systems. The mixed system is evaluated at increasing concentrations, while the in-situ QE is calculated and the number of QD per NPL is estimated from the spectra. All data points are a result of the mean of multiple trials, and error is calculated through the standard error of the mean.*

3.3 The Quantum Efficiency of Energy Transfer

To determine the quantum efficiency (QE) of transfer, we collect absorbance and PL measurements while exciting the system at different wavelengths. We excite both mixed and in-situ 3 ML NPL and QD at 750 nm to observe energy transfer (donor plus acceptor) and isolate the QD (acceptor only) by exciting at 950 nm, below the band-edge of the NPL near 880 nm (Figure 3.2a). After normalizing PL by excitation power this allows us to observe an enhancement in QD PL when exciting into the NPL bandgap. The absorbance of NPL and QD must be noted at both

excitation wavelengths, so we use a sample of NPLs only (no QDs present) and QDs only (no NPLs present).

$$Em_{750} = Abs_{QD,750} * QY_{QD,750} + Abs_{NPL,750} * QE_{FRET} * QY_{QD,750} \quad (3.1)$$

$$Em_{950} = Abs_{QD,950} * QY_{QD,950} + Abs_{NPL,950} * QE_{FRET} * QY_{QD,950} \quad (3.2)$$

We will assume a negligible contribution from the sub-band states in the donor (NPL) despite the presence of an Urbach tail in HgTe NPLs. We rule out a significant contribution to the overall PL from exciting into these states in Figure 3.10. The emission of acceptor only then becomes:

$$Em_{950} = Abs_{QD,950} * QY_{QD,950} \quad (3.3)$$

Note that we are assuming the quantum yield of the acceptor does not change by the presence of the donor and is also independent of excitation wavelength. We can then use the total integrated emission along with the absorption spectra to calculate the quantum efficiency (QE) of energy transfer by:

$$QE = \frac{\frac{Em_{750}}{Em_{950}} * Abs_{QD,950} - Abs_{QD,750}}{Abs_{NPL,750}} \quad (3.4)$$

We repeated the experiment on many different samples and found that overall, the QE of transfer for the in-situ case is always higher than the control case, from > 85% compared to the mixed case of 35-63%. The average QEs of multiple trials are reported in Figure 3.2b (black traces) along with their standard errors of the mean. For the mixed system, we started at low concentrations of added QDs and found that we were not able to observe energy transfer until we reached the concentrations shown above. Even with this much higher ratio of QD per NPL, we were not able to cross the QE threshold that we observed in the in-situ case. We observed that the QE scales with concentration likely because these QDs experience energy transfer through FRET

rather than direct coupling as in the in-situ case (Figure 3.2b). To confirm this, we modeled the efficiency of FRET for the mixed case through the spectral overlap and photoluminescence lifetimes using simulation methods described in Tan et al. and compare the results to our method of using the photoluminescence enhancement.[20] Lifetimes of the HgTe QDs are given in Figure 3.11. To model FRET, we considered that the difference in geometry between the 2D NPL and 0D QD will affect the distance dependence and orientation factor, and report FRET efficiencies for both the typical $1/r^6$ dependence, as well as a $1/r^4$ dependence which better describes 2D to 0D FRET (Figure 3.2b).[21] The average FRET distance between NPL donor and QD acceptor is 7.58 nm for $1/r^6$ and 8.11 nm for $1/r^4$. The details of the simulations are described further in the Supporting Information. Overall, this confirms that the most likely energy transfer path within the mixed case is in fact FRET.

Additional passivation through added ligand (1% w/v% oleylamine in hexanes solvent) before mixing improved the QE by ensuring that all nanocrystals remained suspended in solution during the measurements and passivate surface defects which might affect either nanocrystal (a comparison to no added ligand is given in Figure 3.12). We also attempted to conduct the measurements in tetrachloroethylene (TCE) to avoid significant solvent reabsorption but found that this solvent reduced the QE (1-15% for mixed case and 36% for in-situ case, full results in Figure 3.12) and dissolved the nanocrystals after a few hours, likely by the difference in polarity compared to hexanes. The solvent reabsorption from hexanes should affect the spectra proportionally and therefore should not affect the overall calculations, so all our results are obtained from samples in hexanes. Overall, these results highlight the advantage of in-situ grown QDs as having near complete transfer from the large area NPLs, establishing an efficient energy harvesting system.

To determine the optimal size and thickness for efficient energy transfer, we explored the QE for 2 ML HgTe and 3ML HgTe at both average (~200-500 nm) and extended lateral sizes (~1000 nm, prepared through seeded growth). We observed that for 2 ML, the QE was at or near 0 for both sizes as differences in emission with excitation could be explained by the absorbance of QDs rather than energy transfer. For large 3ML, we observed a QE of 25% (compared to ~80% for smaller 3ML) which suggests that at extremely large NPL length scales, an exciton will not reach a QD trap as efficiently as in smaller NPLs. These results are summarized in Figure 3.13. Finally, we also explored how the QE changes with time in an aged sample of in-situ grown QD/NPLs (Figure 3.14). We find that the QE is high in the days immediately after cation exchange, but after 10 days begins to lower to 23.7%. In this case, the emission when exciting QDs only (below the NPL band-edge) continuously increases indicating an increase in QD growth, but the emission when exciting NPL + QD decreases. This could be interpreted as a dissolution of NPLs in solution over time or a greater concentration of QD growth in solution that are not attached to the NPL.

The high efficiency of energy transfer is consistent with our previous expectation that the in-situ grown QDs are adsorbed or in contact with the surface. It is therefore not surprising that the in-situ case has much higher QE than the mixed case given the distance between donor and acceptor. What is surprising, however, is that the number density of QDs is very low while still reaching near unity transfer. This suggests that there must be long-range exciton transport for nearly every exciton to reach a QD. Even the smaller to averaged sized NPLs represent a ~1000-2500 nm^2 area that the exciton must sample before reaching a QD, and this must outpace the recombination rate. We therefore became interested in exploring the exciton diffusion through modeling to better understand transport within these NPLs.
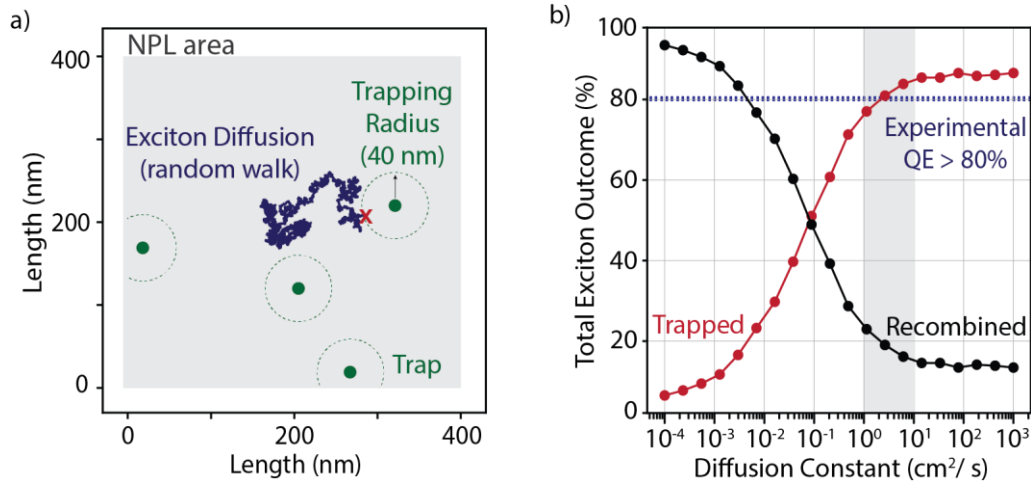
Figure 3.3. a) The 2D random walk model of exciton diffusion over a square sheet representing a NPL. The traps show in green represent QDs on the surface and will quench the exciton when it falls within the trapping radius. b) The results of the Monte Carlo simulation showing the percentage of excitons that trapped (red) and the percentage of excitons that recombined (black). The dashed line is the QE threshold for experimental percentage of trapped excitons.

3.4 Monte Carlo Modeling of Exciton Diffusion.

Experimentally we observe that the energy transfer from NPL to QD results in > 85% quenching. Using a Monte Carlo simulation, we determine a theoretical diffusion constant by modeling an exciton on a NPL with a two-dimensional (2D) random walk (Figure 3.3a). We motivate this choice of model by assuming that the movement of the exciton is diffusive rather than ballistic as we sample at sufficiently short time steps between movements. We do not account for the possibility of direct excitation into the quantum dot or other non-radiative pathways such as Auger recombination. In our model, the exciton is allowed one of two outcomes: it will either recombine according to the timescale of the experimental total photoluminescence lifetime (Figure 3.15), or it will undergo energy transfer by reaching a position within a radius of a trap (set to be the exciton Bohr radius in bulk HgTe, 40 nm although this is discussed further in Figure 3.16). In all simulations, the exciton is confined to a square 2D area which can vary but follows a normal

distribution centered at 500 nm—the average size of a 3 ML HgTe NPL (Figure 3.15). We estimate the trap density to be about 2 traps/NPL, and each NPL is given a Poissonian number of traps distributed randomly across the 2D sheet (Figure 3.15). Additional examples of random walks at different diffusion constants are shown in Figure 3.17.

We observe that in order to reach greater than 80% trapping (or the minimum experimental QE from NPL to QD), the diffusion constant of the exciton is between 1-10 cm^2/s (Figure 3.3b). The trapped exciton population percentage has a non-zero minimum that depends on the average number of traps per NPL—because they are placed randomly this represents the excitons that are immediately quenched by being placed within the radius of the trap during initialization of the walk. We also observe a maximum trapping at 86% and saturation at 10 cm^2/s, which reflects the population of NPLs which have no traps (i.e. the excitons on these NPLs will always recombine). The saturation would only reach 100% quenching if every NPL has at least one trap. Although we show the results of a Poissonian distribution of traps, we also calculate the diffusion constant from a uniform number of traps/NPL in Figure 3.16.
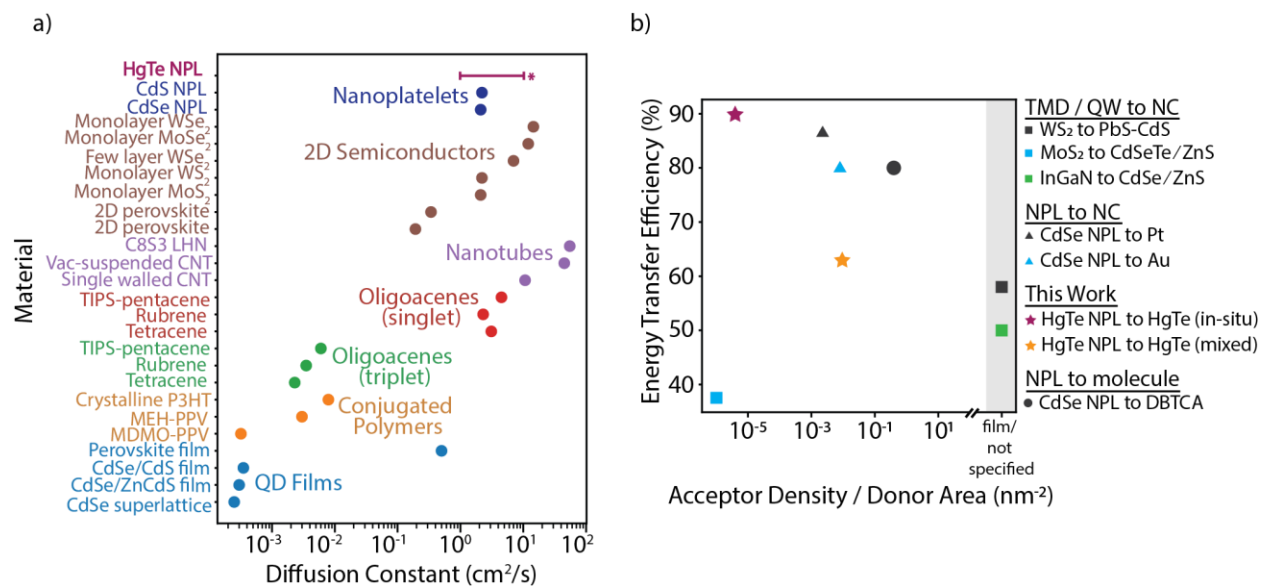
Figure 3.4. a) Literature diffusion constants reported for QD films,[22–25] conjugated polymers,[26,27] oligoacene triplets and singlets,[28] nanotubes,[29–31] 2D semiconductors,[32–39] and nanoplatelets[40,41] at room temperature. b) Energy transfer efficiency rates for 2D to 0D systems including TMDs and quantum well (QW) to NCs,[3,42,43] NPLs to NCs,[18,44] our results, and NPLs to conjugated fluorophores.[45]

3.5 Comparison to Other Materials and Energy Transfer Systems

Finally, in Figure 3.4, we compare the theoretical diffusion constant (indicated by *) to other excitonic materials of interest for optoelectronic applications. Diffusion constants have been studied in organic and inorganic semiconductors such as conjugated polymers, oligoacenes, and 2D TMDs, but literature results in NPLs are limited to small CdSe and CdS. Although we report an estimate, we can compare the order of magnitude from our result for HgTe to different materials and find that NPLs, despite being colloidal nanocrystals, are most comparable to the 2D TMDs, highlighting their similarity to extended 2D semiconductors. NPLs' large areas and exciton diffusion constants are essential for their antenna functionality, and although they draw the strongest comparison to 2D materials, they have the advantage of being extremely good emitters. 2D TMDs commonly have low QY after exfoliation (< 1 to 6%) due to surface defects and require significant efforts to boost the QY, such as with superacid treatment.[46,47] NPLs on the other hand offer high QY after synthesis (~10% here for HgTe NPLs) and have access to milder solution-based treatments like passivation or shelling to minimize defects and reach near unity QY which is essential for maximizing energy transfer. They present a promising path forward towards large area semiconductors for energy collection antennas.

Many other antenna systems have demonstrated extremely high energy transfer efficiencies such as photosynthetic antenna complexes and light harvesting nanotubes.[1,48] Energy concentration from large area 2D to 0D semiconductors of the same composition however has not

been previously explored to our knowledge. It has been shown in 2D TMDs to separately synthesized nanocrystals such as WS_2 to PbS-CdS, WS_2 to CdSe/ZnS, and MoS_2 to CdSeTe/ZnS, as well as in InGaAs quantum wells to CdSe/ZnS QDs.[3,42,43,49] In NPLs, energy transfer from 2D to 0D has been demonstrated from CdSe NPL to metallic nanoparticles such as Pt, Pd, and Au.[18,44,50,51] Similarly, energy transfer from 2D NPLs to molecular chromophores has been demonstrated such as in 3ML CdSe NPLs to conjugated fluorophores.[45] These results are summarized in Figure 3.4b, where the QE is shown as a function of acceptor density (or the number of acceptors per area of donor). In these systems, energy transfer is dominated by FRET and is limited by spectral overlap, distance from donor to acceptor, and high concentrations needed which induce self-quenching. Our system overcomes all these limitations by having tunable spectral overlap, epitaxial contact between donor and acceptor, and extremely low concentrations of acceptor relative to donor. Together these results all highlight the efficiency of this system for infrared energy concentration using a minimal amount of material and demonstrate its promise in applications such as solar concentration.

3.6 Conclusions

Overall, we observe that HgTe NPLs can act as highly efficient energy antennas to HgTe QDs with bandgaps in the shortwave infrared. The energy transfer is highest when the QDs are grown in-situ from the excess precursors in solution during cation exchange. We evaluate the energy transfer of this system to be near unity and determine that excitons within NPLs must diffuse a large area before reaching the QD, and the exciton diffusion constant is higher than reported for other nanocrystals. These results both highlight the similarities between NPLs and extended 2D semiconductors such as transition metal dichalcogenides and provide a promising platform for infrared energy collection and concentration.

3.7 Experimental Details

Cadmium oxide (Alfa Aesar, 99.95%), tellurium powder (Acros, 99.8%), oleic acid (Alfa Aesar, 99%), tri-n-octylphosphine (TOP) (Alfa Aesar, 90%), 1-octadecene (ODE) (Alfa Aesar, 90%), mercury (II) acetate (Chem-Impax International, 98.0%), ethanol (Fisher, 95.27%), hexanes (Fisher, 98.5%), toluene (Alpha Aesar, 99.8%), propionic acid (Fisher), and oleylamine (Tokyo Chemical, 50.0%) were used.

Synthesis of Precursors

Cadmium Propionate (Cd(prop)$_2$). In a round bottom flask, 1.036 g of CdO powder and 10 mL of propionic acid were mixed under argon flow for 1 hour. The flask was then open to atmosphere and heated to 140 C until the volume reduced by half. The while solution was precipitated with acetone and centrifuged. The supernatant was discarded and the solution was dried and stored in a vacuum desiccator.

1M TOP-Te. Following Izquierdo et al.,[13] Te powder (0.254 g) and tri-n-octylphosphine (2 mL) were combined in a small flask and degassed under vacuum at room temperature. Under argon flow, the solution was stirred at 275 C until the dissolution was complete and solution turned yellow. The solution was cooled and diluted to 0.5M with additional tri-n-octylphosphine.

10 mM Mercury Acetate (Hg(OAc)$_2$). In a small vial, 9.2 mg of mercury (II) acetate and 3 mL of oleylamine were stirred at room temperature until dissolved.

Synthesis of 3ML CdTe NPL. Adapted from Izquierdo et al.,[13,14] Cd(prop)$_2$ (260 mg), oleic acid (0.160 mL), and ODE (20 mL) were degassed under vacuum at 90 C for 1 hour in a three-neck flask. Under argon flow, the solution was heated to 210 C and a mixture of 1 M TOP-Te (0.200 mL) and ODE (3.75 mL) was injected with a syringe pump at a rate of 5 mL/hr. The reaction was

quenched with oleic acid (0.500 mL) and cooled to room temperature. The NPLs were precipitated with ethanol and centrifuged at 14000 rpm for 5 min, then resuspended in hexanes (20 mL).

Cation Exchange from CdTe to HgTe NPL. Following Tenney at al.,[14] In a round bottom flask, 6 mM CdTe NPL (0.240 mL) and hexanes (6 mL) were mixed. Then, 10 mM $Hg(OAc)_2$ in oleylamine (0.300 mL) was added and the solution was stirred at room temperature for 3-4 hours until appropriate location of the excitonic features on the absorption spectra. Once complete, the NPLs were centrifuged at 9000 rpm for 5 min then resuspended in hexanes (5 mL).

Synthesis of HgTe QDs. Adapted from Piepenbrock et al.[19] In a three-neck round bottom flask, mercury acetate (330 mg), oleylamine (1.380 mL), and ethanol (15 mL) were heated to 50 C under argon flow until the solution was clear. The flask was then placed in a water bath and 0.5 M TOP-Te (0.1 mL, diluted from the 1M stock solution) was injected once the solution reached the desired temperature. Lower temperatures ($< 25C$) were used for small QDs, while increasing temperatures (30, 40, 50 C) were used for larger QDs. The solution immediately turned brown and was allowed to stir for 30 s before quenching with an ice bath. The QDs were precipitated with an excess of ethanol and centrifuged at 14000 rpm for 5 min, then resuspended in hexanes (10 mL).

Mixing Experiment Procedure. The total volume was maintained at 2 mL across all samples. The volume of NPLs added were determined using measured absorption spectra to ensure sufficient optical density (~ 0.5 OD at the NPL heavy hole). Using the QDs synthesized separately, varied amounts of QDs were added, from 8.5×10^{-5} mM to 3.4×10^{-4} mM total concentration in the mixture. Hexanes was added to ensure that all samples reached a total of 2 mL. The samples were then kept on ice following mixing to minimize growth of QDs during the reaction and absorption and PL spectra were recorded immediately.

Material Characterization.

Absorption spectra were acquired with an Agilent Cary 60 UV-Vis spectrophotometer. Photoluminescence (PL) was collected using an Ocean Optics Flame-S-VIS-NIR-ES Spectrometer and a Horiba Scientific PTI QuantaMaster400 Spectrometer equipped with liquid nitrogen cooled InGaAs photodiode and Si photomultiplier tube detectors. The approximate power used was 0.028 mW for excitation at 750 nm and 0.42 mW for excitation at 950 nm, all photoluminescence shown are normalized to their respective power of excitation to account for these differences. Lifetime measurements were performed on a home-built optical imaging set up, using short wave sensitive superconducting nanowire single photon detectors (SNSPDs) and a time-lagged single photon counting module.[52] For all measurements, the approximate power used was 6.7×10^{-7} J/cm^2 for a 532 nm laser at a 1 MHz repetition rate.

Transmission electron microscopy (TEM) images were acquired with a FEI Tecnai T12 120kV TEM. The nanoplatelets and quantum dots were diluted in hexanes and drop casted on Ted Pella, Inc. carbon/formvar 300 mesh copper grids.

3.8 Supporting Information

Photoluminescence of quantum dots of increasing size
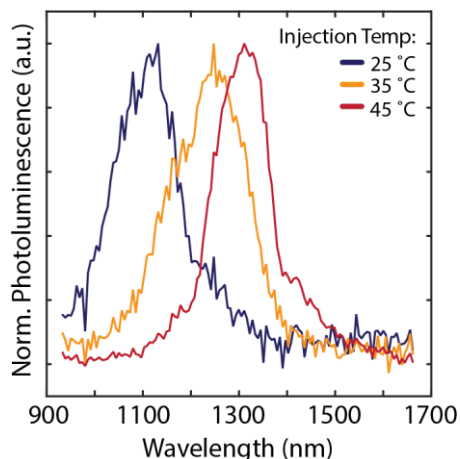
Figure 3.5. *The normalized photoluminescence of a series of quantum dots grown by increasing the injection temperature.*

To match the synthesized QD size as close as possible to the in-situ grown QDs, we synthesized a batch of QDs with increasing size by injection of TOP-Te at higher temperatures. Typically, after heating to dissolve the precursor the solution is cooled to room temperature (blue trace) before the TOP-Te is injected. We found, however, that modifying the procedure by injecting before the solution cools to room temperature will produce larger quantum dots.

Estimation of Nanoplatelet and Quantum Dot Concentrations for In-Situ Grown Heterostructure Nanoplatelet Concentration

To calculate the concentration of HgTe NPLs used during cation exchange, we must first start by estimating the concentration of Te in CdTe NPLs used for the reaction. This requires the first assumption—*the CdTe reaction goes to completion and yield is 100%.* If this is true, the reaction will contain 0.2 mmol Te and 0.26 mmol Cd incorporated into the CdTe NPLs. Following centrifugation and resuspension in 20 mL hexanes, the [Te] will be 10 mM in the original CdTe NPLs.

For cation exchange, the stock solution of CdTe is first diluted to 4.5 mM Te (or 6 mM Cd). Because 0.240 mL of this solution is used and the total volume for cation exchange is 6.84 mL, the final [Te] after cation exchange will be 0.135 mM.

From this concentration, we can then estimate the [NPL] using the following equation:

$$[NPL] = \frac{[Te] * V_{unit}}{4 * V_{NPL}} \tag{3.5}$$

where V_{unit} is the volume of the zinc blende HgTe unit cell, V_{NPL} is the average volume of a NPL, and [Te] is the theoretical concentration of Te in the NPL solution.[53] $V_{unit}/4$ represents the volume occupied by the Te atoms in the unit cell (which has 8 atoms total). This equation requires a second assumption—*the lateral sizes and therefore volume of each NPL is uniform throughout the solution.* We know this is not typically the case and calculated the average lateral area from TEM images of HgTe NPLs directly after cation exchange. Here we use a 225 nm x 225 nm x 1.1 nm rectangular slab to represent the average geometry of our NPLs.

Overall, we estimate the [NPL] after cation exchange to be 1.6×10^{-7} mM. The validity of assumptions 1 and 2 are evaluated in the context of estimating a ratio of QD / NPL in Figure 3.7.

Quantum Dot Concentration
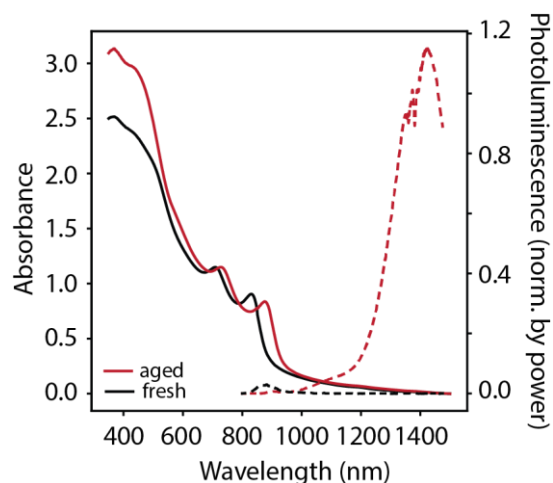
Figure 3.6. *The absorption and photoluminescence of freshly cation exchanged HgTe NPLs showing no QD growth, and aged NPLs showing growth and emission from QDs.*

Directly after cation exchange from CdTe to HgTe we do not observe a significant population of HgTe QDs in our solution of HgTe NPLs, but after aging at room temperature we observe bright PL from QDs (Figure 3.6). The concentration of QDs is too low to resolve the absorption band-edge, and we are unable to separate the QDs from NPL solution so we must estimate the concentration of QDs grown in-situ.

To find the absorbance of QDs grown in situ, we isolated a sample of freshly cation exchanged NPLs (NPLs only) and sealed them in a cuvette. We measured the spectra every day as the QDs grew and took the difference between the aged and fresh spectra at the band edge. We could not use the raw absorbance at the QD band edge because a significant contribution of the absorbance comes from scatter or below-band states in the NPL. Differences in the absorbance within the continuum were also non-ideal because of ligand absorption (some additional oleylamine was required to keep the samples suspended).

Once the absorbance estimate is obtained, we can use the absorption cross section per QD at the band edge to solve for the concentration [QD]:

$$C_{abs} \ (\text{cm}^2) = \frac{2303 \ \epsilon_\lambda}{N_A} \tag{3.6}$$

$$C_{abs} \ (\text{cm}^2) = \frac{2303*A}{[QD]*N_A*l} \tag{3.7}$$

Where C_{abs} is the absorption cross section, ϵ_λ is the extinction coefficient, N_A is Avogadro's number, A is the absorbance, and l is the path length of the cuvette.[54,55] Because we cannot observe the absorbance from only the QD at the band edge (it is within the Urbach tail of the NPL), we will use the absorbance value as a maximum and acknowledge that the resulting concentration will only be an estimate. The [QD] was calculated for many different solutions of in-situ grown QDs and are summarized in Table 3.1.

Estimate of QD to NPL ratio for in-situ grown QDs

Finally, we estimate how many QDs are present per NPL by dividing the above QD concentrations by the concentration of NPL after cation exchange. The results are shown below, as well as in Figure 3.2.

Table 3.1. *The estimated concentrations of both QD and NPL in the in-situ heterostructure systems.*

Sample	Wavelength of PL (nm)	QD concentration estimate (mM)	NPL concentration estimate (mM)	Ratio QD / NPL
1	1300	5.36×10^{-7}	1.6×10^{-7}	3.35
2	1100	3.02×10^{-6}	2.4×10^{-6}	1.26
3	1100	3.21×10^{-6}	2.4×10^{-6}	1.34
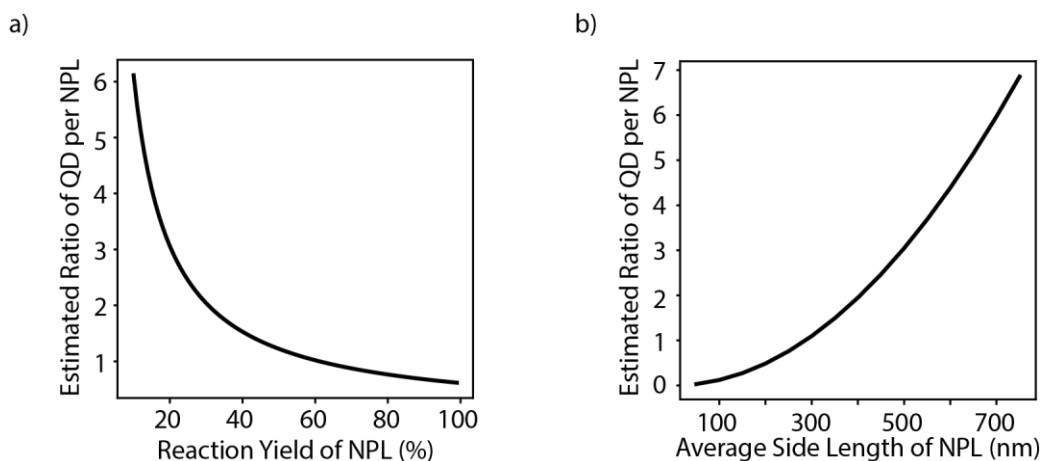
Figure 3.7. *An evaluation on how the assumptions in calculation for [NPL] affect the final estimated ratio of QD to NPL. a) The reaction yield is assumed to be 100%, but a lower yield will result in a higher ratio although still below 10. b) The size of NPL is assumed to be uniform but can also vary the final ratio of QD to NPL.*

We also address how the assumptions used in these calculations will affect the results. For the [NPL], two assumptions were made: the CdTe reaction yield was 100% and the NPL sizes were uniform. In Figure 3.7, we show how the ratio of QD / NPL would change if those parameters were altered. If the reaction yield was lower than 100% (which is very likely the case considering post synthetic workup steps and dilutions), the estimate of QDs/NPL would increase as there are less available NPLs than predicted. Similarly, if the average size is larger, the estimate would also increase as the [Te] would be incorporated into fewer, larger NPLs.
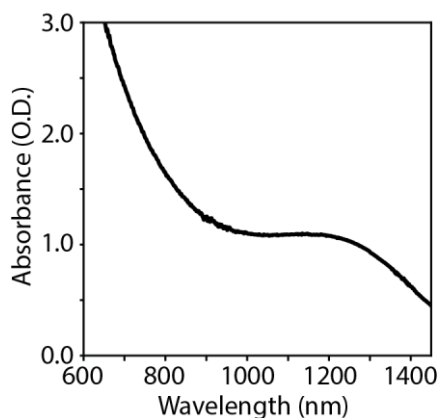
Figure 3.8. *Absorption of quantum dots used in the mixing experiment.*

Starting from our QD/NPL ratio estimate, we aim to replicate these concentrations for the mixing experiment. First, we start with the [NPL] after cation exchange and adjust it such that the OD is near 0.5 in the total volume of 2 mL (hexanes was added to dilute it). We found the concentration of NPLs was around 1.45×10^{-7} mM in the cuvette during the mixing experiments.

Then we found the concentration of synthesized quantum dots through the literature absorption coefficient at the band edge.[54] We diluted the stock QD solution to 0.034 mM and added aliquots to the cuvette containing the NPLs until the QD features were visible and some energy transfer was observed. We then established a series of trials with different [QD] shown below in Table 3.2 and calculated the results QD /NP ratio.

Table 3.2. *Estimates for QD concentration in mixture and the resulting ratio of QD to NPL.*

Volume QD solution added (uL)	[QD] estimate (mM) in mixture	QD / NPL ratio estimate
5	8.5×10^{-5}	586
10	1.7×10^{-4}	1172
15	2.6×10^{-4}	1759
20	3.4×10^{-4}	2345

It is worth noting that these ratios are significantly higher than those estimated in-situ, and we were still unable to reach the QE values we obtain in the in-situ system (Figure 3.2).

Separation of Mixed NPLs and QDs via Centrifugation
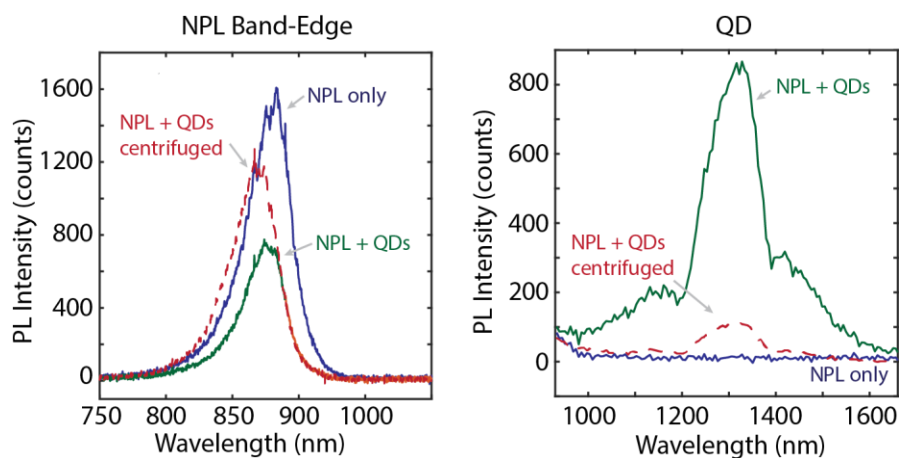
Figure 3.9. *The photoluminescence of NPLs before QDs were added (blue), with QDs added (green), and after QDs were removed with centrifugation (red, dashed). All samples were excited at 750 nm.*

While the in-situ grown QDs are present after the centrifugation step of the synthesis and could not be removed with further centrifugation or syringe filtering, the separately mixed NPLs + QDs can be separated. Initially, added QDs to a solution of NPLs quenches the band-edge emission and shows bright PL in the shortwave infrared. When the solution is then gently centrifuged, the small QDs will remain in the supernatant while the NPLs will crash out. We found that this procedure allowed for recovery of some of the NPL band edge PL along with a decrease in the QD PL. This suggests that while the QDs are in close enough proximity to the NPL to undergo energy transfer, they are not permanently attaching to the surface post-synthetically.
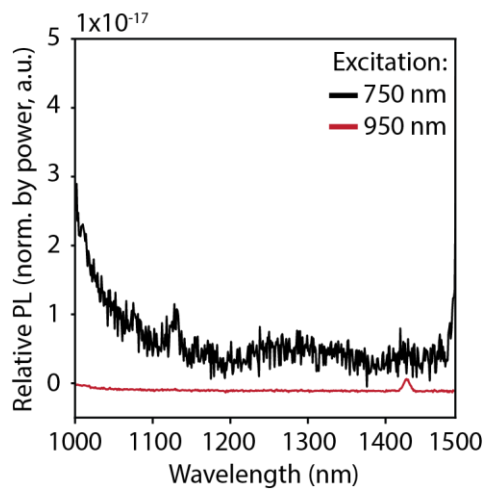
Figure 3.10 *Photoluminescence of NPLs only (isolated before in-situ QD growth) excited above the band gap (750 nm) and below the band gap (950 nm). No significant PL is observed from sub-band excitation in the NPLs.*

Photoluminescence lifetimes of HgTe quantum dots
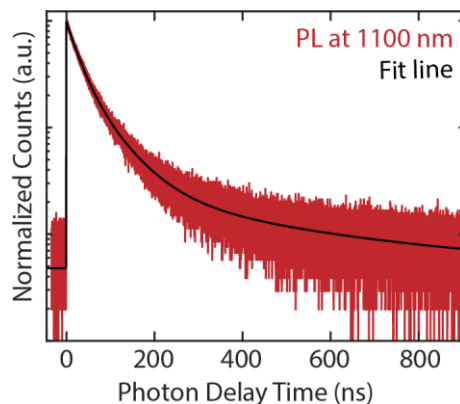
Figure 3.11. *Photoluminescence lifetime of HgTe QDs synthesized in absence of NPLs. The photoluminescence is centered at 1100 nm.*

The photoluminescence lifetimes were obtained for HgTe QDs. The lifetime was fit to a 3-exponential function. The lifetime of each component as well as the weighted average lifetime is given below in Table 3.3.

Table 3.3. *The photoluminescence fit parameters and results for HgTe QDs.*

Component	A	$1/\tau$ (ns⁻¹)	τ (ns)	Amplitude (A%)	Fit R-square	Average Lifetime (ns)
1	13.41	0.002566	389.7	2.27		
2	187.8	0.0146	68.49	31.8	0.997	113
3	389	0.03842	26.02	65.9		

FRET modeling of mixed case

We use the methods by Tan et al. to model the FRET from NPL to QD in the mixed case.[20] The kinetic Monte-Carlo algorithm used in simulations is briefly explained below.

Input. FRET radius is calculated based on spectral overlap between emission spectrum of HgTe NPLs and absorption spectrum of HgTe QDs. The only other inputs are concentrations of nanocrystals solutions.

Initialization. The number of HgTe NPLs and HgTe QDs are first determined. A three-dimensional box consisting of identical discrete smaller boxes is then constructed as a representation of the positions of nanocrystals in colloidal solution. Size of the smaller boxes is also calculated by the total concentration of nanocrystals under corresponding experimental conditions and each nanocrystal, regardless of its chemical composition, is only capable of occupying one box. As the final step of initialization, sets of coordinates are randomly generated as the initial positions of nanocrystals.

Calculation. A distance matrix recording distances of all possible NPL-QD pair is first obtained based on their coordinates. For the rate matrix that will be used for later pathway selection, three types of rates are considered: (1) Total decay/emission rate: The total decay rate extracted from lifetime measuring experiments is used for each excited emitter.; (2) FRET rates: The quenching rates due to FRET from HgTe NPLs to HgTe QDs. These are calculated for every possible NPL-QD pair based on the distance matrix.

Pathway selection. The pathway selection procedure is achieved using the BKL algorithm, where partial sum of the rate matrix and RNG are used.[56] Particles that go through any de-excitation pathway are no longer considered in the next time step.

Updating. To advance the clock, the time step Δt is calculated based on the total rate. The coordinates of nanocrystals and the rate matrix are then updated at each time step for a new round of pathway selection, and only after all emitters get de-excited the simulation ends.

Solvent and ligand effects on QE
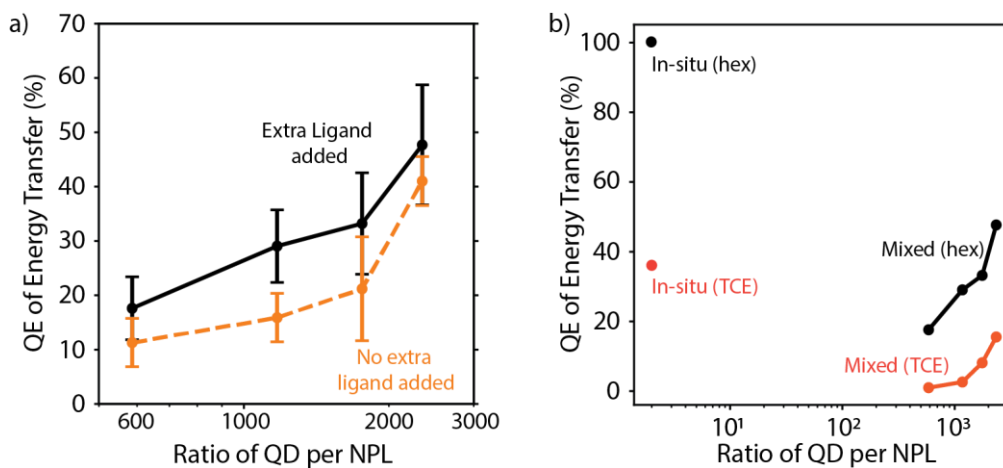
Figure 3.12*. a) The QE of energy transfer for mixed case with extra oleylamine added to the solution (1% w/v, black) copmared to no extra ligand added (orange) . b) The QE for both in-situ and mixed case collected in hexanes (black) and TCE (red)*

116

The effect of NPL size and bandgap on QE of energy transfer.
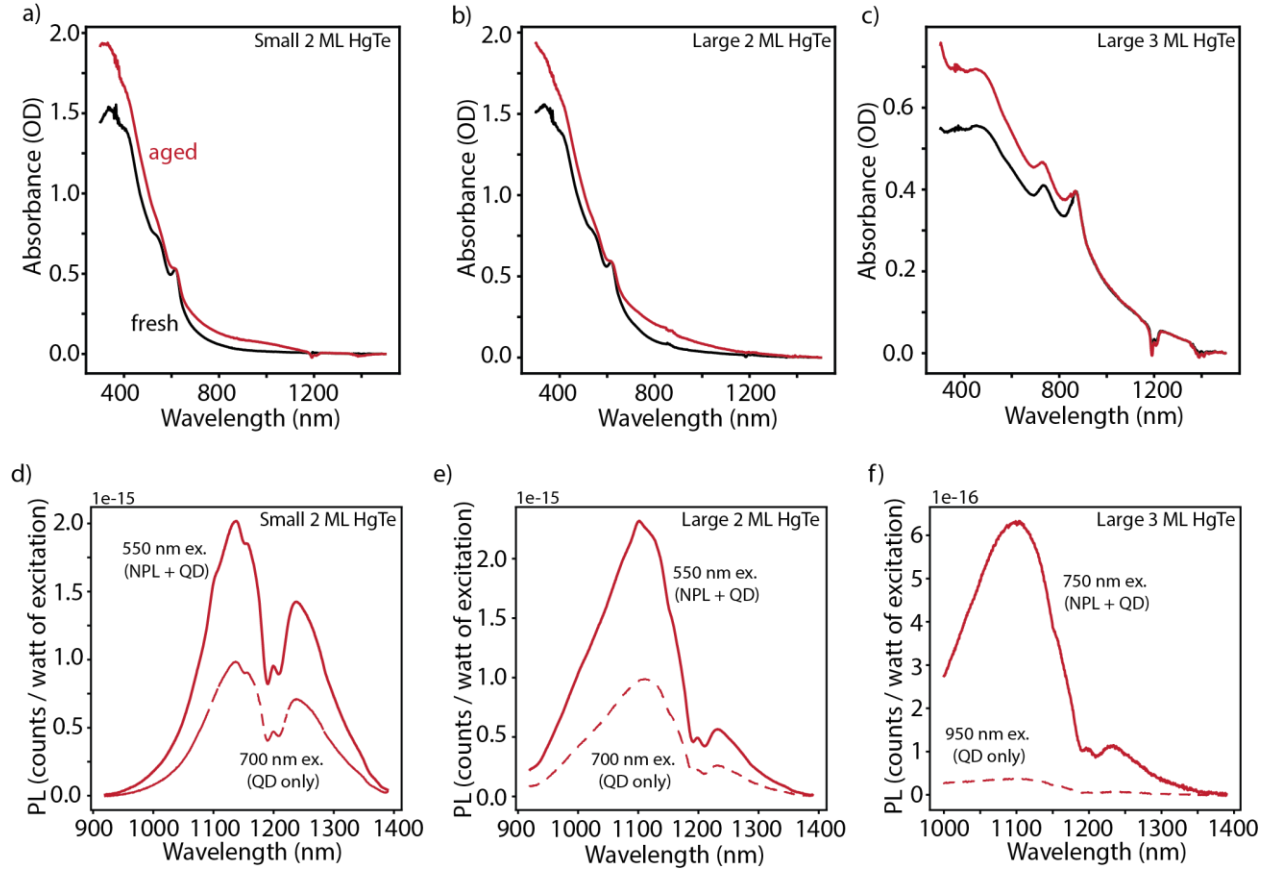
Figure 3.13. *The absorption of a) small 2 ML HgTe, b) large 2 ML HgTe, and c) large 3 ML HgTe shown directly after cation exchange and after aging to grow QDs in-situ. The photoluminescence with excitation both above and below the NPL band-edge for d) small 2 ML HgTe, e) large 2 ML HgTe, and f) large 3 ML HgTe.*

We explored the QE of energy transfer of different sizes and thicknesses of NPLs in Figure 3.13. In 2 ML HgTe NPLs, the QD features are visible after aging because the NPLs do not have absorption beyond 800 nm. The QD features in the 3 ML sample are still obscured by the NPL absorption as it extends into the near-IR. For the photoluminescence, we excited both above the bandgap of the NPL to capture NPL + QD, and below the bandgap of the NPL to capture QD only. Note that while there was still some NPL band-edge emission in when exciting above the bandgap, we only evaluate the PL from the QD for the QE calculations (as reflected in Figure 3.13d-f).

Change in QE with age of NPL / QD Heterostructure
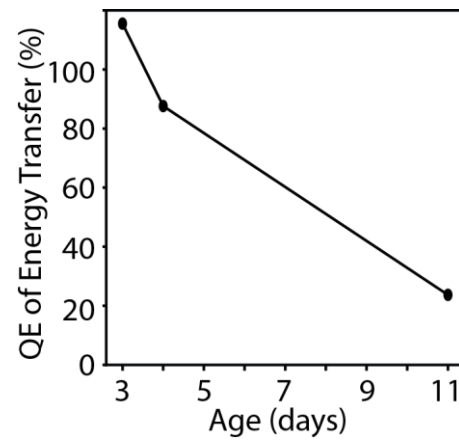
Figure 3.14*. The QE of energy transfer collected for HgTe QD/NPL heterostructures grown in-situ over several days. The sample was sealed in a cuvette and spectra recorded over time.*

Additional details for Monte Carlo simulation
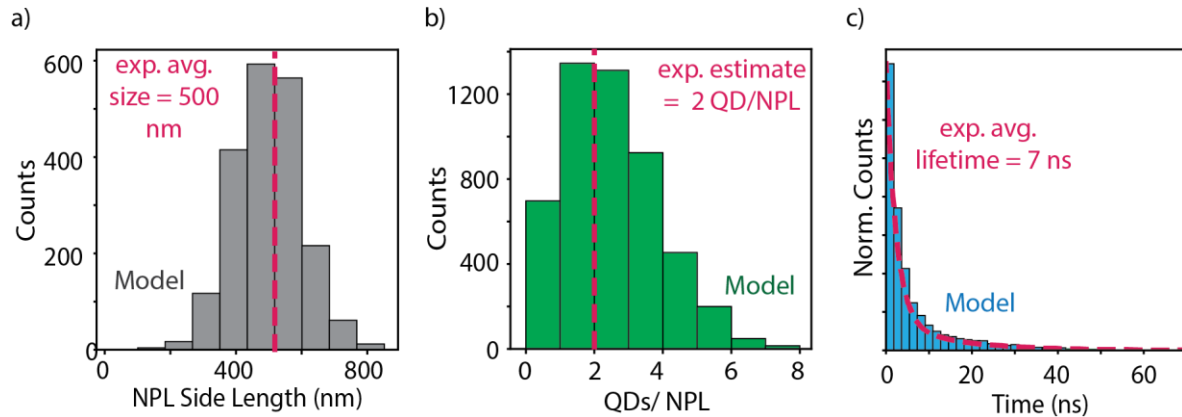
Figure 3.15. *The experimental estimate (red dashed line) compared to model distribution for a) NPL size, b) QD / NPL ratio, and c) photoluminescence lifetime.*

The simulation was run for a series of 20 diffusion constants, ranging from 10^{-4} cm^2/s to 10^3 cm^2/s. For each diffusion constant, 5000 random walks were conducted and the outcome of each walk was classified as either recombined (exciton survived until the set stop time), or trapped (exciton fell within the trapping radius of a randomly placed trap).

We first generated 5000 square 2D sheets to represent NPLs with a normal distribution centered around a side length of 500 nm, and a standard deviation of 100 nm (Figure 3.15a). On each sheet, we then randomly placed a number of points to represent QD traps which was drawn from a Poisson distribution centered at 2 traps/NPL (Figure 3.15b).

Each walk begins by placing the exciton in the center of the 2D sheet and allowing it to randomly diffuse in 2D until it falls within a 40 nm radius of a trap (more details below) or reaches the stop time which represents recombination. The stop times were determined by the lifetime (described below) and the time step was set to be 2×10^{-5} ns to remain in the diffusion regime and so that the step size always remains less than the size of the trapping radius (40 nm). From the time step, the step size was calculated as:

$$\text{Step size} = \sqrt{4 * time\ step * diffusion\ constant} \tag{3.8}$$

The outcome for each walk was then recorded as trapped or recombined, and the total percentages for each diffusion constant presented in Figure 3.3.

Probability of recombination based on experimental lifetime

To represent the possibility of exciton recombination as an outcome within our model, we sampled each exciton's stop time from an inverse cumulative distribution function that follows the experimental lifetime. The inverse cumulative distribution function (ICDF) gives the value associated with a given probability. In this case, we will draw a random number for each exciton between 0-1 and use the ICDF to determine what the lifetime will be for that individual random walk.

The experimental lifetime of HgTe NPLs without any QDs can be fit to two components using a biexponential function. Their contribution to lifetime can be considered as:

$$\text{Percentage Comp. 1} = \frac{\frac{A}{k_1}}{\frac{A}{k_1}+\frac{B}{k_2}} \tag{3.9}$$

$$\text{Percentage Comp. 2} = \frac{\frac{B}{k_2}}{\frac{A}{k_1}+\frac{B}{k_2}} \tag{3.10}$$

If the random number drawn for the theoretical exciton is less than or equal to percentage 1, it is rescaled from 0-1 and the stop time calculated as:

$$\text{Stop time} = \frac{-\ln(rand.num.)}{k_1} \tag{3.11}$$

And if the random number drawn for the theoretical exciton is greater or equal to percentage 2, it is rescaled from 0-1 and the stop time calculated as:

$$\text{Stop time} = \frac{-\ln(rand.num.)}{k_2} \tag{3.12}$$

Using two distributions is necessary because the lifetime contains two exponentials and an analytical form of the ICDF for this was not found. The combined results of these two distributions are shown for 10,000 random walks in Figure 3.15c and is compared to the experimental fit.
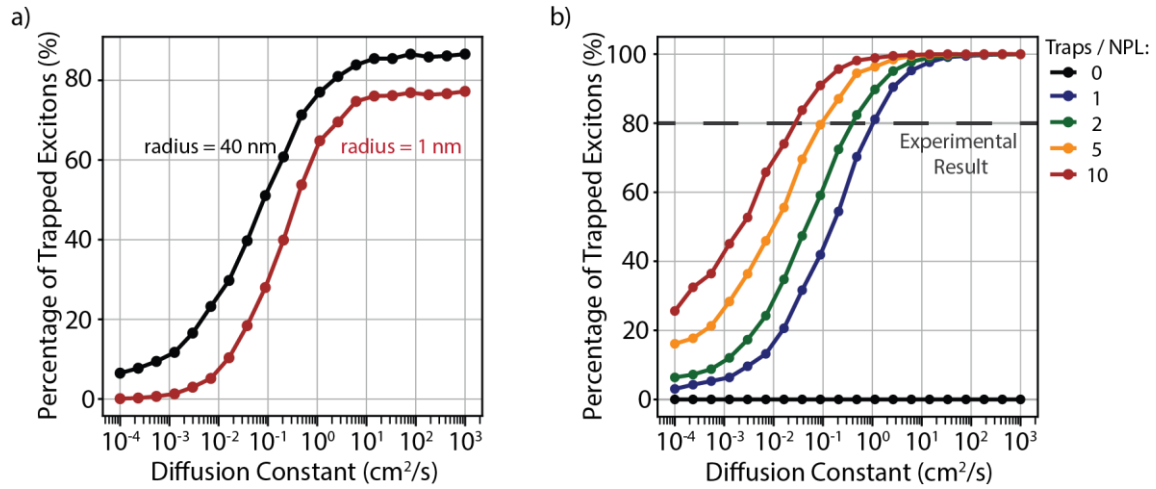
Figure 3.16. *a) simulation result difference in percentage of trapped excitons if the trapping radius is changed from 1 nm to 40 nm, b) the simulation result if a uniform distribution of traps (ranging from 0 – 10) is set.*

Estimation of the trapping radius

Our random walk models the exciton in the NPL as a point, diffusing randomly until it meets a QD trap. We chose to account for the exciton size by setting a radius around the trap, where the exciton must be at an equal or lesser distance from the trap to end its walk. This radius is equal to the Bohr radius.

The exciton Bohr radius in HgTe NPLs has not been reported, but it is known to be 40 nm in bulk HgTe which sets an upper limit, as increased confinement will result in a smaller Bohr radius.[57] We estimate the minimum Bohr radius to be the thickness dimension of a NPL (~1 nm for a 3ML NPL).

Running the simulation at both extremes (Figure 3.16a) shows that the main difference is the saturation threshold where a smaller radius saturates at <80% while a larger radius saturates > 80%. This is likely because it would be easier for the exciton to "trap" if the radius is larger the trap will cover more area and will collect more excitons before recombination compared to a smaller radius. We chose to present the results using the upper limit of 40 nm, because the lateral size of the NPLs we chose far exceeds lateral confinement but acknowledge this does not take into account the effect of dielectric on binding energy.[58]

Random walk using uniform distribution of traps per NPL

Based on observations from TEM images and estimates of the concentration of QDs in a solution of in-situ NPL/QD heterostructures, we presented the results of the simulation using a Poisson distribution with an average of 2 QDs/NPL in Figure 3.3. To examine the bounds of this approximation, we also ran the simulation using uniform distributions by setting a uniform number of traps on every NPL in the simulation. The results are shown in Figure 3.16b and range from 0 – 10 traps/ NPL.

With 0 traps, we confirm that no excitons meet the "trapped" outcome and will therefore all meet the "recombined" outcome. As we increase the number of traps, we observe that the diffusion constant needed to surpass the experimental observation of >80% trapping shifts to lower values. TEM images will show that not every NPL has visible QDs, and as such we decided to use a Poisson distribution to account for the likelihood that most will have 2 or more, but some will have 0. It is unlikely that there are 5 or more QDs/NPL as this would result in more significant contributions to the absorption spectra which are not observed.

Examples of random walk at various diffusion constants
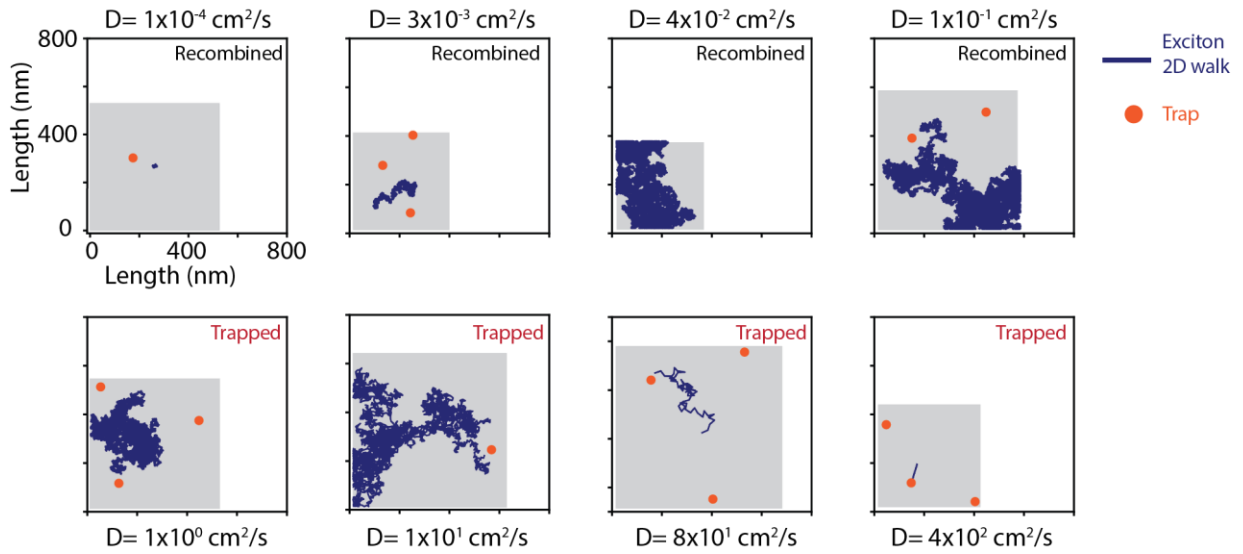
Figure 3.17. One example of a random walk from each set of simulations per diffusion constant. Lower diffusion constants typically recombine before trapping while larger diffusion constants typically trap before the recombination time. NPL sizes vary but are on average, about 500 nm by 500 nm.

REFERENCES

(1)   Freyria, F. S.; Cordero, J. M.; Caram, J. R.; Doria, S.; Dodin, A.; Chen, Y.; Willard, A. P.;
        Bawendi, M. G. Near-Infrared Quantum Dot Emission Enhanced by Stabilized Self-
        Assembled J-Aggregate Antennas. *Nano Lett.* **2017**, *17* (12), 7665–7674.

(2)   Zhang, Q.; Atay, T.; Tischler, J. R.; Bradley, M. S.; Bulović, V.; Nurmikko, A. V. Highly
        Efficient Resonant Coupling of Optical Excitations in Hybrid Organic/Inorganic
        Semiconductor Nanostructures. *Nat. Nanotechnol.* **2007**, *2* (9), 555–559.

(3)   O. A. Tanoh, A.; Gauriot, N.; Delport, G.; Xiao, J.; Pandya, R.; Sung, J.; Allardice, J.; Li,
        Z.; A. Williams, C.; Baldwin, A.; D. Stranks, S.; Rao, A. Directed Energy Transfer from
        Monolayer WS2 to Near-Infrared Emitting PbS–CdS Quantum Dots. *ACS Nano* **2020**, *14*
        (11), 15374–15384.

(4)   Sundström, V.; Pullerits, T.; Van Grondelle, R. Photosynthetic Light-Harvesting:
        Reconciling Dynamics and Structure of Purple Bacterial LH2 Reveals Function of
        Photosynthetic Unit. *J. Phys. Chem. B* **1999**, *103* (13), 2327–2346.

(5)   Scholes, G. D.; Rumbles, G. Excitons in Nanoscale Systems. *Nat. Mater.* **2006**, *5* (9),
        683–696.

(6)   Cnops, K.; Rand, B. P.; Cheyns, D.; Verreet, B.; Empl, M. A.; Heremans, P. 8.4%
        Efficient Fullerene-Free Organic Solar Cells Exploiting Long-Range Exciton Energy
        Transfer. *Nat. Commun.* **2014**, *5* (1), 1–6.

(7)   Ithurria, S.; Tessier, M. D.; Mahler, B.; Lobo, R. P. S. M.; Dubertret, B.; Efros, A. L.
        Colloidal Nanoplatelets with Two-Dimensional Electronic Structure. *Nat. Mater.* **2011**, *10*
        (12), 936–941.

(8)   Yeltik, A.; Delikanli, S.; Olutas, M.; Kelestemur, Y.; Guzelturk, B.; Demir, H. V.
        Experimental Determination of the Absorption Cross-Section and Molar Extinction
        Coefficient of Colloidal CdSe Nanoplatelets. *J. Phys. Chem. C* **2015**, *119* (47), 26768–
        26775.

(9)   Hu, A.; Bai, P.; Zhu, Y.; Song, Z.; Wang, R.; Zheng, J.; Yao, Y.; Zhang, Q.; Ding, Z.;

Gao, P.; Sui, X.; Liu, X.; Gao, Y. Green CdSe/CdSeS Core/Alloyed-Crown Nanoplatelets Achieve Unity Photoluminescence Quantum Yield over a Broad Emission Range. *Adv. Opt. Mater.* **2022**, *10* (13), 2200469.

(10) Scott, R.; Heckmann, J.; Prudnikau, A. V.; Antanovich, A.; Mikhailov, A.; Owschimikow, N.; Artemyev, M.; Climente, J. I.; Woggon, U.; Grosse, N. B.; Achtstein, A. W. Directed Emission of CdSe Nanoplatelets Originating from Strongly Anisotropic 2D Electronic Structure. *Nat. Nanotechnol.* **2017**, *12* (12), 1155–1160.

(11) Tenney, S. M.; Tan, L. A.; Sonnleitner, M. L.; Sica, A. V; Shin, A. J.; Ronquillo, R.; Ahmed, T.; Atallah, T. L.; Caram, J. R. Mesoscale Quantum-Confined Semiconductor Nanoplatelets through Seeded Growth. *Chem. Mater.* **2022**, *34* (13), 6048–6056.

(12) Izquierdo, E.; Dufour, M.; Chu, A.; Livache, C.; Martinez, B.; Amelot, D.; Patriarche, G.; Lequeux, N.; Lhuillier, E.; Ithurria, S. Coupled HgSe Colloidal Quantum Wells through a Tunable Barrier: A Strategy to Uncouple Optical and Transport Band Gap. *Chem. Mater.* **2018**, *30* (12), 4065–4072.

(13) Izquierdo, E.; Robin, A.; Keuleyan, S.; Lequeux, N.; Lhuillier, E.; Ithurria, S. Strongly Confined HgTe 2D Nanoplatelets as Narrow Near-Infrared Emitters. *J. Am. Chem. Soc.* **2016**, *138* (33), 10496–10501.

(14) Tenney, S. M.; Vilchez, V.; Sonnleitner, M. L.; Huang, C.; Friedman, H. C.; Shin, A. J.; Atallah, T. L.; Deshmukh, A. P.; Ithurria, S.; Caram, J. R. Mercury Chalcogenide Nanoplatelet–Quantum Dot Heterostructures as a New Class of Continuously Tunable Bright Shortwave Infrared Emitters. *J. Phys. Chem. Lett.* **2020**, *11*, 3473–3480.

(15) Horani, F.; Meir, I.; Lifshitz, E. Room Temperature Colloidal Coating of II–VI Nanoplatelets with Quantum Dots. *J. Phys. Chem. C.* **2021**, *125* (46), 25729–25738.

(16) Williams, K. R.; Diroll, B. T.; Watkins, N. E.; Rui, X.; Brumberg, A.; Klie, R. F.; Schaller, R. D. Synthesis of Type i PbSe/CdSe Dot-on-Plate Heterostructures with Near-Infrared Emission. *J. Am. Chem. Soc.* **2019**, *141* (13), 5092–5096.

(17) B.V. Salzmann, B.; de Wit, J.; Li, C.; Arenas-Esteban, D.; Bals, S.; Meijerink, A.; Vanmaekelbergh, D. Two-Dimensional CdSe-PbSe Heterostructures and PbSe

Nanoplatelets: Formation, Atomic Structure, and Optical Properties. *J. Phys. Chem. C* **2022**, *126* (3), 1513–1522.

(18)   Medda, A.; Dutta, A.; Bain, D.; Kumar Mohanta, M.; De Sarkar, A.; Patra, A. Electronic Structure Modulation of 2D Colloidal CdSe Nanoplatelets by Au25 Clusters for High-Performance Photodetectors. *J. Phys. Chem. C* **2020**, *124* (36), 19793–19801.

(19)   Piepenbrock, M. O. M.; Stirner, T.; Kelly, S. M.; O'Neill, M. A Low-Temperature Synthesis for Organically Soluble HgTe Nanocrystals Exhibiting near-Infrared Photoluminescence and Quantum Confinement. *J. Am. Chem. Soc.* **2006**, *128* (21), 7087–7090.

(20)   Tan, X.; Caram, J. R. On the Inadequacy of Stern-Volmer and FRET in Describing Quenching in Binary Donor-Acceptor Solutions. **2023**.

(21)   Ludwig Hernández-Martínez, P.; O. Govorov, A.; Volkan Demir, H. Generalized Theory of Förster-Type Nonradiative Energy Transfer in Nanostructures with Mixed Dimensionality. *J. Phys. Chem. C* **2013**, *117* (19), 10203–10212.

(22)   M. Y. Lee, E.; A. Tisdale, W. Determination of Exciton Diffusion Length by Transient Photoluminescence Quenching and Its Application to Quantum Dot Films. *J. Phys. Chem. C* **2015**, *119* (17), 9005–9015.

(23)   M. Akselrod, G.; Prins, F.; V. Poulikakos, L.; M. Y. Lee, E.; C. Weidman, M.; Jolene Mork, A.; P. Willard, A.; Bulović, V.; A. Tisdale, W. Subdiffusive Exciton Transport in Quantum Dot Solids. *Nano Lett.* **2014**, *14* (6), 3556–3562.

(24)   Joon Yoon, S.; Guo, Z.; C. dos Santos Claro, P.; V. Shevchenko, E.; Huang, L. Direct Imaging of Long-Range Exciton Transport in Quantum Dot Superlattices by Ultrafast Microscopy. *ACS Nano* **2016**, *10* (7), 7208–7215.

(25)   Penzo, E.; Loiudice, A.; S. Barnard, E.; J. Borys, N.; J. Jurow, M.; Lorenzon, M.; Rajzbaum, I.; K. Wong, E.; Liu, Y.; M. Schwartzberg, A.; Cabrini, S.; Whitelam, S.; Buonsanti, R.; Weber-Bargioni, A. Long-Range Exciton Diffusion in Two-Dimensional Assemblies of Cesium Lead Bromide Perovskite Nanocrystals. *ACS Nano* **2020**, *14* (6), 6999–7007.

(26)   Mikhnenko, O. V.; Cordella, F.; Sieval, A. B.; Hummelen, J. C.; Blom, P. W. M.; Loi, M.
         A. Temperature Dependence of Exciton Diffusion in Conjugated Polymers. *J. Phys.
         Chem. B* **2008**, *112* (37), 11601–11604.

(27)   Lewis, A. J.; Ruseckas, A.; Gaudin, O. P. M.; Webster, G. R.; Burn, P. L.; Samuel, I. D.
         W. Singlet Exciton Diffusion in MEH-PPV Films Studied by Exciton-Exciton
         Annihilation. *Org. Electron.* **2006**, *7* (6), 452–456.

(28)   Zhu, T.; Wan, Y.; Guo, Z.; Johnson, J.; Huang, L.; Zhu, T.; Wan, Y.; Guo, Z.; Huang, L.;
         Johnson, J. Two Birds with One Stone: Tailoring Singlet Fission for Both Triplet Yield
         and Exciton Diffusion Length. *Adv. Mater.* **2016**, *28* (34), 7539–7547.

(29)   Hertel, T.; Himmelein, S.; Ackermann, T.; Stich, D.; Crochet, J. Diffusion Limited
         Photoluminescence Quantum Yields in 1-D Semiconductors: Single-Wall Carbon
         Nanotubes. *ACS Nano* **2010**, *4* (12), 7161–7168.

(30)   Yoshikawa, K.; Matsuda, K.; Kanemitsu, Y. Exciton Transport in Suspended Single
         Carbon Nanotubes Studied by Photoluminescence Imaging Spectroscopy. *J. Phys. Chem.
         C* **2010**, *114* (10), 4353–4356.

(31)   R. Caram, J.; Doria, S.; M. Eisele, D.; S. Freyria, F.; S. Sinclair, T.; Rebentrost, P.; Lloyd,
         S.; G. Bawendi, M. Room-Temperature Micron-Scale Exciton Migration in a Stabilized
         Emissive Molecular Aggregate. *Nano Lett.* **2016**, *16* (11), 6808–6815.

(32)   Deng, S.; Shi, E.; Yuan, L.; Jin, L.; Dou, L.; Huang, L. Long-Range Exciton Transport
         and Slow Annihilation in Two-Dimensional Hybrid Perovskites. *Nat. Commun.* **2020**, *11*
         (1).

(33)   Seitz, M.; Magdaleno, A. J.; Alcázar-Cano, N.; Meléndez, M.; Lubbers, T. J.; Walraven,
         S. W.; Pakdel, S.; Prada, E.; Delgado-Buscalioni, R.; Prins, F. Exciton Diffusion in Two-
         Dimensional Metal-Halide Perovskites. *Nat. Commun.* **2020**, *11* (1).

(34)   Yu, Y.; Yu, Y.; Li, G.; Puretzky, A. A.; Geohegan, D. B.; Cao, L. Giant Enhancement of
         Exciton Diffusivity in Two-Dimensional Semiconductors. *Sci. Adv.* **2020**, *6* (51), 4823–
         4841.

(35)   Javey, A.; Uddin, S. Z.; Kim, H.; Lorenzon, M.; Yeh, M.; Lien, D. H.; Barnard, E. S.;

Htoon, H.; Weber-Bargioni, A. Neutral Exciton Diffusion in Monolayer MoS2. *ACS Nano* **2020**, *14* (10), 13433–13440.

(36)   Rosati, R.; Brem, S.; Perea-Causin, R.; Schmidt, R.; Niehues, I.; Michaelis De Vasconcellos, S.; Bratschitsch, R.; Malic, E. Strain-Dependent Exciton Diffusion in Transition Metal Dichalcogenides. *2D Mater.* **2020**, *8* (1), 015030.

(37)   Chen, P.; Atallah, T. L.; Lin, Z.; Wang, P.; Lee, S. J.; Xu, J.; Huang, Z.; Duan, X.; Ping, Y.; Huang, Y.; Caram, J. R.; Duan, X. Approaching the Intrinsic Exciton Physics Limit in Two-Dimensional Semiconductor Diodes. *Nature.* **2021**, *599* (7885), 404–410.

(38)   Kumar, N.; Cui, Q.; Ceballos, F.; He, D.; Wang, Y.; Zhao, H. Exciton Diffusion in Monolayer and Bulk MoSe2. *Nanoscale* **2014**, *6* (9), 4915–4919.

(39)   Cadiz, F.; Robert, C.; Courtade, E.; Manca, M.; Martinelli, L.; Taniguchi, T.; Watanabe, K.; Amand, T.; Rowe, A. C. H.; Paget, D.; Urbaszek, B.; Marie, X. Exciton Diffusion in WSe2 Monolayers Embedded in a van Der Waals Heterostructure. *Appl. Phys. Lett.* **2018**, *112* (15), 152106.

(40)   Achtstein, A. W.; Ayari, S.; Helmrich, S.; Quick, M. T.; Owschimikow, N.; Jaziri, S.; Woggon, U. Tuning Exciton Diffusion, Mobility and Emission Line Width in CdSe Nanoplatelets via Lateral Size. *Nanoscale* **2020**, *12* (46), 23521–23531.

(41)   Li, Q.; Wu, K.; Chen, J.; Chen, Z.; McBride, J. R.; Lian, T. Size-Independent Exciton Localization Efficiency in Colloidal CdSe/CdS Core/Crown Nanosheet Type-I Heterostructures. *ACS Nano* **2016**, *10* (3), 3843–3851.

(42)   Li, B.; Gao, Y.; Wu, R.; Miao, X.; Zhang, G. Charge and Energy Transfer Dynamics in Single Colloidal Quantum Dots/Monolayer MoS2 Heterostructures. *Phys. Chem. Chem. Phys.* **2023**, *25* (11), 8161–8167.

(43)   Achermann, M.; Petruska, M. A.; Kos, S.; Smith, D. L.; Koleske, D. D.; Klimov, V. I. Energy-Transfer Pumping of Semiconductor Nanocrystals Using an Epitaxial Quantum Well. *Nature* **2004**, *429* (6992), 642–646.

(44)   Wu, K.; Li, Q.; Du, Y.; Chen, Z.; Lian, T. Ultrafast Exciton Quenching by Energy and Electron Transfer in Colloidal CdSe Nanosheet–Pt Heterostructures. *Chem. Sci.* **2015**, *6*

(2), 1049–1054.

(45)   Halim, H.; Trieb, D.; Huber, N.; Martínez-Negro, M.; Meyer, L.-A.; Basché, T.;
       Morsbach, S.; A. I. Zhang, K.; Riedinger, A. Lateral Size Dependence in FRET between
       Semiconductor Nanoplatelets and Conjugated Fluorophores. *J. Phys. Chem. C* **2020**, *124*
       (45), 25028–25037.

(46)   Yuan, L.; Huang, L. Exciton Dynamics and Annihilation in WS2 2D Semiconductors.
       Nanoscale **2015**, *7* (16), 7402–7408.

(47)   Amani, M.; Lien, D. H.; Kiriya, D.; Xiao, J.; Azcatl, A.; Noh, J.; Madhvapathy, S. R.;
       Addou, R.; Santosh, K. C.; Dubey, M.; Cho, K.; Wallace, R. M.; Lee, S. C.; He, J. H.;
       Ager, J. W.; Zhang, X.; Yablonovitch, E.; Javey, A. Near-Unity Photoluminescence
       Quantum Yield in MoS2. *Science.* **2015**, *350* (6264), 1065–1068.

(48)   Mirkovic, T.; E. Ostroumov, E.; M. Anna, J.; van Grondelle, R.; D. Scholes, G. Light
       Absorption and Energy Transfer in the Antenna Complexes of Photosynthetic Organisms.
       Chem. Rev. **2016**, *117* (2), 249–293.

(49)   Boulesbaa, A.; Wang, K.; Mahjouri-Samani, M.; Tian, M.; A. Puretzky, A.; Ivanov, I.; M.
       Rouleau, C.; Xiao, K.; G. Sumpter, B.; B. Geohegan, D. Ultrafast Charge Transfer and
       Hybrid Exciton Formation in 2D/0D Heterostructures. *J. Am. Chem. Soc.* **2016**, *138* (44),
       14713–14719.

(50)   Mahler, B.; Guillemot, L.; Bossard-Giannesini, L.; Ithurria, S.; Pierucci, D.; Ouerghi, A.;
       Patriarche, G.; Benbalagh, R.; Lacaze, E.; Rochet, F.; Lhuillier, E. Metallic
       Functionalization of CdSe 2D Nanoplatelets and Its Impact on Electronic Transport. *J.
       Phys. Chem. C* **2016**, *120* (23), 12351–12361.

(51)   Naskar, S.; Schlosser, A.; Miethe, J. F.; Steinbach, F.; Feldhoff, A.; Bigall, N. C. Site-
       Selective Noble Metal Growth on CdSe Nanoplatelets. *Chem. Mater.* **2015**, *27* (8), 3159–
       3166.

(52)   Atallah, T. L.; Sica, A. V.; Shin, A. J.; Friedman, H. C.; Kahrobai, Y. K.; Caram, J. R.
       Decay-Associated Fourier Spectroscopy: Visible to Shortwave Infrared Time-Resolved
       Photoluminescence Spectra. *J. Phys. Chem. A* **2019**, *123* (31), 6792–6798.

(53)   She, C.; Fedin, I.; Dolzhnikov, D. S.; Demortière, A.; Schaller, R. D.; Pelton, M.; Talapin, D. V. Low-Threshold Stimulated Emission Using Colloidal Quantum Wells. *Nano Lett.* **2014**, *14* (5), 2772–2777.

(54)   Lhuillier, E.; Keuleyan, S.; Guyot-Sionnest, P. Optical Properties of HgTe Colloidal Quantum Dots. *Nanotechnology* **2012**, *23* (17), 175705.

(55)   Leatherdale, C. A.; Woo, W. K.; Mikulec, F. V.; Bawendi, M. G. On the Absorption Cross Section of CdSe Nanocrystal Quantum Dots. *J. Phys. Chem. B* **2002**, *106* (31), 7619–7622.

(56)   Bortz, A. B.; Kalos, M. H.; Lebowitz, J. L. A New Algorithm for Monte Carlo Simulation of Ising Spin Systems. *J. Comput. Phys.* **1975**, *17* (1), 10–18.

(57)   Goubet, N.; Jagtap, A.; Livache, C.; Martinez, B.; Portalès, H.; Zhen Xu, X.; P. S. M. Lobo, R.; Dubertret, B.; Lhuillier, E. Terahertz HgTe Nanocrystals: Beyond Confinement. *J. Am. Chem. Soc.* **2018**, *140* (15), 5033–5036.

(58)   Shin, A. J.; Hossain, A. A.; Tenney, S. M.; Tan, X.; Tan, L. A.; Foley, J. J.; Atallah, T. L.; Caram, J. R. Dielectric Screening Modulates Semiconductor Nanoplatelet Excitons. *J. Phys. Chem. Lett.* **2021**, *12*, 4958–4964.

Chapter 4

Mesoscale Quantum-Confined Semiconductor Nanoplatelets Through Seeded Growth

In this chapter, we demonstrate the preparation of mesoscale semiconductor (II-VI) nanoplatelets (NPLs) for the first time using colloidal seeded growth. These nanoplatelets are quantum-confined and atomically precise but grown to a length scale compatible with conventional optical imaging and microscopic manipulation (even reaching $> 1 \ \mu m^2$) offering an opportunity to bridge the application space between nanocrystals and 2D materials. Using CdTe as a model system we develop a seeded growth procedure, show the parameters which control extension, and apply them to a variety of thicknesses and compositions. In-situ spectroscopy demonstrates that addition onto the nanoplatelet seeds is not continuous, and likely occurs through ripening. Finally, we use correlative optical and electron microscopy to demonstrate that at large sizes, PL mapping of the entire structure can be resolved including spatial inhomogeneities. Overall, these results show that nanoplatelets can be compared to 2D semiconductors while maintaining the advantages of scalable colloidal synthesis, thickness tunability and solution processability.

4.1 Introduction to Lateral Control in Nanoplatelets

II-VI semiconductor nanoplatelets (NPLs) are a class of nanocrystals with atomically precise confinement in the thickness dimension. They show exceptional photophysical properties,

including narrow linewidths, tunable emission, large absorption cross sections, and high quantum yields.[1–3] They are also structurally versatile, able to vary in composition from CdX (X=S, Se, Te) to HgX, and are amenable towards lateral and longitudinal heterostructures—all while maintaining their discrete monolayer (ML) thicknesses.[1,4–8]

Due to their similar anisotropic structure, a comparison can be made between NPLs and van der Waals (vdW) 2D materials. Both systems display strong exciton binding energy, dielectric screening by external environments, and thickness-dependent band structure.[9–11] Additionally, NPLs may also show exotic properties characteristic of vdW materials, such as single photon emission, topological insulation, spin-orbit effects, and fractional quantum hall effects.[12–14] Unlike conventional exfoliated vdW 2D materials that often display a finite thickness distribution, II-VI semiconductor NPLs may be prepared with monodispersed thickness through colloidal methods, with direct bandgaps for all thicknesses, and chemical tunability through ligand design.[15] Realizing the connections to 2D vdW materials requires NPLs with sufficiently large lateral areas, especially to integrate them into single nanoplatelet devices or high-performance thin film devices.[16]

Prior work has shown CdX and HgX NPLs can be synthesized with lateral dimensions (longest edge) up to ~500 nm using slow injection of precursors, although most procedures utilize fast injection that results in smaller lateral sizes of 100-200 nm or less.[17] Studies of smaller NPLs reveal lateral size dependence of photophysical properties including an enhanced absorption cross section, giant oscillator strength, altered spontaneous and stimulated emission thresholds, modified biexciton quantum yield, and depressed Auger recombination.[18–22] However, the absence of a standardized procedure to synthesize larger NPLs limits the exploration of such properties into bulk II-VI nanosheets, which may behave more similarly to their 2D vdW semiconducting cousins.

132

Ultrathin nanosheets of other semiconducting materials have been colloidally synthesized, such as $Cu_{2-x}S$,[23] In_2Se_3[24], PbS[25], perovskite $CsPbBr_3$[26], and a host of transition metal dichalcogenides (TMDs). Despite this variety, robust control of large area II-VI nanosheets with optical properties akin to their highly-confined small area analogs has not been shown.

To synthesize mesoscale NPLs, we develop a seeded growth method inspired by previously demonstrated growth of core-crown NPLs. In a typical core-crown growth procedure, an amount of pre-synthesized NPLs are used as seeds and a second reaction introduces a chalcogen precursor of a different composition to yield a heterostructure.[7,27–32] The extension method of small CdSe NPLs from ~300 to 4000 nm^2 is similar, but it uses the same precursor compositions injected into a solution of NPL seeds at slower rates.[33–35] We build on these procedures in our seeded growth, but carefully explore the parameters to yield NPLs that are more than double in size while maintaining their size-confinement in the thickness dimension.

We show that careful control of the reaction parameters which affect 2D NPL growth allows us to demonstrate the optimal conditions for mesoscale CdTe NPLs and investigate how the NPL population evolves during the seeded growth process. We then utilize correlative imaging of single NPLs using a combination of fluorescence and electron microscopy to show that large NPLs exhibit lateral heterogeneity in their photoluminescence. Overall, this study demonstrates that mesoscale II-VI NPLs can possess differing electronic structure within a single NPL and represent a new class of colloidal 2D semiconductors rather than confined single emitters. Finally, the advent of mesoscale 2D vdW materials has enabled a generation of novel electronic devices as a result of their microscopic characterization and control, and a similar application space may exist for colloidal NPLs.[36–38] Their size may make them similarly amenable to direct microscopic

manipulation and could pave the way for more advanced, single nanocrystal devices derived from colloidal confined II-VI semiconductors.
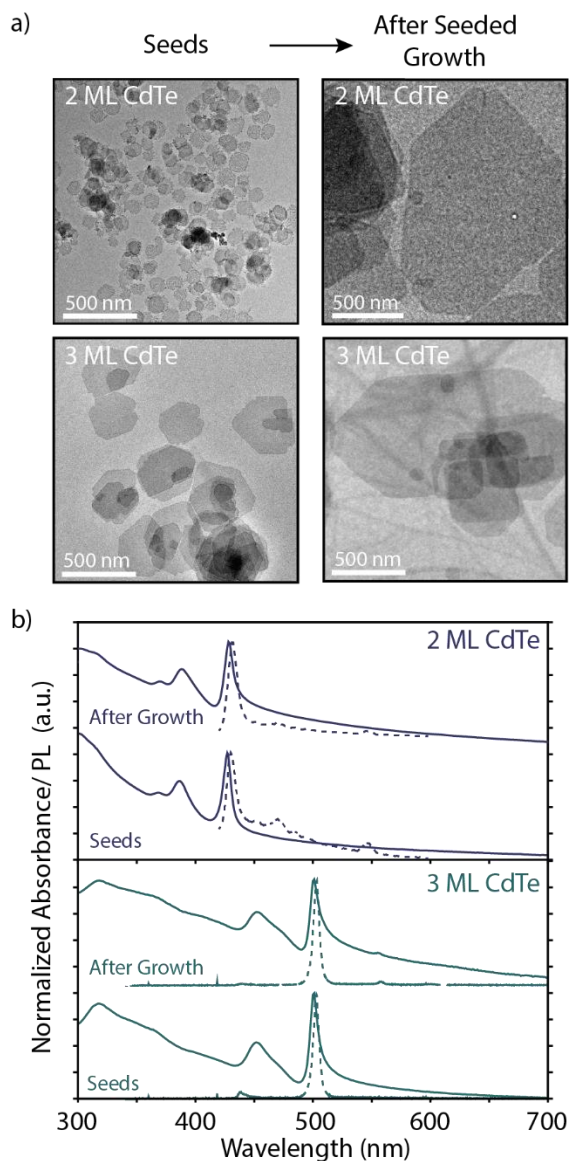
Figure 4.1. a) TEM of 2 and 3 ML CdTe NPL seeds before and after seeded growth. b) Absorption (solid lines) and photoluminescence (PL, dashed lines) spectra before and after seeded growth.

4.2 Development of Seeded Growth Synthesis for Mesoscale CdX NPLs (X= Se,Te)

We start by showing two exemplars of the seeded growth process in Figure 4.1. Following literature procedures, we produce 2 and 3 monolayer (ML) CdTe seeds with an average lateral extent of 90 ± 2 nm and 370 ± 11 nm respectively (results of size counting in Table 4.3).[4–]

[6] 2 ML CdTe seed NPLs are synthesized by a fast injection of trioctylphosphine telluride (TOP-Te) into a cadmium propionate solution at 180 ˚C. For 3 ML seed NPLs, we follow a slow injection method, where TOP-Te is continuously injected into a solution of cadmium propionate at 210 ˚C. All NPL products are then centrifuged and resuspended in fresh solvent to be used as seeds for subsequent growth. We then extend these NPL seeds to lateral sizes of 1000-1500 nm by reintroducing them to a second, slower injection of new chalcogen precursor and carefully control the rate of growth (further details in experimental section). Despite the change in size, the larger NPLs retain their absorption and emission profiles after this seeded growth process (Figure 4.1b), suggesting no change in thickness with increase in lateral size. The quantum yields for CdTe NPLs remain low with <1% before and 3% after seeded growth for 2 ML, and <1% before and after for 3 ML, but this is expected due to their large lateral areas and potential for defects.[39] Photoluminescence lifetimes of NPLs in solution show similar results before and after seeded growth of ~30 ps (Figure 4.7).
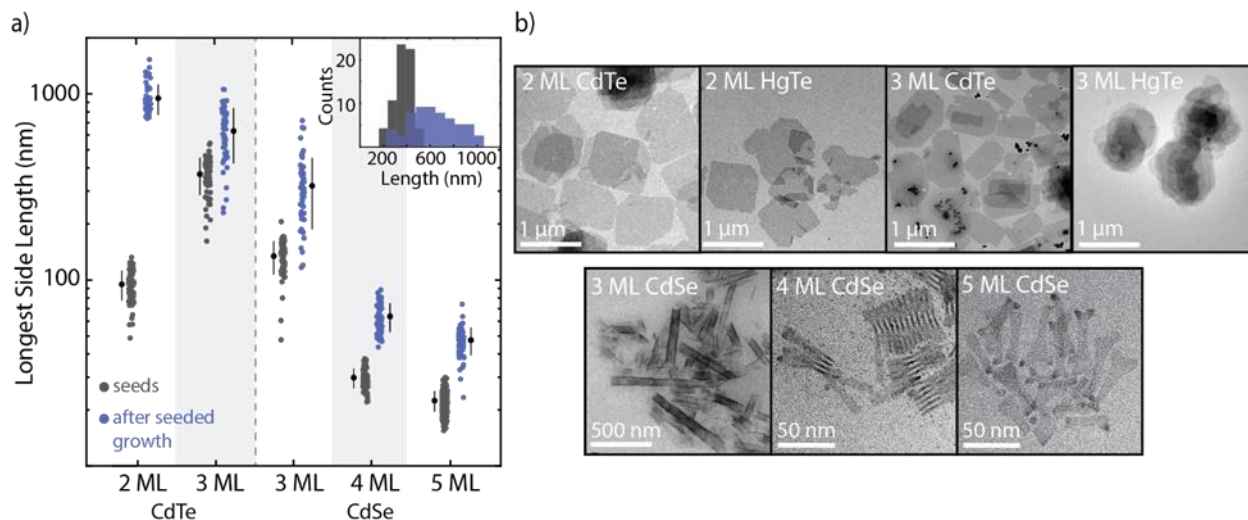
Figure 4.2. *a) The difference in lateral sizes before (grey) and after (blue) seeded growth for various CdX NPL thicknesses. Solid colored circles represent the counts for each size distribution, while the solid black circles show the mean and standard deviation of each condition explored. Inset shows an example of the full histogram of sizes before (grey) and after (blue) seeded growth*

for 3 ML CdTe. b) Representative TEM images of NPLs after seeded growth, including HgTe from cation exchange with large CdTe.

4.3 Lateral Sizes After Seeded Growth in CdX (X=Se, Te) and Cation Exchange to HgX

In Figure 4.2, we demonstrate the scope of this procedure by applying the conditions of seeded growth to various compositions (specifically CdTe NPLs (2-3 ML) and CdSe NPLs (3-5 ML)) and measure the change in lateral extent using TEM (Figure 4.2a). We observe the greatest enhancement in CdTe NPLs, but all materials show a significant change of at least twice the mean size while maintaining their absorption and emission (Figure 4.8 and Table 4.3). We note that, in contrast to the large CdTe, CdSe remain smaller, more rectangular, and show emission from defects or other NCs after seeded growth (Figure 4.8) despite exploring how differing cadmium precursors may affect the growth (Figure 4.9). We found that short chain cadmium precursors work best for CdSe extension (similar to CdTe) and hypothesize that slightly differing synthetic procedures, higher nucleation barriers, and/or surface strain properties result in smaller CdSe NPLs.[40–42] In Figure 4.2b, we show representative TEM of the CdTe and CdSe NPLs after seeded growth as well as extended HgTe NPLs (additional TEM images used for counting are shown in Figure 4.10). Extended 2 and 3 ML CdTe can be isolated after seeded growth and introduced to a solution of mercury acetate dissolved in oleylamine at room temperature to yield large HgTe NPLs through a cation exchange process (further details in experimental section). This demonstrates that large CdTe NPLs are robust enough to undergo a complete cation exchange while maintaining their large-area morphology and thickness, giving access to mesoscale NIR-emissive NPLs (Figure 4.11).
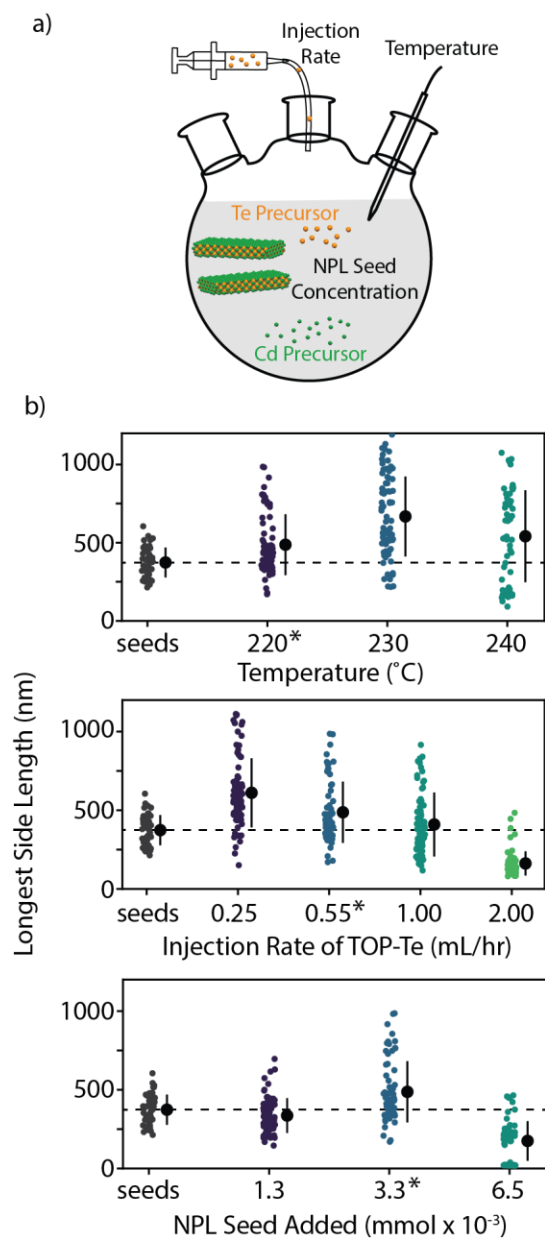
Figure 4.3. *a) Experimental diagram of explored reaction conditions and b) size distributions of the longest edge of 3 ML CdTe NPLs after seeded growth (measured from TEM images, Figure 4.12) compared to the seeds. Solid colored circles represent the counts for each size distribution, while the solid black circles show the mean and standard deviation of each condition explored. The dashed line represents the average size of the initial seeds. The (*) indicate control conditions when changing other variables independently.*

4.4 Experimental Parameters that Drive Seeded Growth

To demonstrate that the seeded growth process is necessary, we performed two control experiments—slow injection without seeds and fast injection with seeds—and both produced NPLs less than ~500 nm in size along with many 3D nanocrystals (Figure 4.13). We then hypothesized that the same parameters which govern 2D NPL nucleation and growth including temperature, injection rate, and precursor concentration are important for controlling size during seeded growth and can be tuned to optimize the procedure. [33,40,43] Additionally, these parameters are important for maintaining a regime of growth which outcompetes the critical supersaturation for nucleation and suppresses secondary nucleation.[33,44,45] We indeed find that the largest NPLs occur within a narrow range of optimized conditions and show how the experimental parameters of the slow injection seeded growth affect the extension in 3ML CdTe by isolating each variable individually (Figure 4.3). First, slightly elevated temperatures relative to the initial seed growth (3 ML CdTe initial seed growth is done at 210 ˚C) result in large extended NPLs, however this also results in a broadening of the size distribution. Beyond 230 ˚C, NPLs smaller than the seed NPLs nucleate during the growth (secondary nucleation). Temperatures below the initial seed temperature also nucleate smaller NPLs and produce a size distribution that has a lower mean size than the seeds (Figure 4.14). Second, the injection rate must be slowed significantly in order to favor large NPL growth (0.55 mL or 0.055 mmol/hr compared to 5mL or 0.25 mmol/hr in a typical 3 ML CdTe NPL synthesis), but must still be high enough to maintain the kinetic instability driving 2D growth.[40] Too slow of an injection rate (< 0.55 mL/hr of 0.1 M TOP-Te) forms many 3D agglomerates alongside the NPLs (Figure 4.12), while too fast (> 1 mL/hr) forms primarily secondary NPLs. Finally, the concentration of seeds affects the amount of edge sites for monomers to be added—too low results in few extended NPLs while too high results in clumps of large NPLs,

both of which lead to many secondary NPLs. The conditions that we use for further spectroscopic investigation are indicated by the (*) in Figure 4.3b.
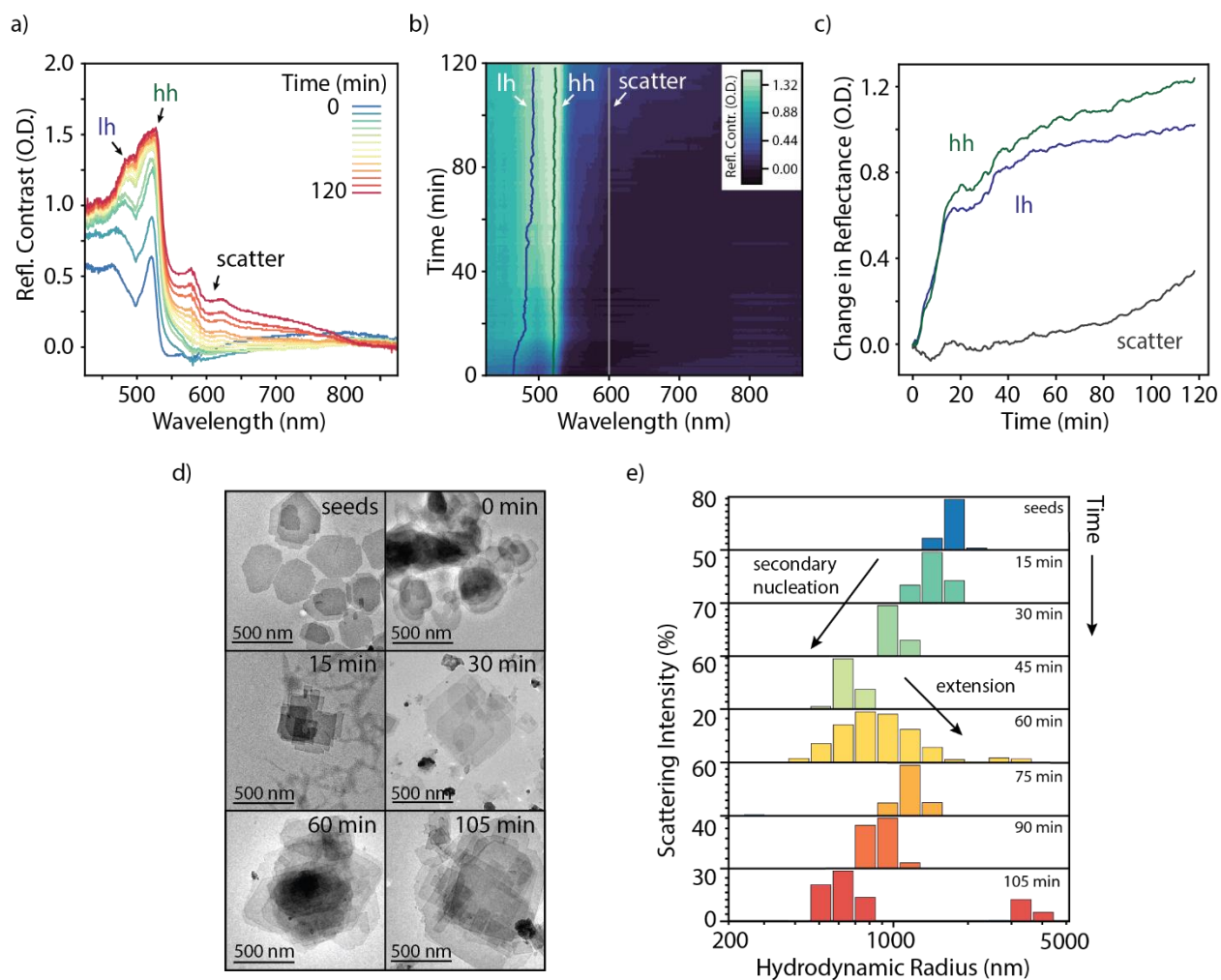
Figure 4.4. *a) Reflectance contrast collected in situ (data shown for every 10 minutes) for the duration of a seeded growth of 3 ML CdTe. b) The reflectance contrast change over time, sampled every 30 s with slices taken at the heavy hole (hh), light hole (lh), and 600 nm (scatter). c) The time slices are shown in more detail, highlighting the evolution of the excitonic transitions during seeded growth. d) TEM during early stages of growth starting with seeds before any precursor was added. e) Dynamic light scattering (DLS) of aliquots taken every 15 minutes during seeded growth of 3 ML CdTe.*

4.5 In-situ Investigation of Seeded Growth Mechanism

To understand how NPL growth is occurring during this process, we now explore the reaction dynamics as a function of time in Figure 4.4. We perform *in situ* and *ex situ* spectroscopy and microscopy on our optimized seeded growth reaction (0.55 mL/hr injection rate of 0.1 M TOP-Te at 220 ˚C). Using a reflectance probe to monitor changes in optical density (OD), we track changes in the light hole (lh) and heavy hole (hh) excitonic features as well as the scatter profile (at 600 nm) over the course of a 2 hr growth period (Figure 4.4a-b, more details in Figure 4.15). Their evolution is highlighted by taking slices of the spectra over time (Figure 4.4c). We interpret the increase in OD of the excitonic features to indicate the formation of new platelet area (either small secondary platelets or extension of the seeds), while we hypothesize that the scatter mostly informs about the formation of the larger platelet structures. We motivate our assignments by noting that scatter increases non-linearly with size of NPL, while absorption is proportional to the number of unit cells in the semiconductor—allowing us to distinguish between the two despite a lower concentration of large NPLs.[46] These assignments allow us to qualitatively follow the reaction as a function of time. We observe two major growth periods of the excitonic features—a rapid initial increase from 0-20 min and another smaller increase from 30-45 min. Beyond this point, the change in OD is slow and continual. The scatter profile at 600 nm shows an oscillatory behavior that appears anticorrelated to the excitonic features during the first hour. We also note the growth of thicker NPL species (indicated by absorption at 550 and 650 nm) after 60 min, but they are not as significant after the reaction is quenched and the nanoplatelets are centrifuged and resuspended. Thicker NPLs appear in relatively low concentration compared to the 3 ML NPLs (Figure 4.16).

To understand the morphological changes in the NPLs during seeded growth, we utilize TEM and dynamic light scattering (DLS) to track the populations of seeds and secondary NPLs during the reaction. In Figure 4.4d, we show TEM of the largest platelets during the stages of growth. Before any TOP-Te has been injected (0 min), there is a slight dissolution around the edges of the NPLs, which can explain the very slight loss of OD during the first few minutes. Once the injection has begun, however, we see the edges fill out and become rectangular. At 30 min, we observe secondary nucleation starting to occur alongside a noticeable extension in the larger NPLs. Interestingly, this extension does not appear to be continuous during the last 30 minutes—a nucleation burst of many small NPLs is noticeable by 45 min, and only after that burst are the largest NPLs formed (60 min).

The composition of seeds and secondary NPLs are homogenous, and we cannot use the excitonic features to distinguish between the two populations. To get an ensemble measure of NPL behavior, we use DLS (Figure 4.4e, more details in experimental section) to obtain insight into the change in total population, both small and large. This results in a relative size measurement that avoids counting bias and indicates the presence of multiple size distributions (Figure 4.4e). We note that the hydrodynamic radius is derived for a spherical particle and does not reflect the absolute size of the NPLs, but DLS has been used with good agreement to TEM sizes for small NPLs (~10-100 nm lateral sizes).[47–49] Our CdTe NPLs are laterally much larger so we do not expect quantitative agreement with TEM size as we do not correct for their greater anisotropy. We observe that from 0-45 min, the overall population distribution is decreasing in size, which is explained by the nucleation of secondary small NPLs. At 60 min, there is some scattering from larger particles, which coincides with the appearance of the ~1 μm NPLs. Continuing the growth beyond an hour continues with yet another nucleation burst of smaller NPLs, while it seems that

the large NPLs have reached a maximum size between 1000-1500 nm and do not continue to extend. The small secondary NPLs appear to become stable and large enough to extend themselves at this point, and reach ~500 nm by 2 hr (Figure 4.17)—limiting the maximum size of the larger seeded NPLs.

By connecting the results from reflectance, TEM, and DLS to describe what is occurring during the seeded growth process, we see stepwise or oscillatory changes in the spectra and size that correlate to secondary nucleation bursts followed by a slowed growth period which results in extension of the seed NPLs. This suggests that the lateral extension is not a continual addition of CdTe unit cells but rather can be explained through the balance of nucleation, growth, and ripening that has been described in the literature.[43,50–52] As discussed previously, a prerequisite for large lateral sizes appears to be the presence of seeds, slow injection and slightly elevated temperatures relative to original nanocrystal growth, further supporting that gradual buildup of monomer concentration and the presence of reactive edges allow for growth accompanied with periodic secondary nucleation. Other aspects of our results also support the understanding of lateral ripening— in a traditional fast injection NPL synthesis, the monomer would continue to be used up until the thinner NPLs are no longer stable, and dissolve onto the next thicker nuclei.[50] In our experiments, the constant injection of monomer maintains the high concentration and prevents major shifts towards thicker NPLs. Further supporting the dominant role of concentration and buildup, if we only consider amount of precursor added, rather than time, we see the stages occurring at certain concentration thresholds (Figures 4.18 and 4.19). This suggests a more dynamic control of concentration may be useful for generating even larger NPL structures.
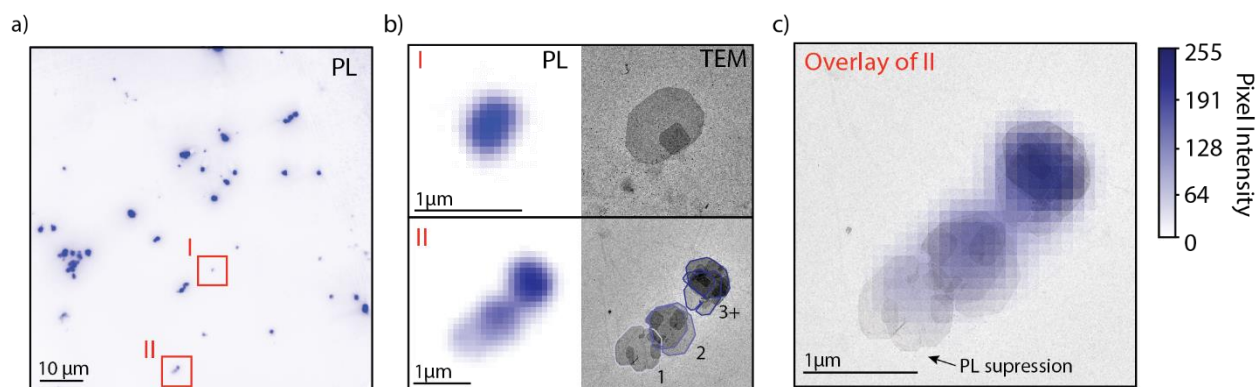
Figure 4.5. *a) Photoluminescence imaging of large 3 ML CdTe NPLs, showing a single NPL (I) and a group of NPLs (II). b) The TEM for spots (I) and (II) correlated to their PL, with the domains of 1, 2, and 3+ NPLs marked in (II). c) Overlayed PL and TEM for spot (II), showing spatial heterogeneity of PL in the single NPL, as well as the integer increase in pixel intensity as size of stack increases.*

4.6 Correlative Electron and Optical Microscopy of Mesoscale NPLs

We turn our efforts to microscopy to further study the photophysical properties of mesoscale NPLs. To confirm the presence of dispersed platelets, we perform correlative light and electron microscopy. Correlative imaging has been used previously on nanocrystals and 2D materials to study photophysical properties such as plasmonic behavior, catalysis, and defect emission in relation to their structure.[53–57] We adapt these methods here to perform photoluminescence (PL) mappings of our large NPLs. In Figure 4.5, we demonstrate that single NPL structures can be observed under conventional light and fluorescence microscopy (similar to their TMD counterparts). The lateral extent of our NPLs allows us to resolve PL beyond the point spread function and the entire NPL can be visualized with standard wide-field microscopy. This is advantageous for studying NPLs because confirming the isolation of single NPLs in the literature relies on resolving fluorescence blinking or single photon emission (through second order photon correlations)—properties of which may not be universal across different compositions and

sizes.[3,21] By imaging the PL over the entire NPL structure, we utilize a method that allows for further studies of singe crystal NPL dynamics.

To correlate light and electron microscopy, large NPLs obtained through seeded growth are diluted and drop cast onto a TEM grid with an alphanumerical reference pattern. The grid is then sealed between microscope slides and the PL is imaged using an inverted microscope equipped with an sCMOS camera (more details in Figure 4.6). Figure 4.5a shows the PL for a square within the grid, along with closeups (Figure 4.5b spots (I) and (II)) correlated to TEM images. The image alignment process is described in Figure 4.20, along with an additional example of correlation with the same methods applied. We can resolve the entire structure of a single NPL that is bright and does not contain any large tears (Figure 4.5b, (I)), and we also examine a set of NPLs (Figure 4.5b (II)) to study defects and NPL stacking.

For image (II), when the PL and TEM images are overlayed (Figure 4.5c), we observe spatial heterogeneity within the lower, single NPL. The lower half of the NPL is non-emissive and may be defective from the large tear. A closer examination (Figure 4.21) shows that PL is suppressed around the edges and what we hypothesize is a screw dislocation. The PL suppression could also be due to quenching from energy transfer that arises from proximity of the multiple large NPL stack.[58] As additional demonstrations of our NPL imaging technique, the number of NPLs within a stack can be resolved using the intensity of the imaged PL (Figure 4.5b-c), as shown by the near integer increase in the intensity that correlates to 1, 2, and 3+ NPLs —confirmed by TEM. We collect PL lifetimes and observe variability depending on the number of NPLs within isolated stacks (Figure 4.22). With increasing number of NPLs the average lifetime decreases, which is consistent with a change in nonradiative pathways due to energy transfer amongst the stack and the increased likelihood of exciton trapping by a nonemissive NPL.[58,59]

Overall, the observation of lateral heterogeneity in PL draws comparison to 2D semiconductors where this can be demonstrated from many effects including defects, strain, chemical heterogeneity, and manipulation by 0D-2D heterostructures.[60–67] These vdW materials exhibit localized electronic structure changes that do not quench the entire nanostructure and can be spatially resolved through PL mapping. The heterogeneity of PL in our large NPLs contrasts them with smaller NPLs which have not demonstrated this behavior. Direct application into single crystal devices will allow for further studies of mesoscale NPL properties.

4.7 Conclusions

We demonstrate the controlled growth of mesoscale II-VI semiconductor NPLs which reach areas up to 2.25×10^6 nm^2 for the first time. We confirm our understanding of NPL growth by applying the parameters that drive 2D extension towards the development of a seeded growth process for CdTe NPLs. *In situ* methods allow us to study the competing growth between secondary nucleation and lateral extension during this process. We also show that this seeded growth procedure can be applied to NPLs of different thicknesses and compositions, with large extensions in 2-3 ML CdTe (as well as HgTe after cation exchange) and limited extension in 3-5 ML CdSe. These mesoscale NPLs have large areas while maintaining thickness confinement that allow them to uniquely contain properties of both quantum dots and 2D materials, showing promise in single nanocrystal devices. In contrast to more traditional 2D materials, these NPLs are amenable to the wide variety of colloidal synthetic techniques (cation exchange and crown/shell growth, ligand exchanges, *etc*.) to develop new and interesting interfaces and may benefit from improved electronic properties through surface ligand protection. Finally, their lateral sizes allow us to apply a method of PL imaging across the entire NPL and correlate it to structure via TEM. Through this method we isolate single NPLs and show that mesoscale NPLs have properties

similar to 2D semiconductors—demonstrating a new class of material to bridge the gap between quantum-confined nanocrystals and 2D materials.

4.8 Experimental Details

Cadmium acetate dihydrate (Acros, 98%), selenium powder (Acros, 99.5%), tellurium powder (Acros, 99.8%), cadmium oxide (Alfa Aesar, 99.95%), cadmium bromide tetrahydrate (Acros, 98%) oleic acid (Alfa Aesar, 99%), tri-n-octylphosphine (TOP) (Alfa Aesar, 90%), 1-octadecene (ODE) (Alfa Aesar, 90%), mercury (II) acetate (Chem-Impax International, 98.0%), ethanol (Fisher, 95.27%), hexanes (Fisher, 98.5%), toluene (Alpha Aesar, 99.8%), propionic acid (Fisher), and oleylamine (Tokyo Chemical, 50.0%) were used.

Synthesis of Precursors

Cadmium propionate (Cd(prop)$_2$). 1.036 g of CdO powder was mixed with 10 mL propionic acid under Argon flow for 1 hour. The flask was then heated at 140 ˚C after opening to atmosphere in order to reduce the volume by half. The white solution was precipitated with acetone and centrifuged. The supernatant was discarded, and the solid was dried and stored in a vacuum desiccator.

TOP-Te (1 M). Following Izquierdo *et al*.,[4] In a small flask, 0.254 g of Te powder and 2 mL of tri-n-octylphosphine (TOP) were degassed under vacuum at room temperature. Then, under Argon flow, the solution was stirred at 275 ˚C until the dissolution was complete, and the solution turned yellow. The solution was cooled and stored under Argon.

TOP-Se (1M). Following Izquierdo *et al*.,[4] 0.144 g of Se powder and 2 mL of tri-n-octylphosphine (TOP) were stirred at room temperature under Argon flow until dissolved to form a clear solution. The solution was stored under Argon.

2 Monolayer CdTe Seed Nanoplatelets. Following Pedetti *et al.*,[4,17] 170 mg cadmium propionate, 104 μL oleic acid, and 10 mL octadecene (ODE) were degassed for 1 hr at 90 °C. Under Argon flow, the temperature was increased to 180 °C and 130 μL of 1 M TOP-Te diluted in 650 μL ODE was swiftly injected. After 20 minutes, 1 mL of oleic acid was added, and the reaction was cooled to room temperature. The crude mixture was precipitated with ethanol and centrifuged twice, then resuspended in 10 mL hexanes.

3 Monolayer CdTe Seed Nanoplatelets (slow injection). Adapted from Izquierdo *et al.*,[4,5] 260 mg of cadmium propionate, 160 μL of oleic acid, and 20 mL of ODE were degassed under vacuum at 90 °C for 1 hr. Under Argon flow, the reaction was heated to 210 °C and 0.200 mL of 1M TOP-Te mixed with 3.75 mL of octadecene was injected with a syringe pump at a rate of 5 mL/hr. Once the injection was complete, 0.500 mL of oleic acid was injected and the solution was cooled to room temperature. The nanoplatelets were precipitated with 15 mL hexanes and 15 mL ethanol, centrifuged, and resuspended in 20 mL hexanes. Assuming that the reaction goes to completion, the 3 ML NPL solution will contain a total of 0.2 mmol of Te and 0.26 mmol of Cd in the NPLs, giving a concentration of 13mM total cadmium in the NPL seed solution.[4]

3 Monolayer CdSe Seed Nanoplatelets (slow injection). Adapted from Izquierdo *et al.*,[4,5] 240 mg of cadmium acetate dihydrate, 0.150 mL of oleic acid and 15 mL of ODE were degassed under vacuum at 80 °C for 1 hr. Under Argon flow, the reaction was heated to 195 °C and 0.4 mL of 1M TOP-Se mixed with 3.75 mL ODE was injected with a syringe pump at a rate of 5 mL/hr. Once the injection was complete, the solution was cooled to room temperature and the nanoplatelets were precipitated with 15 mL hexanes and 15mL ethanol, centrifuged, and resuspended in 20 mL of hexanes.

4 Monolayer CdSe Seed Nanoplatelets. Following Pedetti *et al.*,[27] 340 mg cadmium myristate, 24 mg Se powder, and 30 mL ODE were degassed for 20 minutes at room temperature. The temperature was then increased to 240 °C under Argon flow. When it reached 205 °C, 80 mg of cadmium acetate were added, and the solution turned red. Then when the solution reached 240 °C it was left to react for 12 minutes followed by the addition of 2 mL oleic acid and rapid cooling to room temperature. The crude reaction mixture was added to 30 mL hexanes and 40 mL ethanol and centrifuged at 6000 rpm for 10 min, followed by a resuspension in 10 mL hexanes.

5 Monolayer CdSe Seed Nanoplatelets. Following Pedetti *et al*,[27] 340 mg cadmium myristate and 28 mL ODE were degassed for 20 min at room temperature. Under Argon flow, the solution was heated to 250 °C at which point 24 mg of Se powder suspended in 2 mL ODE was swiftly injected. After 30 s, 300 mg of cadmium acetate was also added. The reaction was held at 250 °C for an additional 7 min, followed by the addition of 1 mL oleic acid and rapid cooling to room temperature. The crude reaction mixture was added to 30 mL hexanes and 40 mL ethanol and centrifuged at 6000 rpm for 10 min, followed by a resuspension in 10 mL hexanes. Further purification was done by adding 1:4 ethanol to hexanes and centrifuging at 6000 rpm.

Seeded Growth

In a three-neck round bottom flask, 65 mg of cadmium propionate (0.25 mmol), 0.040 mL of oleic acid, and 5 mL of octadecene were degassed under vacuum at 80 ˚C for 20 min. Under Ar flow, the solution was heated to a target growth temperature between 200-260 ˚C depending on the thickness (see Table S1) and 0.250 mL of ~13 mM CdX seeds in hexanes were injected when the temperature reached 200 ˚C. The concentration of the seed solutions varies with each synthesis, so the concentration of each was adjusted by measuring the optical density (OD) of the heavy hole relative to the 13 mM CdTe heavy hole OD. Once at the final growth temperature (Table S1), a

solution of 0.050 mL of 1 M TOP-X (X = Te for CdTe and Se for CdSe) mixed with 0.500 mL of ODE was injected with a syringe pump at 0.55 mL/hr. Immediately after the injection was complete, 0.250 mL of oleic acid was injected, and the solution was cooled. The nanoplatelets were then centrifuged at 9000 rpm for 5 min and resuspended in 10 mL hexanes.

Cation Exchange

In a round-bottom flask, 0.240 mL of large CdTe NPLs in hexanes (without further dilution from seeded growth, the concentration will have a maximum of 7.3 mM Cd in the NPLs) and 6.0 mL of hexanes were mixed. Then, 0.600 mL of 10 mM $Hg(OAc)_2$ in oleylamine was added and stirred at room temperature for 3.5 hr, monitored by the absorption of the light and heavy holes. The HgTe absorption spectra stopped changing by 3.5 hr and the heavy hole optical density was greater than the light hole, upon which point the reaction is considered complete.[4] Once complete, the nanoplatelets were then centrifuged at 9000 rpm for 5 minutes and resuspended in 5 mL hexanes.

Characterization

Absorption spectra were acquired with an Agilent Cary 60 UV-Vis spectrophotometer. Photoluminescence (PL) was collected using an Ocean Optics Flame-S-VIS-NIR-ES Spectrometer and a Horiba Scientific PTI QuantaMaster400 Spectrometer. Quantum Yield measurements were collected using an integrating sphere. Reflectance measurements were collected using an Ocean Insight QR200-12-MIXED reflectance probe and an Avantes DH-2000 UV-VIS-NIR light source. Dynamic light scattering (DLS) was collected using a Coulter Beckman Dynamic Light Scattering Analyzer – N4 Plus at an angle of 62.6 degrees.

Transmission electron microscopy (TEM) images were acquired with a FEI Tecnai T12 120kV TEM. The nanoplatelets were diluted in hexanes and drop casted on Ted Pella, Inc. carbon/formvar 300 mesh copper grids.

Photoluminescence imaging experiments were conducted on a home-built optical microscope. All NPLs were excited using a 405 nm pulsed diode laser (LDH-P-C-405 PicoQuant) with a power of 0.15 microwatts. The NPL sample slide is fixed to a piezo stage (Mad City Labs Nano-View/M 200-3), and the epifluorescence is sent through a 100x oil objective (Nikon MRD01905) and filtered using a 425 nm long pass dichroic filter. Wide-field images were collected using an sCMOS camera (Zyla sCMOS, Andor) (Figure S1b). Acquisition time was on average 10s.

For time correlated single photon counting, all NPLs were excited using a 405 nm pulsed diode laser. For NPLs on TEM grids, epifluorescence of the sample was collected through the microscope using a 100x objective (Nikon MRD01905). The laser was filtered using a 425 nm long pass filter and the emission was then focused onto an avalanche photodiode (APD, PD050-CTD, Micro Photon Devices). Photon streams were timed by a HydraHarp 400 (Picoquant) in Time-Tagged Time-Resolved (TTTR) mode. For NPLs in solution, these measurements were collected using superconducting nanowire single-photon detectors (SNSPDs), due to shorter instrument response functions at 405 nm.

4.9 Supporting Information.

This section contains additional experimental details, additional characterization including absorption and photoluminescence, TEM, reflectance, and photoluminescence lifetimes.

Additional Experimental Details

Table 4.1. *Full synthetic parameters for seeded growth of CdX nanoplatelets*

Thickness	Composition	Temperature of seeded growth	Chalcogen Precursor	Injection Rate
2	CdTe	190 ˚C	0.050 mL of 1M TOP-Te diluted in 0.5 mL ODE	0.55 mL /hr
3	CdTe	220 ˚C *	0.050 mL of 1M TOP-Te diluted in 0.5 mL ODE	0.55 mL /hr *
3	CdSe	205 ˚C	0.050 mL of 1M TOP-Se diluted in 0.5 mL ODE	0.55 mL /hr
4	CdSe	250 ˚C	0.050 mL of 1M TOP-Se diluted in 0.5 mL ODE	0.55 mL /hr
5	CdSe	260 ˚C	0.050 mL of 1M TOP-Se diluted in 0.5 mL ODE	0.55 mL /hr

* Both temperature and injection rate were varied for 3ML CdTe as shown in Figure 4.3. Here we report the conditions that gave optimal results.
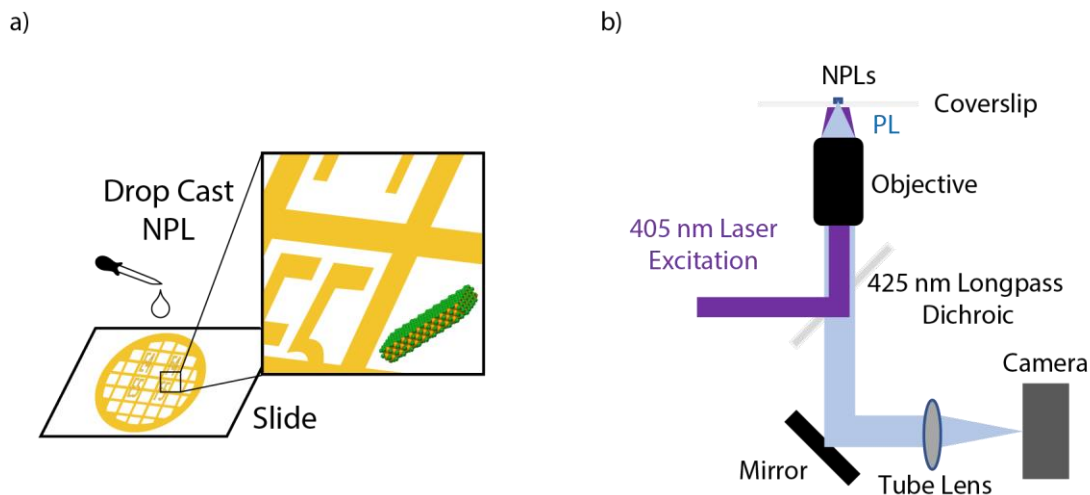
Figure 4.6. a) Sample preparation for correlative TEM. b) Schematic of optical microscope and imaging process.

Photoluminescence Imaging Sample Preparation

Large nanoplatelets (NPLs) were isolated after the seeded growth process, diluted in hexanes until the hh absorbance was below 0.1 O.D, then further diluted to optimize seperation of particles. They were then drop cast onto an alphanumerically patterned carbon/formvar TEM grid, dried, and then epoxy-sealed between microscope slides under N_2 (Figure 4.6a).
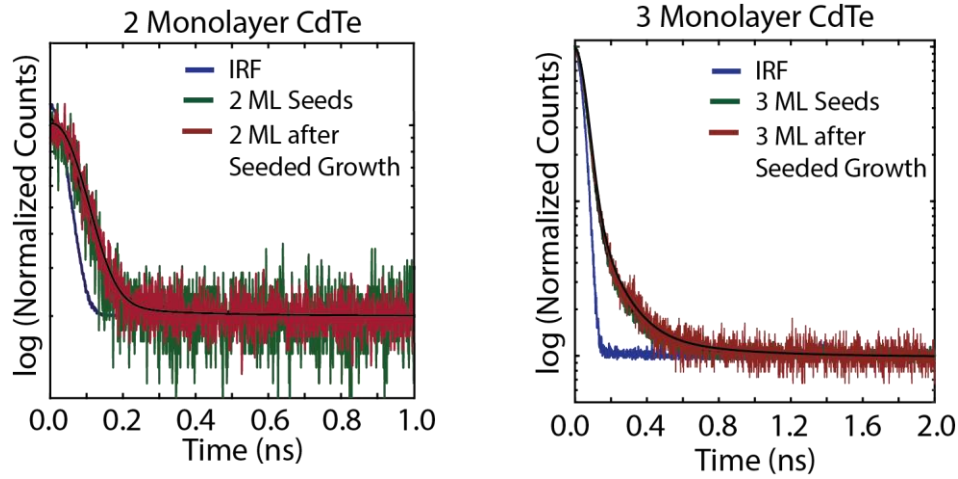
Figure 4.7. *The photoluminescence lifetimes of NPLs before and after seeded growth, shown with their fit lines.*

The solution ensemble lifetimes for NPLs before and after seeded growth are shown in Figure 4.7. A three exponential fit was used and the average lifetime was calculated using Equation 4.1.[68,69]

$$\bar{\tau} = \frac{\alpha_1\tau_1 + \alpha_2\tau_2 + \alpha_3\tau_3}{\alpha_1 + \alpha_2 + \alpha_3} \qquad\qquad (4.1)$$

Table 4.2. *The measured lifetimes and resulting fit for CdTe NPLs before and after seeded growth in solution ensemble.*

Sample	A	$\frac{1}{\tau}$ (ns^{-1})	τ(ns)	Amplitude (%)	Fit R-square	Average Lifetime (ps)
2 ML NPL seeds	3.039	42.75	0.02339	84.85		
					0.7175	33
	0.5105	37.06	0.02698	14.25		
	0.0320	2.927	0.3416	0.89		
2 ML NPLs after seeded growth	1.8900	34.93	0.02863	75.67		
					0.8802	34
	0.5932	35.18	0.02843	23.75		
	0.0144	4.322	0.2314	0.58		

3 ML NPL seeds	1.771	34.06	0.02936	96.32		
	0.0671				0.9997	27
		8.019	0.1247	3.65		
	0.0006195	0.9964	1.004	0.03		
3 ML NPLs after seeded growth	1.83	33.64	0.02973	95.72		
					0.9983	30
	0.07887	8.36	0.1196	4.13		
	0.002977	2	0.5000	0.16		
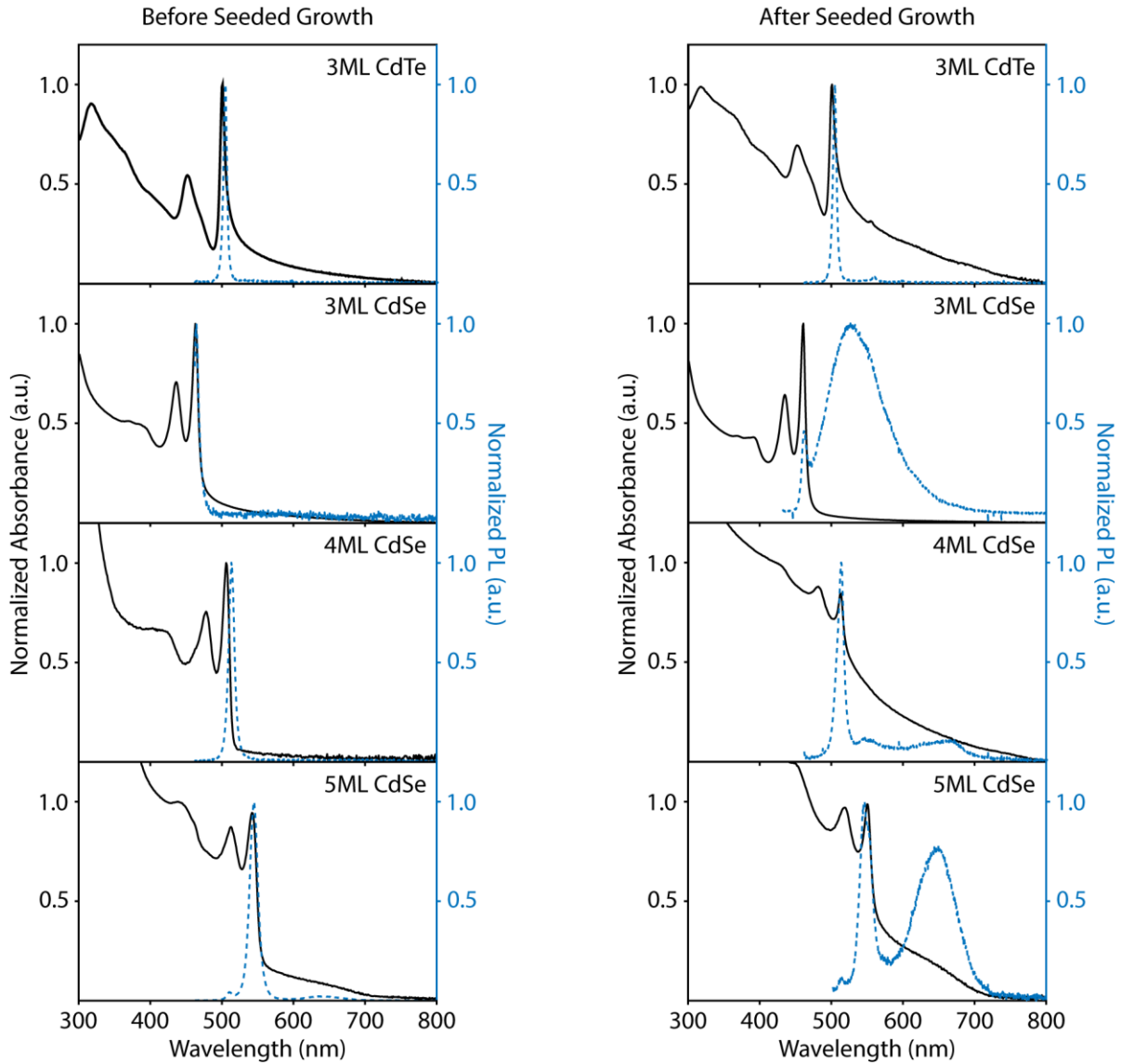
Figure 4.8. *Normalized absorption (black) and photoluminescence (blue) before and after seeded growth for CdTe and CdSe NPLs.*

For all compositions and thicknesses, the absorbance and photoluminescence (PL) are maintained before and after seeded growth. In general, the amount of scatter in the absorption increases after seeded growth but the excitonic features are still present with only minor contributions from thicker NPLs that may have formed through ripening.

Cadmium myristate	Cadmium propionate	Cadmium acetate
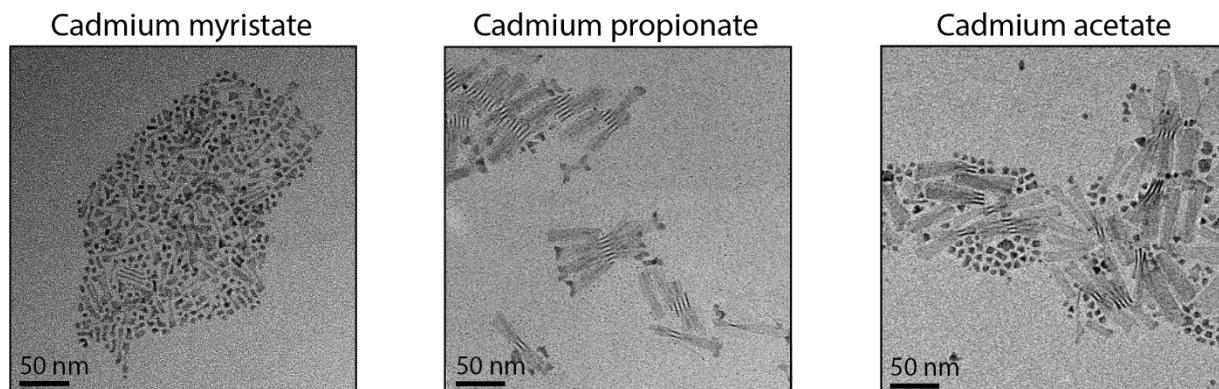
Figure 4.9. *TEM showing 4 ML CdSe NPLs extended through seeded growth using cadmium myristate, cadmium propionate, and cadmium acetate as the cadmium sources.*

The synthesis utilized for CdSe NPL seeds uses cadmium myristate and cadmium acetate as precursors during the fast injection. CdTe NPLs are synthesized using cadmium propionate, so we explored how the cadmium precursor affects the extension of CdSe. We found that shorter chain cadmium precursors give the greatest extension, with cadmium propionate and acetate giving similar lateral lengths between 50-100 nm.

a)
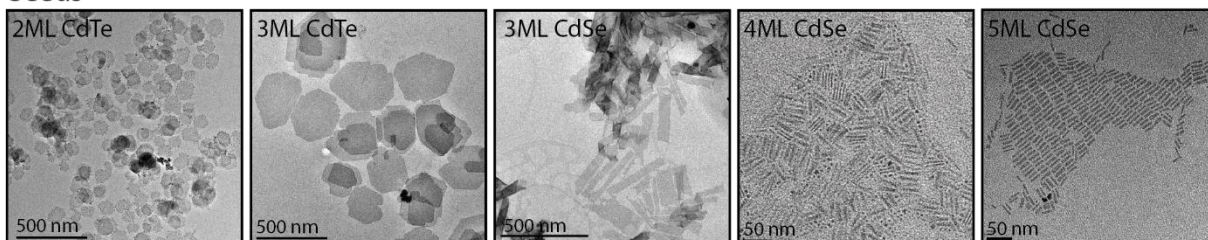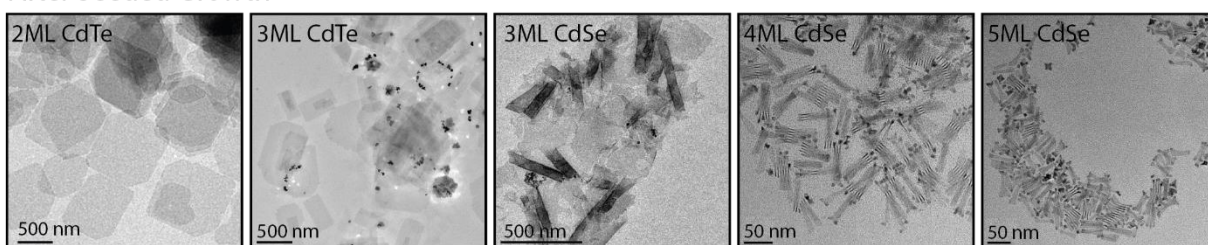
b)
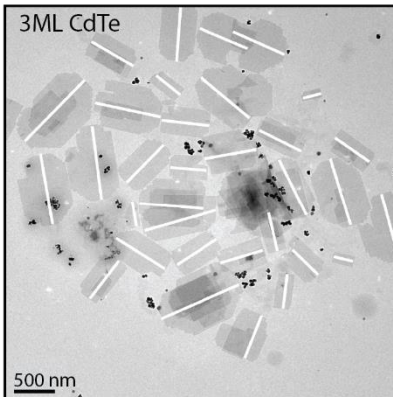
Figure 4.10. *Additional representative TEM images used during the counting of sizes a) before and after seeded growth and b) example image showing measurements of longest side lengths (white lines) for clearly visible NPLs.*

Figure 4.10a shows exemplary TEM images used for counting the size distribution of NPLs before and after growth. For 3ML CdSe, the NPLs curl due to strain so in order to measure the side lengths, they were unrolled using CdBr$_2$ and oleylamine as described in Dufour et al.[70] For all

samples, each image was counted using ImageJ by including length measurements (longest side) of all NPLs with discernable edges while those in large stacks were avoided (example in Figure 4.10b).

Size Counting Results Before and After Seeded Growth

Table 4.3. *The results of NPL size counting*

	Before Seeded Growth				After Seeded Growth			
	N	$\bar{X}$	σ	S^2	$\sigma_{\bar{X}}$	N	$\bar{X}$	σ	S^2	$\sigma_{\bar{X}}$
2 ML CdTe	66	93.3	17.0	290	2.1	51	942	176	31000	25
3 ML CdTe	61	367	83.7	7000	11	46	627	208	43200	31
3 ML CdSe	58	134	27.4	750	3.6	53	320	134	17900	18
4 ML CdSe	73	29.2	3.63	13.2	0.42	64	62.6	11	124	1.4
5 ML CdSe	272	22.0	2.81	7.91	0.170	62	46.6	8	65	1.0

To find the mean size before and after seeded growth we used TEM images described in Figure 4.10 to tabulate the longest side lengths for all NPLs before and after seeded growth. The results are shown in Table 4.3 where N is the sample size, $\bar{X}$ is the sample mean, σ is the standard deviation, S^2 is the variance, and $\sigma_{\bar{X}}$ is the standard error of the mean.

Figure 4.11. *a) Absorption spectra before (black) and after (blue) cation exchange from CdTe to HgTe showing complete exchange, and b) TEM showing that the large area morphology is maintained.*

Cation exchange from large CdTe NPLs (extended through seeded growth) to HgTe NPLs shows that the lateral dimensions are preserved throughout the reaction (Figure 4.11). In 2 ML NPLs, some 3 ML impurities are present along with HgTe quantum dot growth that occurs at room temperature under the cation exchange conditions.[6]
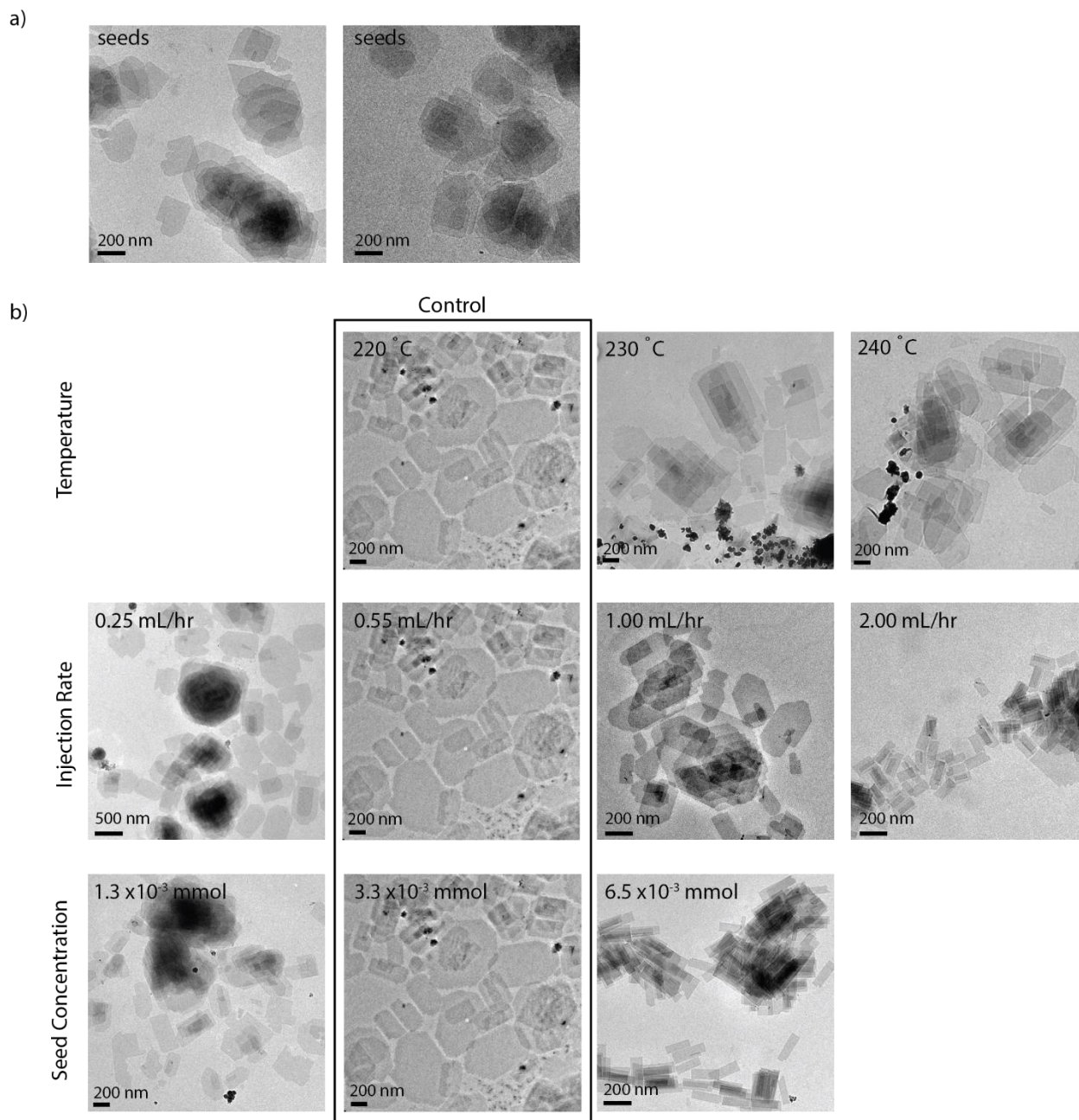
Figure 4.12. *a) 3 ML CdTe Seeds and b) the growth parameters explored for the seeded growth of 3 ML CdTe seeds.*

Figure 4.12a shows the 3 ML CdTe seeds used, while Figure 4.12b shows the TEM of different parameters explored in Figure 4.3. The control conditions are seeded growth at 220 ˚C,

using 3.3×10^{-3} mmol of seeds, and an injection of 0.55 mL 0.1M TOP-Te at a rate of 0.55 mL/hr. For example, while changing temperature, injection rate and concentration were held constant and vice versa for the other parameters. For injection rate, the volume injected (and thus total mmol delivered) was 0.55 mL for each case.

a) seeded growth conditions without NPL seeds present
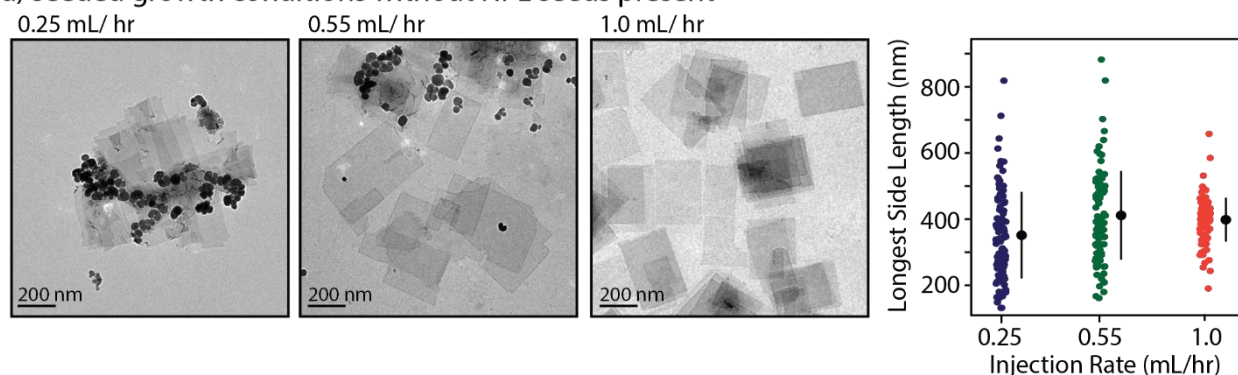
b) fast injection with NPL seeds present
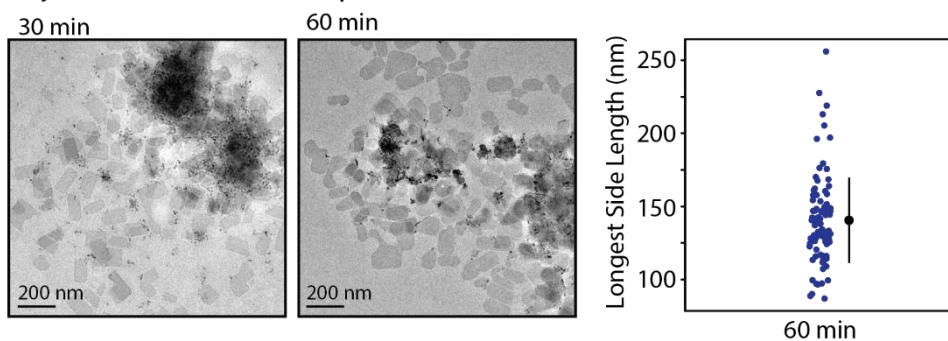
c) heating NPLs without TOP-Te injection
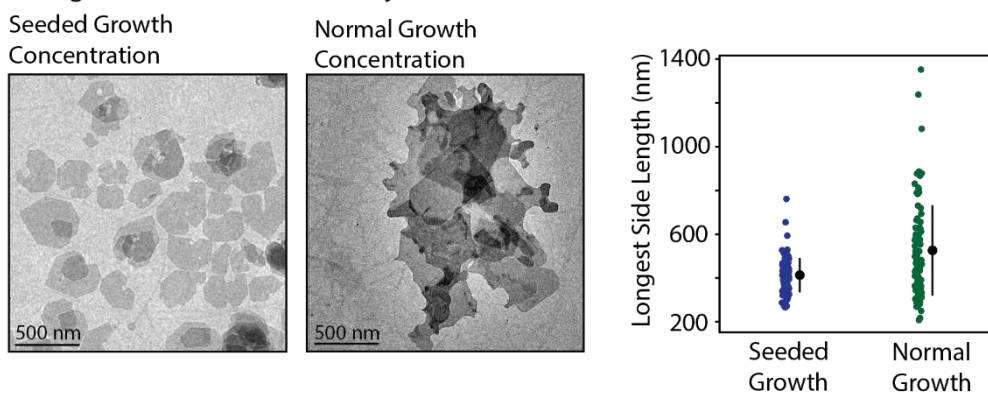
Figure 4.13. *TEM showing NPLs a) grown using slow injection of TOP-Te without any seeds, and b) grown with fast injection of TOP-Te and seeds.*

To determine that a slow seeded growth is necessary for the growth of large area NPLs, we performed two control experiments: a growth without any seeds under slow injection conditions and a growth with seeds but using a fast injection of the TOP-Te. The fast injection was left at the

163

growth temperature for 1 hr to mimic the normal seeded growth conditions. None of these reactions yielded NPLs larger than the average size grown without seeds and under normal CdTe NPL growth conditions (~500 nm). Finally, we explored whether extension could be achieved through ripening amongst just the seeds (without TOP-Te injection) by first performing the seeded growth experiment without any TOP-Te injection, and second by performing a normal 3 ML CdTe synthesis and holding the solution at elevated temperature (220 °C) for 1 hr after completion without further injection. In both cases we find that some extension occurs but produces NPLs with irregular edges (due to dissolution) suggesting that while lateral ripening is occurring, seeded growth with additional monomer addition will produce NPLs with cleaner edges.
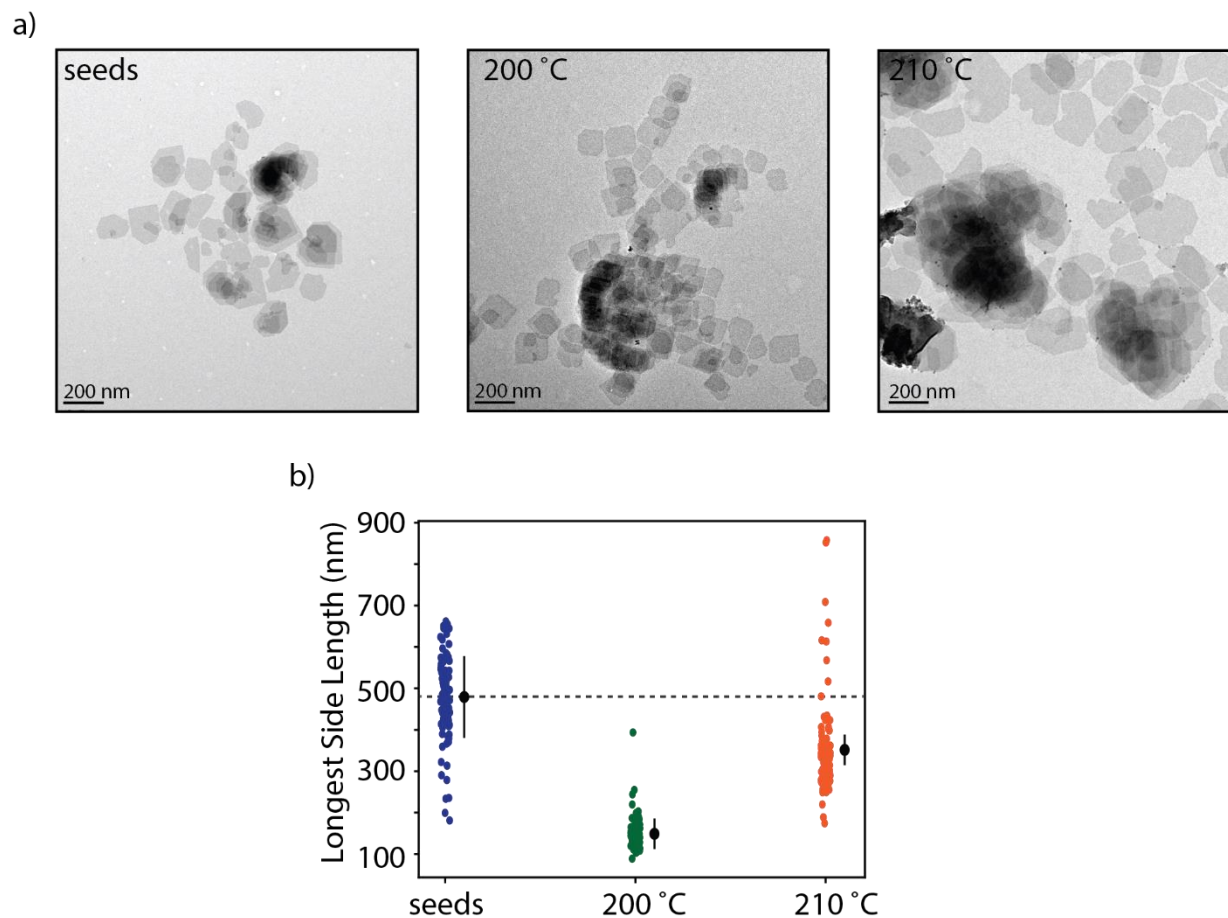
Figure 4.14. *TEM images of NPLs a) before seeded growth (seeds), after seeded growth at 200 ˚C and 210 ˚C, and b) the corresponding size distributions determined by counting the longest edge of NPLs within their TEM images. The solid black circles represent the mean and standard deviation of the distribution.*
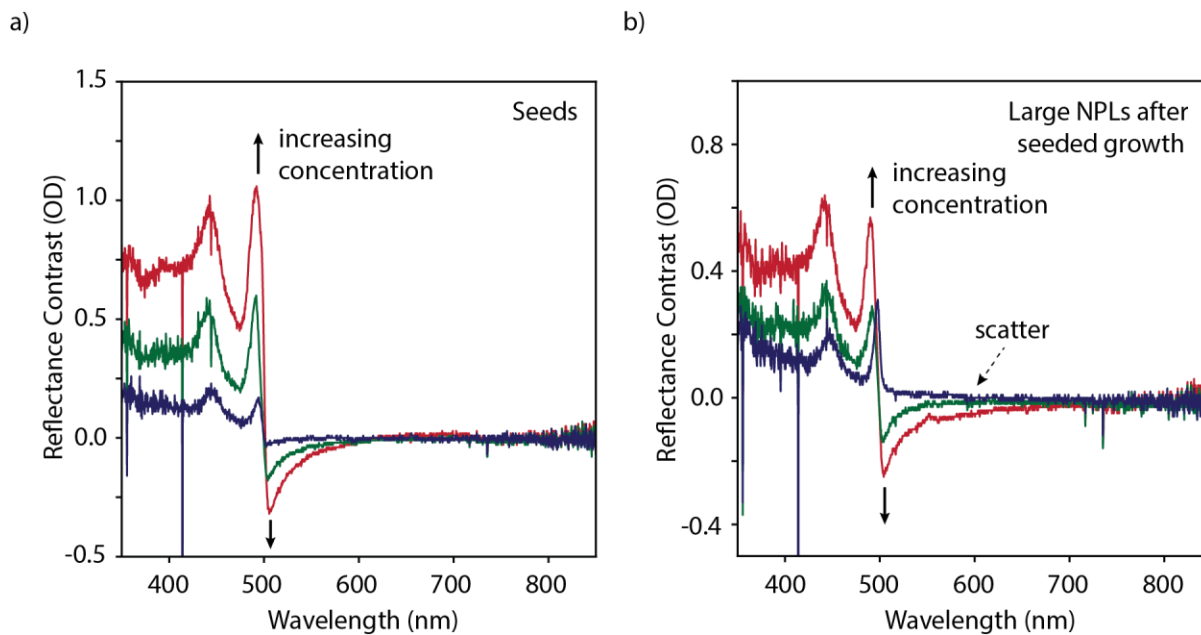
Figure 4.15. *Reflectance contrast of a) seed and b) large NPLs after seeded growth solutions at dilute (blue) and increasing (green and red) concentrations.*

When using the in-situ reflectance probe to monitor the seeded growth reaction progress, we noticed the reflectance contrast reached negative values in the spectral region just after 500 nm. We believe this effect to be a result of the change in refractive index of the media as the solution becomes heavily concentrated with CdX. We tested the reflectance of a room temperature solution of NPLs with increasing concentration for both seeds and large NPLs (Figure 4.15), demonstrating that this is not a size effect but rather from overall the concentration. We observe the scatter at 600 nm to reduce the interference of this with our analysis of NPL growth.
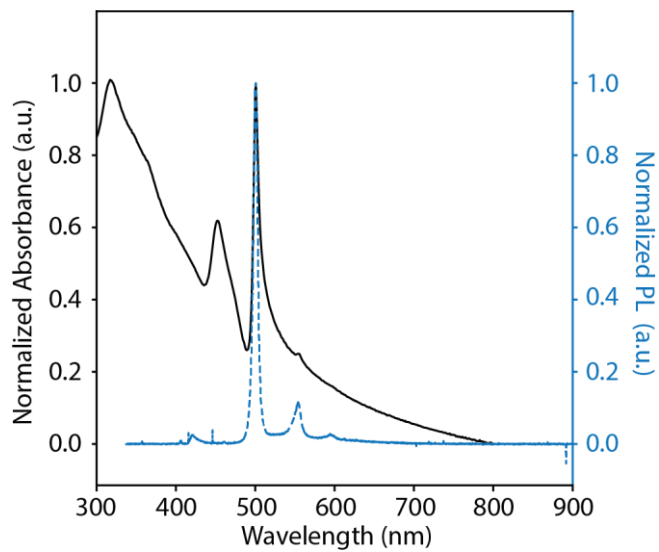
Figure 4.16. *Absorbance (black solid line) and photoluminescence (PL, blue dashed line) after post-synthetic centrifugation and resuspension.*

TEM after Prolonged Seeded Growth (2hr)
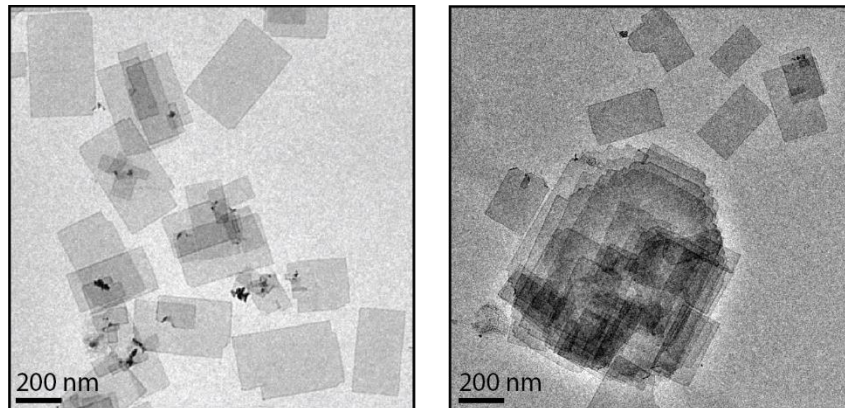
Figure 4.17. *TEM images showing NPLs after an extended 120 min of TOP-Te injection.*

When TOP-Te is injected beyond 1hr (isolated after 120 min in Figure 4.17), we observe that the NPLs from secondary nucleation have begun to extend (~500 nm) and have regular rectangular edges. The large seeded NPLs maintain their size at around 1000 nm and do not continue to extend.

Reflectance Contrast for all Injection Rates Explored
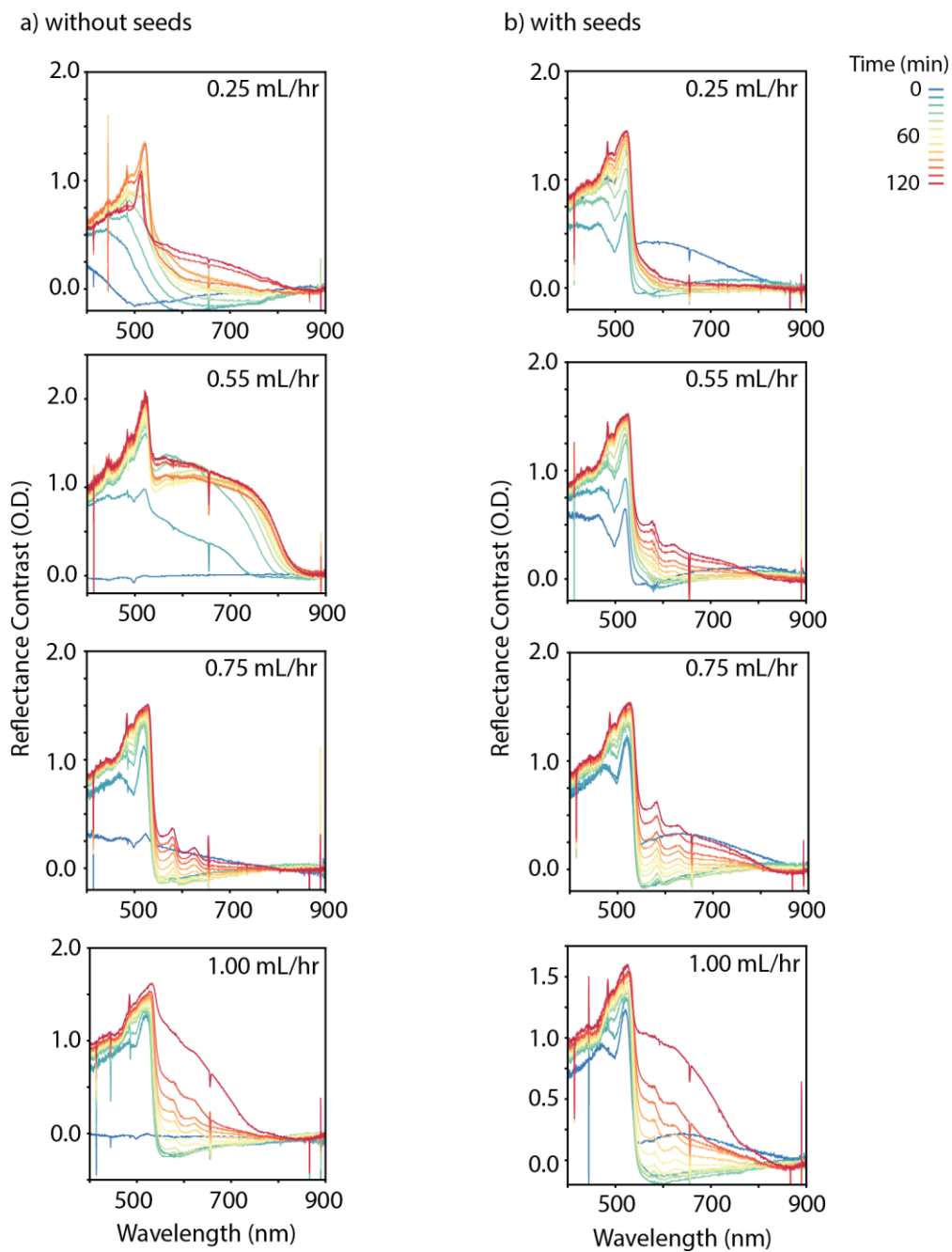
Figure 4.18. *In-situ reflectance for slow injection syntheses a) without seeds and b) with seeds for varying injection rates. The injection was performed over 2 hours total, delivering increasing volumes of TOP-Te chalcogen with increasing injection rate.*

Reflectance Slices for all Injection Rates Explored
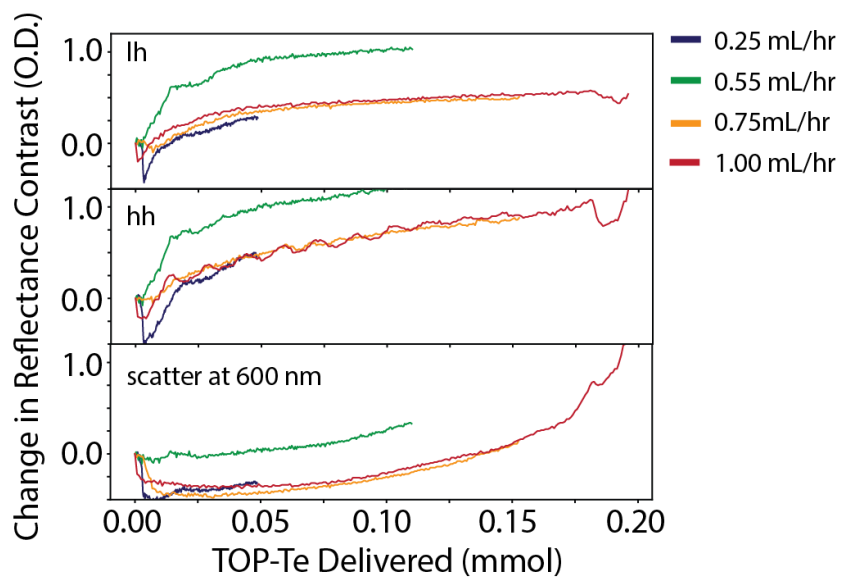
Figure 4.19. Slices taken from the in-situ reflectance contrast spectra collected for seeded growths at varying injection rates, compared by mmol of Te delivered. The light hole (lh), heavy hole (hh) and scatter features are shown.

a)

b)
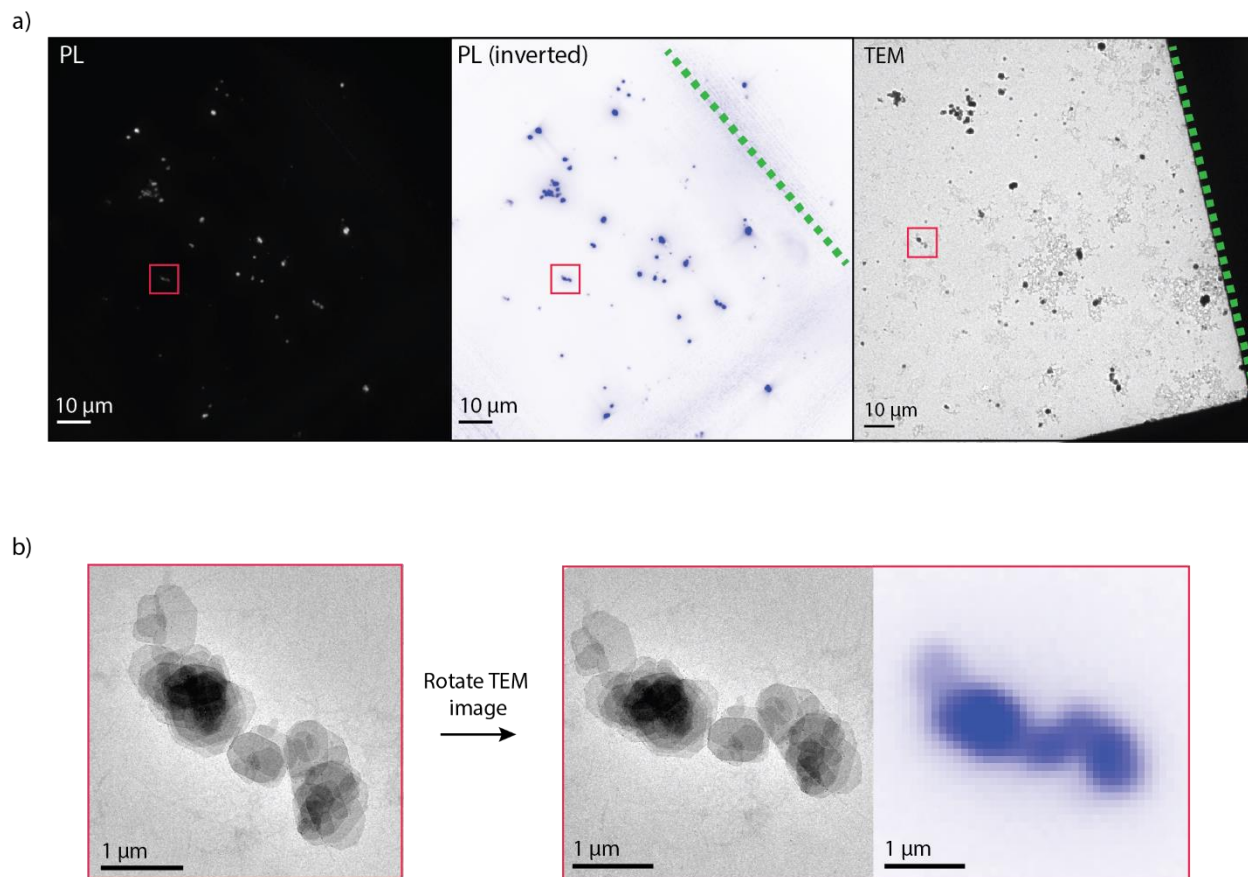
Figure 4.20. *a) PL and correlated TEM images, highlighting a group on NPLs that are imaged in higher magnification and b) rotated to align with a closeup of the PL image.*

The PL images were obtained using a 100x objective (shown in Figure 4.20a) and inverted to more easily see the NPLs. When TEM is taken of the same spot on the grid (correlated using alphanumeric indexing), the features are easily identifiable. Higher magnification TEM images (Figure 4.20b) are taken of these identifiable spots and aligned to the PL image. The scale of the PL images is set as 100 nm/pixel (measured by calibration to translation of the piezostage) and the TEM image is resized to match. The angle of rotation is found using the edges of the grid and the TEM images are rotated to align to the PL image—here a 22 degree difference (shown in Figure 4.20a, dashed green lines).

To overlay the images, the PL and TEM images shown in Figure 4.5 were imported into MATLAB. The colored images were converted to greyscale to save computational cost. A custom function was written to systematically vary the relative offset position and to calculate the summed difference in intensity between the PL and TEM images. The indices of the offset position that produced the minimal difference was incorporated into creating the overlap image seen in Figure 4.5c.

Figure 4.21. *Comparison of PL and TEM images for single and 3+ NPLs mentioned in manuscript (Figure 4.5) to show difference between the PL image and expected PL (i.e. Blurred TEM). a) Left: Grey scale and normalized PL image. Center: Blurred TEM image matching camera resolution. Right: TEM image as reported on manuscript. b) same as (a) but for 3+ NPLs.*

In Figure 4.21, we demonstrate the difference between measured PL and blurred TEM, which is representative of the expected PL assuming that every point on the NPL surface is emissive. In other words, the blurred image is what one would expect to see when assuming that the PL is homogeneous across the NPL surface, with no local heterogeneity. Both blurred TEM images were created by applying an intensity filter to isolate the edges, a Gaussian blur with the measured camera resolution (~100 nm/pixel), and pixilation to match the PL images.

From this image analysis process, we observe two things from the comparison between the PL and the blurred TEM images. First, the PL spans a generally smaller area, indicating that the PL is suppressed at the edges. Second, there appears to be local suppression near screw dislocations,

although it is difficult to tell the difference between a screw and an overlap of small NPLs. Together, these effects highlight the heterogeneity of the NPLs PL, which could suggest surface defects as a dominant source of PL suppression.

Photoluminescence Lifetimes Results

The photoluminescence lifetime results are shown in Figure 4.22 for three different NPL samples: solution ensemble measurement, a stack of ~6 NPLs, and a larger stack of ~10 NPLs both collected from a spot of NPLs deposited on the TEM grid. To approximate the number of NPLs within each stack, ImageJ was used to trace the intensity profile of the TEM image and the maximum intensity at the thickest point was divided by the intensity of the single NPLs along the edges.

A three exponential fit was used and the average lifetime was calculated using Equation 4.1.
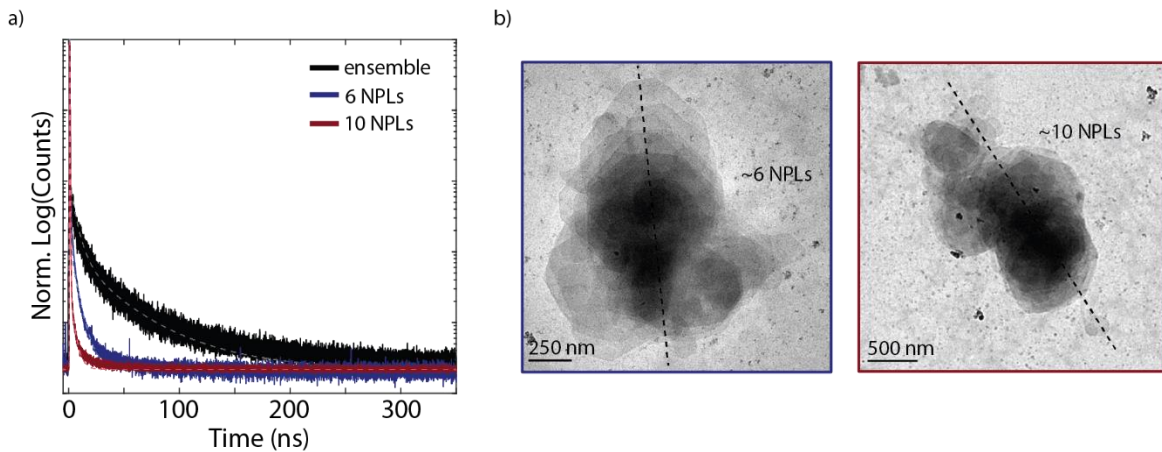
Figure 4.22*. a) Photoluminescence lifetimes for a solution ensemble (black solid), a stack of approximately 6 NPLs deposited on a TEM grid (blue solid), and a similar larger stack of approximately 10 NPLs (red solid). Their corresponding fits are shown by dashed lines. b) The TEM images used to approximate the stack thickness, where the dashed line is the trace used to find the pixel intensity profile.*

Table 4.4. *The measured lifetimes and resulting fit for CdTe NPLs after seeded growth in solution ensemble, a stack of ~6 deposited NPLs, and a larger stack of ~10 deposited NPLs.*

Sample	A	$\frac{1}{\tau}$ (ns^{-1})	τ(ns)	Amplitude (%)	Fit R-square	Average Lifetime (ns)
Ensemble	737.8	4.37	0.228	83.3		
	85.35	0.1253	7.981	9.6	0.9637	5.49
	62.11	0.0155	64.64	7.0		
~6 NPLs	4.91E5	7.644	0.131	93.6		
	3.26E4	2.007	0.498	6.2	0.9994	0.164
	881.5	0.157	6.365	0.2		
~10 NPLs	2.13E5	20	0.05	81.2		
	4.91E4	4.221	0.2369	18.8	0.9998	0.0878
	187.7	0.2484	4.0258	0.1		

REFERENCES

(1)   Ithurria, S.; Tessier, M. D.; Mahler, B.; Lobo, R. P. S. M.; Dubertret, B.; Efros, A. L.
        Colloidal Nanoplatelets with Two-Dimensional Electronic Structure. *Nat. Mater.* **2011**, *10*
        (12), 936–941.

(2)   Tessier, M. D.; Mahler, B.; Nadal, B.; Heuclin, H.; Pedetti, S.; Dubertret, B. Spectroscopy
        of Colloidal Semiconductor Core/Shell Nanoplatelets with High Quantum Yield. *Nano
        Lett.* **2013**, *13* (7), 3321–3328.

(3)   Tessier, M. D.; Javaux, C.; Maksimovic, I.; Loriette, V.; Dubertret, B. Spectroscopy of
        Single CdSe Nanoplatelets. *ACS Nano* **2012**, *6* (8), 6751–6758.

(4)   Izquierdo, E.; Robin, A.; Keuleyan, S.; Lequeux, N.; Lhuillier, E.; Ithurria, S. Strongly
        Confined HgTe 2D Nanoplatelets as Narrow Near-Infrared Emitters. *J. Am. Chem. Soc.*
        2016, *138* (33), 10496–10501.

(5)   Izquierdo, E.; Dufour, M.; Chu, A.; Livache, C.; Martinez, B.; Amelot, D.; Patriarche, G.;
        Lequeux, N.; Lhuillier, E.; Ithurria, S. Coupled HgSe Colloidal Quantum Wells through a
        Tunable Barrier: A Strategy to Uncouple Optical and Transport Band Gap. *Chem. Mater.*
        2018, *30* (12), 4065–4072.

(6)   Tenney, S. M.; Vilchez, V.; Sonnleitner, M. L.; Huang, C.; Friedman, H. C.; Shin, A. J.;
        Atallah, T. L.; Deshmukh, A. P.; Ithurria, S.; Caram, J. R. Mercury Chalcogenide
        Nanoplatelet–Quantum Dot Heterostructures as a New Class of Continuously Tunable
        Bright Shortwave Infrared Emitters. *J. Phys. Chem. Lett.* **2020**, *11*, 3473–3480.

(7)   Tessier, M. D.; Spinicelli, P.; Dupont, D.; Patriarche, G.; Ithurria, S.; Dubertret, B.
        Efficient Exciton Concentrators Built from Colloidal Core/Crown CdSe/CdS

Semiconductor Nanoplatelets. *Nano Lett.* **2014**, *14* (1), 207–213.

(8)   Ithurria, S.; Talapin, D. V. Colloidal Atomic Layer Deposition (c-ALD) Using Self-Limiting Reactions at Nanocrystal Surface Coupled to Phase Transfer between Polar and Nonpolar Media. *J. Am. Chem. Soc.* **2012**, *134* (45), 18585–18590.

(9)   Shin, A. J.; Hossain, A. A.; Tenney, S. M.; Tan, X.; Tan, L. A.; Foley, J. J.; Atallah, T. L.; Caram, J. R. Dielectric Screening Modulates Semiconductor Nanoplatelet Excitons. *J. Phys. Chem. Lett.* **2021**, *12*, 4958–4964.

(10)   Lin, Y.; Ling, X.; Yu, L.; Huang, S.; Hsu, A. L.; Lee, Y. H.; Kong, J.; Dresselhaus, M. S.; Palacios, T. Dielectric Screening of Excitons and Trions in Single-Layer MoS2. *Nano Lett.* **2014**, *14* (10), 5569–5576.

(11)   Chernikov, A.; Berkelbach, T. C.; Hill, H. M.; Rigosi, A.; Li, Y.; Aslan, O. B.; Reichman, D. R.; Hybertsen, M. S.; Heinz, T. F. Exciton Binding Energy and Nonhydrogenic Rydberg Series in Monolayer WS 2. *Phys. Rev. Lett.* **2014**, *113*, 076802.

(12)   Bernevig, B. A.; Hughes, T. L.; Zhang, S. C. Quantum Spin Hall Effect and Topological Phase Transition in HgTe Quantum Wells. *Science.* **2006**, *314* (5806), 1757–1761.

(13)   He, Y. M.; Clark, G.; Schaibley, J. R.; He, Y.; Chen, M. C.; Wei, Y. J.; Ding, X.; Zhang, Q.; Yao, W.; Xu, X.; Lu, C. Y.; Pan, J. W. Single Quantum Emitters in Monolayer Semiconductors. *Nat. Nanotechnol.* **2015**, *10* (6), 497–502.

(14)   Barthelmi, K.; Klein, J.; Hötger, A.; Sigl, L.; Sigger, F.; Mitterreiter, E.; Rey, S.; Gyger, S.; Lorke, M.; Florian, M.; Jahnke, F.; Taniguchi, T.; Watanabe, K.; Zwiller, V.; Jöns, K. D.; Wurstbauer, U.; Kastl, C.; Weber-Bargioni, A.; Finley, J. J.; Müller, K.; Holleitner, A.

W. Atomistic Defects as Single-Photon Emitters in Atomically Thin MoS2. *Appl. Phys. Lett.* **2020**, *117* (7), 070501.

(15) Lin, Z.; Liu, Y.; Halim, U.; Ding, M.; Liu, Y.; Wang, Y.; Jia, C.; Chen, P.; Duan, X.; Wang, C.; Song, F.; Li, M.; Wan, C.; Huang, Y.; Duan, X. Solution-Processable 2D Semiconductors for High-Performance Large-Area Electronics. *Nat.* **2018**, *562* (7726), 254–258.

(16) Lin, Z.; Huang, Y.; Duan, X. Van Der Waals Thin-Film Electronics. *Nat. Electron.* **2019**, *2* (9), 378–388.

(17) Pedetti, S.; Nadal, B.; Lhuillier, E.; Mahler, B.; Bouet, C. C.; Abécassis, B. A.; Xu, X.; Dubertret, B. Optimized Synthesis of CdTe Nanoplatelets and Photoresponse of CdTe Nanoplatelets Films. *Chem. Mater* **2013**, *25*.

(18) Yeltik, A.; Delikanli, S.; Olutas, M.; Kelestemur, Y.; Guzelturk, B.; Demir, H. V. Experimental Determination of the Absorption Cross-Section and Molar Extinction Coefficient of Colloidal CdSe Nanoplatelets. *J. Phys. Chem. C* **2015**, *119* (47), 26768–26775.

(19) Naeem, A.; Masia, F.; Christodoulou, S.; Moreels, I.; Borri, P.; Langbein, W. Giant Exciton Oscillator Strength and Radiatively Limited Dephasing in Two-Dimensional Platelets. *Phys. Rev. B - Condens. Matter Mater. Phys.* **2015**, *91* (12), 121302.

(20) Olutas, M.; Guzelturk, B.; Kelestemur, Y.; Yeltik, A.; Delikanli, S.; Demir, H. V. Lateral Size-Dependent Spontaneous and Stimulated Emission Properties in Colloidal CdSe Nanoplatelets. *ACS Nano* **2015**, *9* (5), 5041–5050.

(21)   Ma, X.; Diroll, B. T.; Cho, W.; Fedin, I.; Schaller, R. D.; Talapin, D. V.; Gray, S. K.;
       Wiederrecht, G. P.; Gosztola, D. J. Size-Dependent Biexciton Quantum Yields and Carrier
       Dynamics of Quasi-Two-Dimensional Core/Shell Nanoplatelets. *ACS Nano* **2017**, *11* (9),
       9119–9127.

(22)   Li, Q.; Lian, T. Area- and Thickness-Dependent Biexciton Auger Recombination in
       Colloidal CdSe Nanoplatelets: Breaking the "Universal Volume Scaling Law." *Nano Lett.*
       2017, *17* (5), 3152–3158.

(23)   Van Der Stam, W.; Akkerman, Q. A.; Ke, X.; Van Huis, M. A.; Bals, S.; De Mello
       Donega, C. Solution-Processable Ultrathin Size- and Shape-Controlled Colloidal Cu2- XS
       Nanosheets. *Chem. Mater.* **2015**, *27* (1), 283–291.

(24)   Almeida, G.; Dogan, S.; Bertoni, G.; Giannini, C.; Gaspari, R.; Perissinotto, S.; Krahne,
       R.; Ghosh, S.; Manna, L. Colloidal Monolayer β-In2Se3 Nanosheets with High
       Photoresponsivity. *J. Am. Chem. Soc.* **2017**, *139* (8), 3005–3011.

(25)   Dogan, S.; Bielewicz, T.; Cai, Y.; Klinke, C. Field-Effect Transistors Made of Individual
       Colloidal PbS Nanosheets. *Appl. Phys. Lett.* **2012**, *101* (7), 073102.

(26)   Shamsi, J.; Dang, Z.; Bianchini, P.; Canale, C.; Stasio, F. Di; Brescia, R.; Prato, M.;
       Manna, L. Colloidal Synthesis of Quantum Confined Single Crystal CsPbBr3 Nanosheets
       with Lateral Size Control up to the Micrometer Range. *J. Am. Chem. Soc.* **2016**, *138* (23),
       7240–7243.

(27)   Pedetti, S.; Ithurria, S.; Heuclin, H.; Patriarche, G.; Dubertret, B. Type-II CdSe/CdTe
       Core/Crown Semiconductor Nanoplatelets. *J. Am. Chem. Soc.* **2014**, *136* (46), 16430–
       16438.

(28)   Kelestemur, Y.; Guzelturk, B.; Erdem, O.; Olutas, M.; Erdem, T.; Usanmaz, C. F.; Gungor, K.; Demir, H. V. CdSe/CdSe1-XTex Core/Crown Heteronanoplatelets: Tuning the Excitonic Properties without Changing the Thickness. *J. Phys. Chem. C* **2017**, *121* (8), 4650–4658.

(29)   Dede, D.; Taghipour, N.; Quliyeva, U.; Sak, M.; Kelestemur, Y.; Gungor, K.; Demir, H. V. Highly Stable Multicrown Heterostructures of Type-II Nanoplatelets for Ultralow Threshold Optical Gain. *Chem. Mater.* **2019**, *31* (5), 1818–1826.

(30)   Schlosser, A.; Graf, R. T.; Bigall, N. C. CdS Crown Growth on CdSe Nanoplatelets: Core Shape Matters. *Nanoscale Adv.* **2020**, *2* (10), 4604–4614.

(31)   Khan, A. H.; Bertrand, G. H. V.; Teitelboim, A.; Sekhar M, C.; Polovitsyn, A.; Brescia, R.; Planelles, J.; Climente, J. I.; Oron, D.; Moreels, I. CdSe/CdS/CdTe Core/Barrier/Crown Nanoplatelets: Synthesis, Optoelectronic Properties, and Multiphoton Fluorescence Upconversion. *ACS Nano* **2020**, *14* (4), 4206–4215.

(32)   Antanovich, A. V.; Prudnikau, A. V.; Melnikau, D.; Rakovich, Y. P.; Chuvilin, A.; Woggon, U.; Achtstein, A. W.; Artemyev, M. V. Colloidal Synthesis and Optical Properties of Type-II CdSe-CdTe and Inverted CdTe-CdSe Core-Wing Heteronanoplatelets. *Nanoscale* **2015**, *7* (17), 8084–8092.

(33)   Bouet, C.; Mahler, B.; Nadal, B.; Abecassis, B.; Tessier, M. D.; Ithurria, S.; Xu, X.; Dubertret, B. Two-Dimensional Growth of CdSe Nanocrystals, from Nanoplatelets to Nanosheets. *Chem. Mater.* **2013**, *25* (4), 639–645.

(34)   Kurtina, D. A.; Garshev, A. V.; Vasil'Eva, I. S.; Shubin, V. V.; Gaskov, A. M.; Vasiliev, R. B. Atomically Thin Population of Colloidal CdSe Nanoplatelets: Growth of Rolled-up

Nanosheets and Strong Circular Dichroism Induced by Ligand Exchange. *Chem. Mater.*
2019, *31* (23), 9652–9663.

(35)   Ithurria, S.; Bousquet, G.; Dubertret, B. Continuous Transition from 3D to 1D
Confinement Observed during the Formation of CdSe Nanoplatelets. *J. Am. Chem. Soc.*
2011, *133* (9), 3070–3077.

(36)   Liu, Y.; Weiss, N. O.; Duan, X.; Cheng, H. C.; Huang, Y.; Duan, X. Van Der Waals
Heterostructures and Devices. *Nat. Rev. Mater.* **2016**, *1* (9), 1–17.

(37)   Chhowalla, M.; Jena, D.; Zhang, H. Two-Dimensional Semiconductors for Transistors.
Nat. Rev. Mater. **2016**, *1* (11), 1–15.

(38)   Beck, M. E.; Hersam, M. C. Emerging Opportunities for Electrostatic Control in
Atomically Thin Devices. *ACS Nano* **2020**, *14* (6), 6498–6518.

(39)   Di Giacomo, A.; Rodà, C.; Khan, A. H.; Moreels, I. Colloidal Synthesis of Laterally
Confined Blue-Emitting 3.5 Monolayer CdSe Nanoplatelets. *Chem. Mater.* **2020**, *32* (21),
9260–9267.

(40)   Riedinger, A.; Ott, F. D.; Mule, A.; Mazzotti, S.; Knüsel, P. N.; Kress, S. J. P.; Prins, F.;
Erwin, S. C.; Norris, D. J. An Intrinsic Growth Instability in Isotropic Materials Leads to
Quasi-Two-Dimensional Nanoplatelets. *Nat. Mater.* **2017**, *16* (7), 743–748.

(41)   Jana, S.; Frutos, M. de; Davidson, P.; Abécassis, B. Ligand-Induced Twisting of
Nanoplatelets and Their Self-Assembly into Chiral Ribbons. *Sci. Adv.* **2017**, *3* (9),
e1701483.

(42)   Jana, S.; De Frutos, M.; Davidson, P.; Abécassis, B. Ligand-Induced Twisting of

Nanoplatelets and Their Self-Assembly into Chiral Ribbons. *Sci. Adv.* **2017**, *3* (9), e1701483.

(43)   Cunningham, P. D.; Coropceanu, I.; Mulloy, K.; Cho, W.; Talapin, D. V. Quantized Reaction Pathways for Solution Synthesis of Colloidal ZnSe Nanostructures: A Connection between Clusters, Nanowires, and Two-Dimensional Nanoplatelets. *ACS Nano* **2020**, *14*, 12.

(44)   Nakonechnyi, I.; Sluydts, M.; Justo, Y.; Jasieniak, J.; Hens, Z. Mechanistic Insights in Seeded Growth Synthesis of Colloidal Core/Shell Quantum Dots. *Chem. Mater.* **2017**, *29* (11), 4719–4727.

(45)   Yang, H.; Hamachi, L. S.; Rreza, I.; Wang, W.; Chan, E. M. Design Rules for One-Step Seeded Growth of Nanocrystals: Threading the Needle between Secondary Nucleation and Ripening. *Chem. Mater.* **2019**, *31*, 4173–4183.

(46)   Moreels, I.; Lambert, K.; Smeets, D.; De Muynck, D.; Nollet, T.; Martins, J. C.; Vanhaecke, F.; Vantomme, A.; Delerue, C.; Allan, G.; Hens, Z. Size-Dependent Optical Properties of Colloidal PbS Quantum Dots. *ACS Nano* **2009**, *3* (10), 3023–3030.

(47)   Lhuillier, E.; Hease, P.; Ithurria, S.; Dubertret, B. Selective Electrophoretic Deposition of CdSe Nanoplatelets. *Chem. Mater.* **2014**, *26* (15), 4514–4520.

(48)   Kodanek, T.; Banbela, H. M.; Naskar, S.; Adel, P.; Bigall, N. C.; Dorfs, D. Phase Transfer of 1- and 2-Dimensional Cd-Based Nanocrystals. *Nanoscale* **2015**, *7* (45), 19300–19309.

(49)   Antanovich, A.; Prudnikau, A.; Matsukovich, A.; Achtstein, A.; Artemyev, M. Self-Assembly of CdSe Nanoplatelets into Stacks of Controlled Size Induced by Ligand

Exchange. *J. Phys. Chem. C* **2016**, *120* (10), 5764–5775.

(50)   Ott, F. D.; Riedinger, A.; Ochsenbein, D. R.; Knüsel, P. N.; Erwin, S. C.; Mazzotti, M.; Norris, D. J. Ripening of Semiconductor Nanoplatelets. *Nano Lett.* **2017**, *17* (11), 6870–6877.

(51)   Knüsel, P. N.; Riedinger, A.; Rossinelli, A. A.; Ott, F. D.; Mule, A. S.; Norris, D. J. Experimental Evidence for Two-Dimensional Ostwald Ripening in Semiconductor Nanoplatelets. *Chem. Mater.* **2020**, *32* (7), 3312–3319.

(52)   Pun, A. B.; Mazzotti, S.; Mule, A. S.; Norris, D. J. Understanding Discrete Growth in Semiconductor Nanocrystals: Nanoplatelets and Magic-Sized Clusters. *Acc. Chem. Res.* **2021**, *20*, 21.

(53)   Ji, B.; Giovanelli, E.; Habert, B.; Spinicelli, P.; Nasilowski, M.; Xu, X.; Lequeux, N.; Hugonin, J. P.; Marquier, F.; Greffet, J. J.; Dubertret, B. Non-Blinking Quantum Dot with a Plasmonic Nanoshell Resonator. *Nat. Nanotechnol.* **2015**, *10* (2), 170–175.

(54)   Andoy, N. M.; Zhou, X.; Choudhary, E.; Shen, H.; Liu, G.; Chen, P. Single-Molecule Catalysis Mapping Quantifies Site-Specific Activity and Uncovers Radial Activity Gradient on Single 2D Nanocrystals. *J. Am. Chem. Soc.* **2013**, *135* (5), 1845–1852.

(55)   Zou, N.; Chen, G.; Mao, X.; Shen, H.; Choudhary, E.; Zhou, X.; Chen, P. Imaging Catalytic Hotspots on Single Plasmonic Nanostructures via Correlated Super-Resolution and Electron Microscopy. *ACS Nano* **2018**, *12* (6), 5570–5579.

(56)   Hayee, F.; Yu, L.; Zhang, J. L.; Ciccarino, C. J.; Nguyen, M.; Marshall, A. F.; Aharonovich, I.; Vučković, J.; Narang, P.; Heinz, T. F.; Dionne, J. A. Revealing Multiple

Classes of Stable Quantum Emitters in Hexagonal Boron Nitride with Correlated Optical and Electron Microscopy. *Nat. Mater.* **2020**, *19* (5), 534–539.

(57)   Dahlberg, P. D.; Perez, D.; Su, Z.; Chiu, W.; Moerner, W. E. Cryogenic Correlative Single-Particle Photoluminescence Spectroscopy and Electron Tomography for Investigation of Nanomaterials. *Angew. Chemie* **2020**, *132* (36), 15772–15778.

(58)   Kim, W. D.; Yoon, D.-E.; Kim, D.; Koh, S.; Bae, W. K.; Chae, W.-S.; Lee, D. C. Stacking of Colloidal CdSe Nanoplatelets into Twisted Ribbon Superstructures: Origin of Twisting and Its Implication in Optical Properties. *J. Phys. Chem. C* **2019**, *123* (14), 9445–9453.

(59)   Guzelturk, B.; Erdem, O.; Olutas, M.; Kelestemur, Y.; Demir, H. V. Stacking in Colloidal Nanoplatelets: Tuning Excitonic Properties. *ACS Nano* **2014**, *8* (12), 12524–12533.

(60)   Comtet, J.; Glushkov, E.; Navikas, V.; Feng, J.; Babenko, V.; Hofmann, S.; Watanabe, K.; Taniguchi, T.; Radenovic, A. Wide-Field Spectral Super-Resolution Mapping of Optically Active Defects in Hexagonal Boron Nitride. *Nano Lett.* **2019**, *19* (4), 2516–2523.

(61)   Stern, H. L.; Wang, R.; Fan, Y.; Mizuta, R.; Stewart, J. C.; Needham, L.-M.; Roberts, T. D.; Wai, R.; Ginsberg, N. S.; Klenerman, D.; Hofmann, S.; Lee, S. F. Spectrally Resolved Photodynamics of Individual Emitters in Large-Area Monolayers of Hexagonal Boron Nitride. *ACS Nano* **2019**, *13* (4), 4538–4547.

(62)   Magnozzi, M.; Pflug, T.; Ferrera, M.; Pace, S.; Ramó, L.; Olbrich, M.; Canepa, P.; Ağircan, H.; Horn, A.; Forti, S.; Cavalleri, O.; Coletti, C.; Bisio, F.; Canepa, M. Local Optical Properties in CVD-Grown Monolayer WS2 Flakes. *J. Phys. Chem. C* **2021**, *125* (29), 16059–16065.

(63)   Liu, Z.; Amani, M.; Najmaei, S.; Xu, Q.; Zou, X.; Zhou, W.; Yu, T.; Qiu, C.; Birdwell, A.
         G.; Crowne, F. J.; Vajtai, R.; Yakobson, B. I.; Xia, Z.; Dubey, M.; Ajayan, P. M.; Lou, J.
         Strain and Structure Heterogeneity in MoS2 Atomic Layers Grown by Chemical Vapour
         Deposition. *Nat. Commun.* **2014**, *5* (1), 1–9.

(64)   Zhang, K.; Wang, Y.; Joshi, J.; Zhang, F.; Subramanian, S.; Terrones, M.; Vora, P.;
         Crespi, V.; Robinson, J. A. Probing the Origin of Lateral Heterogeneities in Synthetic
         Monolayer Molybdenum Disulfide. *2D Mater.* **2019**, *6* (2), 025008.

(65)   Gutiérrez, H. R.; Perea-López, N.; Elías, A. L.; Berkdemir, A.; Wang, B.; Lv, R.; López-
         Urías, F.; Crespi, V. H.; Terrones, H.; Terrones, M. Extraordinary Room-Temperature
         Photoluminescence in Triangular WS2 Monolayers. *Nano Lett.* **2012**, *13* (8), 3447–3454.

(66)   Ma, C.; Yan, J.; Huang, Y.; Yang, G. Photoluminescence Manipulation of WS2 Flakes by
         an Individual Si Nanoparticle. *Mater. Horizons* **2019**, *6* (1), 97–106.

(67)   Yan, J.; Ma, C.; Liu, P.; Yang, G. Plasmon-Induced Energy Transfer and
         Photoluminescence Manipulation in MoS2 with a Different Number of Layers. *ACS
         Photonics* **2017**, *4* (5), 1092–1100.

(68)   Lakowicz, J. R. *Principles of Fluorescence Spectroscopy*, 3rd ed.; Springer, 2006.

(69)   Sillen, A.; Engelborghs, Y. The Correct Use of "Average" Fluorescence Parameters.
         Photochem. Photobiol. **1998**, *67* (5), 475–486.

(70)   Dufour, M.; Qu, J.; Greboval, C.; Méthivier, C.; Lhuillier, E.; Ithurria, S. Halide Ligands
         to Release Strain in Cadmium Chalcogenide Nanoplatelets and Achieve High Brightness.
         ACS Nano **2019**, *13* (5), 5326–5334.

Chapter 5

Slow-Injection Gives Access to Lateral Size Control in CdTe Nanoplatelets

This chapter contains unpublished work by Stephanie M. Tenney, Ricky Ronquillo, Jillian

Williams, Tasnim Ahmed, and Justin R. Caram. The results are preliminary and based on

available data.

In this chapter, we expand on our understandings of nanoplatelet (NPL) growth by developing a

synthesis for controlling the NPL lateral area. The precise thickness control in II-VI semiconductor

NPLs has been well-developed and attracted much interest in these materials for optoelectronic

application. Control over their lateral size, however, is still not well understood but crucial for

further development of single-NPL technologies. We systematically explore the conditions of

slow-injection NPL synthesis and demonstrate that two factors play a dominant role in determining

the NPL lateral size: i) decomposition of the cadmium precursor must be avoided to delay lateral

ripening (and thickness evolution), and ii) the presence of cadmium carboxylate with chain length

longer than 6 carbons will result in small, narrow NPLs. We use this understanding to *directly*

synthesize CdTe NPLs with lateral extent of 5-10 μm for the first time. Finally, we characterize

these NPLs using standard optical microscopy and Raman spectroscopy to show spatial resolution

of properties such as strain in NPLs is now possible.

5.1 Introduction to Nanoplatelets as 2D Semiconductors

Two-dimensional (2D) semiconductors are semiconducting materials of typically single to

few monolayers. Within recent years, much attention has been drawn to transition metal

dichalcogenides (TMDs) because they offer direct bandgaps in their single-layer form, high

electron mobilities, and mechanical strength and have been well integrated into low-dimensional

devices such as Field effect transistors (FETs), photodetectors, and spintronics.[1–4] Their 2D

morphology has advantages over their bulk counterparts, largely due to their atomic confinement. For example, FETs the 2D semiconductors show enhanced efficiency because the carrier confinement leads to greater coupling to the gate voltage—limiting the amount of current leakage.[2] They also experience less dielectric screening giving rise to stronger electrostatic interactions, stronger exciton and trion binding, and lateral device structures.[5]

Semiconductor nanoplatelets (NPLs) have are a class of nanocrystal that are a unique hybrid of nanocrystal and 2D semiconductor. They are colloidally synthesized but can have lateral dimensions of many microns while maintaining few-monolayer confinement.[6] They have seen been implemented into optoelectronic devices such as LEDs, photodetectors, transistors, and scinitillators.[7–11] While they offer a promising range of application due to their large degree of bandgap tunability, possibility of doping, carrier mobility, and ease of synthesis, the major obstacle limiting the efficiency of NPL devices is that it still relies on ensembles of NPLs and intraparticle charge/exciton transfer.[9] This can lead to resistive losses and low carrier diffusion throughout the film. If NPLs can be realized at the length scale of typical 2D materials, they can be more widely implemented in these applications by using single particles within the device construction. Large area semiconductor nanosheets (or nanoplatelets, NPLs) may be promising materials for optoelectronic devices due to their solution based processability, tunable direct bandgap from 1-2 eV, and low dielectric screening.[12] In addition they have very high absorption cross-sections (which scale with area) and photoluminescence quantum yields compared to TMDs, and may show better performance in light absorbing or emitting applications.[13]

5.2 Synthetic Efforts Towards Lateral Control in Nanoplatelets

Controlling NPL thickness has been well explored through temperature,[14,15] precursor choice,[16,17] and post-synthetic modifications.[18,19] Through these treatments, a range of thicknesses

from 2 - 10 ML for a number of compositions have been successfully demonstrated with a high degree of monodispersity. Their narrow linewidths gives rise to excellent color purity for light emitting diodes.[20–22] Control of their lateral dimensions, however, has seen much less attention despite being a defining property of the NPL morphology. Some studies have shown that aspect ratio and total area can be correlated to the precursors used during synthesis. For example, Bertrand et al. demonstrated that the presence of water can control the aspect ratio which can be tuned by the proportion of hydrated cadmium salt used.[23] Gerdes et al. showed that injected halogenated alkanes during CdSe NPL hot injection can tune the shape from six-sided to three-sided along with a phase change from zinc blende to wurtzite.[24] More recently, one study showed that a change in cadmium-carboxylate chain length was correlated to a change in the aspect ratio for 3 and 4 ML CdSe while another study attributed aspect ratio control to the cadmium-to-selenium precursor ratio.[25,26] To our knowledge, there have been very few if any reports of how best to control overall NPL surface area and literature reports that begin to explore this are inconsistent with one another. We have explored secondary seeded growth procedures to extend already synthesized NPLs, but a rational synthetic design to directly control lateral size from few hundred nanometers to many microns is still needed.[6]

A mechanistic understanding of NPL growth has only recently converged to the kinetic instability model proposed by Riedinger et al.[27] Their model captures many nuances of NPL growth such as the origin of their anisotropic shape and why only integer thicknesses (from 2+ ML) are observed. While this work is critical for understanding the origin of NPL growth, it did not address what parameters affect the lateral extent until further work explored lateral ripening. In the lateral ripening model, NPLs nucleate and grow from the surface reaction limited kinetics described in the previous study, but they progress from thinner NPLs to thicker NPLs through

solubility effects.[28,29] When the free monomer concentration is high, the thermodynamic driving force for crystallization is also high and thin NPLs nucleate and grow rapidly. The free monomer concentration will drop as it is consumed (in a typical fast injection reaction) and these thin NPLs become unstable and dissolve laterally. The monomer will then become incorporated onto the next thickest nuclei in solution, leading to lateral ripening. Together these results may help reason experimental trends observed in lateral size. Different compositions display different average areas (CdS < CdSe < CdTe) which could arise from the trend in decreasing island growth energy, and different thickness also display progressively different areas (thicker < thinner) which can be attributed to an increased growth rate in thinner NPLs relative to thicker NPLs.[27] This explains why some NPLs are generally larger than others, but the limiting factor on area may in fact be the onset of lateral ripening.

Several questions about NPL growth and lateral extent remain, however. For example, 4 or 5 ML CdSe can be either directly synthesized or ripened from 3 ML, but neither pathway produces pure 4 ML CdTe without significant formation of CdO or CdTe NCs to our knowledge. In addition, the method used for direct synthesis can have different results. Fast injection can be used for almost all reported thicknesses, but slow injection only works for 2 or 3 ML (CdTe and CdSe).[6,30] An understanding of how all of the growth parameters work together is needed to explain these additional questions and afford size control. In this paper we establish a synthetic procedure for direct growth of mesoscale NPLs, focusing on CdTe NPLs as they have demonstrated larger lateral sizes than CdSe. To do so we systematically explore the slow injection method of NPL synthesis where we observe that lateral ripening, diminishing precursor concentration, and cadmium-carboxylate precursor type are all limiting factors for size control. When we overcome these limitations, we can reproducibly synthesize NPLs with lateral extents of 5-10 um. Finally,

we explore the structural properties of these NPLs through TEM, AFM, and Raman to demonstrate their tendency to form layered structures and that their size allows for a mapping of properties such as strain to reveal how properties may differ across a single nanocrystal.
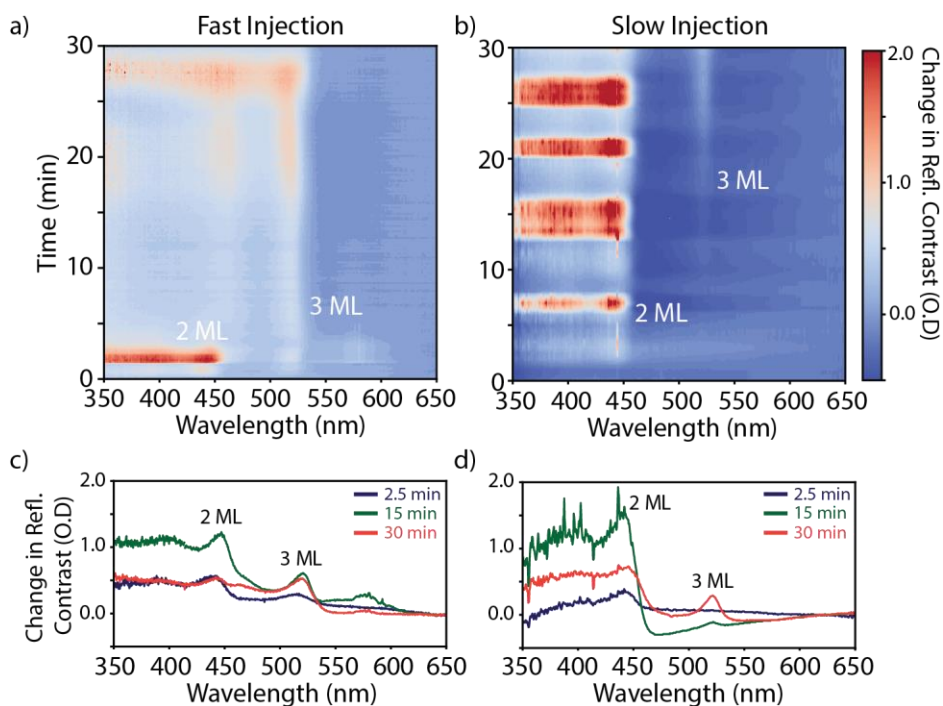
Figure 5.1. *In-situ reflectance spectra collected for a) fast injection of 3 M CdTe NPLs, and b) slow injection of 3 ML CdTe NPLs. The change in reflectance contrast is indicated by the color bar where a higher optical density indicates a larger concentration of NPL. Selected spectra at 2.5, 15, and 30 min are shown for c) fast injection and d) slow injection as well.*

5.3 Comparison of Fast and Slow Injection for Nanoplatelet Growth

We first explored NPL growth dynamics by monitoring reactions using reflectance spectroscopy. The reflectance spectra are collected in-situ with a dip probe and used as an absorption-like measurement by conversion to optical density (O.D.). The temporal resolution of this method allows for a much closer look at the populations that grow and decay throughout the NPL reaction. We start by comparing a fast injection of TOP-Te into a solution of cadmium-propionate, oleic acid, and octadecene (ODE) (Figure 5.1a) to a slow injection of diluted TOP-Te

into a solution with identical concentrations of precursors (Figure 5.1b). In the 2D reflectance spectra for fast injection, we observe an early (2-3 min) burst of 2 ML NPL growth after the TOP-Te is injected, followed by a decrease in that population and a slower but immediate rise in the 3 ML population (Figure 5.1o). In contrast, the slow injection shows an extended growth period for 2 ML and a much slower appearance of the 3 ML population. In Figures 5.1c and d, this is more apparent by examining the time slices at early points (2.5 min), midway through the reaction (15 min), and near the end (30 min)—fast injection is nearly completely converted to 3 ML while slow injection shows a mixture of 2 and 3 ML.

These results can be reasoned by the literature's accounts of lateral ripening. The NPLs themselves have a solubility that depends on the concentration of monomer in solution; monomers will add onto existing NPLs if the [monomer] is high, but will detach or dissolve laterally from NPL edges if the [monomer] is low.[28,29] The stability of the NPL also depends on thickness—because the thicker NPLs are more thermodynamically stable than thinner ones, the dissolved monomers will deposit onto the next thickest nuclei that still remain in solution. This leads to a sequential lateral ripening from thin to thick NPLs and spectrally appears as evolution from one integer monolayer to another. We observe this behavior most predominantly in the fast injection case where the monomer is injected all at once (nucleating many 2 ML NPLs), and then depletes almost immediately leading to ripening towards 3 ML NPLs. This implies that even though fast injection reactions happen much quicker and tend to result in one major ML product, they still evolve through growth of previous thicknesses. Interestingly, we also observe ripening from 2 to 3 ML in slow injection. This seems counterintuitive since the concentration of monomer is continuously delivered over time and theoretically maintains a constant level of precursor in solution. As a slow, controlled growth of fewer but larger particles is more likely to produce large

area NPLs, we set out to understand how the parameters of the slow injection reaction leads to this result to try and maximize size.
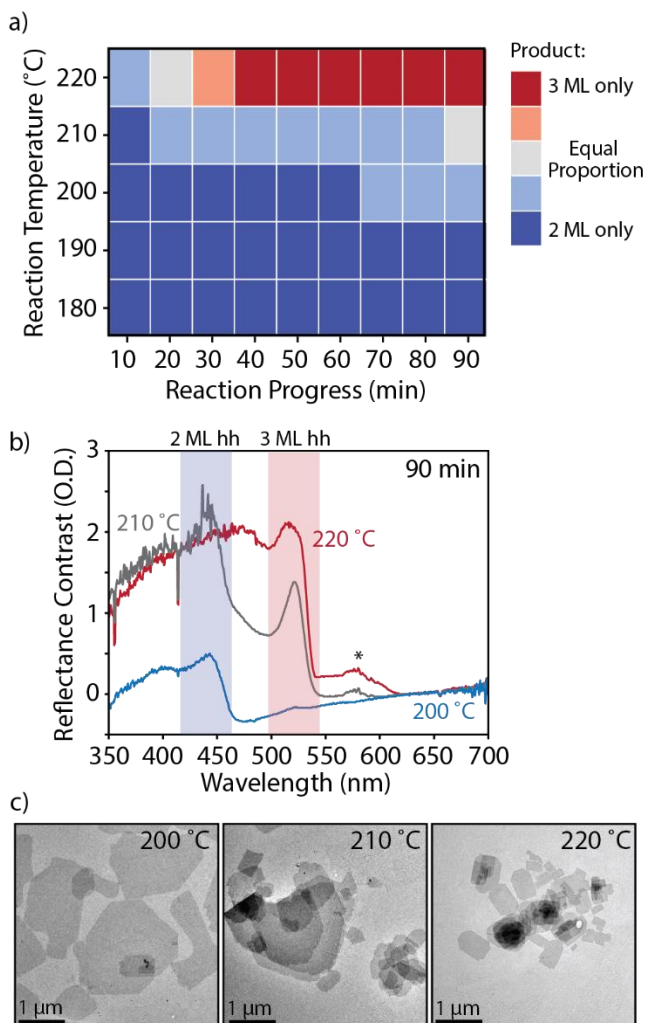
Figure 5.2. *Summary of slow injection reactions for the formation of CdTe NPLs using cadmium-propionate as the precursor. a) the approximate ratio of 2 to 3 ML NPL population throughout the reaction as a function of reaction temperature. Higher temperatures favor a faster conversion from 2 to 3 ML but all reactions begin as 2 ML. c) The final reflectance traces (90 min) of the reactions at 200, 210, and 220 ˚C demonstrating the relative amount of 2 and 3 ML populations. The (*) indicates noise from the lamp. b) Corresponding TEM images at the end of the three reactions showing only 2 ML (200 ˚C), a mixture of 2 and 3 ML (210 ˚C), and only 3 ML (220 ˚C).*

5.4 Lateral Ripening in Nanoplatelet Slow Injection Growth

We examined the slow injection synthesis of CdTe NPLs at increasing temperatures in Figure 5.2a. The synthesis involves degassing a solution of cadmium propionate, oleic acid, and ODE in a rection flask followed by injection of TOP-Te over the course of 90 min (more details in Experimental Methods). Using our in-situ reflectance probe we can monitor the thickness populations by tracking the excitonic features throughout the reaction (full spectra for each reaction are shown in Figure 5.11). We first observe that at low temperatures (180-200 ˚C), the major product throughout the entire reaction is 2 ML CdTe. The NPLs extend to the few-micron scale (Figure 5.2b). Between 200 and 220 ˚C, we see the emergence of 3 ML NPLs which continue to grow in optical density as time progresses. For the higher temperature reactions, the population more rapidly switches from 2 ML to entirely 3 ML. At 210 ˚C, we observe both 2 and 3 ML NPLs in the final product after 90 min, although the large 2 ML NPLs have rounded/scalloped edges unlike the smaller 3 ML NPLs. This suggests that when the two populations exist at the same time, the 2 ML NPLs are dissolving at their edges while the 3 ML NPLs are extending, and is in agreement with the current understanding of lateral ripening as well as previous findings.[6] At 220 ˚C, the final product is entirely 3 ML but laterally much smaller than the 2 ML.

Our results strongly suggest that our system is undergoing lateral ripening at elevated temperatures and explain how one can use time and temperature to favor the growth of 2 ML or 3 ML NPLs using seeded growth. The puzzling nature of this, however, is that lateral ripening is understood to be triggered by a loss of free monomer concentration and we maintain a continuous concentration through the slow TOP-Te injection. A sudden drop in monomer could be explained by either a) the TOP-Te being used up faster than it can be replenished, or b) the cadmium precursor being used up before the end of the reaction despite being in large excess.

While increased temperature will result in a larger thermodynamic driving force for crystallization and therefore faster growth, if the TOP-Te were being used immediately upon addition of a droplet we would expect to see more pronounced oscillatory behavior on the timescale of droplet addition and corelated increases in the 3 ML population. Instead, we see a steady increase in 2 ML, followed by a steady increase in 3ML. We do sometimes observe periodic oscillations in the intensity of the excitonic features, but this happens on the time scale of about 10 min, and we believe it can be attributed to heating cycles of the temperature controller (we also observe a very small shift in the wavelength of absorption). The time to build up enough TOP-Te for nanocrystal nucleation is ~2.5 min, indicated by the period after the reaction is started but before any excitonic features appear (Figure 5.12). Therefore, we decided to examine the role of the cadmium precursor and oleic acid ligand.
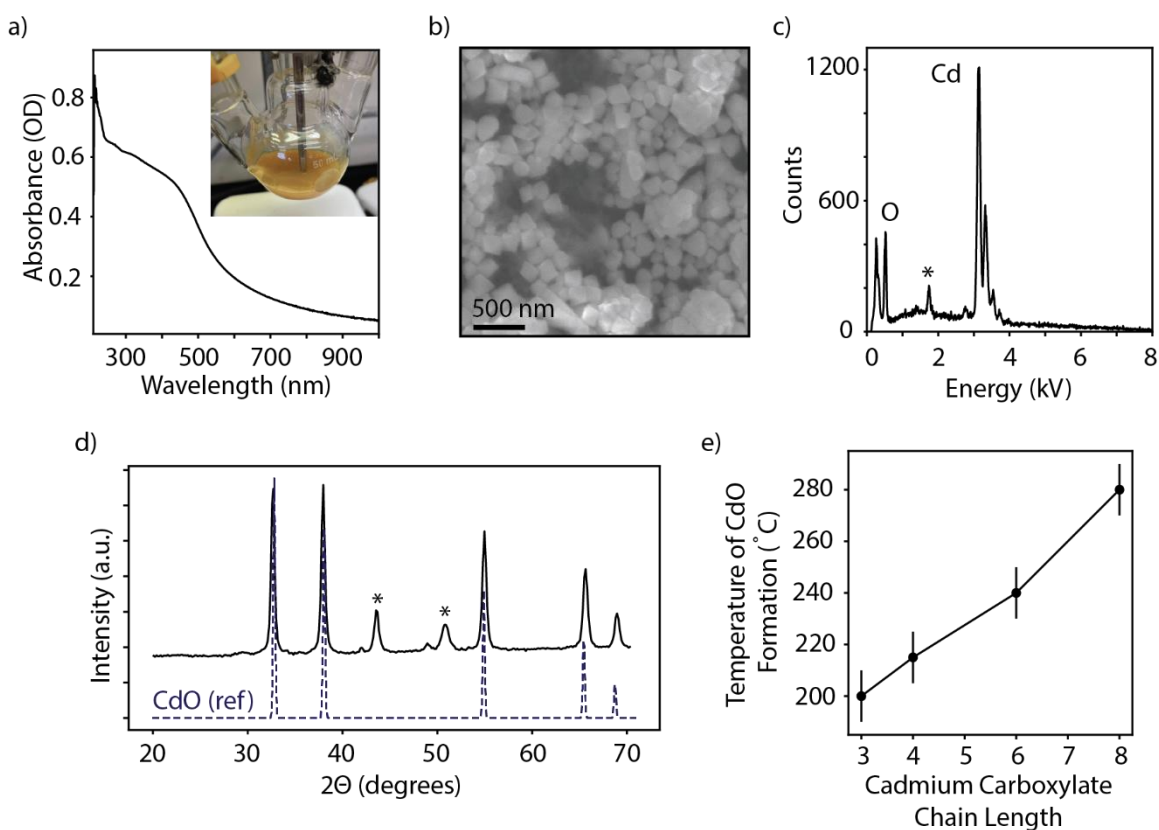
Figure 5.3. The formation of cadmium oxide (CdO) by heating the cadmium carboxylate precursor at temperatures relevant for NPL reactions. a) The solution is strongly yellow colored and shows an absorption spectrum consistent with semiconductor nanocrystals. b) The particles are ~100-200 nm in size, and c) are comprised of cadmium and oxygen. d) Powder x-ray diffraction of the product matches the expected pattern for CdO. e) The temperature at which this conversion happens is dependent on carboxylate chain length, where a longer chain requires higher temperatures. The (*) indicates features from the substrate or sample holder.

5.5 Cadmium Oxide Formation Depletes Cadmium Carboxylate Precursor

Literature results show that a rapid drop in monomer concentration will cause lateral ripening to occur. As we have ruled out the role of TOP-Te, we examined the stability of the cadmium precursor in the presence (and absence) of the ligand oleic acid. We predict that because cadmium oleate is formed by heating cadmium oxide in oleic acid at 160-190 ˚C, the temperatures used for NPL synthesis (~180-220 ˚C) will lead to an exchange of the short chain carboxylates (propionate for example), for the long chain oleate). [31,32] Partial exchange has been demonstrated in the literature through H-NMR, where the shorter the carboxylate bound to cadmium, the more likely it is to exchange with oleic acid.[27] Although oleic acid is widely used in almost every NPL synthesis for passivation and maintaining separation between individual particles, we believe that it leads to an unintended formation of cadmium oxide. We tested this hypothesis by heating a reaction vessel with cadmium propionate, oleic acid, and ODE at temperatures used for synthesis (and in the same concentrations) and observing the evolution of the cadmium precursor (Figure 5.3). We found that in a very short amount of time (~2 min), the flask began changing color from yellow to orange to brown (Figure 5.3a) without any addition of Te precursor. The isolated product is cadmium oxide, and we believe we observe the formation of nanoparticle CdO (Figure 5.3b-d). We tested a range of carboxylate lengths, and found that with increasing length, the temperature at which CdO formation became visible increased (Figure 5.3e). This is likely due to a higher

temperature required for the exchange from cadmium carboxylate to cadmium oleate. Interestingly, without oleic acid we were unable to form CdO.

Thermal decomposition of metal carboxylates and oleates has been explored in the literature and shows that metal oleate compounds will decompose into metal oxide particles at elevated temperatures. This decomposition was suggested to proceed to a greater extent by the presence of the vinyl group (not observed to the same extent in saturated carboxylates).[33–35] Decomposition of saturated fatty acids involves deoxygenation into a high molecular weight product, while pyrolysis of an unsaturated fatty acid will favor allylic C-C bond breaking before this deoxygenation occurs.[36,37] Unsaturated fatty acids experience greater decomposition than saturated fatty acids—conversion of oleic acid into its decomposition products was found to be 75% at 390 ˚C whereas stearic acid was only 32% at 350 ˚C.[36,38] We believe that decomposition of cadmium oleate to cadmium oxide is occurring during the initial stages of the NPL synthesis and may be acting as a cadmium precursor sink–lowering the available cadmium feedstock and triggering lateral ripening. To our knowledge, CdO has not been shown to be a reactive cadmium precursor towards NPL growth at these low temperatures. To avoid this process, and hopefully delay ripening during growth of NPLs, one can either eliminate oleic acid or use longer chain carboxylates to slow the exchange towards cadmium oleate.
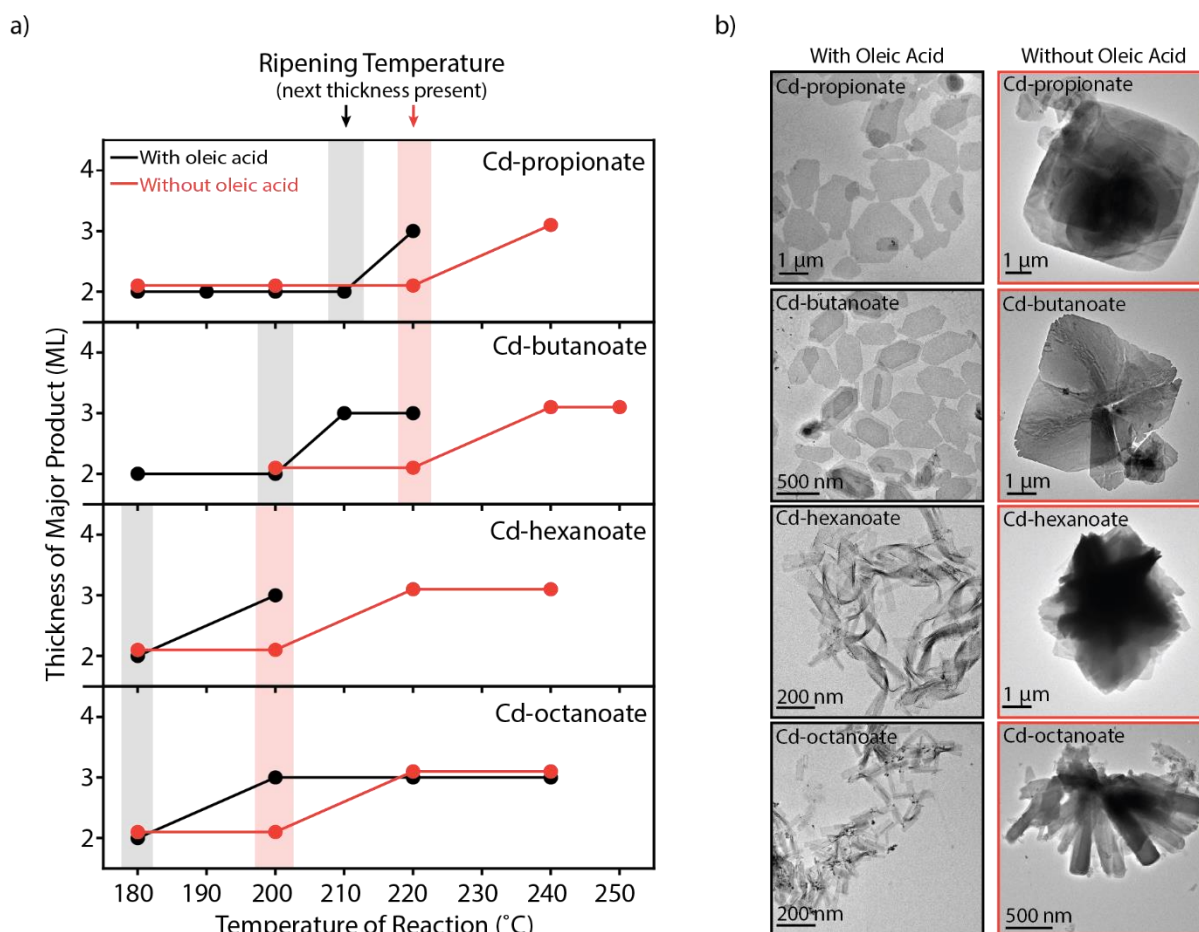
Figure 5.4. *The effect of cadmium carboxylate chain length on thickness control. a) The major product at the end of the NPL reaction was assessed for four different carboxylate lengths, as well as at increasing temperatures, and in the presence or absence of oleic acid. In general, the longer chain carboxylates (and those with oleic acid) will favor thicker NPLs. b) TEM images comparing NPLs synthesized in the presence (black) and absence (red) of oleic acid.*

5.6 Chain Length of Cadmium Carboxylate Precursor gives Thickness and Area Control

We explore both effects in Figure 5.4. We tested CdTe NPL synthesis at increasing temperatures for four different carboxylate lengths both with and without oleic acid. All reactions were run for the same reaction time of 90 min and the major product was evaluated at the end of the trial. For both cases, we found that our results largely agree with observed trends in size in the literature. Longer carboxylates tend to favor smaller, thicker NPLs (more isotropic) which may be

due to their increased solubility relative to shorter carboxylates.[27] This may be one aspect as to why CdSe NPLs are typically smaller than CdTe—their syntheses utilize long chain cadmium myristate and oleate.[15] With oleic acid, we see that the 2 ML CdTe NPLs are only possible with short chain carboxylates, and only reach ~1-2 micron before ripening causes a population change to 3 ML (TEM images for all reactions with oleic acid are shown in Figure 5.13). Without oleic acid, however, the temperature for ripening is elevated by 10-20 ˚C, and complete conversion from 2 to 3 ML populations happens at much higher temperatures which may indicate a slowed formation of CdO. We did not observe any yellowing color in the flask before the injection began like we did with oleic acid. More strikingly, we observe that the lateral size of NPLs is significantly larger, up to 5-10 um in 2 ML CdTe which is likely an effect of ligand length not CdO formation (TEM images for all reactions without oleic acid are shown in Figure 5.14). Removing long chain ligands altogether allows us to directly make significantly extended NPLs, with the shorter the chain the larger (and thinner) the NPL. We also see difference in NPL size and twisting behavior in CdSe in the absence of oleic acid (Figure 5.15). The greater driving force for lateral growth in the absence of oleic acid could be explained by a lower precursor solubility or a different surface energy when using the shorter carboxylates. The saturated short chain acids may have a greater propensity to form denser, highly-ordered passivating layers which may in turn affect the energetic differences between the top and side facets and consequently, size.[27,39–41] The surface properties of these mesoscale NPLs is the focus of a future study.

Overall, we find that size extension in the slow injection of 2 and 3 ML NPLs relies on two major factors: i) the precursor of choice must be used at appropriate temperatures to maintain a high concentration and avoid lateral ripening, and ii) the precursor should be a short-chain carboxylate if large NPLs with a high aspect ratio are desired. We are continuing to explore how

to introduce longer chain ligands to enhance separation when syntheses exclude them from the initial growth periods.

We believe that our findings can address some of the limitations of NPL synthesis. The formation of CdO during NPL synthesis has been alluded to in the literature prior to our work but has not been thoroughly explored. For example in early synthetic work by Pedetti et al., the authors found that cadmium acetate must be used at lower temperatures than typical to avoid ripening (120 ˚C), while cadmium propionate did not display any ripening until up to 210 ˚C (the same temperature range we observe ripening and formation of CdO for cadmium propionate).[42] The shorter the carboxylate, the lower the temperature this process occurs. Cadmium oxide was also found as an intermediate in a reaction of cadmium propionate and selenium melt, with decomposition occurring also around 200 ˚C.[43] Our results can also explain some of the unclear aspects of NPL synthesis. For example, we commonly observe CdO in TEM images of samples grown through slow injection, but not fast injection. The fast injection of TOP-Te likely favors conversion of the cadmium precursor into NPL monomer faster than CdO formation can occur. We believe this is why synthesis of 4 or 5 ML CdSe is possible—it avoids decomposition by using long chain myristate to reach the reaction temperature and shocking the system with short chain carboxylates only once the temperature is reached (a pseudo-fast injection). Slow injection only works for 2 and 3 ML CdTe and CdSe; this is because the temperature needed for thicker NPLs exceeds the temperature of precursor decomposition and the injection is too slow to favor NPL nucleation before this occurs—the synthesis will largely produce only CdO or 3D NCs. It may not be possible to extend 4+ ML NPLs to the mesoscale through direct synthesis without finding an alternative cadmium precursor that can withstand high temperatures. In addition, this could be why pure 4 ML CdTe (without presence of other ML) has not been demonstrated before via either fast

or slow injection—the temperature needed to exceed 3 ML is far higher than the decomposition temperature of shorter chain carboxylate needed to trigger lateral growth. Our attempts to replicate the methods used for CdSe fast injection for CdTe were unsuccessful and likely requires even higher temperatures than CdSe. In general, removal of oleic acid helps to delay these CdO formation events to higher temperatures, but precursor decomposition still occurs and needs to be considered in the context of synthetic conditions.
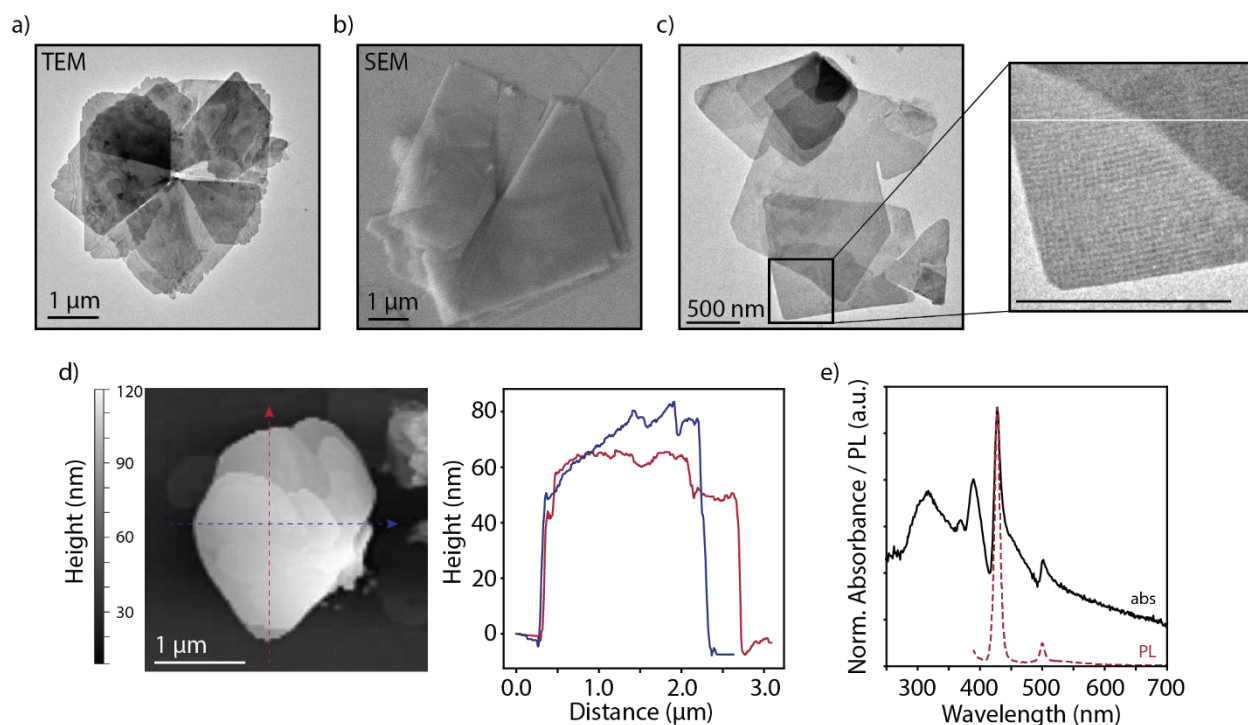
Figure 5.5*. Examination of the largest mesoscale NPLs synthesized through exclusion of oleic acid. a) TEM and b) SEM of 2 ML CdTe showing the layering and screw-dislocation around which the NPLs appear to extend. c) Moiré patterns can be observed in the TEM indicating the presence of ordered but slightly offset layers. d) AFM confirms that the observed particles are in fact many NPL thick, but the layers themselves e) still maintain 2 ML quantum confinement.*

5.7 Structural Investigation of Mesoscale Nanoplatelets

Of the largest mesoscale NPLs we synthesized, we further examine the structure of the 2 ML NPLs synthesized from cadmium butanoate without oleic acid because they show less stacking

than cadmium propionate while reaching similar sizes. Aside from the extended lateral area, the major structural difference between NPLs grown with and without oleic acid is that an absence of oleic acid leads to a high degree of stacking. In fact, it appears that the NPL growth proceeds in an upwards spiral, and some even appear to be nucleating from a screw dislocation (Figure 5.5a-b). These dislocations may be driven by the low supersaturation conditions of slow injection and large driving force for lateral growth.[44-46] The origin of the defect initiating the spiral growth is still unknown, but this growth mode may be of interest for exploring chirality. We are also able to observe Moiré-like patterns in the TEM images (Figure 5.5c) which indicates that there is interference between adjacent layers that are slightly offset (additional examples shown in Figure 5.16). Moiré patterns are most commonly explored in materials such as twisted bilayer graphene, hexagonal boron nitride, and other 2D materials, but were also observed in stacked nanosheets such as PbS.[47-51] Many NPLs are layered in this system as seen in AFM (Figure 5.5d), where a particle is > 50 nm thick (this also includes the inter-layer ligands). We confirm that the individual layers maintain their 2 ML quantum confinement by their absorption and photoluminescence (Figure 5.5e), and their relative stoichiometry via elemental dispersive x-ray spectroscopy (Figure 5.17). The trade-off for large lateral size by only using short chain carboxylates is NPL layering. We were unable to separate individual layers by quenching the reaction with long chain oleic acid indicating that the layers form in solution during the growth stage, not after drop casting.
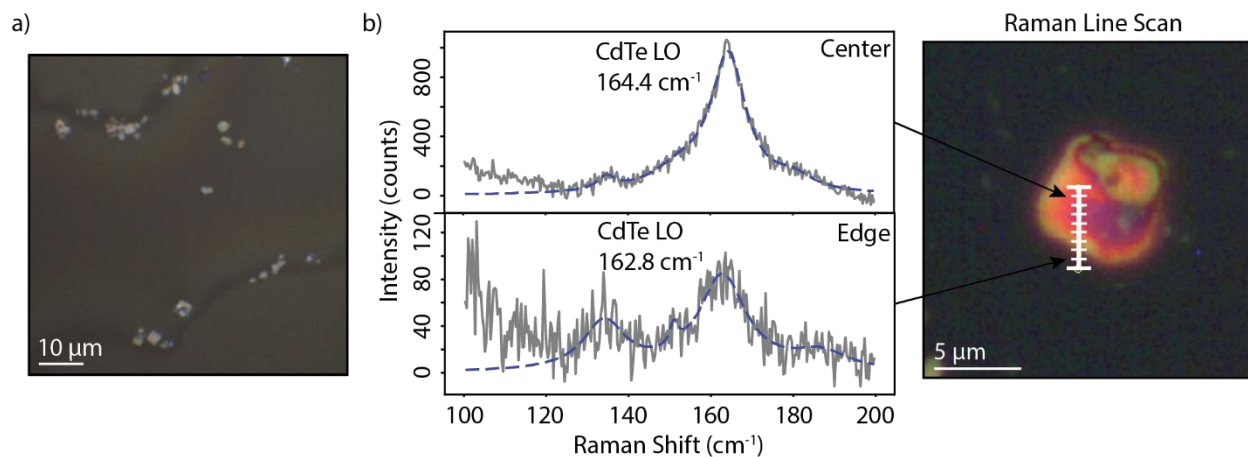
Fig 5.6*: Raman spectroscopy of single mesoscale CdTe particles. a) The NPLs are now visible using standard optical microscopes. b) Raman spectra collected at different spatial locations along the surface of a NPL stack reveals a shift in the CdTe LO phonon frequency.*

5.8 Measurements of Nanoplatelet Strain with Raman Spectroscopy

Finally, we demonstrate that the many-micron lateral extent of these NPLs allows us to characterize them using standard reflectance optical microscopy (Figure 5.6a), and study spatial properties such as strain by Raman spectroscopy. In Figure 5.6b, we imaged a single particle using reflectance and could observe thickness variations in color by thin film interference with the underlying silicon substrate. We were then able to focus the laser to the center of the particle and collect Raman spectra in a line scan outward towards the edge. This is the first time, to our knowledge, that Raman has been collected on a single NPL particle without the use of surface-enhancement techniques and with spatial resolution. In the literature, the longitudinal optical (LO) phonon frequency of CdTe nanocrystals (167 to 169 cm^{-1}) has been demonstrated to red shift with decreasing size relative to bulk (170 cm^{-1}).[52] This decreasing effect was also observed in CdSe NPLs, but CdTe NPLs have not been studied to the same extent.[53,54] Other features in the Raman spectra may be attributed to a transverse optical (TO), surface optical (SO), and high frequency shoulder modes, but we only focus on the LO mode it is better understood (there is debate on the

assignment of the other features in CdSe nanocrystals).[55–57] We observe a LO frequency much lower than CdTe bulk and nanocrystals at 164.4 cm^{-1} (Figure 5.18). This is unsurprising given that NPLs are in an extreme confinement regime even relative to quantum dots. When we fit the spectra to four Lorentzians (to account for the possibility of 4 features), we assign the LO phonon mode and observe a shift across the NPL. We acknowledge that the large laser spot size (1-2 μm) does not allow for fine spatial resolution, but we generally see a net decrease in the LO phonon frequency near the edges compared to the center (Figure 5.6b). The results at each position are shown in Figure 5.19. This shift could point towards differential strain in the NPL; the center near the screw dislocation likely experiences a greater distortion compared to the edges. Strain has been shown to blue shift the LO phonon in the case of CdSe NPLs with a lattice mismatched CdS shell.[58,59] On the other hand, the shift could also be a result of differential passivation as mass loading can cause shifts in the Raman spectra of NPLs, but this effect is small and only seen in the acoustic phonon modes.[60,61]

5.9 Conclusions

Overall, we demonstrate that lateral size of II-VI semiconductor NPLs can be controlled by careful consideration of precursor concentrations and chain length. We show that the cadmium carboxylate precursor will decompose at temperatures used during NPL growth and causes an onset of lateral ripening. Exclusion of the unsaturated fatty acid ligand oleic acid both prolongs the onset of this decomposition and favors large lateral extension. By using these reaction design principles, we demonstrate mesoscale NPLs on the order of 5-10 micron in size and show that their lateral extent allows for spatial resolution of properties such as strain through Raman Spectroscopy.

5.10 Experimental Details

Cadmium acetate dihydrate (Acros, 98%), cadmium oxide (Alfa Aesar, 99.95%), propionic acid (Fisher), butyric acid (Sigma Aldrich, 99%), hexanoic acid (Sigma Aldrich, 99%), octanoic acid (Sigma Aldrich, 99.5%), oleic acid (Alfa Aesar, 99%), selenium powder (Acros, 99.5%), tellurium powder (Acros, 99.8%), tri-n-octylphosphine (TOP) (Alfa Aesar, 90%), 1-octadecene (ODE) (Alfa Aesar, 90%), ethanol (Fisher, 95.27%), hexanes (Fisher, 98.5%), and toluene (Alpha Aesar, 99.8%), were used.

Synthesis of Cadmium Precursors

All cadmium carboxylate precursors were synthesized following the same method, but at different temperatures depending on the chain length. Cadmium oxide (1.036 g, 8.07 mmol) and carboxylic acid (10 mL propionic, butanoic, hexanoic, or octanoic) was added to a round bottom flask and mixed under Argon. The solution was heated until the red solids dissolved, and the solution became clear and colorless. The temperature needed increased with chain length: ~70 ˚ C for propionic acid, ~130 ˚ C for butanoic acid, ~150 ˚ C for hexanoic acid, and ~200 ˚ C for octanoic acid. Once the solution was clear, the heating element was removed, and the flask was submerged in a cool water bath. An excess of acetone was used to precipitate out the product, although the longer chain cadmium hexanoate and octanoate precipitated simply with cooling.

The final product was a white solid. ^{1}H-NMR (400 MHz, r.t.) was used to confirm the complete conversion of carboxylic acid to cadmium carboxylate in deuterated methanol. Cadmium propionate: δ=2.30 [q, 2H, CH_2], δ=1.13 [t, 3H, CH_3]. Cadmium butanoate: δ = 2.27 [t, 2, CH_2], δ = 1.64 [m, 2, CH_2], δ = 0.95 [t, 3, CH_3]. Cadmium octanoate: δ = 2.29 [t, 2, CH_2], δ = 1.62 [m, 2, CH_2], δ = 1.31 [m, 8, CH_2], δ = 0.91 [t, 3, CH_3].

Synthesis of Chalcogen Precursor

Tri-n-octylphosphine telluride (TOP-Te). 1 M TOP-Te was prepared by combining Te powder (0.254 g) and tri-n-octylphosphine (2 mL) in a small flask. The solution was degassed under vacuum at room temperature. Once the pressure reached ~150 mtorr or less, the solution was heated under argon flow to 275 ˚C and held until dissolution was complete forming a yellow solution (~10-15 min). The solution was then cooled to room temperature. If the TOP-Te was used for fast injection, the concentration was kept at 1 M. For all slow injection trials, the TOP-Te was further diluted to 0.05 M in degassed octadecene.

Tri-n-octylphosphine selenide (TOP-Se). 1 M TOP-Se was prepared similarly, by combining Se powder (0.144 g) and tri-n-octylphosphine (2 mL) in a small flask. The solution was degassed at room temperature, and then subsequently switched to Argon flow at room temperature until the solids dissolved and the solution was clear. No heating is necessary for TOP-Se.

Fast Injection

3 ML CdTe. Cadmium propionate (0.260 g, 1 mmol), oleic acid (160 μL), and octadecene (20 mL) were added to a 3-neck round bottom flask. The solution was degassed under vacuum at 80 ˚C for 20 min, or until the pressure was ~150 mtorr or less. The temperature was then raised to 215 ˚C under Ar. Once at temperature, 1 M TOP-Te (0.2 mL) mixed with octadecene (0.4 mL) was swiftly injected. The reaction was left for 30 min, then quenched with oleic acid (0.5 mL) and cooled in a water bath. The solution was centrifuged at 9000 rpm for 10 min and the pellet was resuspended in 20 mL hexanes.

Slow Injection

CdX (X= Te, Se). Cadmium carboxylate precursor (1 mmol) and octadecene (20 mL) were added to a 3-neck round bottom flask. If the reaction included oleic acid, it was also added at the step

(160 μL). The solution was degassed under vacuum at 80 ° C for 20 min, or until the pressure was ~150 mtorr or less (the longer chain carboxylates produced more gas evolution). The solution was then placed under argon and heated to the reaction temperature. We explored 180 ° C, 200 ° C, 220 ° C, and 240 ° C for each cadmium precursor. Once at temperature, 0.05 M TOP-X was injected at a rate of 5 mL/hr for 90 minutes. At the end of the injection, the heating element was removed, oleic acid (0.5 mL) was injected, and the flask was submerged in a cool water bath. The solution was then centrifuged at 9000 rpm for 5 min and the pellet was resuspended in 20 mL hexanes.

Characterization

Absorption spectra were acquired with an Agilent Cary 60 UV-Vis spectrophotometer. Photoluminescence (PL) was collected using a Horiba Scientific PTI QuantaMaster400 Spectrometer. Reflectance measurements were collected using an Ocean Insight QR200-12-MIXED reflectance probe and an Avantes DH-2000 UV-VIS-NIR light source.

H-NMR was collected on a Bruker AV400 operated at 400MHz.

Transmission electron microscopy (TEM) images were acquired with a FEI Tecnai T12 120kV TEM. The nanoplatelets were diluted in hexanes and drop casted on Ted Pella, Inc. carbon/formvar 300 mesh copper grids. Scanning electron microscopy (SEM) was obtained on a JEOL JSM-6700F FE scanning electron microscope equipped with an EDX detector, using an operating bias of 9kV. SEM of NPLs was collected by coating Si wafers with gold, and dropcasting a dilute solution of NPLs. SEM of CdO particles was collected by dropcasting the CdO directly onto the Si wafer.

Powder X-Ray diffraction was obtained on a Panalytical X'Pert Pro X-ray Powder Diffractometer using Cu Kα, operated at 40kV and 40 mA.

Raman was obtained with a Horiba LabRAM HR Evolution spectrometer using a 488 nm laser excitation (spot size 1-2 μm) and a 100x objective. NPLs were dropcast from a dilute solution of hexanes onto a Si wafer.

5.11 Supporting Information

H-NMR of Cadmium Precursors
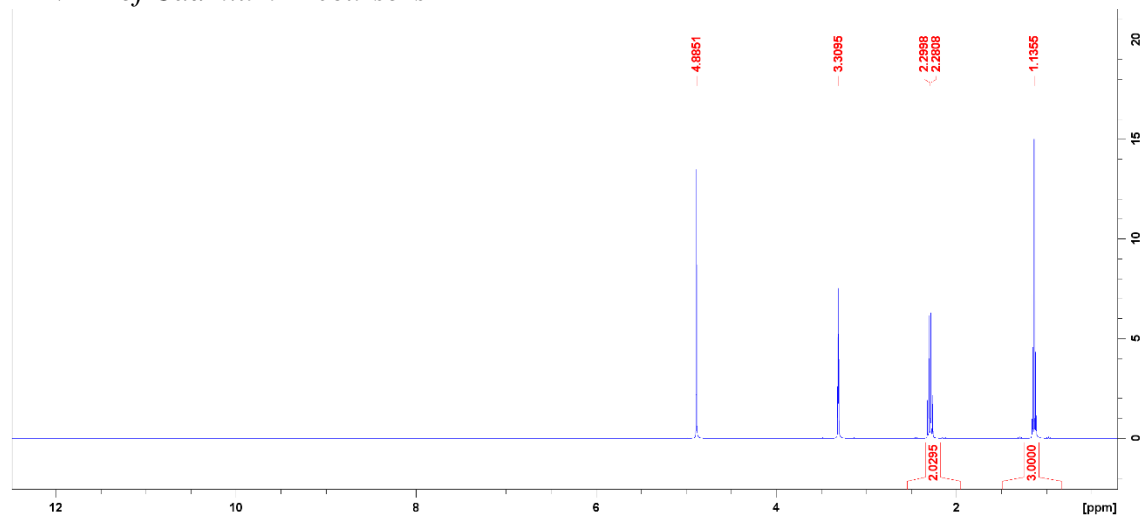
Figure 5.7. *^{1}H-NMR (400 MHz, r.t.) of cadmium propionate in methanol-d4. Absence of carboxylic acid proton at 12 ppm indicates complete conversion to cadmium carboxylate.*
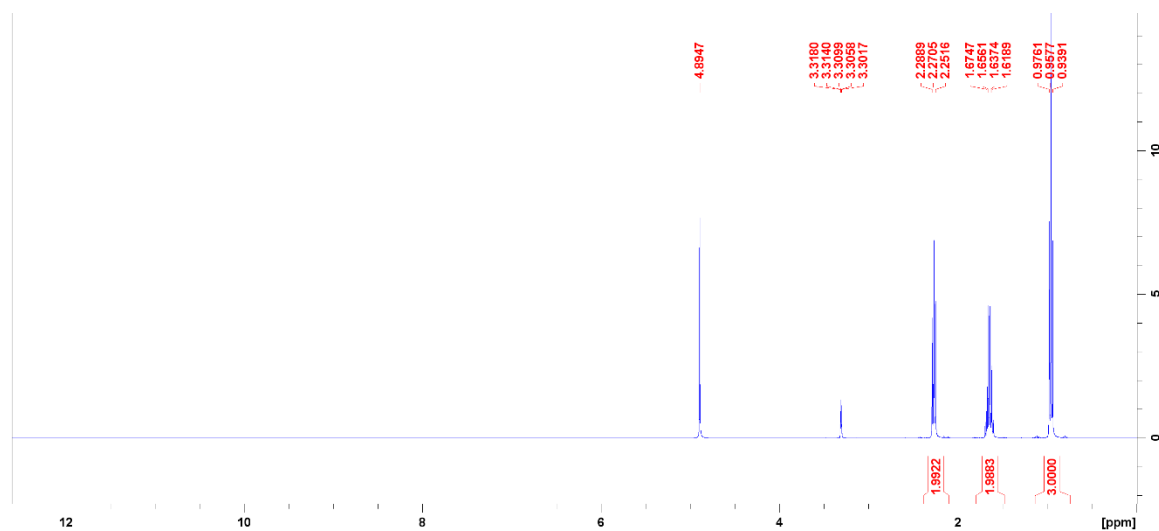
Figure 5.8 *^{1}H-NMR (400 MHz, r.t.) of cadmium butanoate in methanol-d4. Absence of carboxylic acid proton at 12 ppm indicates complete conversion to cadmium carboxylate.*
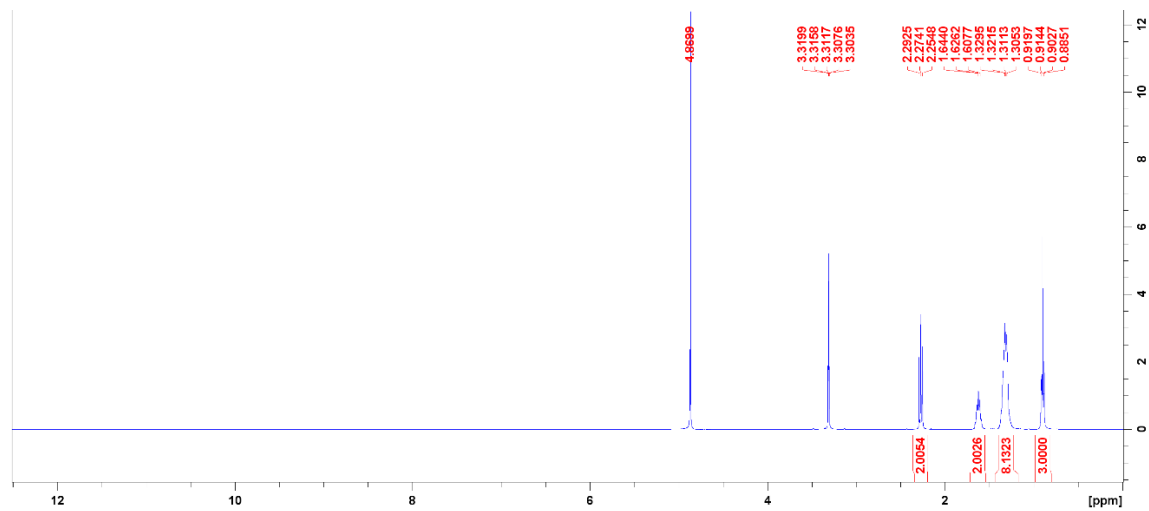
Figure 5.9. *¹H-NMR (400 MHz, r.t.) of cadmium octanoate in methanol-d4. Absence of carboxylic acid proton at 12 ppm indicates complete conversion to cadmium carboxylate.*

Time trace of 2 ML and 3 ML heavy hole excitonic features for fast and slow injection

a) Fast Injection of CdTe NPLs

b) Slow Injection of CdTe NPLs
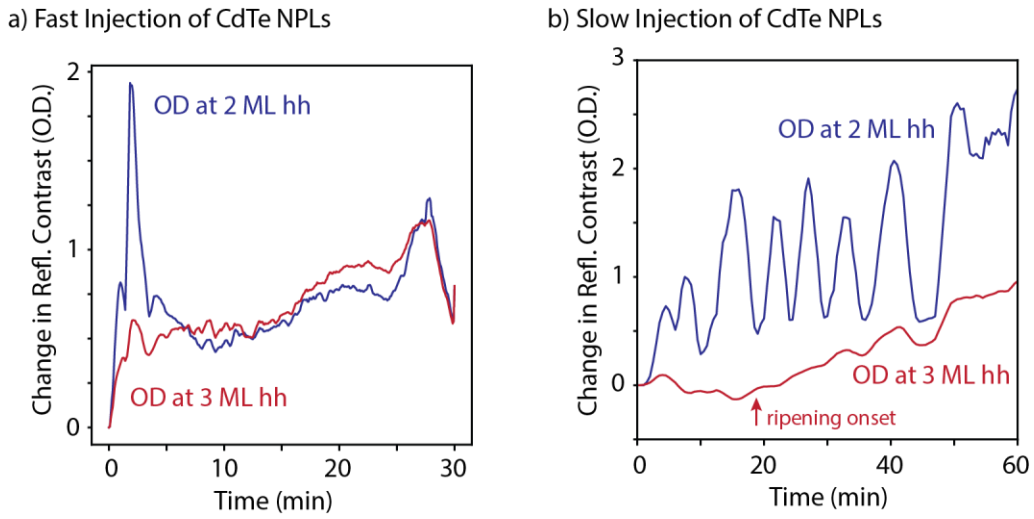
Figure 5.10. The change in optical density at the wavelength of the 2 ML and 3 ML heavy hole features for a) fast injection, and b) slow injection as each reaction proceeds. The 3 ML population is present at the start of the fast injection reaction, while the ripening onset that leads to the appearance of 3 ML in slow injection is indicated with an arrow.

Full 2D spectra for slow injection with cadmium propionate
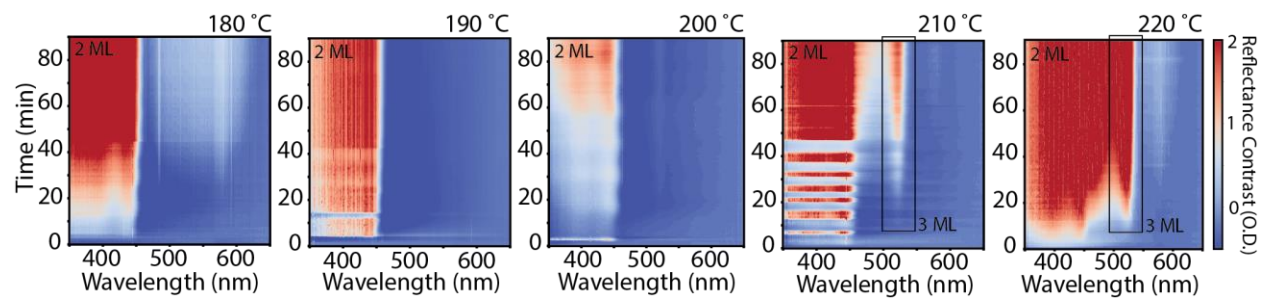
Figure 5.11. *The full 2D reflectance spectra for the cadmium propionate trials at increasing temperatures.*

Early Reaction Timepoints Showing Nucleation
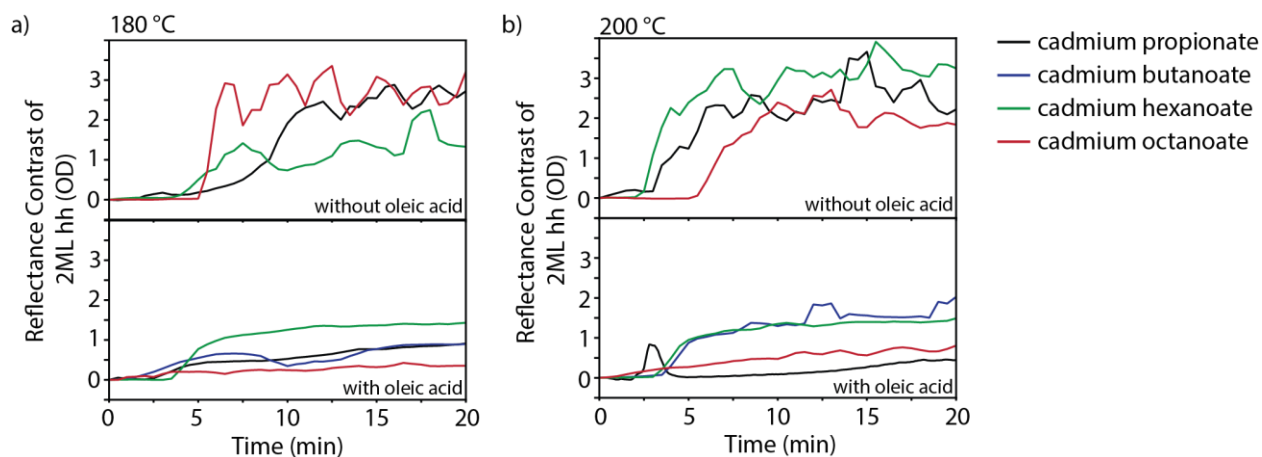
Figure 5.12. *Reflectance contrast of the 2 ML heavy hole over time for each cadmium precursor used. a) The slow injection reaction at 180 ºC both with and without oleic acid and b) the slow injection reaction at 200 ºC with and without oleic acid. The onset of 2 ML NPL formation occurs between 2.5-5 min for all reactions, but the OD is much stronger when oleic acid is excluded.*

TEM of each cadmium carboxylate synthesis with oleic acid

a) Cadmium Propionate
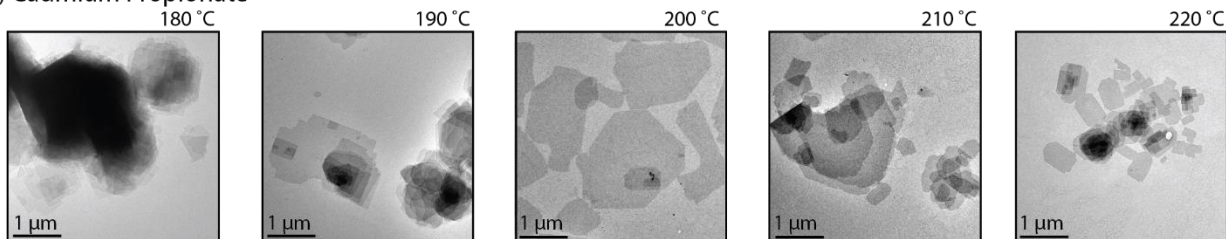
b) Cadmium Butanoate
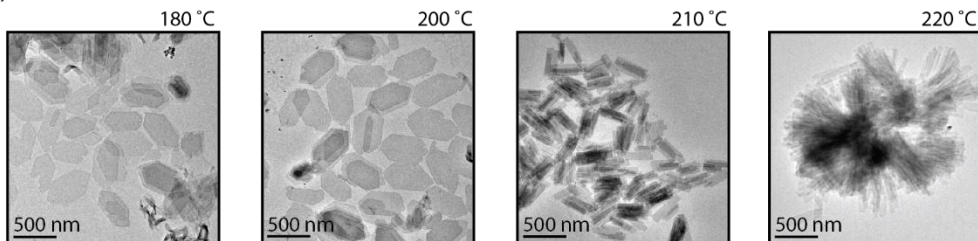
c) Cadmium Hexanoate
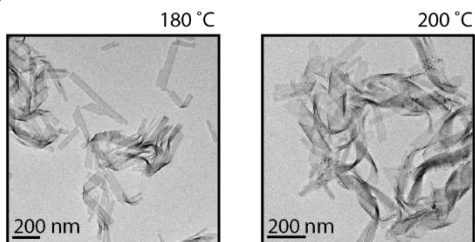
d) Cadmium Octanoate
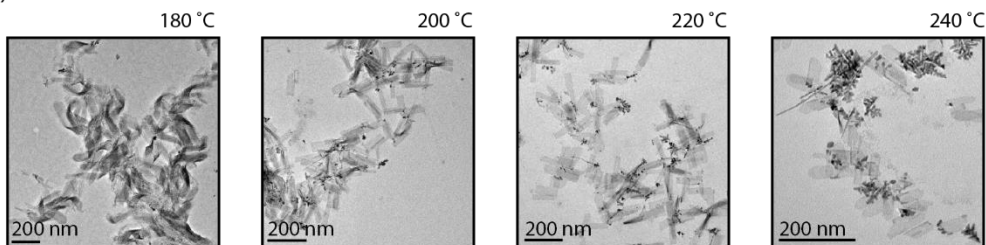
Figure 5.13. *TEM images accompanying the different conditions explored with oleic acid present in Figure 4. The precursors a) cadmium propionate, b) cadmium butanoate, c) cadmium hexanoate, and d) cadmium octanoate.*

TEM of each cadmium carboxylate synthesis without oleic acid

a) Cadmium Propionate

b) Cadmium Butanoate

c) Cadmium Hexanoate

d) Cadmium Octanoate
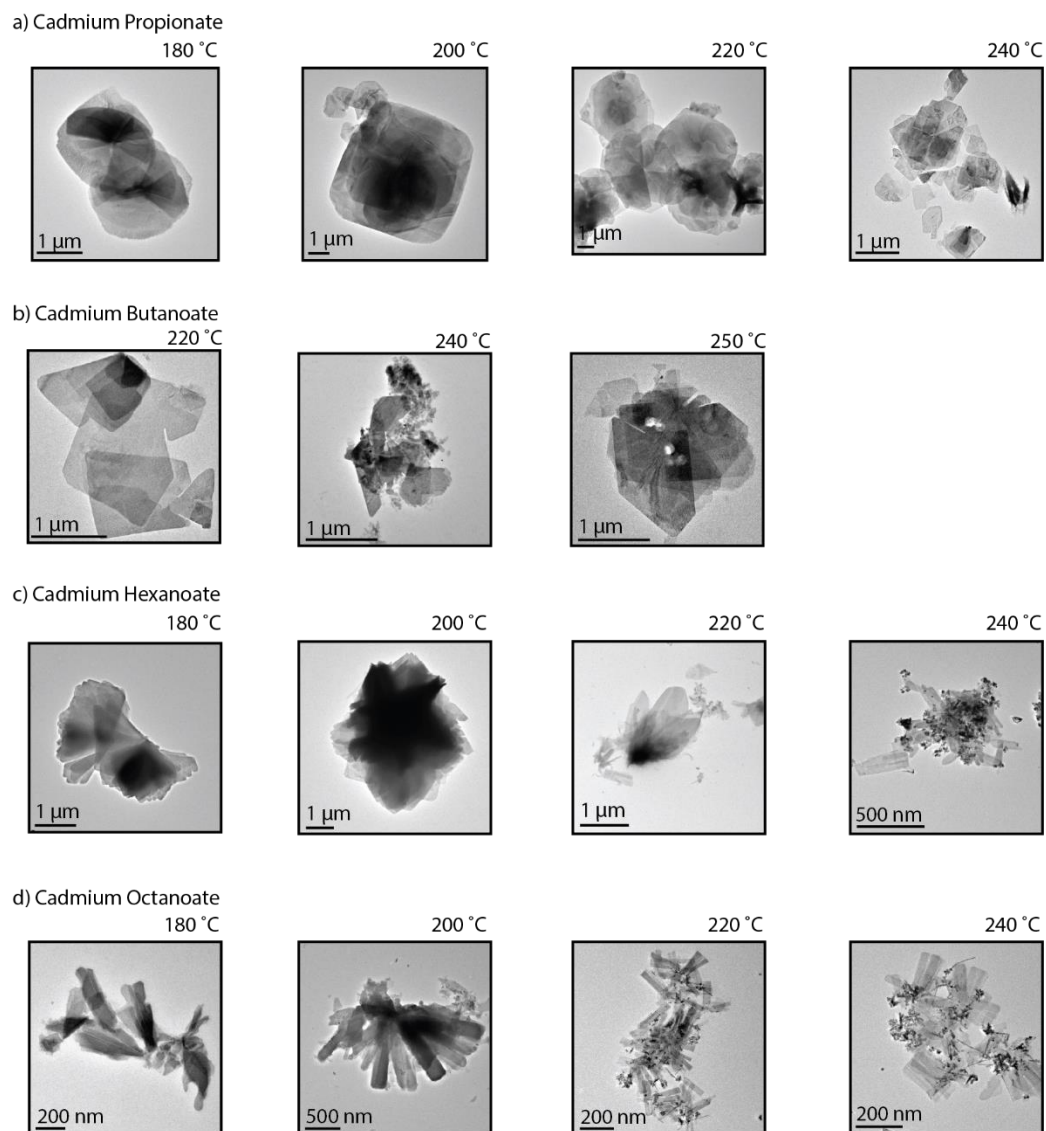
Figure 5.14. *TEM images accompanying the different conditions explored without oleic acid present in Figure 4. The precursors a) cadmium propionate, b) cadmium butanoate, c) cadmium hexanoate, and d) cadmium octanoate.*

Slow injection of CdSe without oleic acid

a) cadmium acetate
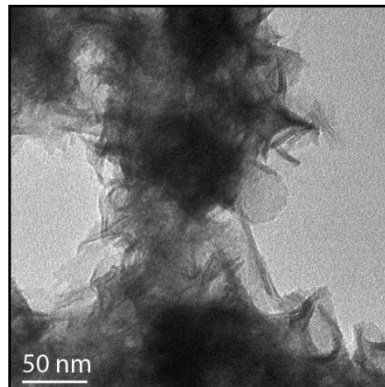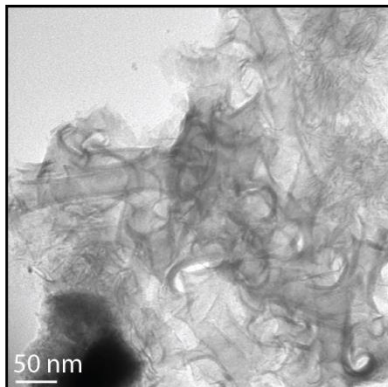
b) cadmium propionate
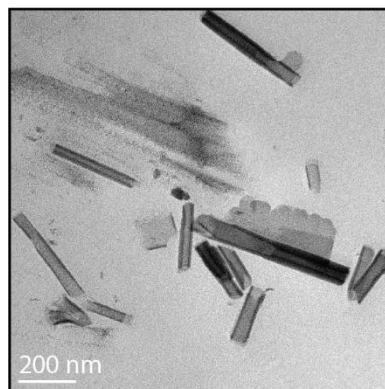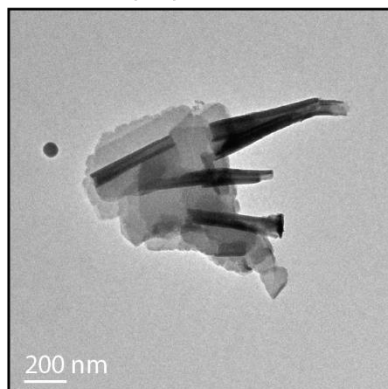
Figure 5.15. *CdSe NPLs synthesized in the absence of oleic acid. Both reactions were run at 195 ºC, but with different cadmium precursors: a) cadmium acetate, and b) cadmium propionate.*

Additional examples of Moiré patterns and fringes
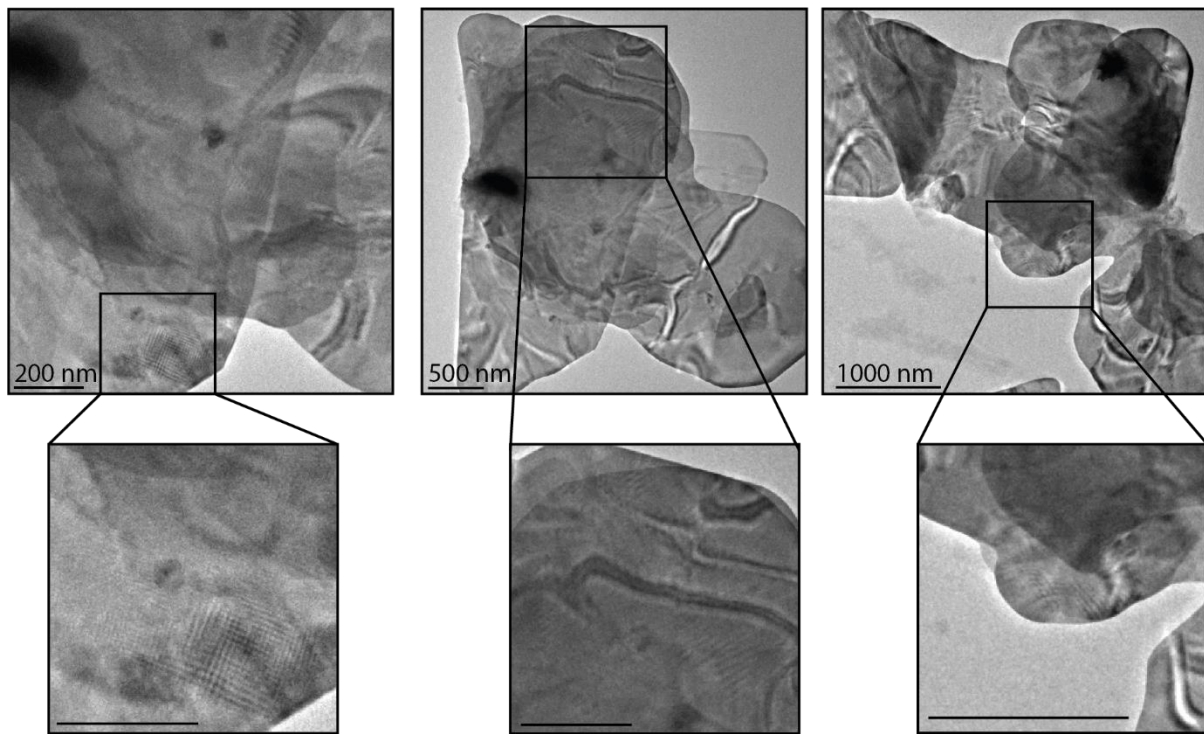
Figure 5.16. *TEM images of mesoscale NPLs highlighting regions where Moiré patterns and fringes can be observed.*
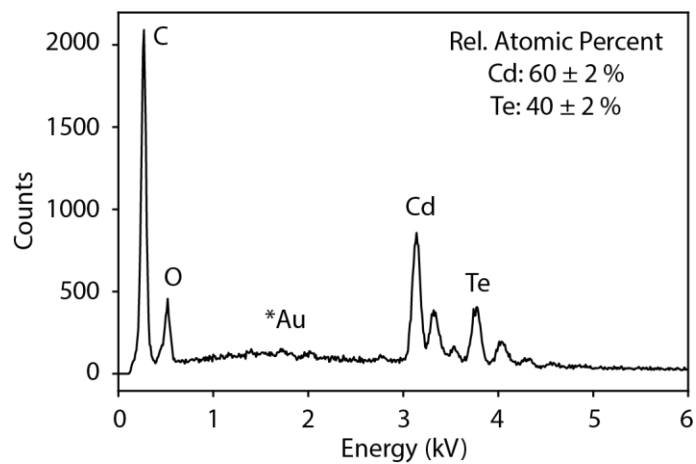
Figure 5.17. *Elemental composition of mesoscale NPLs obtained through SEM-EDS. The (*) indicates the substrate (gold coated Si wafer).*
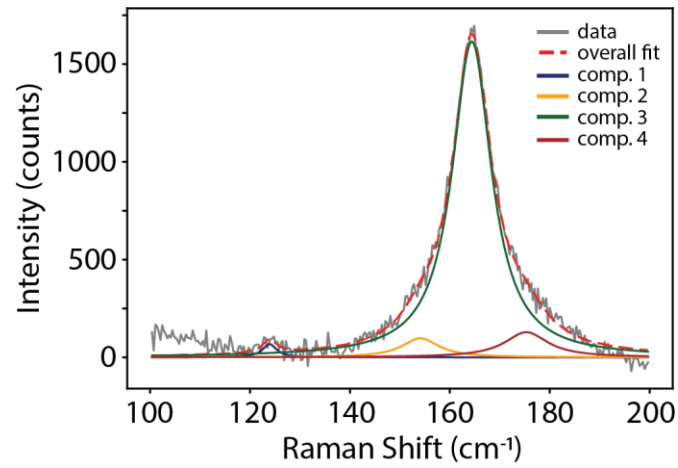
Figure 5.18. *The fitting of a concentrated film of mesoscale NPLs using four Lorentzian curves. The raw data (grey) can be approximated by the combination of these four curves (red, dashed) but we only analyze the main LO phonon frequency at 164.4 cm^{-1}.*

Full Raman Line Scan Results

a)

b)

c)
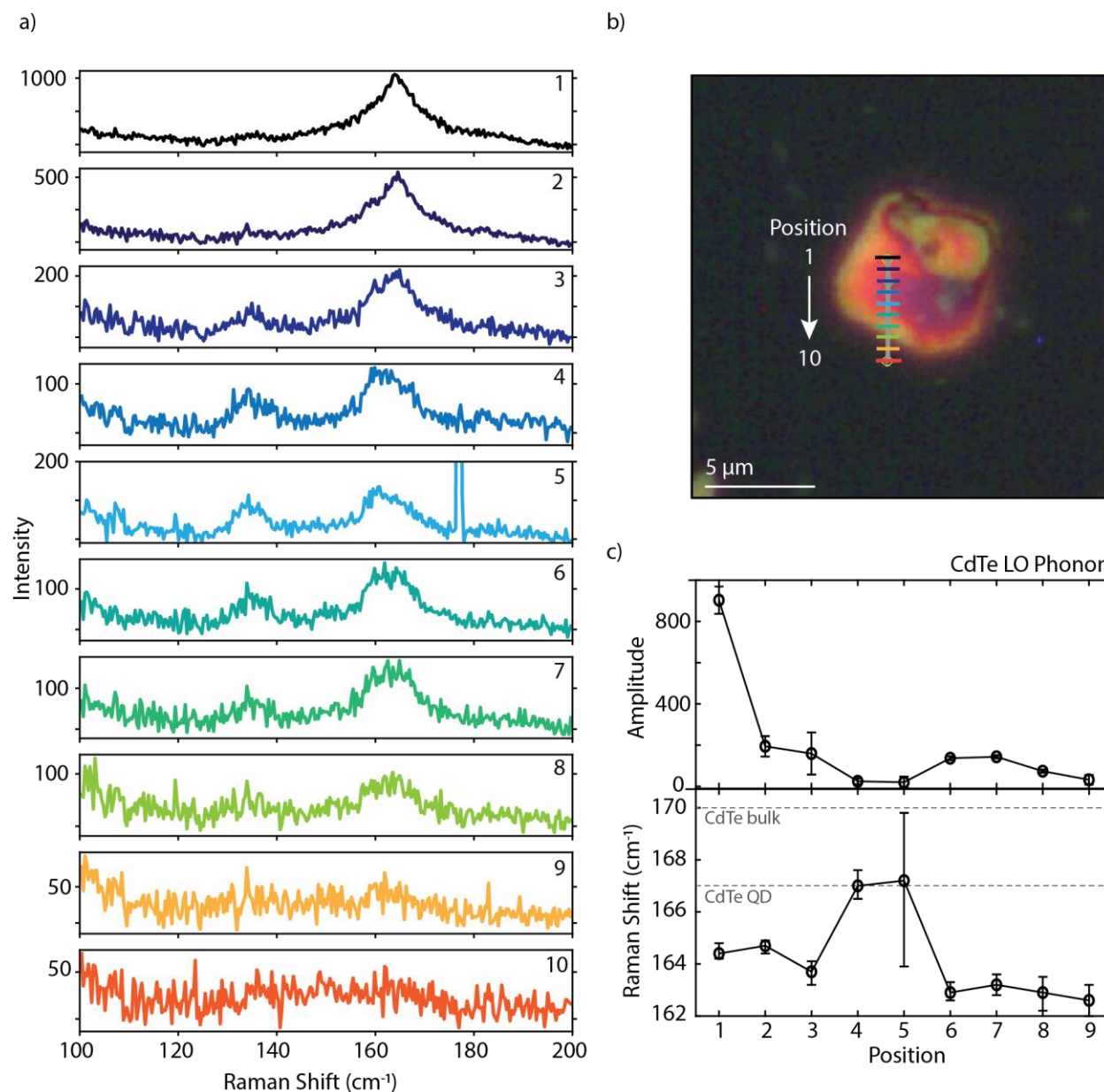
Figure 5.19. *The results of the Raman line scan at different points along the surface of the NPL. The full spectra a) show that the intensity of the features becomes weaker as the laser is scanned off of the edge of the NPL, b) from position 1 to 10 as shown in the image. c) Fitting of spectra 1-9 allows us to extract an approximate LO phonon frequency for each point. Although we observe an increase in frequency across the thicker portion of the NPL, the LO phonon shifts from higher frequencies at the center to lower frequencies at the edge.*

REFERENCES

(1)   Manzeli, S.; Ovchinnikov, D.; Pasquier, D.; Yazyev, O. V; Kis, A. 2D Transition Metal
        Dichalcogenides. *Nat. Rev. Mater.* **2017**, *2* (17033).

(2)   Chhowalla, M.; Jena, D.; Zhang, H. Two-Dimensional Semiconductors for Transistors.
        Nat. Rev. Mater. **2016**, *1* (11), 1–15.

(3)   Z. Butler, S.; M. Hollen, S.; Cao, L.; Cui, Y.; A. Gupta, J.; R. Gutiérrez, H.; F. Heinz, T.;
        Sae Hong, S.; Huang, J.; F. Ismach, A.; Johnston-Halperin, E.; Kuno, M.; V. Plashnitsa,
        V.; D. Robinson, R.; S. Ruoff, R.; Salahuddin, S.; Shan, J.; Shi, L.; G. Spencer, M.;
        Terrones, M.; Windl, W.; E. Goldberger, J. Progress, Challenges, and Opportunities in
        Two-Dimensional Materials Beyond Graphene. *ACS Nano* **2013**, *7* (4), 2898–2926.

(4)   Wang, Q. H.; Kalantar-Zadeh, K.; Kis, A.; Coleman, J. N.; Strano, M. S. Electronics and
        Optoelectronics of Two-Dimensional Transition Metal Dichalcogenides. *Nat.
        Nanotechnol.* **2012**, *7* (11), 699–712.

(5)   Beck, M. E.; Hersam, M. C. Emerging Opportunities for Electrostatic Control in
        Atomically Thin Devices. *ACS Nano* **2020**, *14* (6), 6498–6518.

(6)   Tenney, S. M.; Tan, L. A.; Sonnleitner, M. L.; Sica, A. V; Shin, A. J.; Ronquillo, R.;
        Ahmed, T.; Atallah, T. L.; Caram, J. R. Mesoscale Quantum-Confined Semiconductor
        Nanoplatelets through Seeded Growth. *Chem. Mater.* **2022**, *34* (13), 6048–6056.

(7)   Giovanella, U.; Pasini, M.; Lorenzon, M.; Galeotti, F.; Lucchi, C.; Meinardi, F.; Luzzati,
        S.; Dubertret, B.; Brovelli, S. Efficient Solution-Processed Nanoplatelet-Based Light-
        Emitting Diodes with High Operational Stability in Air. *Nano Lett.* **2018**, *18* (6), 3441–

3448.

(8)   Bai, P.; Hu, A.; Deng, Y.; Tang, Z.; Yu, W.; Hao, Y.; Yang, S.; Zhu, Y.; Xiao, L.; Jin, Y.; Gao, Y. CdSe/CdSeS Nanoplatelet Light-Emitting Diodes with Ultrapure Green Color and High External Quantum Efficiency. *J. Phys. Chem. Lett.* **2022**, *13* (39), 9051–9057.

(9)   Jana, S.; Martins, R.; Fortunato, E. Stacking-Dependent Electrical Transport in a Colloidal CdSe Nanoplatelet Thin-Film Transistor. *Nano Lett.* **2022**, *22* (7), 2780–2785.

(10)   Izquierdo, E.; Robin, A.; Keuleyan, S.; Lequeux, N.; Lhuillier, E.; Ithurria, S. Strongly Confined HgTe 2D Nanoplatelets as Narrow Near-Infrared Emitters. *J. Am. Chem. Soc.* **2016**, *138* (33), 10496–10501.

(11)   Anand, A.; L. Zaffalon, M.; Cova, F.; Pinchetti, V.; Hossain Khan, A.; Carulli, F.; Brescia, R.; Meinardi, F.; Moreels, I.; Brovelli, S. Optical and Scintillation Properties of Record-Efficiency CdTe Nanoplatelets toward Radiation Detection Applications. *Nano Lett.* **2022**, *22* (22), 8900–8907.

(12)   Shin, A. J.; Hossain, A. A.; Tenney, S. M.; Tan, X.; Tan, L. A.; Foley, J. J.; Atallah, T. L.; Caram, J. R. Dielectric Screening Modulates Semiconductor Nanoplatelet Excitons. *J. Phys. Chem. Lett.* **2021**, *12*, 4958–4964.

(13)   Yeltik, A.; Delikanli, S.; Olutas, M.; Kelestemur, Y.; Guzelturk, B.; Demir, H. V. Experimental Determination of the Absorption Cross-Section and Molar Extinction Coefficient of Colloidal CdSe Nanoplatelets. *J. Phys. Chem. C* **2015**, *119* (47), 26768–26775.

(14)   Nasilowski, M.; Mahler, B.; Lhuillier, E.; Ithurria, S.; Dubertret, B. Two-Dimensional

Colloidal Nanocrystals. *Chem. Rev.* **2016**, *116* (18), 10934–10982.

(15)   Ithurria, S.; Tessier, M. D.; Mahler, B.; Lobo, R. P. S. M.; Dubertret, B.; Efros, A. L. Colloidal Nanoplatelets with Two-Dimensional Electronic Structure. *Nat. Mater.* **2011**, *10* (12), 936–941.

(16)   Meerbach, C.; Wu, C.; Erwin, S. C.; Dang, Z.; Prudnikau, A.; Lesnyak, V. Halide-Assisted Synthesis of Cadmium Chalcogenide Nanoplatelets. *Chem. Mater.* **2020**, *32* (1), 566–574.

(17)   Christodoulou, S.; Climente, J. I.; Planelles, J.; Brescia, R.; Prato, M.; Martín-Garciá, B.; Khan, A. H.; Moreels, I. Chloride-Induced Thickness Control in CdSe Nanoplatelets. *Nano Lett.* **2018**, *18* (10), 6248–6254.

(18)   Ithurria, S.; Talapin, D. V. Colloidal Atomic Layer Deposition (c-ALD) Using Self-Limiting Reactions at Nanocrystal Surface Coupled to Phase Transfer between Polar and Nonpolar Media. *J. Am. Chem. Soc.* **2012**, *134* (45), 18585–18590.

(19)   Hazarika, A.; Fedin, I.; Hong, L.; Guo, J.; Srivastava, V.; Cho, W.; Coropceanu, I.; Portner, J.; T. Diroll, B.; P. Philbin, J.; Rabani, E.; Klie, R.; V. Talapin, D. Colloidal Atomic Layer Deposition with Stationary Reactant Phases Enables Precise Synthesis of "Digital" II–VI Nano-Heterostructures with Exquisite Control of Confinement and Strain. *J. Am. Chem. Soc.* **2019**, *141* (34), 13487–13496.

(20)   Zhang, F.; Wang, S.; Wang, L.; Lin, Q.; Shen, H.; Cao, W.; Yang, C.; Wang, H.; Yu, L.; Du, Z.; Xue, J.; Li, L. S. Super Color Purity Green Quantum Dot Light-Emitting Diodes Fabricated by Using CdSe/CdS Nanoplatelets. *Nanoscale* **2016**, *8* (24), 12182–12188.

(21)   Yang, Y.; Zhang, C.; Qu, X.; Zhang, W.; Marus, M.; Xu, B.; Wang, K.; Sun, X. W. High Quantum Yield Colloidal Semiconducting Nanoplatelets and High Color Purity Nanoplatelet QLED. *IEEE Trans. Nanotechnol.* **2019**, *18*, 220–225.

(22)   Dabard, C.; Guilloux, V.; Gréboval, C.; Po, H.; Makke, L.; Fu, N.; Xu, X. Z.; Silly, M. G.; Patriarche, G.; Lhuillier, E.; Barisien, T.; Climente, J. I.; Diroll, B. T.; Ithurria, S. Double-Crowned 2D Semiconductor Nanoplatelets with Bicolor Power-Tunable Emission. *Nat. Commun.* **2022**, *13* (1), 1–10.

(23)   Bertrand, G. H. V. V.; Polovitsyn, A.; Christodoulou, S.; Khan, A. H.; Moreels, I. Shape Control of Zincblende CdSe Nanoplatelets. *Chem. Commun.* **2016**, *52* (80), 11975–11978.

(24)   Gerdes, F.; Navío, C.; Juárez, B. H.; Klinke, C. Size, Shape, and Phase Control in Ultrathin CdSe Nanosheets. *Nano Lett.* **2017**, *17* (7), 4165–4171.

(25)   Di Giacomo, A.; Rodà, C.; Khan, A. H.; Moreels, I. Colloidal Synthesis of Laterally Confined Blue-Emitting 3.5 Monolayer CdSe Nanoplatelets. *Chem. Mater.* **2020**, *32* (21), 9260–9267.

(26)   Yoon, D. E.; Lee, J.; Yeo, H.; Ryou, J.; Lee, Y. K.; Kim, Y. H.; Lee, D. C. Atomistics of Asymmetric Lateral Growth of Colloidal Zincblende CdSe Nanoplatelets. *Chem. Mater.* **2021**, *33* (12), 4813–4820.

(27)   Riedinger, A.; Ott, F. D.; Mule, A.; Mazzotti, S.; Knüsel, P. N.; Kress, S. J. P.; Prins, F.; Erwin, S. C.; Norris, D. J. An Intrinsic Growth Instability in Isotropic Materials Leads to Quasi-Two-Dimensional Nanoplatelets. *Nat. Mater.* **2017**, *16* (7), 743–748.

(28)   Ott, F. D.; Riedinger, A.; Ochsenbein, D. R.; Knüsel, P. N.; Erwin, S. C.; Mazzotti, M.;

Norris, D. J. Ripening of Semiconductor Nanoplatelets. *Nano Lett.* **2017**, *17* (11), 6870–6877.

(29)   Knüsel, P. N.; Riedinger, A.; Rossinelli, A. A.; Ott, F. D.; Mule, A. S.; Norris, D. J. Experimental Evidence for Two-Dimensional Ostwald Ripening in Semiconductor Nanoplatelets. *Chem. Mater.* **2020**, *32* (7), 3312–3319.

(30)   Izquierdo, E.; Dufour, M.; Chu, A.; Livache, C.; Martinez, B.; Amelot, D.; Patriarche, G.; Lequeux, N.; Lhuillier, E.; Ithurria, S. Coupled HgSe Colloidal Quantum Wells through a Tunable Barrier: A Strategy to Uncouple Optical and Transport Band Gap. *Chem. Mater.* **2018**, *30* (12), 4065–4072.

(31)   Calvin, J. J.; Ben-Moshe, A.; Curling, E. B.; Brewer, A. S.; Sedlak, A. B.; Kaufman, T. M.; Alivisatos, A. P.; Alivisatos, A. P. Thermodynamics of the Adsorption of Cadmium Oleate to Cadmium Sulfide Quantum Dots and Implications of a Dynamic Ligand Shell. *J. Phys. Chem. C* **2022**, *126* (30), 12958–12971.

(32)   Nasilowski, M.; Spinicelli, P.; Patriarche, G.; Dubertret, B. Gradient CdSe/CdS Quantum Dots with Room Temperature Biexciton Unity Quantum Yield. *Nano Lett.* **2015**, *15* (6), 3953–3958.

(33)   Kim, T.; Jung, Y. K.; Lee, J. K. The Formation Mechanism of CdSe QDs through the Thermolysis of Cd(Oleate) 2 and TOPSe in the Presence of Alkylamine. *J. Mater. Chem. C* **2014**, *2* (28), 5593–5600.

(34)   Zhang, H.; Jing, L.; Zeng, J.; Hou, Y.; Li, Z.; Gao, M. Revisiting the Coordination Chemistry for Preparing Manganese Oxide Nanocrystals in the Presence of Oleylamine and Oleic Acid. *Nanoscale* **2014**, *6* (11), 5918–5925.

(35)   Choi, D.; Jeong, G. H.; Kim, S. W. Fabrication of Size and Shape Controlled Cadmium Oxide Nanocrystals. *Bull. Korean Chem. Soc.* **2011**, *32* (11), 3851–3852.

(36)   Asomaning, J.; Mussone, P.; Bressler, D. C. Thermal Deoxygenation and Pyrolysis of Oleic Acid. *J. Anal. Appl. Pyrolysis* **2014**, *105*, 1–7.

(37)   Asomaning, J.; Mussone, P.; Bressler, D. C. Pyrolysis of Polyunsaturated Fatty Acids. *Fuel Process. Technol.* **2014**, *120*, 89–95.

(38)   Maher, K. D.; Kirkwood, K. M.; Gray, M. R.; Bressler, D. C. Pyrolytic Decarboxylation and Cracking of Stearic Acid. *Ind. Eng. Chem. Res.* **2008**, *47* (15), 5328–5336.

(39)   J. Calvin, J.; A. O'Brien, E.; B. Sedlak, A.; D. Balan, A.; Paul Alivisatos, A. Thermodynamics of Composition Dependent Ligand Exchange on the Surfaces of Colloidal Indium Phosphide Quantum Dots. *ACS Nano* **2021**, *15* (1), 1407–1420.

(40)   Elimelech, O.; Aviv, O.; Oded, M.; Peng, X.; Harries, D.; Banin, U. Entropy of Branching Out: Linear versus Branched Alkylthiols Ligands on CdSe Nanocrystals. *ACS Nano* **2022**, *16* (3), 4308–4321.

(41)   Jiang, Y.; Ojo, W.-S.; Mahler, B.; Xu, X.; Abécassis, B.; Dubertret, B. Synthesis of CdSe Nanoplatelets without Short-Chain Ligands: Implication for Their Growth Mechanisms. *ACS Omega* **2018**, *3* (6), 6199–6205.

(42)   Pedetti, S.; Nadal, B.; Lhuillier, E.; Mahler, B.; Bouet, C. C.; Abécassis, B. A.; Xu, X.; Dubertret, B. Optimized Synthesis of CdTe Nanoplatelets and Photoresponse of CdTe Nanoplatelets Films. *Chem. Mater* **2013**, *25*.

(43)   Riedinger, A.; Mule, A. S.; Knüsel, P. N.; Ott, F. D.; Rossinelli, A. A.; Norris, D. J.

Identifying Reactive Organo-Selenium Precursors in the Synthesis of CdSe Nanoplatelets. *Chem. Commun.* **2018**, *54* (83), 11789–11792.

(44) A. Morin, S.; Forticaux, A.; J. Bierman, M.; Jin, S. Screw Dislocation-Driven Growth of Two-Dimensional Nanoplates. *Nano Lett.* **2011**, *11* (10), 4449–4455.

(45) Meng, F.; A. Morin, S.; Forticaux, A.; Jin, S. Screw Dislocation Driven Growth of Nanomaterials. *Acc. Chem. Res.* **2013**, *46* (7), 1616–1626.

(46) D. Golze, S.; Porcu, S.; Zhu, C.; Sutter, E.; Carlo Ricci, P.; C. Kinzel, E.; A. Hughes, R.; Neretina, S. Sequential Symmetry-Breaking Events as a Synthetic Pathway for Chiral Gold Nanostructures with Spiral Geometries. *Nano Lett.* **2021**, *21* (7), 2919–2925.

(47) Liu, L.; Sun, Y.; Cui, X.; Qi, K.; He, X.; Bao, Q.; Ma, W.; Lu, J.; Fang, H.; Zhang, P.; Zheng, L.; Yu, L.; Singh, D. J.; Xiong, Q.; Zhang, L.; Zheng, W. Bottom-up Growth of Homogeneous Moiré Superlattices in Bismuth Oxychloride Spiral Nanosheets. *Nat. Commun.* **2019**, *10* (1), 1–10.

(48) Susarla, S.; Sassi, L. M.; Zobelli, A.; Woo, S. Y.; Tizei, L. H. G.; Stéphan, O.; Ajayan, P. M. Mapping Modified Electronic Levels in the Moiré Patterns in MoS2/WSe2Using Low-Loss EELS. *Nano Lett.* **2021**, *21* (9), 4071–4077.

(49) Liao, Y.; Cao, W.; Connell, J. W.; Chen, Z.; Lin, Y. Evolution of Moiré Profiles from van Der Waals Superstructures of Boron Nitride Nanosheets. *Sci. Reports* **2016**, *6* (1), 1–10.

(50) Cao, Y.; Fatemi, V.; Fang, S.; Watanabe, K.; Taniguchi, T.; Kaxiras, E.; Jarillo-Herrero, P. Unconventional Superconductivity in Magic-Angle Graphene Superlattices. *Nat.* **2018**, *556* (7699), 43–50.

(51)   Jiang, Z.; Bhandari, G. B.; Premathilaka, S. M.; Khan, S.; Dimick, D. M.; Stombaugh, C.; Mandell, A.; He, Y.; Peter Lu, H.; Sun, L. Growth of Colloidal PbS Nanosheets and the Enhancement of Their Photoluminescence. *Phys. Chem. Chem. Phys.* **2015**, *17* (36), 23303–23307.

(52)   Dzhagan, V.; Lokteva, I.; Himcinschi, C.; Jin, X.; Kolny-Olesiak, J.; Zahn, D. R. Phonon Raman Spectra of Colloidal Cdte Nanocrystals: Effect of Size, Non-Stoichiometry and Ligand Exchange. *Nanoscale Res. Lett.* **2011**, *6* (1), 1–10.

(53)   Lebedev, A. I. Lattice Dynamics of Quasi-Two-Dimensional CdSe Nanoplatelets and Their Raman and Infrared Spectra. *Phys. Rev. B* **2017**, *96*, 184306.

(54)   Sigle, D. O.; Hugall, J. T.; Ithurria, S.; Dubertret, B.; Baumberg, J. J. Probing Confined Phonon Modes in Individual CdSe Nanoplatelets Using Surface-Enhanced Raman Scattering. *Phys. Rev. Lett.* **2014**, *113* (8), 087402.

(55)   Lin, C.; F. Kelley, D.; Rico, M.; Myers Kelley, A. The "Surface Optical" Phonon in CdSe Nanocrystals. *ACS Nano* **2014**, *8* (4), 3928–3938.

(56)   Dzhagan, V. M.; Lokteva, I.; Valakh, M. Y.; Raevska, O. E.; Kolny-Olesiak, J.; Zahn, D. R. T. Spectral Features above LO Phonon Frequency in Resonant Raman Scattering Spectra of Small CdSe Nanoparticles. *J. Appl. Phys.* **2009**, *106* (8), 084318.

(57)   Dzhagan, V.; Lokteva, I.; Himcinschi, C.; Jin, X.; Kolny-Olesiak, J.; Zahn, D. R. Phonon Raman Spectra of Colloidal Cdte Nanocrystals: Effect of Size, Non-Stoichiometry and Ligand Exchange. *Nanoscale Res. Lett.* **2011**, *6* (1).

(58)   I. Lebedev, A.; M. Saidzhonov, B.; A. Drozdov, K.; A. Khomich, A.; B. Vasiliev, R.

Raman and Infrared Studies of CdSe/CdS Core/Shell Nanoplatelets. *J. Phys. Chem. C* **2021**, *125* (12), 6758–6766.

(59) Llusar, J.; Planelles, J.; I. Climente, J. Strain in Lattice-Mismatched CdSe-Based Core/Shell Nanoplatelets. *J. Phys. Chem. C* **2019**, *123* (34), 21299–21306.

(60) Girard, A.; Saviot, L.; Pedetti, S.; Tessier, M. D.; Margueritat, J.; Gehan, H.; Mahler, B.; Dubertret, B.; Mermet, A. The Mass Load Effect on the Resonant Acoustic Frequencies of Colloidal Semiconductor Nanoplatelets. *Nanoscale* **2016**, *8* (27), 13251–13256.

(61) Martinet, Q.; Baronnier, J.; Girard, A.; Albaret, T.; Saviot, L.; Mermet, A.; Abecassis, B.; Margueritat, J.; Mahler, B. Ligand-Dependent Nano-Mechanical Properties of CdSe Nanoplatelets: Calibrating Nanobalances for Ligand Affinity Monitoring. *Nanoscale* **2021**, *13* (18), 8639–8647.

Chapter 6

Unpublished Work and Additional Considerations

In this chapter, we outline a handful of preliminary data or projects that, while useful for our general understanding of our materials, were not applicable or developed enough for publication. These sections are primarily synthetic observations or techniques but also describe experiments that were insightful but unsuccessful.

6.1 Unpublished work on HgTe NPLs

Slowing the growth of HgTe QDs to isolate HgTe NPL Band-Edge PL

Throughout our cation exchange reactions from CdTe to HgTe NPLs, we observe that the formation of HgTe QDs occurs very quickly. In certain cases, such as when characterizing the HgTe NPLs it is more desirable to prevent the growth of the NPL/QD heterostructure. To do so we attempted three different methods: 1) passivation with oleic acid to re-cover the surfaces and prevent any attachment or growth, 2) cast the sample into a polymer film, and 3) store the sample at low temperatures. The most ideal method would be re-passivation as it would allow the NPLs to remain suspended in solution and easily separated from QDs if they did begin to nucleate as they would not be attached to the surfaces. Unfortunately, by adding neat oleic acid the NPLs readily degraded—they are sensitive to acid, base, or polar solvents. It may be possible to re-passivate them through an excess of mercury oleate however, as the cation exchange removed some of the surface metal atoms (this may even improve or reduce defect sites). Casting the NPLs into a polymer film by using ~5% PMMA in toluene and mixing with HgTe NPLs in hexanes with a 1:5 ratio PMMA:NPL was successful in slowing the QD growth. We found this useful for photoluminescence and temperature-dependent data where we needed the sample to remain

constant for extended periods of time. Finally, we also observed that storage of the solution in a freezer or on ice will slow but not stop the growth of HgTe QDs. This was useful in situations where multiple sample measurements needed to be taken in succession but did not permanently stop the growth of QDs.

6.2 Unpublished work on CdTe NPLs

Attempts at Colloidal Atomic-Layer Deposition and Capping with CdS

We became interested in exploring alternative methods for growing CdTe NPLs thicker than 3 ML, as direct synthesis has limitations based on the precursors used. This would possibly give access to cation exchange towards thicker HgTe as well as more spectral tunability. We were also interested in creating core-shell NPLs consisting of a CdTe core with a CdS shell as an inorganic layer to passivate defects and improve quantum yields, as well as reduce the aggregation that occurs when using organic fatty acid ligands. We attempted shell growth based on literature precedent for CdSe/CdS QDs and colloidal ALD based on literature for CdSe NPLs.[1–3] For shelling reactions, briefly we degassed a solution of CdTe NPLs in the presence of cadmium oleate before raising the temperature to 300 C under argon. We then injected a solution of octanethiol in octadecene and held the solution at the elevated temperature for 10 min. After centrifugation and washing of the solution, we determined that this method simply formed CdS nanocrystals rather than shelling the CdTe NPLs. We did observe that the CdTe NPLs had a red-shifted absorption and concluded that the thiol was capping the NPLs as a ligand, but not proceeding to form a CdS shell. When attempting colloidal ALD to add a CdS layer, we first exchanged the NPLs into an ammonium sulfide (NH_4S) in DMF solution and observed that the first addition of S was successful by color change to red. The NPLs rapidly turned brown, however and degraded before they were

able to be transferred to the solution of cadmium acetate for the next layer. The isolation of the brown product showed no PL, and we were unable to complete one full layer of CdS.
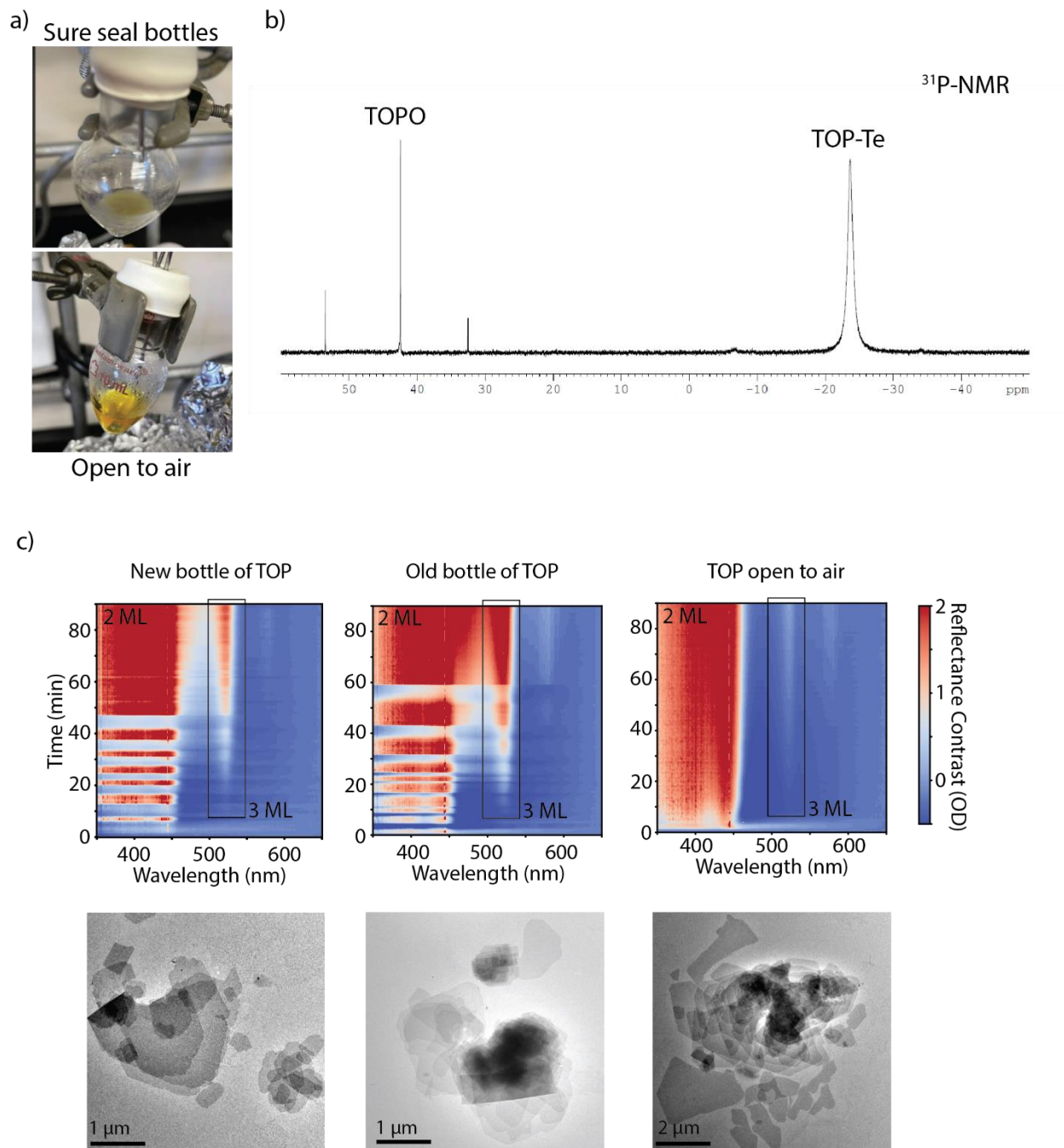
Figure 6.1. *The effect of TOP-Te purity on CdTe NPL growth. a) The TOP-Te reagent can range in color from cloudy yellow to clear orange depending on the TOP source used. b) Phosphorus NMR shows that the major product is TOP-Te, but TOPO is still present as an impurity. We*

became interested to see if TOPO impurities influenced c) NPL size but saw no consistent size control with increasing exposure of TOP precursor to air.

Effect of Tri-octylphosphine (TOP) reagent Purity on Ripening

When exploring the slow injection synthesis of CdTe NPLs, we observed that the TOP-Te reagent varied drastically in color depending on the TOP used to prepare the solution. It ranged from grey (when not fully formed) to yellow, to orange (Figure 6.1a) and began developing a white precipitate over time despite being stored in an air-free flask. As impurities in the TOP reagent has been shown to affect reactivity and morphology in nanocrystal reactions, we were interested in exploring if it had any effect on the shape or size of our CdTe NPLs.[4,5] We examined three different bottles of TOP, two stored under Ar with a sure seal (one fresh one aged), and one bottle completely open to air. Through phosphorus NMR, we identified that the main impurity in TOP-Te from each bottle is the oxide TOPO (Figure 6.1b), however it appeared in similar amounts for each case despite varying exposure of the TOP precursor to air. When comparing how these TOP-Te reagents affect the slow injection dynamics (Figure 6.1c), we were unable to find a consistent trend—the onset of ripening was nearly identical for TOP-Te from fresh vs aged sure seal bottles and ripening still occurred from the completely open bottle but to a lesser extent. In all cases, the morphology of the final product was very similar, and we decided to look more closely at the cadmium precursor as the TOP-Te purity did not seem to provide control over shape. It could be possible, however, that using alternative phosphine precursors will affect the reactivity of the phosphine telluride and change the driving force for lateral growth.

Conditions for Device Preparation

As a preliminary step towards preparing our mesoscale NPLs for device measurements, we explored various conditions for casting a solution of NPLs onto a substrate to maintain seperation

232

but still a high enough density to observe particles. This was also useful for correlative imaging, SEM measurements etc. While we found that spin coating is most ideal for uniform coverage of NPLs, we observed clear seperation of particles simply by drop-casting a solution onto either glass or silicon wafer. As a metric, we kept the concentrations to be about 1 drop of 26 mM CdTe NPL solution into about 2-3 mL of hexanes. The color of the solution was just barely visible by eye. This gave separation as seen in Figure 5.6 but was diluted further for single particle photophysical measurements in Chapter 4. For measurement of single particles, we also want to avoid stacking or aggregation which is especially problematic for CdTe. For the largest mesoscale NPLs in chapter 5, we attempted to separate the stacks by sonication and treatment with long chain oleic acid after synthesis but were unsuccessful. Therefore, to isolate single NPLs it may be necessary to treat them similarly to VdW materials and use mechanical exfoliation.

6.3 Other Practical Considerations

NPLs are easily characterized in either solution or film because they are readily exchanged into different solvent systems or simply drop/spin cast and dried. Their films commonly have residual oils from organic ligands and solvents which is undesirable for achieving resolution in imaging and leaves impurity traces in measurements such as FTIR. For QDs, these impurities are easily removed through subsequent washings, but CdTe and HgTe NPLs are more sensitive to degradation with rigorous washing, and it is challenging to clean them thoroughly. We found that an optimal method for removing small impurities is through utilizing syringe filtration. With a filter pore size less than 200 nm (typically 50 nm), the NPLs are collected on the inside of the filter while the solution containing extra ligand or solvent can be passed through. Backwashing the filter with clean hexanes or solvent will then resuspend the NPLs and this process can be repeated. The yield will be significantly lower than the initial concentration because many NPLs will remain

stuck to the filter, but this process is gentle enough to maintain passivation and avoid degradation while cleaning the solvent of residual oils.

REFERENCES

(1)   Ithurria, S.; Talapin, D. V. Colloidal Atomic Layer Deposition (c-ALD) Using Self-Limiting Reactions at Nanocrystal Surface Coupled to Phase Transfer between Polar and Nonpolar Media. *J. Am. Chem. Soc.* **2012**, *134* (45), 18585–18590.

(2)   Chen, O.; Zhao, J.; Chauhan, V. P.; Cui, J.; Wong, C.; Harris, D. K.; Wei, H.; Han, H. S.; Fukumura, D.; Jain, R. K.; Bawendi, M. G. Compact High-Quality CdSe–CdS Core–Shell Nanocrystals with Narrow Emission Linewidths and Suppressed Blinking. *Nat. Mater.* **2013**, *12* (5), 445–451.

(3)   Hanifi, D. A.; Bronstein, N. D.; Koscher, B. A.; Nett, Z.; Swabeck, J. K.; Takano, K.; Schwartzberg, A. M.; Maserati, L.; Vandewal, K.; van de Burgt, Y.; Salleo, A.; Alivisatos, A. P. Redefining Near-Unity Luminescence in Quantum Dots with Photothermal Threshold Quantum Yield. *Science.* **2019**, *363* (6432), 1199–1202.

(4)   M. Evans, C.; E. Evans, M.; D. Krauss, T. Mysteries of TOPSe Revealed: Insights into Quantum Dot Nucleation. *J. Am. Chem. Soc.* **2010**, *132* (32), 10973–10975.

(5)   Wang, F.; Tang, R.; E. Buhro, W. The Trouble with TOPO; Identification of Adventitious Impurities Beneficial to the Growth of Cadmium Selenide Quantum Dots, Rods, and Wires. *Nano Lett.* **2008**, *8* (10), 3521–3524.

Chapter 7

Critiquing Lab Technique Videos Prior to Class. Can it Improve Demonstrated Technique?

This chapter contains unpublished work by Stephanie Tenney, Jennifer Casey, and Arlene Russell.

This chapter focuses on educational research conducted in the general chemistry lab courses for life science majors at UCLA. During COVID-19 remote instruction, instructors were tasked with providing students with authentic laboratory experiences in an out-of-class learning environment. One solution developed for our introductory general chemistry laboratory involved students critiquing several technique videos with the intention to distinguish between correct and incorrect laboratory technique. Since returning to in-person labs in Fall 2021, we have incorporated this assessment into the pre-lab assignments in an effort to reduce the cognitive load of learning a new technique. We explored whether this critical review exercise translates to improved technique (as measured by precision and accuracy when using a 10-mL volumetric pipet) as well as if it improved technique in instances when TA involvement in a lab section is low. We define TA involvement as engaging with students by demonstrating or correcting techniques during the experiments. We found that while students self-report the exercise as useful towards their learning, there are no significant changes in performance for most students. However, we did find a reduction in the overall outliers as well as a significant improvement in sections with low TA involvement (compared to those with high TA involvement), highlighting that the exercise is most useful for students who make large errors and who receive little individualized feedback.

7.1 Introduction to the Role of Chemistry Laboratory and Development of Skills

The development of laboratory skills is seen as a critical aspect of STEM undergraduate education. For instance, in order for a chemistry department to grant an ACS-certified bachelor's degree, students are required to complete 400 hours of laboratory work.[1] The chemistry lab is viewed as a place where important skills can be developed, such as problem solving, safety awareness, communication, and teamwork. While there may not be complete consensus on the purpose of laboratory practice,[2,3] many agree that lab is a place where students can learn technical skills.[4,5] The focus on the development of technical skills is to ensure that graduates can safely and accurately work in a laboratory environment, as dictated by the Quality Assurance Agency.[6] Unfortunately, employers often feel that graduates do not possess these required skills.[7–9]

Much effort has gone towards improving the technical skills of students. According to a comprehensive review conducted by DeMeo, this includes performing live demonstrations, providing opportunities for practice, assigning pre-lab activities, and engaging in "elbow instruction."[10] The use of pre-lab activities has been particularly popular, given that the preparation availed by the pre-lab may allow for more meaningful learning to occur during the lab itself.[11] While pre-laboratory assignments vary in terms of focus, they frequently include video demonstrations of equipment usage. Many studies indicate that assigning pre-lab activities can be beneficial; students who complete pre-lab assignments tend to be more efficient in the lab, receive higher assessment scores, and feel an increase in self-confidence.[12–15]

With that said, it is unclear if these efforts are resulting in better lab technique. A recent study done by Sanchez applied quality control methods to assess student laboratory results.[16] The labs under investigation required the use of basic laboratory skills (e.g., weighing, solution preparation, use of volumetric equipment), yet a surprisingly large number of results were considered incorrect or questionable - this was despite the fact that students were enrolled in upper-division lab courses and had received 240 to

330 hours of lab training. The primary source of error came from poor lab skills, either from improper weighing procedures or the incorrect use of volumetric glassware.

Part of the difficulty stems from misalignment between instructor goals and assessments. Lab technique is often not evaluated nor graded, making it difficult for students to recognize the importance of mastering these skills.[3] While instructors see the lab as place to improve technical proficiency, students tend to be more concerned about finishing the lab quickly, thereby forgoing opportunities to improve their technique.[17] In an attempt to address this issue, some instructors have begun to explicitly incorporate skills assessment into the laboratory. This includes the lab practical,[18] digital badging,[19–21] and structured chemistry examinations (SChemES).[22] While the implementation varies for each of these methods, all require students to demonstrate specific lab skills, either in person or through videos.

7.2 Motivation for This Study

With the start of the COVID-19 pandemic and the abrupt transition to remote learning, chemistry students around the world were denied the key essence of lab: "the lab must allow students to make [their own] observations and measurements and then seek to interpret them."[23] Despite our best efforts, our students were unable to practice important manipulative skills such as quantitatively transferring materials or making solutions of precise concentrations. In the absence of in-person labs, lab faculty at our university fell back on the 40-year-old practice of showing students how to do the lab via videos – an instructional practice pioneered by one of the PI's.[24] We embedded videos into our LMS and had students view them prior to analyzing artificial data; however, students were unable to assess the mastery of their technique as evidenced by the accuracy and precision of their own data.

In an effort to better align our teaching beliefs with our practices,[25] we decided to change the modality of the video instruction so that students could evaluate multiple videos to assess each for the many nuanced and subtle steps involved in mastering a specific technique. In effect, our students became evaluators rather than performers for digital badges. Students were shown two to three videos of people

demonstrating the use of a particular piece of equipment, (e.g., volumetric pipet, volumetric flask); one of these videos was an exemplar, while the others contained some small mistakes. Students were also given a detailed rubric outlining the procedural steps that must be performed to use the piece of equipment both accurately and precisely (see Supporting Information for an example). Students then evaluated each video based on the rubric.

When in-person classes resumed, we were interested in continuing the critical evaluation of lab technique, but now as part of a pre-lab report. Prior student data showed wide deviations in both accuracy and precision– results that far exceeded the manufacturer's tolerance for the equipment and gave rise to meaningless results that were difficult to interpret. Our hypothesis was that with this additional scaffolding, students could better learn the detailed steps required to master these techniques, resulting in increased accuracy and precision. A similar experiment was performed by Accettone et al., where students were given two technique videos, one of which showed the technique performed properly while the other video contained mistakes.[26] Students were asked to distinguish between the two videos, as well as identify the errors and the potential consequences of these errors. Students viewed the activity positively and generally reported feeling more confident in performing the technique in lab, but the study did not discuss whether student technique improved as a result of the intervention.

The majority of studies interested in improving student technique focus on student experience,[13,14,19–21] and for those studies that do consider technique as an outcome, the emphasis tends to be on general observations and analysis of a final result that relies on a combination of techniques.[15,27,28] For this reason, we wanted to investigate the impact our intervention had specifically on student mastery of a particular technique. We chose the use of a 10-mL volumetric pipet since this is a critical skill that students are known to struggle with,[16,29] and the accuracy and precision can easily be determined and is directly connected to correct usage of the equipment.

7.3 Theoretical Framework: Cognitive Load Theory

Cognitive load theory forms the basis for our premise that an incremental rather than a holistic approach will improve student learning of lab techniques.[30] It is understood that learning which consists of high element interactivity (i.e., learning that requires connecting a large number of elements) increases cognitive load. For this type of learning, it is critical that we find effective instructional methods to reduce the overall cognitive load associated with the task. A few such techniques include implementing a goal-free strategy or using worked examples that clearly outline necessary steps. The laboratory is well known for being an environment that can induce cognitive overload, and this is in fact one of the reasons why pre-laboratory activities are commonly implemented.[31,32] But in watching a technique video, a student must assimilate multiple individual manipulative steps each with its own set of sub-technique procedures. Even more challenging, students must distinguish these specific steps themselves. The hope is that students can separate the 'noise' from the 'message', but that can be quite challenging for a novice. Cognitive load research tells us that, at best, working memory can retain seven, usually fewer, items particularly if the task is complex.[33]

It is for these reasons that Johnstone and El-Banna initially recommended sequencing a procedure into steps.[34] However rather than focus on the procedural steps of an entire experiment, we characterized the ten distinct manipulative steps required for successful pipetting (see Supporinting Information). By having students critically evaluate technique videos following the steps outlined, we hoped to reduce the cognitive load associated with learning how to properly pipet and, therefore, improve student pipetting technique. The use of an exemplary video followed by a video containing errors was based in part on work by Hendry, which highlights exemplars as a means for students to better understand expectations before performing a task.[35,36] We decided to also incorporate a video that contained errors as this simulates the process of peer review, which can engage students in reflection on their own work.[37]

7.4 Research Questions

1) Does becoming a critical reviewer of multiple procedure videos translate into improved technique (as measured by precision and accuracy when using a 10-mL volumetric pipet) compared to passively watching an exemplary video?

2) Does critical watching of procedure videos result in better technique in instances when a student's TA has low involvement in their lab section?

7.5 Methods

Study Setting. The study occurred at a public research university in the southwest United States during the Winter 2019 and Fall 2021 quarters. The study focused on the first chemistry laboratory class taken in the chemistry series designed for Life Science majors. The breakdown of students was: 11.3 % first year, 68.0 % second year, 18.4 % third year, and 2.3 % fourth year for Winter 2019, and 3.5 % first year, 75.4 % second year, 17.2 % third year, and 4.0 % fourth year for Fall 2021. This course is not necessarily taken concurrently with general chemistry; the second quarter of general chemistry is a co- or pre-requisite. The course consists of a 50-minute lecture and 170-minute lab each week during a ten-week quarter. The lecture is focused on exploring the chemistry concepts behind the experiments, while the lab section is focused on performance of the experiments and data collection. The lab sections are run by graduate teaching assistants (TAs), who usually give a short (~10 min) presentation on the experiment. Data analysis is done outside of the lab, and lab reports are submitted weekly. The course consists of a midterm and final exam but does not involve any lab practical. IRB approval (#21-001672) was obtained for the collection of student data within this study.
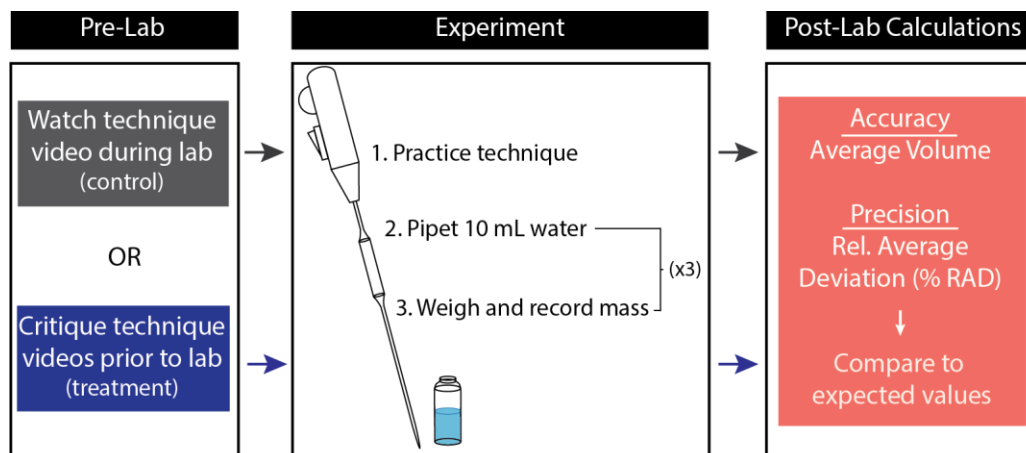
Figure 7.1. The comparison of two student groups evaluated in this study. The control group was shown a single technique video at the start of lab while the treatment group completed a critique of two technique videos before attending lab. Both groups completed the same pipetting lab and calculated the same values in their post-lab assignments.

Pipetting Experiment. The pipetting experiment (Figure 7.1) begins by first practicing the transfer of water using a 10-mL volumetric pipet. Once students feel they have had sufficient practice, students (1) weigh three empty vials on an analytical balance, (2) transfer a 10-mL aliquot of water to each vial using the 10-mL volumetric pipet, and (3) re-weigh the vials that now contain the 10-mL aliquots of water. During the lab section, students record the weights of the empty vials, the weights of the vials with the 10-mL aliquot of water, and the temperature of the water. In the post-lab report, students are asked to convert the weight of water transferred to volume using the appropriate density given the water temperature, and then to calculate the average volume transferred as well as the percent relative average deviation (%RAD).

Implementation of Video Critique Pre-Lab Assignment. In Winter 2019, the lecture and lab sections were taught in-person. The pre-lab assignment for the pipetting experiment consisted of filling in a partially completed flowchart and noting what values would be recorded during the lab period as well as what calculations would be required after completing the experiment. During the lab period, the TAs were instructed to show an exemplary technique video on pipetting before students attempted the experiment.[38] This cohort contained 434 students and will be known as the "control group."

241

In Fall 2021, the lecture and lab sections were also taught in-person. The pre-lab assignment for the pipetting experiment consisted of a drag-and-drop flowchart, followed by two technique videos (both were implemented through our university LMS). Students were asked to watch the technique videos and then determine whether ten critical steps of pipetting were performed correctly (listed in detail in the Supporting Information). The first technique video students were given was the same exemplary video used in Winter 2019. The second video was randomly assigned.[39–42] Students had a week before their lab section met to complete the assignment, and three attempts of the pre-lab assignment were allowed. The TAs were not asked to show the students any technique videos during the lab section. This cohort contained 451 students and will be known as the "treatment group."

Collection of Student Data. Although students calculated the average volume and %RAD within their post-lab report, the raw values recorded for weight of water were tabulated for each student, and the %RAD and average volume were recalculated for this study to avoid potential student calculation errors. A temperature of 20 °C was assumed. Student feedback about the usefulness of the pre-lab assignment was collected through an instructor-designed anonymous mid- and end-of-course surveys with a 73% response rate.

TA Evaluation. All TAs included in this study participated in a required general training program through the chemistry department (30 hr. total), in addition to weekly TA meetings for the specific course to discuss the experiments and logistics. While formal TA evaluations were collected by the university, the instructors created their mid-quarter and end-of-quarter surveys to elicit feedback on student experience, including the quality of their teaching assistants either midway through the course (Winter 2019) or at the end of the course (Fall 2021). The survey used in Fall 2021 was slightly different than the survey used during Winter 2019 (see Supporting Information for specific details), but both provided insight into student perceptions of their TA. The surveys were de-identified and TAs were given a random identifier to remove potential bias. Three people (two instructors and one graduate researcher) then independently reviewed the survey results and discussed which survey questions best captured the TA involvement as perceived by the students. Once a consensus was reached, the de-identified TAs were then ranked from low to high

involvement. Data from the sections led by the most and least involved TAs for both Winter 2019 and Fall 2021 was then used for further analysis (4 TAs total for Winter 2019 and 4 TAs total for Fall 2021).

Data analysis. Statistical analyses were performed using R version 4.1.1. A two-tailed paired t-test was conducted to compare both the accuracy and precision of student data from Winter 2019 and Fall 2021 and a p value of < 0.05 was considered statistically significant. Outliers were identified by finding values both above and below 1.5x the interquartile range but were not removed from the data since they are informative about whether the pipet was used properly or not (see the Table 7.2 for the analysis excluding outliers, although general conclusions remain the same). Multiple logistic regression was conducted to test the association between TA involvement and student performance. The odds ratio represents the likelihood of a successful outcome, in this case reaching their expected accuracy or precision target as determined by the tolerance rating of the volumetric pipet. Two models were evaluated: one testing the association of TA involvement on lab performance adjusted for pre-lab type (control or treatment), and one testing the association of pre-lab type on lab performance adjusted for TA involvement. Both models are reported. A p value of < 0.05 was also considered statistically significant for these odds ratios.

7.6 Impact of Video Critique on Student Pipetting Technique.

In order to determine whether actively critiquing technique videos is a more effective primer for learning lab skills than passively watching an exemplary video, we compared student results after implementation of the critique to a control group of students who completed the traditional pre-lab assignment (Figure 7.1). We chose to conduct this study for the first laboratory experiment in the course because the quantitative results obtained by the students can be directly correlated to the quality of their pipetting technique. The average mass of water (equation 7.1) delivered provides us with a measure of how accurately a student used the 10-mL volumetric pipet, where x is the measured mass and n is the number of trials.

$$\text{Average } \bar{x} = \frac{\sum_{i=1}^{n} x_i}{n} \tag{7.1}$$

Although the temperature, which affects the water density, was not rigorously held constant across each laboratory room, we discount the negligible contribution of temperature fluctuations to error (details in Supporting Information, equation 7.7) and generally expect the 10-mL volumetric pipet to deliver 10.00 ± 0.02 mL. Similarly, the percent relative deviation (%RAD, equation 7.2) is a measure of the spread in a data set, and as such it provides us with information on the precision of the collected data.

$$\% \text{ RAD} = \frac{\sum_{i=1}^{n}|x_i - \bar{x}|}{n} * 100 \tag{7.2}$$

The lower the %RAD, the more consistently the student used the 10-mL volumetric pipet across the three trials. With that said, the student could still be pipetting improperly (low accuracy), yet just doing so in a very reproducible way. The 10-mL volumetric pipets used in this experiment had a manufacturer precision of 0.2 %.
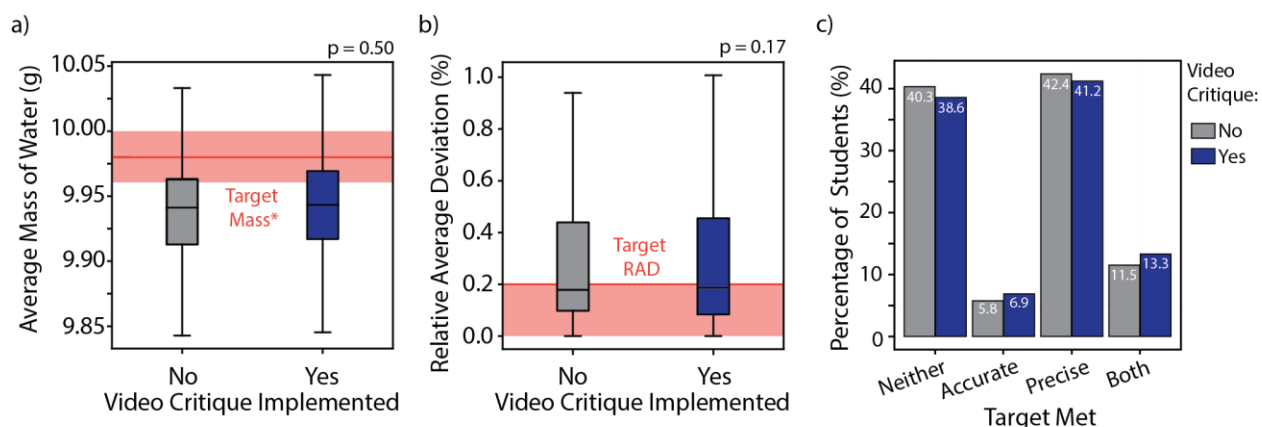
Figure 7.2. The overall distributions of student data for the control group (no video critique, grey) compared to the treatment group (video critique, blue). a) The average mass informs about the accuracy while b) the %RAD informs about the precision of pipet measurements. Only the interquartile ranges are shown to highlight the acceptable range of values (red shaded region) if the pipet was used properly, with the red line indicating the expected value (full distributions are shown in Figure 7.6). The target mass was calculated assuming a room temperature of 20 °C. c) The categorical breakdown of student outcomes. Each student's data was evaluated as whether it fell within the acceptable range or not and then subsequently categorized by how many targets were met. The percentage of students within each category is given within the bars.

Examining the interquartile range of the student data for both the control and treatment groups reveal that the majority of students are near the expected values, but outside of the desired range (Figure 7.2 a-b, full distributions with outliers are shown in Figure 7.6). There was not a significant difference in the average volume between the control and treatment groups (p=0.50), but the mean was closer to the target (9.98 g) in the treatment group at 9.95 g compared to 9.92 g in the control. The statistics are summarized in Tables 7.1 and 7.2. Similarly, there was not a significant difference in %RAD for treatment and control groups (p = 0.17) but the same trend of an improvement in the mean is observed. In the treatment group, the mean %RAD was 0.627 % compared to 0.967 % in the control group. Overall, a greater portion of students are within the acceptable range for precision than accuracy, which may indicate that students are prone to making an error but doing so consistently for each trial. For both average volume and %RAD, the median is nearly unchanged by the implementation of the video critique exercise, indicating that the exercise does not seem to have a strong impact for the class as a whole.

Since our goal of this study is to help students pipet both accurately and precisely, it is also important to evaluate if students are improving on only one or both metrics. If we classify each student's data as either agreeing with the expected value or not, we can categorically group students by whether they met one or both of their targets. Overall, ~ 40% of students are meeting neither target and ~ 40% of students are only meeting their precision target—meaning the majority of students are missing the accuracy target (Figure 7.2c). Less than 15% of students met both targets, indicating that while the video critique exercise does seem to help a portion in the "neither" category, it is not significant enough to address errors that most students seem to be making. Given that the median for accuracy was very close but just under the target, it is possible that the inaccuracy comes from either parallax error by looking down at the meniscus or from droplets being left behind on the walls of the pipet. We observed some students during the experiment and noted that the most commonly skipped steps were the rinsing of the pipette and drawing the meniscus above the line before carefully lowering it to the correct volume. We did find about a 1.7% reduction in students

who met neither of their targets with implementation of the intervention, a 1.1% increase in accuracy only, a 1.2% reduction in precise only, and a 1.8% increase in both accuracy and precision.

Because most students are already near their targets, this exercise seems to be most impactful for students who make large errors and collect outlying values as data. The percentage of students with outlying data reduces with implementation of the video critique exercise from 16% to 14% for average volume and 13% to 10% for % RAD (Table 7.1). The reduction of outliers has been seen in other pre-lab interventions and may by itself be an important finding.[13] A study investigating common sources of struggle in the laboratory found that one major aspect is when tools did not perform as expected.[43] The authors found that students' common response was to assume the tool was broken or guess about the expected result rather than addressing the origin of the discrepancy. It can be difficult for a student to draw meaning from an anomalous result, so reducing these types of outliers is certainly a desired outcome.

The fact that the pre-lab intervention introduced in Fall 2021 did not significantly affect the majority of students indicates that the cognitive load required during the experiment may still be too high. While sequencing the specific steps of a technique can potentially help students separate 'noise' from the 'message', Kempa and Palmer point out that success in performing a manipulative skill requires these sub-skills to be linked in the learner's mind.[27] Ultimately, it seems our approach may have been too passive. According to Johnstone's ten commandments, meaningful learning requires feedback and assurance in addition to limiting the amount of information to be processed.[11] To ensure that students are properly learning lab skills, specific and individual feedback may be required. This poses challenges for large laboratory classrooms where the student to instructor ratio is very large, although recent work on digital badging, where students upload videos of themselves performing the technique and receive instructor feedback, has been used in large courses to good effect.[19–21] In the absence of structured evaluation, our hope was that the TAs, who work with no more than 20 students in a lab section, would be providing individual feedback during the pipetting experiment. We examine this idea further in the following section.
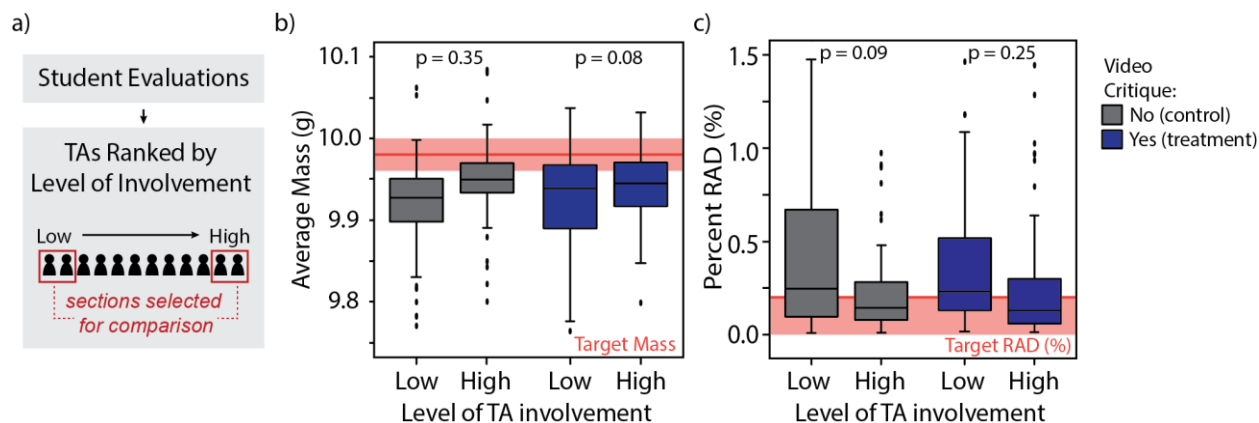
Figure 7.3. *Student results when stratified by the level of TA involvement in their section. a) Student evaluations were used to rank each TA's level of involvement, and student data from the two lowest and two highest from each group (control and treatment) were used for further analysis. The comparison of high and low TA involvement within both control (grey) and treatment groups (blue) for b) average mass (accuracy) and c) percent relative average deviation (precision). Note that only the IQR region is shown although outlying values were not excluded from the data set, and these outliers affect the reported p-values (see Figure 7.7 for full range).*

7.7 The Association Between Teaching Assistant Involvement and Technique Performance.

To investigate the effect of individualized feedback on student technique, we first ranked each TA's level of involvement during lab (more information in Supporting Information). Our hypothesis was that students whose TAs do not frequently check on them during the experiment may see a greater benefit from the video critique exercise as these students may not otherwise have any interventions for correcting poor technique. In Figure 7.3, we compare student data within the low and high TA involvement sections for both control and treatment groups and see more drastic differences in performance for the control group. The ranges are set to highlight the IQR, and the full range with all outlying values is shown in Figure 7.7.

Although we again found no significant differences between the means of the distribution when comparing high to low TA involvement (Figures 7.3b-c), we did find improvement in the mean, median, and standard deviation in high TA involvement sections (statistics summarized in Tables 7.3 through 7.5). For average mass, when comparing high to low TA involvement we observe a mean of 9.965 g compared

to 9.904 g (target = 9.98 g), a median of 9.95 g compared to 9.92 g, and a standard deviation of 0.15 compared to 0.55. For %RAD we observe similar results when comparing high to low TA involvement sections—a mean of 0.483 % compared to 1.820 % (target ≤ 0.2 %), median of 0.143 % compared to 0.247 %, and a standard deviation of 1.16 compared to 6.70. The percentage of outlying values was also lower for high TA involvement sections. These results demonstrate that although the mean performance is largely skewed by outliers (leading to non-significance in p values), the middle 50% of the students demonstrate better technique in high TA involvement sections compared to low TA involvement sections. This points to the impact of having additional guidance during the experiment—those TAs designated as high involvement were all reported to frequently check on the students during the lab and help correct student technique. It has been shown in the literature that highly interactive TAs result in students who are more engaged, and students who perceive their TAs as supportive believe they learn more content.[44,45]

We want students to have an equitable experience in their lab sections, but the motivation a TA has for engaging with their students varies greatly. As such we were interested in determining if the video critique pre-lab assignment provided an extra resource for students outside of lab that might reduce their dependence on the TA for ensuring proper technique. Between the control and treatment groups, we observe that the treatment group has a median closer to the target than the control group in all cases (high and low TA). The mean and standard deviation for treatment compared to control improve for some cases but are still affected by the magnitude of the outlying values. The percentage of outlying values, however, shows a reduction for all cases with implementation of the video critique—the most drastic effect being the reduction of outliers amongst students with low TA involvement (23% of data for the control group versus 10% for the treatment group). Categorical breakdown of targets met also showed that the video critique exercise increased the percentage of students meeting both of their goals from 1.3% to 11.8% in the low TA involvement sections (Figure 7.8). Overall, these results again highlight that the intervention seems to have the greatest impact on the outliers, but it also standardizes some of the differences between the high and low TA involvement sections.
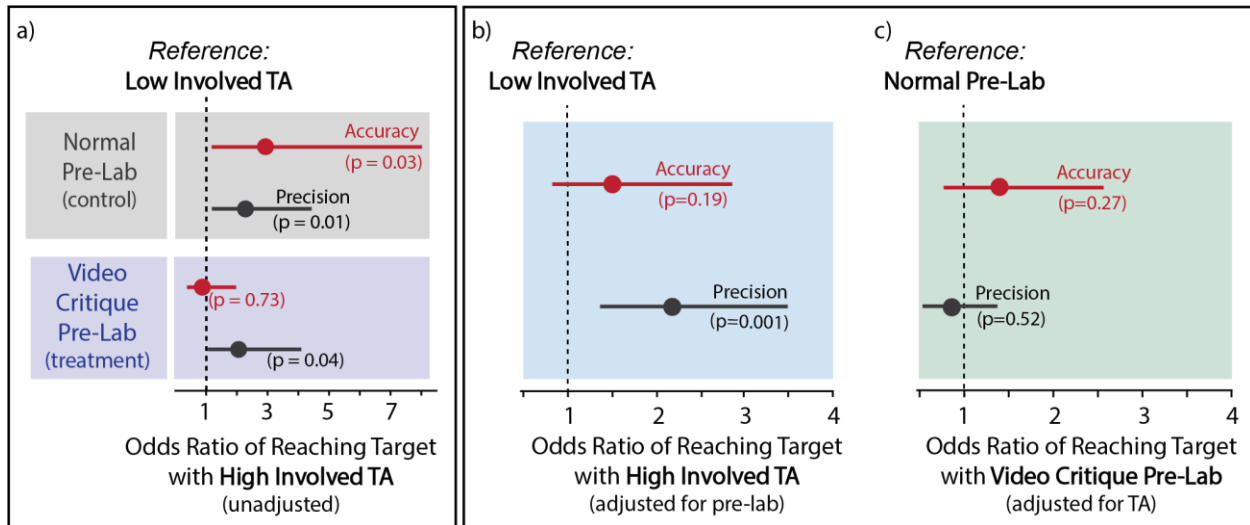
Figure 7.4. *Logistic regressions measuring the association between TA involvement and the odds ratio of students meeting their target measurements. a) The unadjusted models comparing the odds ratio of students in a high TA section compared to those in a low TA (reference) section. The p values are given along with the 97.5% confidence intervals. b) The odds ratio of all students in a high TA section (now adjusted for pre-lab) compared to all students in a low TA section. c) The odds ratio of all students in the treatment group (now adjusted for TA involvement level) compared to all students in the control group.*

To quantify the association between TA involvement and performance, we next turn to logistic regression to find the odds ratios of students meeting their accuracy and precision targets. The odds ratio (OR) is a measure of association between an outcome (in this case, proper technique) and an exposure (their TA). It provides a ratio between the outcome in one group to the outcome in another group (reference) to quantify success. An OR = 1 means the two groups can expect the same outcome; an OR > 1 means the group in question is more likely to have a successful outcome than the reference; an OR < 1 means the reference group is more likely to have a successful outcome. The magnitude of the odds ratio can inform how many times more or less likely an outcome is expected to occur (OR of 2 means success is 2x more likely). In Figures 4a-c, we plot the ORs and their 97.5% confidence intervals, to highlight the increased or decreased likelihood of the group (indicated in the x-axis) having a successful outcome compared to the reference group (dashed line). If the OR and its confidence interval do not cross 1, it indicates there is a significant difference between the group in question and reference group (type of exposure). We will use

the ORs to discuss the increased or decreased odds of students demonstrating proper technique based on which TA or pre-lab assignment they were exposed to.

We first used the binomial outcomes of meeting the target or not for both accuracy and precision to define a successful outcome and ran separate models for high and low TA involvement (Figure 7.4a). Compared to students with low TA involvement, students with high TA involvement in the control group had significantly increased odds of meeting both accuracy (OR = 2.93, p = 0.03) and precision (OR = 2.28, p = 0.01) targets. For the treatment group, the odds of high TA involvement sections meeting their accuracy target became equally as likely (no significant difference, OR= 0.87, p = 0.73) as the low TA involvement students, while the odds of reaching the precision target remained higher than for students with low TA involvement (OR=2.06, p = 0.04). These results show that without any intervention (control group), the level of TA involvement is a strong predictor of student success, in this case demonstrating proper technique, and emphasizes the importance of instructor feedback during the experiment. With the video critique pre-lab, the association between TA and student success becomes non-significant for accuracy and suggests that the exercise may in fact mitigate some of the differences in guidance or feedback that students might experience in different sections. The intervention has a stronger effect on accuracy compared to precision, and this could be because it may be hard to achieve consistent results as a novice. Additionally, a highly involved TA is more likely to encourage students with a wide spread in their measurements to redo a trial, and this too may explain why TA involvement still remains a stronger predictor of success for precision, even with the video critique implementation.

Finally, we ran a multiple logistic regression to control for confounding of both TA involvement and pre-lab type. This regression is used when the outcome is dependent on more than one variable and can control for the confounding of one variable by another, giving the true relationship between a variable and outcome by removing the influence of the other. By first controlling for pre-lab type (control and treatment, Figure 7.4b) we see that regardless of which pre-lab the student completed, having high TA involvement remains a significant predictor of success for precision (OR = 2.17, p = 0.001). For accuracy, students have

increased odds of success with high TA involvement, but non-significantly (OR = 1.50, p = 0.19). On the other hand, if we control for TA (high and low involvement, Figure 7.4c), students with the video critique pre-lab have increased (although non-significant) odds of success for accuracy compared to the control group (OR = 1.40, p = 0.27), and an equal likelihood of success for precision compared to the control group (OR = 0.86, p = 0.52). While we hoped to see a significant improvement by use of the video critique pre-lab, we did still observe two promising outcomes: 1) the dependency on having high TA involvement for success in accuracy is weaker, and 2) there are slightly increased odds of success in accuracy when the video critique is introduced. These results are also summarized in Tables 7.6 through 7.8.
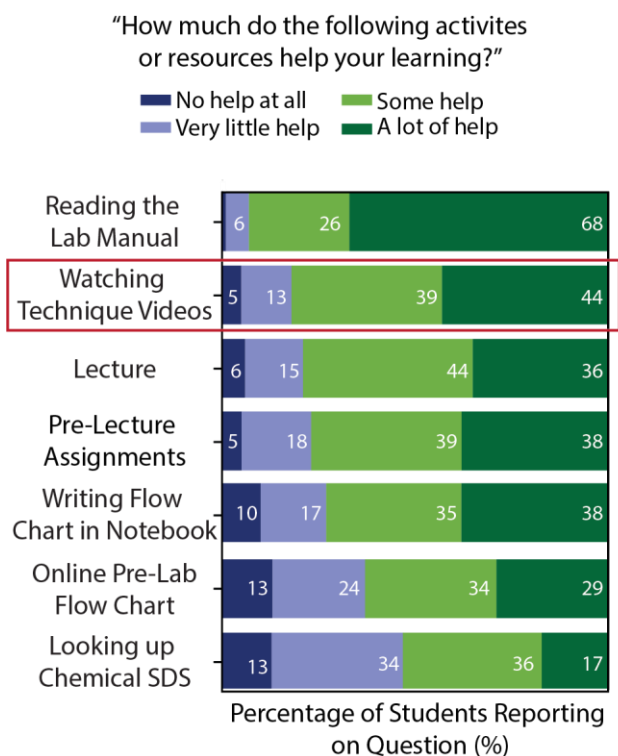
Figure 7.5. *The end-of-quarter survey question from Fall 2021 (treatment group) where students were asked to evaluate how useful the given resources were to their learning. The breakdown of percentage of students reporting is given within each bar, and the resources are ordered by their average "helpfulness" rank. The technique video portion of the pre-lab assignment is highlighted.*

7.8 Student Perceptions of Video Critique Usefulness.

Finally, if considering this type of exercise, it is useful for instructors to be aware of what students find useful or frustrating. We asked students for feedback on how helpful the technique video critique exercise was in their learning process through both mid- and end-of-quarter surveys. The survey contained questions with numerical rankings as well as free-response entries. On the mid-quarter survey (summarized in Figure 7.9), 30% of students in the control group said technique videos were "a lot of help", yet when the treatment group was asked about analyzing the technique videos through the pre-lab assignment, only 23% stated it was a "a lot of help." Overall, students in the treatment group expressed frustration with having to watch the videos so carefully for the pre-lab as they were graded on their responses. Even with three attempts, some felt like it was "nit-picky" and therefore seemed to focus more on getting the right answer than critically evaluating the technique. Selected quotes expressing frustration from students within the treatment group on the mid-quarter survey:

"The most difficult part of the pre-lab is analyzing the videos because when completing these questions, **students are more concerned about getting the answer right than actually learning the lab procedure**."

"[The biggest challenge of this course is] a **sense of frustration when completing flowcharts and technique analysis** videos during prelab."

"The flowcharts and analyzing the technique videos are very frustrating. […] When analyzing the videos, sometimes the person in the video did part of a step, so **I don't really know to answer yes or no if they completed it correctly.**"

This is in line with the findings reported by Accettone et al., in which students expressed difficulty with determining how many errors were present in a video.[26] Following their implementation of this exercise, students may have been less frustrated if they were allowed to miss one error without being penalized.

And quotes from the mid-quarter survey expressing helpfulness:

> "Constructing the flowchart myself, or doing the pre-lab in the notebook and having it checked by the TA is way more helpful than filling out a quiz on CCLE. **The videos in the pre-lab analyzing the technique [are] helpful too**."

> "I really enjoyed being able to work with people in person and I appreciated being able to get back to the in-person environment. **For lab section I think more of the videos would help so we know what we are doing more in lab.**"

Interestingly, on the end-of-quarter survey, 44% of students in the treatment group stated that watching technique videos was "a lot of help". The end-of-quarter ranking of resources used by the treatment group is shown in Figure 7.5 where the technique videos are highlighted as the second highest resource. Shortly after the mid-quarter survey, students had learned all the techniques used in the course and technique videos were no longer part of the pre-lab assignment. After getting past their initial frustration, students seemed to view the technique videos more favorably. While we did not track whether students continued to use the technique videos after the assignments, they were allowed to re-visit the videos to prepare for subsequent experiments although this was not required.

While it has been demonstrated that students generally perceive skills-based assignments as having a positive impact on their learning, it may not be enough to look at student perceptions of what is helpful.[26] Although the majority of our students self-reported this resource as useful, most of the class saw no

significant improvement compared to previous students. This agrees with literature where students' confidence in their skills was shown to improve with online preparation videos, but their cognitive performance was not necessarily correlated.[46] In general, students tend to focus on the outcomes of graded assignments as measuring their skills or learning and their perception of usefulness of an assignment is likely affected by the grade they received on it. For example, when students were actively completing and receiving a grade for the video critique pre-lab (mid-quarter), much of the feedback we received was negative and centered around not getting the correct answers. By the time they were no longer graded on those assignments, their perception shifted to mostly positive. This points to a misalignment between students and instructors on perceptions or goals of the lab experience and must be considered when trying to measure the impact of new teaching methods.[17]

In addition, we found that a more significant predictor of student success is the quality of their TA and although highly valued TAs received recognition in student feedback, there were no comments expressing frustration about TAs other than grading. Students don't have the frame of reference to recognize a TA's responsibilities and would not necessarily be able to predict that their progress in learning a skill might be correlated to the amount of TA involvement they receive.[47] While the surveys were insightful to understand the affective factors of the lab experience, our findings could not have been deduced simply from the student perspectives and highlights the importance of using additional quantitative analyses to measure impact on their performance.

7.9 Limitations of this study

The main limitation of this study is that the control group completed their chemistry laboratory coursework *before* the COVID-19 pandemic and were not disrupted by virtual learning. The treatment group completed this course just after the return to in-person instruction, meaning their preparation from any previous laboratory courses was most likely impacted by the pandemic and they may have had less exposure to technical skills that require hands-on manipulation. This must be considered in the context of

our results as an additional confounding factor—the treatment group may very well have had a lower baseline of technical skills even before introducing the pre-lab exercise.

We were also only able to use student data after performing this exercise for one experiment. The pre-lab exercise was conducted for multiple experiments, but the pipetting lab was the only experiment where just a single technique was used, and skill mastery could directly be correlated to the student results. Therefore, we do not have a measure of how the impact of this assignment scales with the complexity or cognitive load of the experiments. We also did not correlate the student scores (pre-lab or final grades) to their technique performance.

Another limitation was inconsistency of survey questions. The study was designed after the control group took the course, so their questions and responses were more generic than the treatment group who was actively taking the course while the study was underway. The evaluation of TAs was much more specific about involvement in the treatment group than the control group and is likely more accurate in the distinction between low and high TA involvement. Observation of the TAs could be a useful supplement when considering the ranking.

7.10 Implications

Overall, our work demonstrates that the cognitive load associated with performing a lab technique for the first time presents challenges for students and may require more intervention in addition to the pre-lab exercise to ensure skill mastery. In addition to this pre-lab exercise, it may be more effective to incorporate active feedback such as in the form of working in pairs to critique each other's technique, self-assessments by recording and then comparing a student's own technique to the exemplary video, or structured feedback from the TA or learning assistants through means such as digital badging. Along with providing personal feedback, we believe that it may be necessary for students to receive sufficient interleaved practice to master a lab skill—one lab period dedicated to pipetting technique may not have provided sufficient practice. Interleaved practice gives students periods of rest between sessions when they are actively learning or practicing and has been shown to be effective for higher cognitive learning in math,

255

science, and physics as well as in the development of motor skills.[48–51] As pipetting is a technical skill that is used repeatedly in subsequent experiments, a future study looking at how the students improve over the duration of the course may give insight on when students master the skill and whether there is a latent effect of a higher cognitive preparation on the time required. Having periods of rest between each lab section in addition to reflection about technique on post-lab assignments may be more effective than providing students with highly detailed instructions prior to their first attempt at a technique.

Nonetheless, a promising outcome of our study is that we found the exercise to be helpful in scenarios where a student is either performing very poorly (outliers) or has very little feedback on their technique (low TA involvement). While we initially set out to improve performance for the entire class, we uncovered a major challenge in large classrooms and found this exercise to be more impactful for addressing that concern. In a large laboratory setting such as this study, instructors must rely on many TAs to run multiple sections at once, yet the TAs' and instructor's goals do not always align.[47,52] This exercise may not be necessary in small classrooms where the instructor can be present and provide individualized feedback, but it does have implications for larger classrooms where this can be a challenge. Addressing the differing nature of TAs' motivations for student involvement may require additional tools such as student feedback, evaluations, etc. to ensure a standardized experience. But it appears that using technologies such as pre-lab videos can reduce pressure on the instructor and TA to give each student the same level of feedback. While previous studies suggested that online pre-lab activities may standardize the laboratory experience across TA's, our study has provided evidence that this is the case.[12,15]

7.11 Conclusions

To better prepare students for learning a new lab skill and decrease cognitive load during their lab experiment, we implemented a pre-lab exercise which involved students watching a technique video (volumetric pipetting) and completing a critique of the demonstration. After the pre-lab exercise, students then completed a volumetric pipette lab, and we compared their data to a cohort who did not complete the

same video critique pre-lab assignment. We found that using this pre-lab exercise alone was not enough to significantly improve the students' performance, despite their perception of the assignment as being useful towards their learning. We did find that the assignment reduces the number of students who report outlying values and improves overall performance in student sections where the TA is less engaged with providing feedback to the students.

7.12 Supporting Information

Video Critique Exercise Evaluation Form

Identification			
Title: Use of a Pipet	URL: https://youtu.be/YMjy2sK_kBo		
Video clip (if applicable)	5:04 – 12:06 minutes		
Procedure Performance			
		Correct	Incorrect or omitted
1	checking to see if the pipet is clean by observing whether droplets cling to the inside of the pipet		
2	rinsing the pipet including a portion of the stem above the calibration mark with small amounts of the solution to be transferred		
3	carefully placing the pipet pump or bulb on the top of the pipet		
4	(a) Bulb suction: holding the pipet with one hand and moving the INDEX finger (not thumb) to the top of the pipet when the liquid has been drawn above the calibration mark with the bulb in the other hand (b)Pipet pump: holding the pipet with one hand and manipulating the pipet wheel with the thumb of the other hand to draw the liquid up the pipet above the calibration mark		
5	wiping off the outside of the tip of the pipet while the liquid is above the calibration mark		
6	slowly lowering the liquid level just to the calibration mark by (a) lessening the pressure of the index finger on the pipet top by turning the pipet (not lifting the finger off the pipet) if you are using a bulb or (b) turning the wheel slowly to lower the plunger if using a pipet pump		
7	touching the tip of the pipet to a dry edge of the container holding the solution before moving the pipet to the receiving container		
8	transferring the pipet to the receiving vessel and releasing the pressure by lifting the finger completely or pressing the release valve on the pump		
9	allowing the pipet to drain freely while touching the inside wall of the receiving vessel above the level of the liquid		
10	leaving residual liquid in the tip after draining appears complete		
Safety			
Proper PPE	Eye protection Yes_____ No _____ Not visible _____		
	Lab coat Yes_____ No _____ Not visible _____		
Badge Certification Recommendation (select one)			

Recommended	**Provisional**	**Not recommended**
All procedure steps correctly performed, PPE used if visible	One or two steps omitted or incorrect; Proper PPE used if visible	Improper PPE if visible and/or more than two steps omitted or incorrectly performed

Feedback: (no more than three sentences) based on recommendation	
Positive: (what was done correctly)	
Constructive: (what was omitted and/or what experimenter should do to improve incorrectly performed steps)	

Error Analysis of Water Density Fluctuations

The volumetric pipet is rated to deliver 10.00 ± 0.02 mL at 20 ˚C which, in mass, is equivalent to 9.98 ± 0.02 g. Because this study was conducted over 24 different laboratory sections it was not possible to ensure that the temperature of the room was always held constant. As such, we evaluated how the temperature fluctuations would contribute to the error of the expected volume. We first assume that the room temperature was held within a range of 15-25 ˚C. The density is expressed by:

$$\rho = \frac{m}{V} \tag{7.3}$$

And varies with temperature as:

$$\rho \text{ at } 15 \text{ ˚C} = 0.9991 \text{ g/mL} \tag{7.4}$$

$$\rho \text{ at } 20 \text{ ˚C} = 0.9982 \text{ g/mL} \tag{7.5}$$

$$\rho \text{ at } 25 \text{ ˚C} = 0.9970 \text{ g/mL} \tag{7.6}$$

The greatest difference in density from the expected density at 20 ˚C within this range is 0.0012 g/mL. If we set this as the error in density, the total error of the mass of water including the inherent error of the pipet and error in water density is:

$$\frac{\Delta mass_{H2O}}{9.982 \ g \ H2O} = \sqrt{(\frac{0.02 \ mL}{10.00 \ mL})^2 + (\frac{0.0012 \ g/mL}{0.9982 \ g/mL})^2} \tag{7.7}$$

$$\Delta mass_{H2O} = 0.0233 \tag{7.8}$$

The expected mass delivered by the pipet is then simply 9.98 ± 0.02 g. The inherent error of the pipet is larger than the error in density and as such, the reported error is unchanged by any differences in room temperature from one lab section to another.

Average Mass and Percent RAD Distributions for the Entire Class
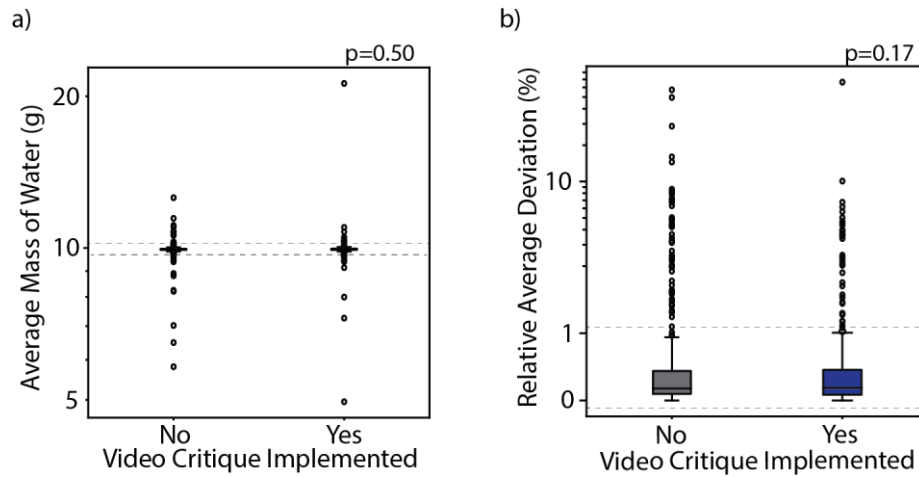
Figure 7.6. *The full distributions of all student data for a) accuracy and b) precision. The grey dashed lines indicate the data show in Figure 7.2 (the IQR ranges), and the outliers are represented by the circles.*

Table 7.1. *The statistics describing the distributions for accuracy and precision for the control and treatment groups. All of the students within each group are included in this dataset.*

Measurement	Accuracy	Accuracy	Precision	Precision
Video Implementation	No (control)	Yes (treatment)	No (control)	Yes (treatment)
Sample Size	434	451	434	451
Mean	9.92 g	9.95 g	0.976 %	0.623 %
Median	9.94 g	9.94 g	0.179 %	0.187 %
Standard Deviation	0.38 g	0.59 g	4.16 %	3.14 %
Outliers (%)	16	14	13	10

Table 7.2. *The results of the t-test comparing the means of the control and treatment groups for both accuracy and precision.*

Outlier Treatment	Student Measurement	Accuracy	Precision
Included (reported in main text)	**t statistic**	-0.681	1.383
	p value	0.50	0.17
	95% Confidence Interval	(-0.091, 0.044)	(-0.146, 0.842)
	Effect Size (Cohen's d)	0.060	0.096
Excluded	**t statistic**	-2.116	-1.107
	p value	0.035	0.269
	95% Confidence Interval	(-0.011, 0)	(-0.048, 0.013)
	Effect Size (Cohen's d)	0.153	0.079

TA Evaluation Survey Questions

Since this study was conducted after the Winter 2019 (control group) students completed the course, we did not have the same survey questions used to assess TA involvement in Fall 2021 (treatment). We used the general student evaluations of their TAs, and decided that the following questions most closely assessed the TA's level of engagement with students:

Please indicate the level to which you agree with the following statements relating to your TA.

1 - strongly disagree

2 - somewhat disagree

3 - somewhat agree

4 - strongly agree

"My TA is helpful."

"My TA is approachable."

"My TA encourages me to participate in my lab section."

"My TA makes me feel welcome in the lab."

We weighted the TA's score on the question about encouraging participation twice more than the others but used their score on all questions to find an overall involvement ranking. For the Fall 2021 (treatment group) students, we were able to ask more specifically if the TA was involved with demonstrating or correcting technique and used these questions with equal weighting to determine the TA's overall rank:

Please indicate the level to which you agree with the following statements relating to your TA.

1 - strongly disagree

2 - somewhat disagree

3 - somewhat agree

4 - strongly agree

"My TA checked in with me during lab and helped me correct my technique when necessary"

"My TA demonstrated proper handling of glassware and equipment, either to the entire class or individually at my bench"

"My TA wasn't a useful resource for learning techniques"

Full Distributions for Average Mass and Precision by TA Invovlement
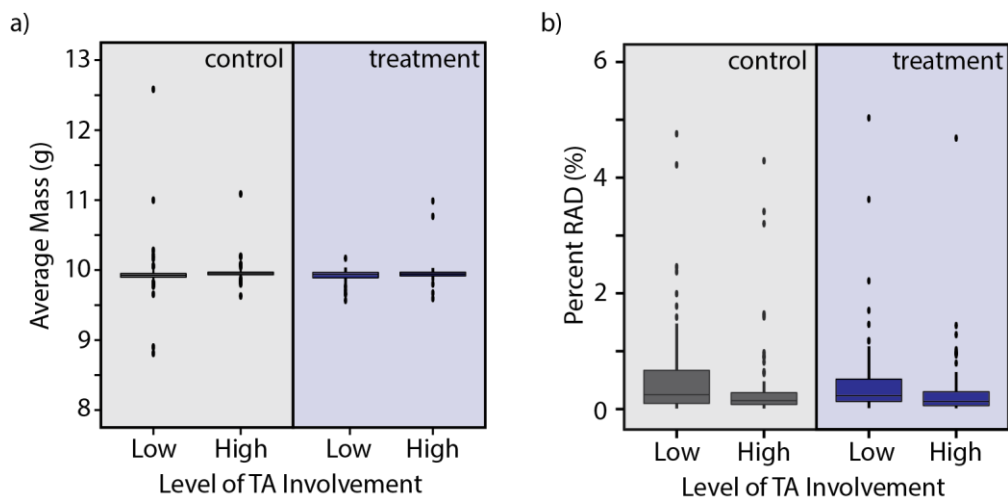
Figure 7.7. *The full distributions of student data for a) average mass and b) percent RAD. The outliers are shown in these plots, while they are not in Figure 7.4 for clarity of visualizing the IQR.*

Table 7.3. *The statistics describing the distributions for accuracy for the control and treatment groups, broken down by level of TA involvement. Only students within the high and low TA sections are included in these datasets.*

Measurement	Accuracy	Accuracy	Accuracy	Accuracy
Video Implementation	No (control)	No (control)	Yes (treatment)	Yes (treatment)
TA Involvement	High	Low	High	Low
Sample Size	75	77	71	68
Mean	9.965 g	9.9035 g	9.9600 g	9.8785 g
Median	9.9499 g	9.9275 g	9.9454 g	9.9390 g
Standard Deviation	0.1500 g	0.5478 g	0.1721 g	0.3363 g
Outliers (%)	16	23	7	10

Table 7.4. *The statistics describing the distributions for precision for the control and treatment groups, broken down by level of TA involvement. Only students within the high and low TA sections are included in these datasets.*

Measurement	Precision	Precision	Precision	Precision
Video Implementation	No (control)	No (control)	Yes (treatment)	Yes (treatment)
TA Involvement	High	Low	High	Low
Sample Size	75	77	71	68
Mean	0.4834	1.8195	0.3188	1.4600
Median	0.1432	0.2465	0.1294	0.2316
Standard Deviation	1.1569	6.698	0.6110	8.0346
Outliers (%)	16	14	11	12

Table 7.5. *Results of the t-tests comparing the means of the high and low TA subgroups, within the control and treatment groups.*

Student Measurement	Accuracy (control)	Accuracy (treatment)	Precision (control)	Precision (treatment)
t statistic	-0.943	-1.788	1.724	1.168
p value	0.35	0.08	0.09	0.25
Confidence Interval	(-1.190, 0.068)	(-0.172, 0.009)	(-0.206, 2.878)	(-0.808, 3.091)
Effect Size (Cohen's d)	0.153	0.305	0.278	0.200
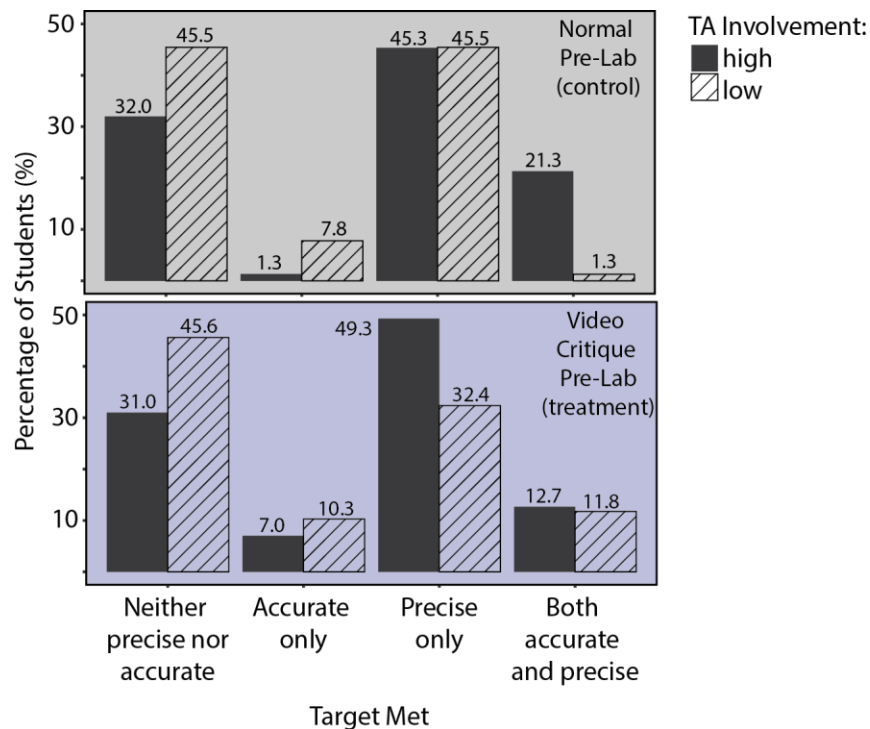
Figure 7.8. The categorical breakdown of student outcomes depending on the level of TA involvement, shown for both control (grey) and treatment (blue) groups. Each student's data was evaluated as falling within the acceptable range or not and then subsequently categorized by how many targets were met. The percentage of students within each category is given above the bars.

Summary of Logistic Regression Results

Table 7.6. *The results of logistic regression for individual models showing the association between TA involvement and the odds of reaching each target.*

|	**Accuracy**	**Precision**	**Accuracy**	**Precision**
Group	Control	Control	Treatment	Treatment
Odds Ratio of High TA	2.93	2.28	0.87	2.06
p value	0.03	0.01	0.73	0.04
97.5% CI upper	8.02	4.43	0.38	1.05
2.5 % CI lower	1.18	1.19	1.97	4.10

Table 7.7. *The results of multiple logistic regression showing the association between TA involvement and the odds of reaching accuracy and precision targets. The odds are calculated for the students in a high TA section (with the reference being students in low TA) adjusted for which pre-lab assignment was completed (control or treatment).*

	Accuracy	**Precision**
Group	All	All
Odds Ratio of High TA (adjusted for pre-lab)	1.50	2.17
p value	0.19	0.001
97.5% CI upper	2.77	3.49
2.5 % CI lower	0.82	1.36

Table 7.8. *The results of multiple logistic regression showing the association between pre-lab completed and the odds of reaching accuracy and precision targets. The odds are calculated for the treatment group (with the reference being control group) adjusted for which TA the student had (high or low).*

	Accuracy	**Precision**
Group	All	All
Odds Ratio of Treatment (adjusted for TA)	1.40	0.86
p value	0.27	0.52
97.5% CI upper	0.77	0.53
2.5 % CI lower	2.56	1.37
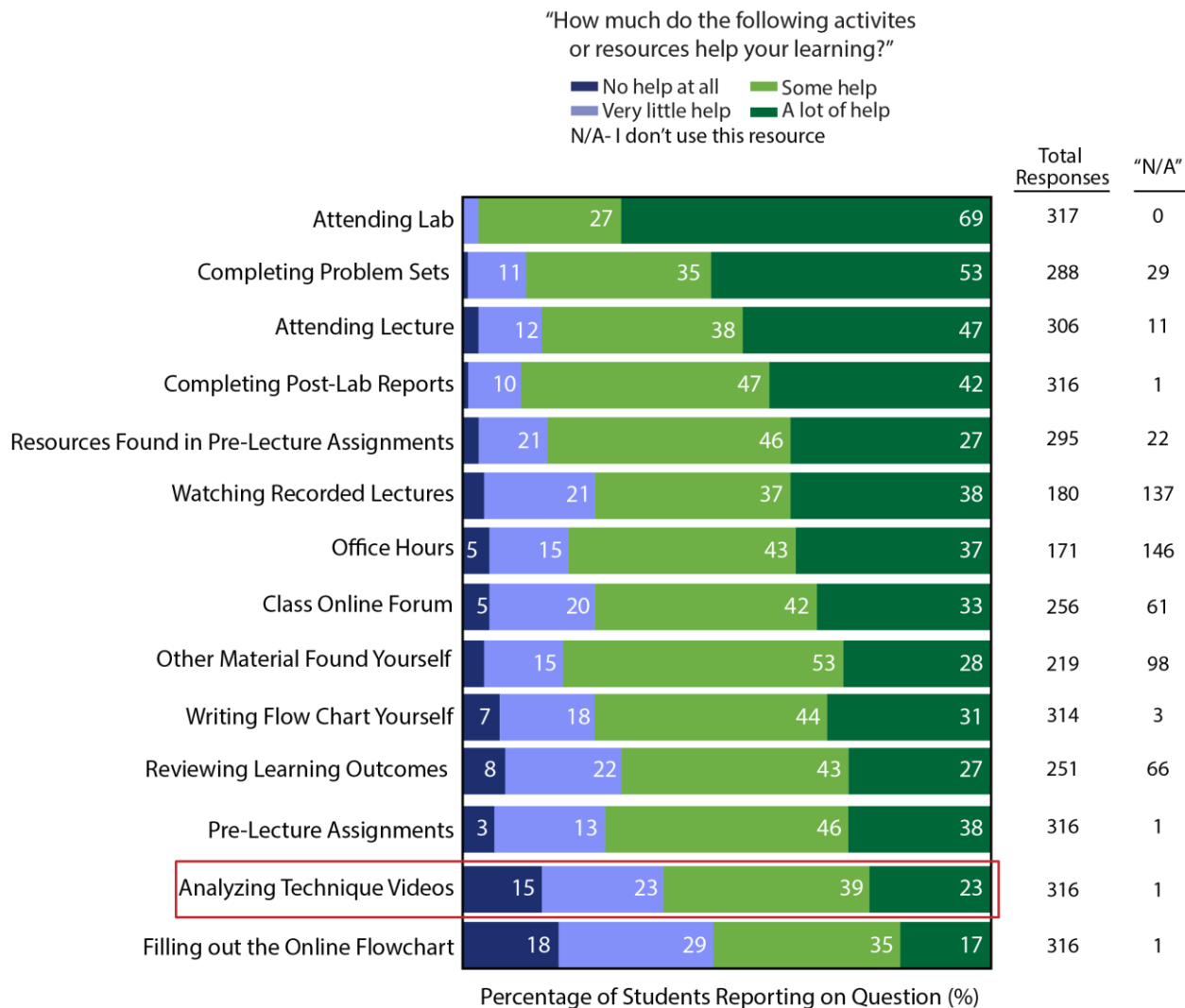
Figure 7.9. *Results of the Fall 2021 (treatment group) mid-quarter survey question addressing the usefulness of the various resources used during the course and experiments.*

REFERENCES

(1) *Undergraduate Professional Education in Chemistry: ACS Guidelines and Evaluation Procedures for Bachelor's Degree Programs*; American Chemical Society: Washington, D.C, 2015. https://www.acs.org/content/dam/acsorg/about/governance/committees/training/2015-acs-guidelines-for-bachelors-degree-programs.pdf (accessed 2023-03-22).

(2) Reid, N.; Shah, I. The Role of Laboratory Work in University Chemistry. *Chem. Educ. Res. Pract.* **2007**, *8* (2), 172–185. https://doi.org/10.1039/B5RP90026C.

(3) Seery, M. K. Establishing the Laboratory as the Place to Learn How to Do Chemistry. *J. Chem. Educ.* **2020**, *97* (6), 1511–1514. https://doi.org/10.1021/acs.jchemed.9b00764.

(4) Bruck, A. D.; Towns, M. Development, Implementation, and Analysis of a National Survey of Faculty Goals for Undergraduate Chemistry Laboratory. *J. Chem. Educ.* **2013**, *90* (6), 685–693. https://doi.org/10.1021/ed300371n.

(5) Connor, M. C.; Rocabado, G. A.; Raker, J. R. Revisiting Faculty Members' Goals for the Undergraduate Chemistry Laboratory. *Chem. Educ. Res. Pract.* **2023**, *24* (1), 217–233. https://doi.org/10.1039/D2RP00215A.

(6) The Quality Assurance Agency for Higher Education. *Subject Benchmark Statement: Chemistry*; The Quality Assurance Agency for Higher Education, 2022. https://www.qaa.ac.uk/docs/qaa/sbs/sbs-chemistry-22.pdf?sfvrsn=46b1dc81_4 (accessed 2023-03-22).

(7) *From Analysis to Action: Undergraduate Education in Science, Mathematics, Engineering, and Technology*; National Academy of Science; The National Academy Press: Washington, D.C, 1996.

(8)   Hanson, S.; Overton, T. *Skills Required by New Chemistry Graduates and Their Development in Degree Programmes*; Higher Education Acadamy UK Physical Sciences Centre: University of Hull, 2010. https://edu.rsc.org/download?ac=509473.

(9)   Sarkar, M.; Overton, T.; Thompson, C. D.; Rayner, G. Academics' Perspectives of the Teaching and Development of Generic Employability Skills in Science Curricula. *High. Educ. Res. Dev.* **2019**, *39* (2), 346–361. https://doi.org/10.1080/07294360.2019.1664998.

(10)   DeMeo, S. Teaching Chemical Technique. A Review of the Literature. *J. Chem. Educ.* **2001**, *78* (3), 373. https://doi.org/10.1021/ed078p373.

(11)   Johnstone, A. H. Chemistry Teaching - Science or Alchemy? 1996 Brasted Lecture. *J. Chem. Educ.* **1997**, *74* (3), 262. https://doi.org/10.1021/ed074p262.

(12)   Nadelson, L. S.; Scaggs, J.; Sheffield, C.; McDougal, O. M. Integration of Video-Based Demonstrations to Prepare Students for the Organic Chemistry Laboratory. *J Sci Educ Technol* **2015**, *24* (4), 476–483. https://doi.org/10.1007/s10956-014-9535-3.

(13)   Canal, J. P.; Lowe, J.; Fong, R. Improving Students' Practical Laboratory Techniques through Focused Instruction and Assessment. In *Technology and Assessment Strategies for Improving Student Learning in Chemistry*; ACS Symposium Series; American Chemical Society, 2016; Vol. 1235, pp 137–157. https://doi.org/10.1021/bk-2016-1235.ch008.

(14)   Jolley, D. F.; Wilson, S. R.; Kelso, C.; O'Brien, G.; Mason, C. E. Analytical Thinking, Analytical Action: Using Prelab Video Demonstrations and e-Quizzes To Improve Undergraduate Preparedness for Analytical Chemistry Practical Classes. *J. Chem. Educ.* **2016**, *93* (11), 1855–1862. https://doi.org/10.1021/acs.jchemed.6b00266.

(15) Stieff, M.; Werner, S. M.; Fink, B.; Meador, D. Online Prelaboratory Videos Improve Student Performance in the General Chemistry Laboratory. *J. Chem. Educ.* **2018**, *95* (8), 1260–1266. https://doi.org/10.1021/acs.jchemed.8b00109.

(16) Sanchez, J. M. Are Basic Laboratory Skills Adequately Acquired by Undergraduate Science Students? How Control Quality Methodologies Applied to Laboratory Lessons May Help Us to Find the Answer. *Anal Bioanal Chem* **2022**, *414* (12), 3551–3559. https://doi.org/10.1007/s00216-022-03992-x.

(17) DeKorver, B. K.; Towns, M. H. General Chemistry Students' Goals for Chemistry Laboratory Coursework. *J. Chem. Educ.* **2015**, *92* (12), 2031–2037. https://doi.org/10.1021/acs.jchemed.5b00463.

(18) Hancock, L. M.; Hollamby, M. J. Assessing the Practical Skills of Undergraduates: The Evolution of a Station-Based Practical Exam. *J. Chem. Educ.* **2020**, *97* (4), 972–979. https://doi.org/10.1021/acs.jchemed.9b00733.

(19) Towns, M.; Harwood, C. J.; Robertshaw, M. B.; Fish, J.; O'Shea, K. The Digital Pipetting Badge: A Method To Improve Student Hands-On Laboratory Skills. *J. Chem. Educ.* **2015**, *92* (12), 2038–2044. https://doi.org/10.1021/acs.jchemed.5b00464.

(20) Hensiek, S.; DeKorver, B. K.; Harwood, C. J.; Fish, J.; O'Shea, K.; Towns, M. Improving and Assessing Student Hands-On Laboratory Skills through Digital Badging. *J. Chem. Educ.* **2016**, *93* (11), 1847–1854. https://doi.org/10.1021/acs.jchemed.6b00234.

(21) Seery, M. K.; Agustian, H. Y.; Doidge, E. D.; Kucharski, M. M.; O'Connor, H. M.; Price, A. Developing Laboratory Skills by Incorporating Peer-Review and Digital Badges. *Chem. Educ. Res. Pract.* **2017**, *18* (3), 403–419. https://doi.org/10.1039/C7RP00003K.

(22) Kirton, S. B.; Al-Ahmad, A.; Fergus, S. Using Structured Chemistry Examinations (SChemEs) As an Assessment Method To Improve Undergraduate Students' Generic, Practical, and Laboratory-Based Skills. *J. Chem. Educ.* **2014**, *91* (5), 648–654. https://doi.org/10.1021/ed300491c.

(23) Reid, N. *The Johnstone Triangle: The Key to Understanding Chemistry*; Royal Society of Chemistry, 2021.

(24) Russell, A. A.; Mitchell, B. L. The Use of Videotapes in Large Lab Courses. *J. Chem. Educ.* **1979**, *56* (11), 753. https://doi.org/10.1021/ed056p753.

(25) Sansom, R. L. Pressure from the Pandemic: Pedagogical Dissatisfaction Reveals Faculty Beliefs. *J. Chem. Educ.* **2020**, *97* (9), 2378–2382. https://doi.org/10.1021/acs.jchemed.0c00657.

(26) Accettone, S. L. W.; DeFrancesco, C.; King, C. A.; Lariviere, M. K. Laboratory Skills Assignments as a Teaching Tool to Develop Undergraduate Chemistry Students' Conceptual Understanding of Practical Laboratory Skills. *J. Chem. Educ.* **2023**, *100* (3), 1138–1148. https://doi.org/10.1021/acs.jchemed.2c00710.

(27) Kempa, R. F.; Palmer, C. R. The Effectiveness of Video-Tape Recorded Demonstrations in the Learning of Manipulative Skills in Practical Chemistry. **1974**, *5* (1), 62–71. https://doi.org/10.1111/j.1467-8535.1974.tb00623.x.

(28) Canal, J. P.; Hanlan, L.; Key, J.; Lavieri, S.; Paskevicius, M.; Sharma, D. Chemistry Laboratory Videos: Perspectives on Design, Production, and Student Usage. In *Technology and Assessment Strategies for Improving Student Learning in Chemistry*; ACS Symposium Series; American Chemical Society, 2016; Vol. 1235, pp 159–177. https://doi.org/10.1021/bk-2016-1235.ch009.

(29) Prichard, E. Basic Skills of Analytical Chemistry: Do We Take Too Much for Granted? *Accred Qual Assur* **1999**, *4* (1), 37–39. https://doi.org/10.1007/s007690050308.

(30) Sweller, J. Cognitive Load Theory, Learning Difficulty, and Instructional Design. *Learning and Instruction* **1994**, *4* (4), 295–312. https://doi.org/10.1016/0959-4752(94)90003-5.

(31) Johnstone, A. H.; Wham, A. J. B. The Demands of Practical Work. *Education in Chemistry* **1982**, *19* (3), 71–73.

(32) Johnstone, A. H. New Stars for the Teacher to Steer By? **1984**, *61* (10), 847–849.

(33) Shell, D. F.; Brooks, D. W.; Trainin, G.; Wilson, K. M.; Kauffman, D. F.; Herr, L. M. Working Memory. In *The Unified Learning Model: How Motivational, Cognitive, and Neurobiological Sciences Inform Best Teaching Practices*; Shell, D. F., Brooks, D. W., Trainin, G., Wilson, K. M., Kauffman, D. F., Herr, L. M., Eds.; Springer Netherlands: Dordrecht, 2010; pp 19–31. https://doi.org/10.1007/978-90-481-3215-7_3.

(34) El-Banna, H.; Johnstone, A. H. Capacities, Demands and Processes: A Predictive Model for Science Education. *Education in Chemistry* **1986**, *23*, 80–84.

(35) Hendry, G. Using Exemplars to Scaffold Learning. In *Reconceptualising Feedback in Higher Education*; Merry, M., Carless, D. P., Taras, Eds.; Abingdon: Routledge, 2013; pp 133–141.

(36) Hendry, G. D.; Anderson, J. Helping Students Understand the Standards of Work Expected in an Essay: Using Exemplars in Mathematics Pre-Service Education Classes. *Assessment & Evaluation in Higher Education* **2013**, *38* (6), 754–768. https://doi.org/10.1080/02602938.2012.703998.

(37) Nicol, D.; Thomson, A.; Breslin, C. Rethinking Feedback Practices in Higher Education: A Peer Review Perspective. *Assessment & Evaluation in Higher Education* **2014**, *39* (1), 102–122. https://doi.org/10.1080/02602938.2013.795518.

(38) *Use of A Pipette Pump*. http://www.molsci.ucla.edu/downloads/Use_of_a_pipette_pump.mp4 (accessed 2023-03-20).

(39) *Lab Technique Video: Pipetting*; 2014. https://www.youtube.com/watch?v=IXLgDnUVc3I (accessed 2023-03-20).

(40) *The Volumetric Pipet and Pipetting Technique*; 2014. https://www.youtube.com/watch?v=HC44xjs7dho (accessed 2023-03-20).

(41) *Calibration and Use of a Volumetric Pipet*; 2017. https://www.youtube.com/watch?v=0NmbYqERfoo (accessed 2023-03-20).

(42) *General and Organic Chemistry - Use of a Pipet*; 2017. https://www.youtube.com/watch?v=YMjy2sK_kBo (accessed 2023-03-20).

(43) Keen, C.; Sevian, H. Qualifying Domains of Student Struggle in Undergraduate General Chemistry Laboratory. *Chem. Educ. Res. Pract.* **2022**, *23* (1), 12–37. https://doi.org/10.1039/D1RP00051A.

(44) Wheeler, L. B.; Maeng, J. L.; Chiu, J. L.; Bell, R. L. Do Teaching Assistants Matter? Investigating Relationships between Teaching Assistants and Student Outcomes in Undergraduate Science Laboratory Classes. *Journal of Research in Science Teaching* **2017**, *54* (4), 463–492. https://doi.org/10.1002/tea.21373.

(45) Wan, T.; Geraets, A. A.; Doty, C. M.; Saitta, E. K. H.; Chini, J. J. Characterizing Science Graduate Teaching Assistants' Instructional Practices in Reformed Laboratories and

Tutorials. *International Journal of STEM Education* **2020**, *7* (1), 30. https://doi.org/10.1186/s40594-020-00229-0.

(46) Altowaiji, S.; Haddadin, R.; Campos, P.; Sorn, S.; Gonzalez, L.; Villafañe, S. M.; Groves, M. N. Measuring the Effectiveness of Online Preparation Videos and Questions in the Second Semester General Chemistry Laboratory. *Chem. Educ. Res. Pract.* **2021**, *22* (3), 616–625. https://doi.org/10.1039/D0RP00240B.

(47) Rodriques, R. A. B.; Bond-Robinson, J. Comparing Faculty and Student Perspectives of Graduate Teaching Assistants' Teaching. *J. Chem. Educ.* **2006**, *83* (2), 305. https://doi.org/10.1021/ed083p305.

(48) Eglington, L. G.; Kang, S. H. K. Interleaved Presentation Benefits Science Category Learning. *Journal of Applied Research in Memory and Cognition* **2017**, *6* (4), 475–485. https://doi.org/10.1016/j.jarmac.2017.07.005.

(49) Foster, N. L.; Mueller, M. L.; Was, C.; Rawson, K. A.; Dunlosky, J. Why Does Interleaving Improve Math Learning? The Contributions of Discriminative Contrast and Distributed Practice. *Mem Cogn* **2019**, *47* (6), 1088–1101. https://doi.org/10.3758/s13421-019-00918-4.

(50) Samani, J.; Pan, S. C. Interleaved Practice Enhances Memory and Problem-Solving Ability in Undergraduate Physics. *npj Sci. Learn.* **2021**, *6* (1), 1–11. https://doi.org/10.1038/s41539-021-00110-x.

(51) Brown, P. C.; III, H. L. R.; McDaniel, M. A. *Make It Stick: The Science of Successful Learning*; Belknap Press: Cambridge, MA, 2014.

(52) Duffy, E. M.; Cooper, M. M. Assessing TA Buy-in to Expectations and Alignment of Actual Teaching Practices in a Transformed General Chemistry Laboratory Course. *Chem. Educ. Res. Pract.* **2020**, *21* (1), 189–208. https://doi.org/10.1039/C9RP00088G.